AN INVESTIGATION OF THE COMPLEX MOTIONS INHERENT TO MACHINING SYSTEMS VIA A DISCONTINUOUS SYSTEMS THEORY APPROACH

A Dissertation

by

BRANDON CHRISTOPHER GEGG

Submitted to the Office of Graduate Studies of
Texas A&M University
in partial fulfillment of the requirements for the degree of

DOCTOR OF PHILOSOPHY

May 2009

Major Subject: Mechanical Engineering

AN INVESTIGATION OF THE COMPLEX MOTIONS INHERENT TO MACHINING SYSTEMS VIA A DISCONTINUOUS SYSTEMS THEORY APPROACH

A Dissertation

by

BRANDON CHRISTOPHER GEGG

Submitted to the Office of Graduate Studies of
Texas A&M University
in partial fulfillment of the requirements for the degree of

DOCTOR OF PHILOSOPHY

Approved by:

Chair of Committee,	Steve C. Suh
Committee Members,	Jean Luc Guermond
	Bryan Rasmussen
	Arun Srinivasa
	Albert C.J. Luo
Head of Department,	Dennis O'Neal

May 2009

Major Subject: Mechanical Engineering

ABSTRACT

An Investigation of the Complex Motions Inherent to Machining

Systems via a Discontinuous Systems Theory Approach. (May 2009)

Brandon Christopher Gegg, B.S., Southern Illinois University at Edwardsville;

M.S. Southern Illinois University at Edwardsville

Chair of Advisory Committee: Dr. Steve C. Suh

The manufacturing process has been a heavily studied area over the past century. The study completed herein has established a foundation for the future of manufacturing research. The next step of this industry is to become proficient at the micro and nano scale levels of manufacturing. In order to accomplish this goal, the modeling of machining system needs to be completely understood throughout the entire process. In effort to attack this problem, this study will focus on the boundaries present in machining systems; and will define and interpret the associated phenomena.

This particular focus is selected since nearly all manufacturing related studies concentrate on continuous processes; which by definition considers only one particular operation. There is a need to understand the phenomena corresponding to interactions of multiple processes of manufacturing systems. As a means to this end, the nonlinear phenomena associated in the continuous domains of machining systems will be modeled as linear to ensure the boundary interactions are clearly observed. Interference of additional nonlinearities is not the focus of this research. In this dissertation, the mechanical model for a widely accepted machine-tool system is presented.

The state and continuous domains are defined with respect to the boundaries in this system (contact and frictional force acting at the point of tool and work-piece contact). The switching sets defining plane boundaries for the continuous systems of this machine-tool will be defined and studied herein. The forces and force products, at the point of switching from one continuous system to another, govern the pass-ability of the machine-tool through the respective boundary. The forces and force product components at the switching points are derived according to discontinuous systems theory Luo [1]. Mapping definitions and notations are developed through the switching sets for each of the boundaries.

A mapping structure and notation for periodic interrupted cutting, non-cutting and chip seizure motions are defined. The interruption of the chip flow for a machining system will be investigated through a range of system parameters. The prediction of interrupted periodic cutting, non-cutting and chip seizure motion will be completed via closed form solutions for this machine-tool. The state of this system is defined to utilize the theory of Luo [1]. This is necessary to properly handle the frictional force boundary at the chip/tool interface, the onset of cutting boundary and the contact boundary between the tool and work-pieces.

The predictions by this method will be verified via numerical simulation and comparison to existing research. A goal of this research is to illustrate the effects of the dynamical systems interacting at the frictional force (chip/tool) boundary and the chip onset of growth and vanishing boundary. The parameter space for this machine-tool model is studied through numerical and analytical predictions, which provide limits on the existence of interrupted periodic cutting, non-cutting and chip seizure motions.

ACKNOWLEDGMENTS

I thank my committee chair, Dr. Steve Suh, and committee members, Dr. Jean Luc Guermond, Dr. Bryan Rasmussen, Dr. Arun Srinivasa, and Dr. Albert Luo, for their efforts in making my graduate experience and education meaningful and prosperous. Additionally, I thank my family and friends for their continued support and encouragement in my endeavors.

NOMENCLATURE

State and Coordinate Definitions:

$\mathbf{e}_X$ global vector definition X;

$\mathbf{e}_Y$ global vector definition Y;

$\overline{\mathbf{x}}$ state vector in the $\mathbf{e}_X$-direction;

$\overline{\mathbf{y}}$ state vector in the $\mathbf{e}_Y$-direction;

$\overline{\mathbf{r}}$ vector definition of the displacement states $(\overline{x}, \overline{y})$;

$d\overline{\mathbf{r}}/d\overline{t}$ vector definition of the velocity states $(\dot{\overline{x}}, \dot{\overline{y}})$;

$d^2\overline{\mathbf{r}}/d\overline{t}^2$ vector definition of the acceleration states $(\ddot{\overline{x}}, \ddot{\overline{y}})$;

$\mathbf{s}$ state vector for s.d.o.f.;

$\mathbf{x}$ state vector in the $\mathbf{e}_X$-direction;

$\mathbf{y}$ state vector in the $\mathbf{e}_Y$-direction;

$\tilde{\mathbf{x}}$ state vector in the $\tilde{x}$-direction;

$\tilde{\mathbf{y}}$ state vector in the $\tilde{y}$-direction;

$\overline{t}$ time variable;

t normalized time variable with respect to the eccentric excitation frequency Ω;

t_s time variable for s.d.o.f.;

s displacement measure for s.d.o.f.;

$\dot{s}$ velocity measure for s.d.o.f.;

$\ddot{s}$ acceleration measure for s.d.o.f.;

$\overline{x}$ displacement measure in the $\mathbf{e}_X$-direction from the equilibrium (X_{eq}, Y_{eq});

$\overline{y}$ displacement measure in the $\mathbf{e}_Y$-direction from the equilibrium (X_{eq}, Y_{eq});

$\dot{\overline{x}}$ velocity measure in the $\mathbf{e}_X$-direction;

$\dot{\overline{y}}$ velocity measure in the $\mathbf{e}_Y$-direction;

$\ddot{\overline{x}}$ acceleration measure in the $\mathbf{e}_X$-direction;

$\ddot{\overline{y}}$ acceleration measure in the $\mathbf{e}_Y$-direction;

x normalized displacement measure in the $\mathbf{e}_X$-direction;

y normalized displacement measure state in the $\mathbf{e}_Y$-direction;

$\dot{x}$ normalized velocity measure state in the $\mathbf{e}_X$-direction;

$\dot{y}$ normalized velocity measure state in the $\mathbf{e}_Y$-direction;

$\ddot{x}$ normalized acceleration measure state in the $\mathbf{e}_X$-direction;

$\ddot{y}$ normalized acceleration measure state in the $\mathbf{e}_Y$-direction;

$(\tilde{x}, \tilde{y})$ displacement normal and parallel to the tool-rake surface, respectively;

$(\dot{\tilde{x}}, \dot{\tilde{y}})$ velocity normal and parallel to the tool-rake surface, respectively;

$(\ddot{\tilde{x}}, \ddot{\tilde{y}})$ acceleration normal and parallel to the tool-rake surface, respectively;

$\tilde{y}_0$ initial $\tilde{y}$-direction measure at the point of switching on the friction boundary;

x_t second hand notation for the displacement measure $\tilde{x}$;

y_t second hand notation for the displacement measure $\tilde{y}$;

$\dot{x}_t$ second hand notation for the displacement measure $\dot{\tilde{x}}$;

$\dot{y}_t$ second hand notation for the displacement measure $\dot{\tilde{y}}$;

Λ coordinate transformation from the $(\tilde{x}, \tilde{y})$ system to the (x, y) system;

$M\left(\dot{\tilde{x}}, \dot{\tilde{y}}\right)$ cutting process $\mathbf{e}_X$-direction vector component;

$N\left(\dot{\tilde{x}}, \dot{\tilde{y}}\right)$ cutting process $\mathbf{e}_Y$-direction vector component.

Dynamic and Geometry Parameters:

m_{ch} mass of the chip;

m_e equivalent mass of eccentricity;

m_{eq} equivalent mass of a tool-piece and support structure;

m_s mass of single degree of freedom oscillator (s.d.o.f.);

Q_0 forcing amplitude of s.d.o.f.;

A_s normalized total force amplitude for s.d.o.f.;

A_e eccentric excitation force amplitude;

A_F normalized eccentric excitation force amplitude;

A_0 eccentricity excitation amplitude for chip adhesion (seizure) motion in the $\tilde{x}$-direction;

B_0 external force rate time-amplitude for chip adhesion (seizure) motion in the $\tilde{x}$-direction;

$F_p(\bar{t})$ eccentric excitation periodical force;

Ω eccentric excitation frequency;

Ω_s excitation frequency of s.d.o.f.;

k_s stiffness coefficient for s.d.o.f.;

c_s normalized stiffness coefficient for s.d.o.f.;

c_j *jth* domain normalized stiffness coefficient for s.d.o.f.;

k_x equivalent linear stiffness coefficient in the *x*-direction of the tool-piece;

k_y equivalent linear stiffness coefficient in the *y*-direction of the tool-piece;

k_1 equivalent linear stiffness coefficient in the y_β-direction of the work-piece;

k_2 equivalent linear stiffness coefficient in the $\tilde{x}$-direction of the chip;

$\bar{K}_{ij}$ normalized stiffness component in the *ij*-plane;

$K_{jk}^{(i)}$ re-normalized stiffness component in the *jk*-plane in the *ith* domain;
ω natural frequency for chip adhesion (seizure) motion in the $\tilde{x}$-direction;
ω_d damped natural frequency for chip adhesion (seizure) motion in the $\tilde{x}$-direction;
r_s damping coefficient for s.d.o.f.;
d damping coefficient for chip adhesion (seizure) motion in the $\tilde{x}$-direction;
d_s normalized damping coefficient for s.d.o.f.;
d_j *jth* domain normalized damping coef. for s.d.o.f.;
d_x equivalent linear viscous damping coef. in the *x*-direction of the tool-piece;
d_y equivalent linear viscous damping coef. in the *y*-direction of the tool-piece;
d_1 equivalent linear viscous damping coef. in the y_β-direction of the work-piece;
d_2 equivalent linear viscous damping coef. in the $\tilde{x}$-direction of the chip;
$\bar{D}_{ij}$ normalized damping comp. in the *ij*-plane;
$D_{jk}^{(i)}$ re-normalized damping comp. in the *jk*-plane in the *ith* domain;
d normalized damping coef. for chip adhesion (seizure) motion in the $\tilde{x}$-direction;
μ_{ks} friction coefficient for s.d.o.f.;
v belt velocity for s.d.o.f.;
$\dot{\bar{z}}$ relative velocity of the chip and tool-piece rake equilibrium measure;
$\bar{V}$ chip velocity $(=\Omega V)$;
V normalized chip velocity;
α tool-piece rake angle measure from a vertical reference line;
β tool-piece flank angle measure from a horizontal reference line;
g gravitational acceleration;
$\overline{OA}$ comp. measure from point *O* to *A*;
$\overline{OB}$ comp. measure from point *O* to *B*;
X_1 comp. measure from point *O* to *A*;
Y_1 comp. measure from point *O* to *B*;
δ_1 distance boundary 1 offset;
δ_2 distance boundary 2 offset;
η angle of applied eccentric/excitation force;
D_1 boundary 1 measure for contact with work-piece;
D_2 boundary 2 measure for cutting onset;
$\bar{x}_1^*$ work-piece contact point in the $\mathbf{e}_X$-direction;
$\bar{y}_1^*$ work-piece contact point in the $\mathbf{e}_Y$-direction;
$\bar{x}_2^*$ cutting process contact point in the $\mathbf{e}_X$-direction;
$\bar{y}_2^*$ cutting process contact point in the $\mathbf{e}_Y$-direction;

L_c chip contact length;

e_r coefficient of restitution for tool and work-piece impact.

Force Parameters:

b_j frictional force acting on m_s;

$\bar{F}_{fs}(\dot{s})$ frictional force for s.d.o.f.;

F_{fs} normalized frictional force acting on m_s;

F_{Ns} normal force for s.d.o.f.;

F_s normalized total force acting on m_s;

$\mathbf{n}^T_{\partial\Sigma_{jk}}$ transposed normal direction vector for the boundary $\partial\Sigma_{jk}$ for s.d.o.f.;

Σ_j *jth* domain reference for the s.d.o.f.;

$F_j(\mathbf{s}, t_s)$ *jth* domain frictional boundary force or normalized total force for s.d.o.f. ;

$\mathbf{F}_j^{(j)}(t)$ force vector field of the *jth* domain parameters in the *jth* domain for s.d.o.f.;

$F_j(t)$ normal comp. of *jth* domain vector field with respect to the friction boundary;

$\mathbf{F}_1(\bar{\mathbf{x}}, \bar{\mathbf{y}})$ tool-piece and work-piece contact force vector;

$\mathbf{F}_2(\bar{\mathbf{x}}, \bar{\mathbf{y}})$ cutting process force vector;

$F_{n1}(\bar{\mathbf{x}}, \bar{\mathbf{y}})$ tool-piece and work-piece contact force amplitude;

$F_{n2}(\bar{\mathbf{x}}, \bar{\mathbf{y}})$ cutting process force amplitude;

F_{1x} tool-piece and work-piece contact force, *x* component;

F_{2x} cutting process force, *x* component;

F_{1y} tool-piece and work-piece contact force, *y* component;

F_{2y} cutting process force, *y* component;

$\bar{A}_x$ normalized eccentric excitation amplitude in the $\mathbf{e}_X$-direction;

$A_x^{(i)}$ re-normalized *ith* domain eccentric excitation amplitude in the $\mathbf{e}_X$-direction;

$\bar{A}_y$ normalized eccentric excitation amplitude in the $\mathbf{e}_Y$-direction;

$A_y^{(i)}$ re-normalized *ith* domain eccentric excitation amplitude in the $\mathbf{e}_Y$-direction;

$\bar{C}_x$ normalized equilibrium forces in the $\mathbf{e}_X$-direction;

$C_x^{(i)}$ re-normalized *ith* domain equilibrium forces in the $\mathbf{e}_X$-direction;

$\bar{C}_y$ normalized equilibrium forces in the $\mathbf{e}_Y$-direction;

$C_y^{(i)}$ re-normalized *ith* domain equilibrium forces in the $\mathbf{e}_Y$-direction;

C_0 external equilibrium force constant for chip adhesion motion in the $\tilde{x}$-direction.

Boundary References and Notations:

C^0 reference for continuity of the zero derivative;

C^1 reference for continuity of the first derivative;
$\mathbf{D}_1$ boundary 1 measure vector field $(D_1, \dot{D}_1)$;
$\mathbf{D}_2$ boundary 2 measure vector field $(D_2, \dot{D}_2)$;
$\mathbf{D}_3$ boundary 3 measure vector field $(D_3, \dot{D}_3)$;
$\mathbf{D}_4$ boundary 4 measure vector field $(D_4, \dot{D}_4)$;
$\dot{\mathbf{D}}_1$ boundary 1 measure force vector field $(\dot{D}_1, F_{D_1}^{(i)}(\mathbf{D}_1, t))$;
$\dot{\mathbf{D}}_2$ boundary 2 measure force vector field $(\dot{D}_2, F_{D_2}^{(i)}(\mathbf{D}_2, t))$;
$\dot{\mathbf{D}}_3$ boundary 3 measure force vector field $(\dot{D}_3, F_{D_3}^{(i)}(\mathbf{D}_3, t))$;
$\dot{\mathbf{D}}_4$ boundary 4 measure force vector field $(\dot{D}_4, F_{D_4}^{(i)}(\mathbf{D}_4, t))$;
$\Omega_1(x, y)$ domain 1 ref., tool-piece vib. and no contact with the work-piece;
$\Omega_2(x, y, \dot{x}, \dot{y})$ domain 2 ref., tool-piece vib. and no cutting contact with the work-piece;
$\Omega_3(x, y, \dot{x}, \dot{y})$ domain 3 ref., tool-piece vib. and cutting contact with the work-piece $(\dot{\tilde{y}} < V)$;
$\Omega_4(x, y, \dot{x}, \dot{y})$ domain 4 ref., tool-piece vib. and cutting contact with the work-piece $(\dot{\tilde{y}} > V)$;
$F_{D_1}^{(i)}(\mathbf{D}_1, t)$ total *ith* domain force comp. acting on m_{eq} in the y_β-direction, w.r.t. $\mathbf{D}_1$;
$F_{D_2}^{(i)}(\mathbf{D}_2, t)$ total *ith* domain force comp. acting on m_{eq} in the $\tilde{x}$-direction, w.r.t. $\mathbf{D}_2$;
$F_{D_3}^{(i)}(\mathbf{D}_3, t)$ total *ith* domain force comp. acting on m_{eq} in the $\tilde{y}$-direction, w.r.t. $\mathbf{D}_3$;
$F_{\tilde{y}}^{(2)}(\tilde{\mathbf{x}}, \tilde{\mathbf{y}}, , t)$ total domain 2 force comp. acting on m_{eq} in the $\tilde{y}$-direction, w.r.t. $\mathbf{D}_3$;
$F_{\tilde{y}}^{(4)}(\tilde{\mathbf{x}}, \tilde{\mathbf{y}}, , t)$ total domain 4 force comp. acting on m_{eq} in the $\tilde{y}$-direction, w.r.t. $\mathbf{D}_3$;
$F_{D_4}^{(i)}(\mathbf{D}_4, t)$ total *ith* domain force comp. acting on m_{eq} in the $\tilde{y}$-direction, w.r.t. $\mathbf{D}_4$;
$\partial\Omega_{12}(x, y, \dot{x}, \dot{y})$ boundary 1 defined by $D_1(x, y) = 0$;
$\partial\Omega_{24}(x, y, \dot{x}, \dot{y})$ boundary 2 or 3 defined by $D_2(x, y) = 0$ or $D_3(\dot{x}, \dot{y}) = 0$, resp.;
$\partial\Omega_{32}(x, y, \dot{x}, \dot{y})$ boundary 2 or 4 defined by $D_2(x, y) = 0$ or $D_4(\dot{x}, \dot{y}) = 0$, resp.;
$\partial\Omega_{34}(x, y, \dot{x}, \dot{y})$ boundary 3 defined by $D_3(x, y) = 0$;
$\Xi_{D_j}^i$ switching set/plane near boundary D_j in domain Ω_i;
$\Xi_{\tilde{y}}^i$ switching set/plane near boundary D_3 in domain Ω_i;
$P_{(jk)i}$ mapping beg. on boundary D_j ending on bound. D_k and traversing domain Ω_i;
P_{ij} periodic motion traversing domain Ω_j then Ω_i with period-one motion.

Closed Form Solution Parameters:
C_i homogeneous coefficients for a two-degree-of-freedom linear oscillator;

r_{ij} mode shape for a two-degree-of-freedom linear oscillator;

$\lambda_i^{(j)}$ *ith* eigenvalue in the *jth* domain for a two-degree-of-freedom linear oscillator;

A_{Px} particular solution amplitude in the *x*-direction (cosine term);

A_{Py} particular solution amplitude in the *y*-direction (cosine term);

B_{Px} particular solution amplitude in the *x*-direction (sine term);

B_{Py} particular solution amplitude in the *y*-direction (sine term);

C_{Px} particular solution amplitude in the *x*-direction (constant term);

C_{Py} particular solution amplitude in the *y*-direction (constant term);

α_i real valued component of *ith* eigenvalue;

β_i imaginary valued component of *ith* eigenvalue;

$\tilde{C}_i$ homogeneous coefficient for chip adhesion motion in the $\tilde{x}$-direction;

A_5 particular solution amplitude in the $\tilde{x}$-direction (cosine term); for chip adhesion (seizure);

B_5 particular solution amplitude in the $\tilde{x}$-direction (sine term); for chip adhesion (seizure);

C_5 particular solution amplitude in the $\tilde{x}$-direction (time rate term); for chip adhesion (seizure);

D_5 particular solution amplitude in the $\tilde{x}$-direction (constant term); for chip adhesion (seizure).

Acronyms:

U.D. Underlying Dynamics - natural characteristics associated with a physical system;

S.S.C Semi-stable characteristics - periodic motion with undesirable traits;

S.C. Stable characteristics – periodic motion with desirable traits;

U.C. Unstable characteristics – no discernable quantitative periodic traits;

Qual.D. Qualitative definition – non-numeric description;

Quan.D. Quantitative definition – numeric description;

H.S.O. High speed operation – special material design for conditions outside of traditional operating speeds;

H.Q.M.S. High quality machined surface – surface roughness value remaining less than traditional expectations;

I.R.P. Increased rate of production – any increase due to advances in machine design;

M.O.C. Minimize operating costs – any reduction as a result of advances in machine design;

I.C. Interrupted cutting – any motions attributed to reduction of rate or halt of cutting;

C.M. Common mapping – any motion traditionally observed in the machining systems.

TABLE OF CONTENTS

Page

CHAPTER Page

CHAPTER Page

LIST OF TABLES

Page

LIST OF FIGURES

Page

Page

Page

Page

Page

Page

Page

Page

Page

Page

Page

Page

Page

Page

Page

CHAPTER I

INTRODUCTION: THE MACHINING PROBLEM

The manufacturing process has been scrutinized in nearly all aspects in the past several decades. Among these studies are those which focus on various approaches to the manufacturing process, such as *mechanics of materials*, *energy* and *dynamics* techniques. Among the earliest studies of manufacturing systems was Merchant in 1945 [2,3]. Merchant developed theory predicting the shear angle solution from the principle of *minimum work*. From a materials point of view, Oxley [4] studied the *mechanics* of metal cutting by examining the shear plane solutions with ideal slip-line theory Childs [5].

The *stick-slip* motion has been termed in machining studies as early as 1969 Rubenstien and Storie [6]. The *stick-slip* phenomenon is predominantly observed in dynamical systems and contact material flow problems. In 1979, *plasticity* theory was applied to metal cutting in theory Shouchry [7]. A rounded tool edge was studied for the stagnation depths of material flow in Basuray [8]. The stagnation point (or neutral angle, defining the source of work-piece material flow) was derived by equating the *power* of the ploughing tool and cutting forces.

This dissertation follows the style of the *Transactions of the ASME Journal of Manufacturing Science and Engineering.*

The boundary conditions for a comparison between *seizure* and *sliding* motions of a chip based on the seized area to real contact area ratio was studied by Wright et. al. [9]. The study shows the *sticking* region of the chip on the tool rake surface is characterized by a constant shear stress at the chip/tool interface. The fundamental classification of chip structures in past research and a current model was developed to predict and discuss the stability of a certain type of chip formation. The stability of a chip structure is mainly contributed to the seizure of the work-piece chip material to the tool-piece rake surface Astakhov et. al. [10]. Two structures contributed to this phenomenon are the continuous and fragmentary hump-backed chip.

Son et al. [11] extended Basuray et al.'s [8] work of a rounded edge tool to determine the minimum cutting depth. Experimental results showed the surface quality was best when cutting was conducted near the minimum cutting depth (continuous chip formation was observed). Liu and Melkote [12] derived surface roughness due to stress fields, feed rates, and tool edge radius. Son et al. [13] considered vibration cutting applied to determine the response with respect to minimum cutting thickness. Recent studies including the stick-slip phenomena, which specifically point out the stick-slip in the cutting process, are typically modeled by Finite Element methods, validated via approximate methods and high speed photography by Simoneau et al [14], Woon et al [15], Wahi and Chaterjee [16], and Vela-Martinez et. al. [17].

The breakdown of the manufacturing process has been traditionally completed by considering continuous processes. However, recently researchers have begun to recognize the importance in comprehensive modeling of the process. For instance,

following the dynamics approach to modeling a machine-tool will lead to a web of interacting continuous systems. Through this complex network the prediction of realistic phenomena; such as frictional chatter, regenerative chatter, cutting to ploughing transition transient effects etcetera, is possible. To model vibration of the machine tool problem, many mechanical models have been developed.

Popular models are those given by a one-degree of freedom oscillator (e.g., Moon and Kalmar-Nagy [18]) and two-degree of freedom oscillator (e.g., [19]-[28]). In many cases, the single degree of freedom model is not adequate to describe such vibration of the machine tool in cutting process Wiercigroch and Budak [29]. Thus, the two-degree of freedom oscillators were developed with the practical combinations of the nonlinearities through mode coupling and the loss of contact with the work-piece, etc. Moon and Kalmar-Nagy [18]. Analytical investigations of machine tools in cutting process were studied through the two-degree of freedom oscillator (e.g., [19]-[22]). The chaotic dynamics of the machine tool system were also investigated (e.g., [23]-[25]).

Moon and Kalmar-Nagy [18] reviewed various models of complex dynamics in machine tool systems. Wiercigroch and Budak [29] reviewed fundamental cutting forces and discussed sources of nonlinearities in metal cutting similar to those discussed by Moon and Kalmar-Nagy [18]. Fang and Jawahir [30] surveyed restricted contact machining operations including: delay models, nonlinear stiffness, hysteretic cutting forces, visco-elastics and nonlinear cutting forces. Through these studies, a clear description of the nature of nonlinearities in the machine tool systems has *not* been

provided. Luo and Gegg [31] applied a general theory of discontinuous systems on connectable domains to a forced dry friction oscillator.

The stick and non-stick motions and grazing phenomenon with respect to a friction (velocity) boundary were presented through the vector fields of the oscillator. The necessary and sufficient conditions defining the pass-ability of the motion from one continuous system to another are derived and validated. In this dissertation, such an idea will be extended and the model for dynamics of a machine-tool in the cutting, non cutting and chip seizure processes will be developed. Wu and Liu presented an analytical model of cutting dynamics to explain chatter vibration, friction and mode coupling effects [19,20]. The two-degree of freedom system included friction, on the rake face of the machine-tool, simulated by a traveling belt.

Wiercigroch [32] studied the stick-slip phenomenon, associated with a traveling belt analogy, for a machine-tool. Among research, the intermittent loss of cutting Chandiramani and Pothala [28] and chip stick-slip motion Gegg et al. [33] have been initially studied. Wiercigroch [25] modeled cutting forces for a two degree of freedom machine tool model through multiple discontinuities; which considered loss of contact with the chip [25]. Wiercigroch and Cheng [24] developed an orthogonal cutting model with stochastic dynamics; where various phenomena such as grazing and stick motion were observed. Wiercigroch and de Kraker [34] reviewed the traditional approaches to non-smooth systems; with applications ranging from one and two degree of freedom systems to multiple degrees of freedom in orthogonal machine-tool systems.

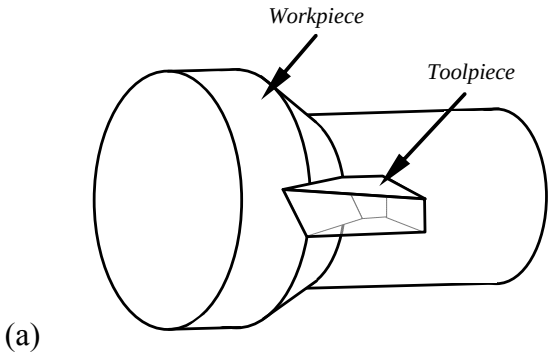

(a)

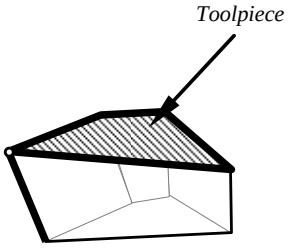

(b)

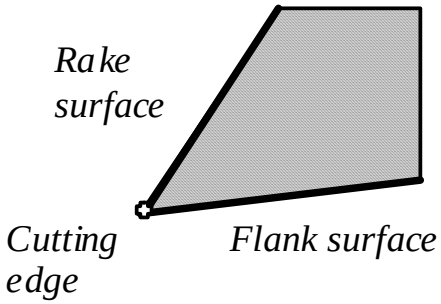

(c)

Fig. 1 Physical Setup: (a) tool and work-piece sample configuration, (b) tool-piece with rake and flank surface bolded, (c) 2-D tool-piece surface definition.

Warminski et al. [35] studied a nonlinear cutting force model with multiple discontinuities, based on Grabec's model [23,27]. The system was analyzed through a perturbation scheme. The various types of machine-tool orientations in the manufacturing environment consist of: the fixed work-piece with a rotating and/or traversing tool-piece; and the fixed tool-piece with a rotating and/or traversing work-piece. One such configuration is shown in Fig. 1(a). Limits on the machining systems include, but are not limited to: operation over a broad range of conditions; quality of the work-piece finish; rate of production; and maintenance intervals.

Understanding the underlying dynamics of machining systems is necessary for these limits to be altered. For example, the ever-present drive towards higher operating speeds, in manufacturing, requires an advanced understanding and analysis. In order to study these dynamics we must first consider the specific type of problem setup. A basic representation of the machine-tool network can be described by three general situations. One exists when there is no contact of the tool-piece and work-piece.

The second exists where the tool contacts the work-piece and no cutting occurs. The last situation exists when there is motion of the tool in contact with the work-piece and cutting occurs. At the contact point, forces sufficient to produce cutting of material, friction on the tool rake face of the tool is present, see Fig. 1(b,c). The friction forces generated on the surface are velocity dependent and discontinuous. This type of boundary is susceptible to stick-slip motions.

A multitude of discontinuities, such as, the cutting and thrust forces, elastic deformation and stagnation effects are a natural occurrence in machining systems. The

discontinuities considered to be the most basic to machine-tool systems are: displacement boundaries (loss of contact with the work-piece); force boundaries (onset of cutting); and velocity boundaries (chip/tool rake and work-piece/tool flank stick-slip). Study of these boundaries is paramount to the defining the underlying physics and interpretation of the bifurcations observed in machine-tool systems. A limited amount of research has been completed on such machine-tool systems. The loss of cutting and contact represent special cases of discontinuities.

Some of the earliest studies of discontinuous systems were those by Hartog (1931) [36]; the author investigated the forced vibration with Coulomb and viscous damping in theory and experiment. Among the first to approach discontinuous systems in general, was Filippov [37,38]. Additional theoretical work was completed by Aubin [39,40]. In 2005, Luo developed a general theory for the local singularity of non-smooth dynamical systems on connectable domains; which is employed herein [1]. In effort to simply present the application of discontinuous systems theory, a friction model will be presented.

Consider a periodically forced oscillator consisting of a mass m_s, a spring of stiffness k_s and a damper of viscous damping coefficient r_s, as shown in Fig. 2. Also, this oscillator rests on a horizontal belt surface. The belt travels with a constant speed v. The absolute coordinate system $s(t)$ is for the mass. Consider a periodical force $Q_0 \cos \Omega_s t_s$ exerting on the mass, where Q_0 and Ω_s are the excitation strength and frequency, respectively.

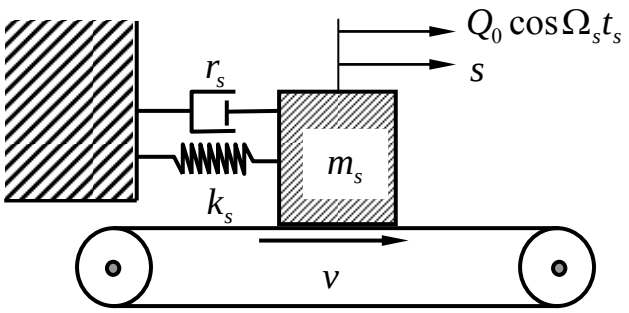

Fig. 2 The schematic for a mechanical model of a linear oscillator with dry-friction.

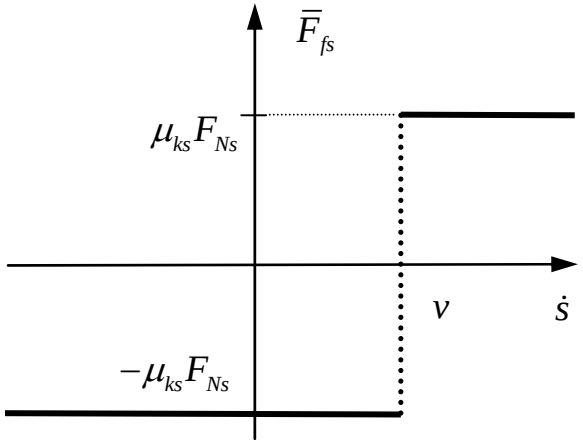

Fig. 3 The friction force for a mechanical model of a linear oscillator with dry-friction.

Since the mass contacts the moving belt with friction, the mass can move along, or rest on, the belt surface. Further, a kinetic friction force shown in Fig. 3 is described as

$$\bar{F}_{fs}(\dot{s}) = \begin{cases} \mu_{ks} F_{Ns}, & \dot{s} \in [v, \infty) \\ [-\mu_{ks} F_{Ns}, \mu_{ks} F_{Ns}], & \dot{s} = v \\ -\mu_{ks} F_{Ns}, & \dot{s} \in (-\infty, v] \end{cases} \tag{1.1}$$

where $\dot{s} \triangleq ds/dt$, μ_{ks} and F_{Ns} are the friction coefficient and the normal force to the contact surface, respectively. For the model in Fig. 2, the normal force is $F_{Ns} = m_s g$, where g is the gravitational acceleration. For the mass moving with the same speed as the belt surface, the normalized non-friction forces acting on the mass in the *s*-direction is defined as

$$F_s = A_s \cos \Omega_s t_s - 2dv - cs, \quad \text{for } \dot{s} = v \tag{1.2}$$

where $A_s = Q_0/m_s$, $d_s = r_s/2m_s$ and $c_s = k_s/m_s$. This force cannot overcome the friction force for stick motions, i.e., $|F_s| \le |F_{fs}|$ and $F_{fs} = \bar{F}_{fs}/m_s$.

Therefore, the mass has zero relative motion, with respect, to the belt; and no acceleration exists, i.e.,

$$\ddot{s} = 0, \qquad \text{for } \dot{s} = v. \tag{1.3}$$

If $|F_s| > |F_{fs}|$, the non-friction force will overcome the static friction force on the mass and the non-stick motion will appear. The F_s only exists during the stick motion; hence, the expression $|F_s| > |F_{fs}|$ holds only during the stick motion. For the non-stick motion, the mass has non-zero relative motion, the total force acting on the mass is

$$F = A_s \cos \Omega_s t_s - F_f \operatorname{sgn}(\dot{s} - v) - 2d_s \dot{s} - c_s s, \quad \text{for } \dot{s} \neq v; \tag{1.4}$$

$\operatorname{sgn}(.)$ is the sign function. The equation of the non-stick motion for this oscillator with friction is

$$\ddot{s} + 2d_s\dot{s} + c_s s = A_s \cos\Omega_s t_s - F_{fs}\,\mathrm{sgn}\left(\dot{s} - v\right), \text{ for } \dot{s} \neq v. \tag{1.5}$$

Since Eq.(1.5) is discontinuous, the theory of Luo [1] is employed as a systematic and alternative approach for investigation of friction induced vibration. The investigation presented herein focuses on the discontinuity as the basis for solutions. According to the general theory presented in Luo [1] and summarized in the appendix, the forces are

$$F_j\left(\mathbf{s}, t_s\right) = A_s \cos\Omega_s t_s - b_j - 2d_j\dot{s} - c_j s, \quad (j \in \{1,2\}). \tag{1.6}$$

Note that $b_i = \mu_{ks} g\,\mathrm{sgn}\left(\dot{s} - v\right)$, $d_i = d_s$ and $c_i = c_s$ for the model in Fig. 2. The stick and non-stick motion is also known as the non-passable and passable motion, respectively.

Since the dynamic systems have been defined, the conditions for the passage of the motion through the friction boundary of Eq.(1.1) are presented through the vector fields. From Eq.(A12) in the appendix, the stick motion (mathematically a special case of the sliding motion) through the real flow is guaranteed in general form by

$$\left[\mathbf{n}_{\partial\Sigma_{jk}}^T \bullet \mathbf{F}_j^{(j)}\left(t_{m-}\right)\right] \times \left[\mathbf{n}_{\partial\Sigma_{jk}}^T \bullet \mathbf{F}_k^{(k)}\left(t_{m-}\right)\right] < 0. \tag{1.7}$$

Note that t_m represents the time for the motion on the velocity boundary, and $t_{m\pm} = t_m \pm 0$ indicates responses in the two domains rather than on the boundary. The stick criterion presented thus far represents the real flow of the motion at the boundary. Implying, if the criterion of Eq.(1.7) is satisfied the stick motion (non-passable motion) is predicted.

When the stick motion exists along the boundary the imaginary flow exists in a similar manner as Eq.(1.7). The imaginary flow is the vector field defined by the computation of the forces in Eq.(1.6) with the parameters of both domains. In actuality the motion is moving along the boundary, and not in the domain governed by Eq.(1.5).

Rather the motion is actually governed by Eq.(1.3), while on the boundary. From Eq.(A9) and Eq.(A10) in the appendix, the non-stick motion (or called passable motion through the boundary in Luo [1,41] through the real or imaginary flows is guaranteed by

$$\left.\begin{aligned}\left[\mathbf{n}^T_{\partial\Sigma_{jk}}\bullet\mathbf{F}^{(j)}_j\left(t_{m-}\right)\right]\times\left[\mathbf{n}^T_{\partial\Sigma_{jk}}\bullet\mathbf{F}^{(k)}_k\left(t_{m+}\right)\right]>0,\\ \left[\mathbf{n}^T_{\partial\Sigma_{jk}}\bullet\mathbf{F}^{(j)}_j\left(t_{m-}\right)\right]\times\left[\mathbf{n}^T_{\partial\Sigma_{jk}}\bullet\mathbf{F}^{(k)}_j\left(t_{m-}\right)\right]>0.\end{aligned}\right\} \tag{1.8}$$

From Eq.(A11) of the appendix the normal vector of the frictional boundary is

$$\mathbf{n}_{\partial\Sigma_{12}}=\mathbf{n}_{\partial\Sigma_{21}}=\left(0,1\right)^T. \tag{1.9}$$

Therefore, we have

$$\left.\begin{aligned}\mathbf{n}^T_{\partial\Sigma_{jk}}\bullet\mathbf{F}^{(j)}_j\left(t\right)=\mathbf{n}^T_{\partial\Sigma_{kj}}\bullet\mathbf{F}^{(j)}_j\left(t\right)=F_j\left(\mathbf{s},t\right),\\ \mathbf{n}^T_{\partial\Sigma_{jk}}\bullet\mathbf{F}^{(k)}_j\left(t\right)=\mathbf{n}^T_{\partial\Sigma_{kj}}\bullet\mathbf{F}^{(k)}_j\left(t\right)=F_k\left(\mathbf{s},t\right).\end{aligned}\right\} \tag{1.10}$$

From Eq.(1.7) and Eq.(1.10), the conditions for stick and non-stick motions in the simplest form, respectively, are:

$$F_1\left(t_{m-}\right)\times F_2\left(t_{m-}\right)<0 \text{ and } F_1\left(t_{m\pm}\right)\times F_2\left(t_{m\mp}\right)>0. \tag{1.11}$$

From the theory for non-smooth dynamical systems in Luo and Gegg [41-45], the conditions for onset and vanishing of the stick motions are

$$F_1\left(t_{m-}\right)\times F_2\left(t_{m-}\right)=0. \tag{1.12}$$

Eq.(1.12) is verified physically by the frictional forces matching the static friction force; thus creating a zero total force on the mass.

The stick motion or motion along the friction boundary is defined, for model of Fig. 2, as the mass moving at a constant velocity. Direct integration of Eq.(1.3) with initial conditions (s_i,v,t_i) yield

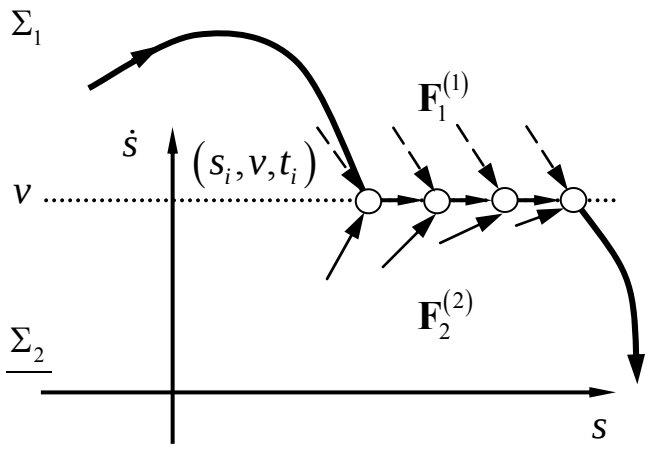

Fig. 4 Vector fields for stick motion in a linear oscillator with dry-friction.

$$s = v\left(t_s - t_{si}\right) + s_i. \tag{1.13}$$

Substitution of Eq.(1.3) and Eq.(1.13) into Eq.(1.6) gives the forces in the very small δ-neighborhood of the stick motion ($\delta \to 0$) in the two domains Σ_k ($k \in \{1,2\}$), i.e.,

$$F_k\left(t_{m-}\right) = -2d_k v - c_k\left[v\left(t_{m-} - t_i\right) + s_i\right] + A_0 \cos \Omega t_{m-} - b_k. \tag{1.14}$$

A sketch of the stick motion is illustrated in Fig. 4. The condition for the stick motion is presented through the vector fields $\mathbf{F}_1^{(1)}(t)$ and $\mathbf{F}_2^{(2)}(t)$.

The disappearance condition for stick (or sliding) motion along the velocity boundary is illustrated with $F_2\left(t_{m-}\right) = 0$ (stick vanishing point, S.V.P.). The vector field maintains a zero slope in the phase plane at the point of vanishing. The sketch of Fig. 4 is illustrated in the phase plane simulation of Fig. 5(a). Through the actual simulation of the motion throughout the phase plane, the forces both real and imaginary are shown

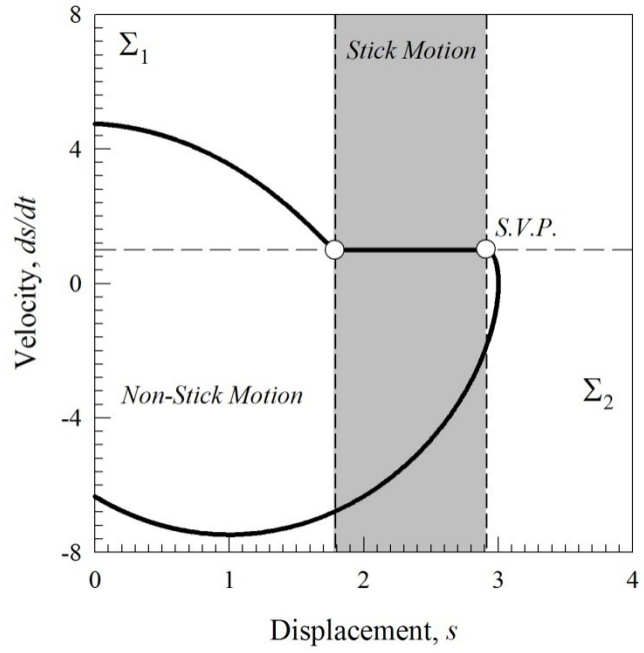

(a)

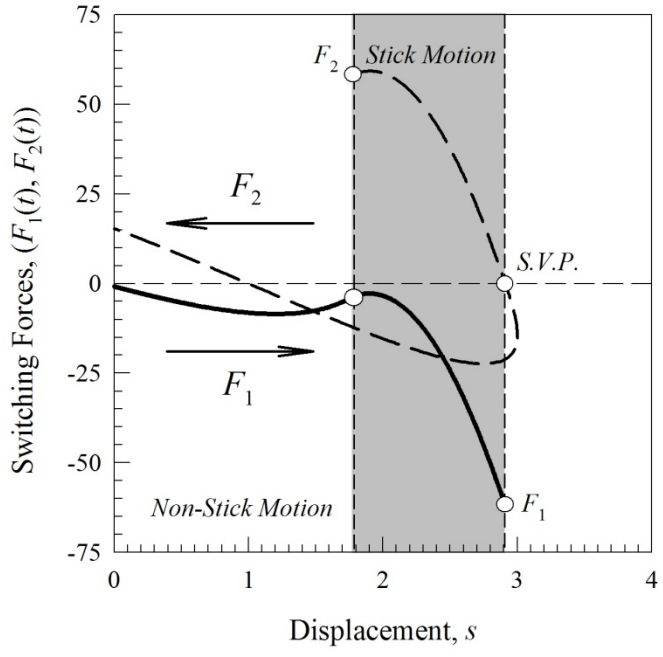

(b)

Fig. 5 Simulation for stick motion in a linear oscillator with dry-friction: (a) phase plane, (b) force plane; $c_1 = c_2 = 30, d_1 = 1, d_2 = 0, b_1 = -b_2 = 30, \Omega_s = 1.158, A_0 = 90, V = 1.$

during stick motion in Fig. 5(b). The thin and thick lines in Fig. 5(b) denote the total force acting on the mass with respect to the domain Σ_1 and Σ_2, respectively. The forces are computed with Eq.(1.14). The dark shaded region denotes the existence of stick motion where the imaginary flow is illustrated.

Objectives

The ambitions of this research are: to establish definitions of the underlying dynamics of interrupted cutting motions in a machining-system and to establish modeling guidelines for a machine-tool system as a means to the end of operating a machine-tool system over a broad range of parameters exhibiting semi-stable / stable characteristics. Research within this focus leads to a qualitative and quantitative definitions of how the semi-stable interrupted cutting periodic motions lead to unstable motions and vice versa.

Research Pathway

This research will analyze a machine-tool system inspired by the work of Wu and Liu [19,20] and Grabec [23,27]. Wu and Liu analyzed a two degree of freedom model of the tool-piece with applied external forces acting on the rake and flank tool-piece faces. The force model contained several discontinuities defined by the three previously mentioned situations: no contact of the tool and work-pieces; contact of the tool and work-pieces with no cutting; and contact of the tool and work-pieces with cutting. The system of discontinuous forces has been investigated by authors such as Berger [26], Wiercigroch

and Cheng [25] and Warminski et al. [35].

In each of these cases the discontinuities were acknowledged but they were not sufficiently investigated.

In this study:

1. The methodology for discontinuous systems of Luo [1] will be applied to investigate the machine-tool system;
2. The mappings of motion in the vicinity of the system constraints will be defined and discussed;
3. The criteria for the interrupted cutting periodic motions will be developed through the state and mapping forms;
4. The methodology for prediction of interrupted cutting periodic motions in a machining system will be developed;
5. The periodic interrupted cutting motions in such a model will be numerically predicted and discussed via closed form solutions;
6. Simulations of the interrupted cutting periodic motions in the machine-tool system will be completed;
7. The near interruption of cutting phenomena in the machine-tool system will be illustrated and discussed;
8. The chip and tool-piece seizure in the machine-tool system will also be illustrated and discussed;
9. The analytical prediction of periodic interrupted cutting motions will be completed via closed form solutions for two common mappings;
10. The simulations to verify the analytical predictions of such mappings will be

completed.

The justification of this research lies in the fact the above methodology clearly defines the interrupted cutting motions in this machine-tool system. The distinct criteria of passable and non-passable motions will be formed through these definitions. This describes bifurcations caused by interactions of neighboring continuous dynamical systems.

Contributions and Impact

This research provides a clear and concise approach to an existing problem, in the manufacturing environment, from an alternative view. The main contributions to machining systems are:

- The network of continuous systems are well defined and mapped for a clear definition of how such a system is traversed;
- The underlying dynamics of a machining system are well defined, hence the bifurcation causing phenomena is defined;
- The quantitative definitions of passage and non-passage of motion for the frictional and contact boundaries in a machine-tool system are derived for the first time in literature;
- The dominant routes to unstable motions in this machining system are well defined;
- The detailed parameter investigation provides guidelines for future research of such boundaries.

Concentrating this study on the apparent discontinuities allows the nature of the complex motions in this machine-tool system to be well defined. The application of non-smooth systems theory to such a complicated model is the first research to well define the nature of interrupted cutting with respect to the boundaries considered herein. The impact on the area of discontinuous systems is in the understanding of interrupted cutting due to the grazing phenomena / chip seizure in a network of multiply connected continuous systems. The application of modern discontinuous systems theory to this machine-tool and the interpretation herein is unique among literature. The next chapter will develop the mechanics of the motion for the machine-tool model considered herein.

CHAPTER II

MECHANICAL MODEL: DEVELOPMENT

The cutting process in manufacturing can be fundamentally modeled by a two-degree of freedom tool-piece model with external force effects due to contact and cutting of a work-piece Moon and Kalmar-Nagy [18]. For example, the turning process is a common machining practice consisting of "a single point tool that removes unwanted material to produce a surface of revolution," Shaw [45] see Fig. 6. Cutting actions similar to lathing, known as orthogonal cutting, are sawing, planing, and broaching Shaw [45]. Orthogonal cutting is the flow of removed material across the tool surface at a perpendicular angle to the cutting edge. The evolution of the mechanical model describing orthogonal cutting begins where the tool and work-pieces are noted by masses m and m_{eq}; respectively, see Fig. 7(a).

The tool-piece is governed by viscous damping and linear stiffness forces of coefficients d_x, d_y, and k_x, k_y; respectively. As noted in Fig. 7(a), the large arrows mark two paths or phases a machine-tool could experience. Phase one is the contact of the tool and work-piece without cutting occurring, see Fig. 7(b). The contact forces transmitted by the work-piece are resolved into the normal direction with respect to the contact surface. The equivalent response of the work-piece is modeled by viscous damping and linear stiffness forces of coefficients d_1 and k_1; respectively (Fig. 7(c)).

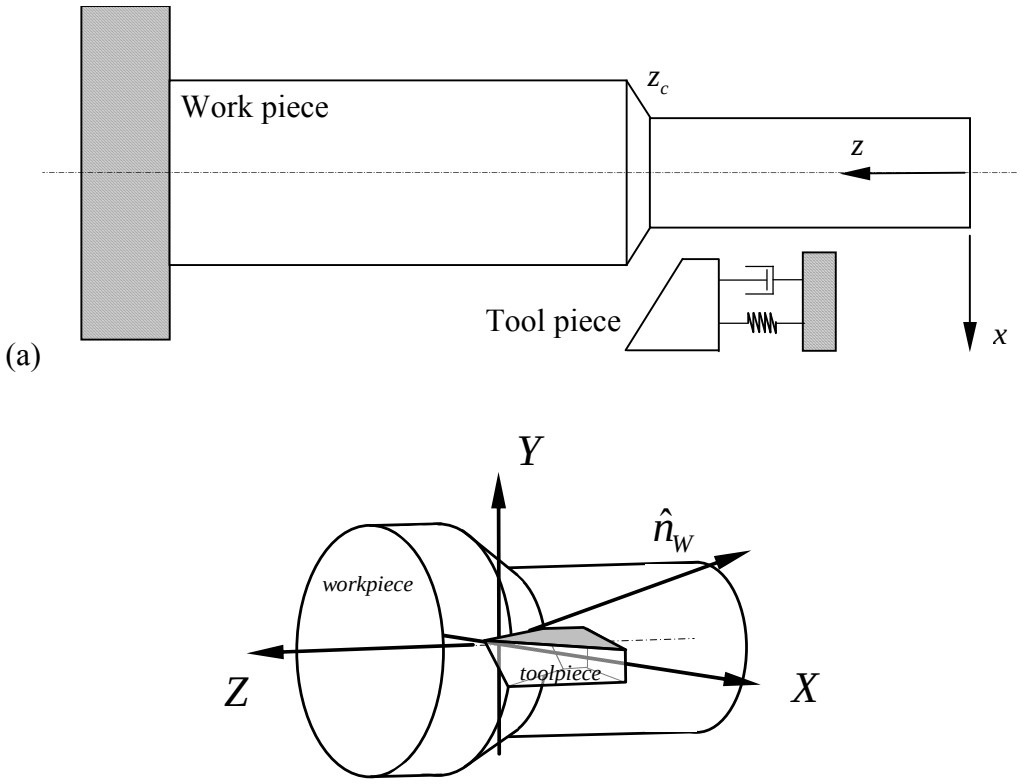

Fig. 6 Tool piece and work piece configuration at point of cutting.

In this case the contact surface is the bottom face (or flank surface), see Fig. 7. The non-cutting phase can be resolved to the model of Fig. 7(e); where the forces acting on the tool-piece rake face do not exist. The tool rake surface, cutting edge and flank surface are shown in Fig. 7 (a). Phase two is the case where the tool contacts the work-piece and the cutting conditions are satisfied. A chip will form on the top-left face (or rake surface) of the tool-piece, see Fig. 7(b).

Since the typical mass of a chip m_{ch} is quite small the chip simply transmits forces and has no significant acceleration independent of the tool or work-pieces (as far

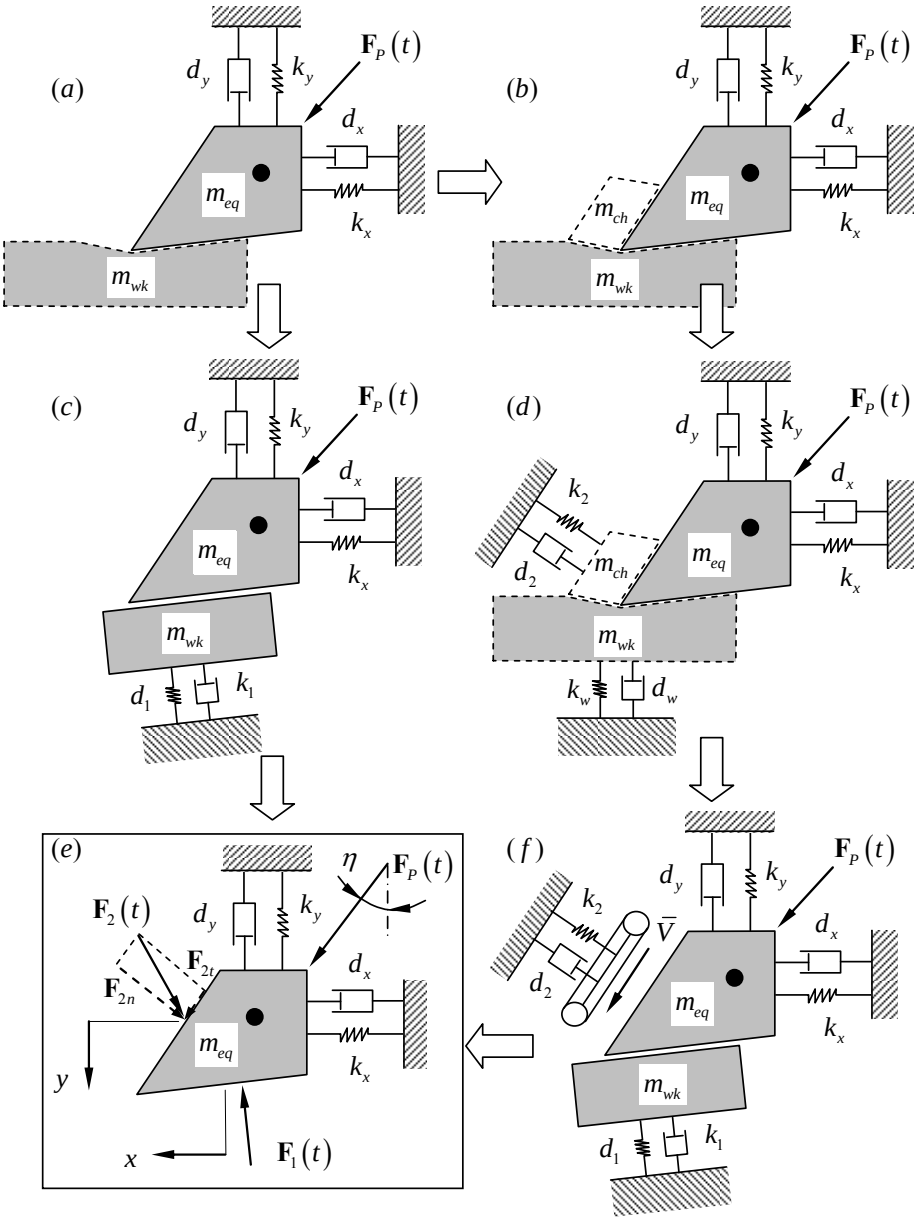

Fig. 7 Cutting tool mechanical model: (a) tool and work-pieces in contact (no cutting), (b) tool-piece, work-piece and chip in contact (cutting), (c) tool-piece and work-piece equivalent forces, (d) tool-piece, work-piece and chip dynamic system, (e) equivalent machine-tool analogy, (f) tool-piece, equivalent work-piece and chip dynamics with frictional surface.

as this study is concerned), see Fig. 7(b) Dassanayake [46]. The forces transmitted by a chip to the tool-piece are governed by the shearing action of the cutting process (cutting depth, width and shearing angle) and the motion of the work-piece. The cutting processis modeled by viscous damping and linear stiffness forces of coefficients d_2 and k_2; respectively (see Fig. 7(d)). The exertion of the chip on the rake surface creates a normal force and frictional force. Since the frictional force is typically dependent on the relative velocity of the chip and rake surfaces, the chip can be modeled by a traveling belt with a dynamical normal force, see Fig. 7(f) Wiercigroch [25] and Warminiski et. al. [35].

The forces transmitted to the tool-piece by the chip and work-pieces are resolved into their vector forms in Fig. 7(e). The model of Fig. 8(b) will be referenced throughout this study as the machine-tool.

Machine-Tool Analogy

The tool and supports in free vibration are modeled by a two degree of freedom oscillator, of mass *m,* controlled by dampers (i.e., d_x and d_y) and two springs (i.e., k_x and k_y) in the $(\mathbf{e}_X, \mathbf{e}_Y)$ directions. The deflection of the tool piece is measured from the equilibrium point, by $(\overline{x}, \overline{y})$ (see Fig. 8(c)). An external force is applied to the flank of the tool in the form of a normal force (contact of the tool and work-pieces, but no cutting) with a damper of d_1 and a spring of k_1. The onset of cutting exerts an additional external force, in the form of a normal and frictional force, with a damper of d_2 and a

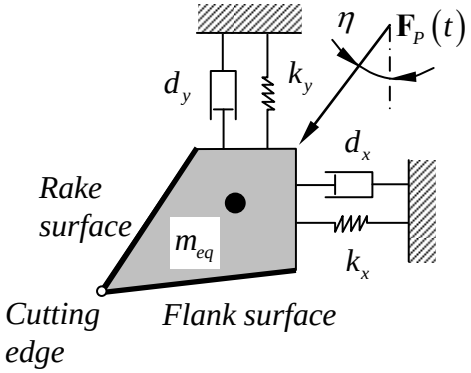

(a)

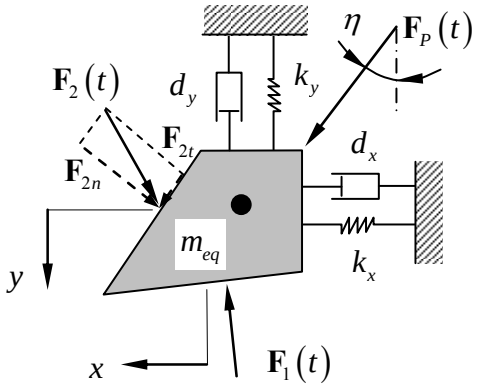

(b)

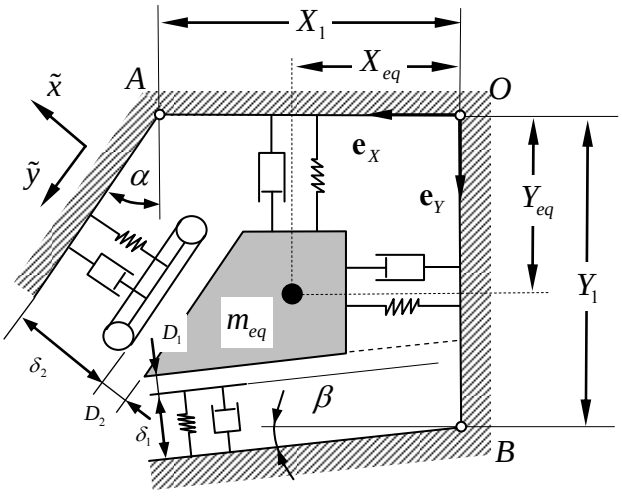

(c)

Fig. 8 Cutting tool mechanical model: (a) surface description, (b) external forces, (c) geometry and equilibrium.

spring of k_2. The periodical force $F_p(\bar{t}) = A\cos\Omega\bar{t}$ at an angle of η off the vertical direction, and A and Ω are excitation amplitude and frequency, respectively. Such a mechanical model is shown in Fig. 8(c). The flank surface has an angle of β from the horizontal surface.

The rake surface has an angle of α from the vertical surface, and the distance between the origin and point A (i.e., $\overline{OA}$) is X_1. The distances from the *flank* and *rake* surfaces to the equilibrium of the un-stretched springs are δ_1 and δ_2, respectively. For the flank and rake surfaces, two distances are defined as

$$D_1 = (X_{eq} + \bar{x})\sin\beta + (Y_1 - Y_{eq} - \bar{y})\cos\beta - \delta_1, \tag{2.1}$$

$$D_2 = (Y_{eq} + \bar{y})\sin\alpha + (X_1 - X_{eq} - \bar{x})\cos\alpha - \delta_2. \tag{2.2}$$

For $D_1 > 0$ and $D_2 > 0$, the machine tool is free running (no external forces from the work-piece in any form). The equations of motion for the tool-piece are

$$\begin{bmatrix} 1 & 0 \\ 0 & 1 \end{bmatrix}\begin{Bmatrix} \ddot{\bar{x}} \\ \ddot{\bar{y}} \end{Bmatrix} + \frac{1}{m}\begin{bmatrix} d_x & 0 \\ 0 & d_y \end{bmatrix}\begin{Bmatrix} \dot{\bar{x}} \\ \dot{\bar{y}} \end{Bmatrix} + \frac{1}{m}\begin{bmatrix} k_x & 0 \\ 0 & k_y \end{bmatrix}\begin{Bmatrix} \bar{x} \\ \bar{y} \end{Bmatrix} = A_F\cos(\Omega\bar{t})\begin{bmatrix} \sin(\eta) \\ \cos(\eta) \end{bmatrix}, \tag{2.3}$$

where $A_F = A_e/m$; which is considered the *first region,* Fig. 9(a).

If $D_1 \le 0$, the special case may occur which reduces Eq.(2.1) to

$$(X_{eq} + \bar{x})\sin\beta + (Y_1 - Y_{eq} - \bar{y})\cos\beta = \delta_1. \tag{2.4}$$

The force at the contact point with mass *m* on the flank surface is

$$\mathbf{F}_1(\bar{\mathbf{x}}, \bar{\mathbf{y}}) = \begin{Bmatrix} F_{1x} \\ F_{1y} \end{Bmatrix} = F_{n1}(\bar{\mathbf{x}}, \bar{\mathbf{y}})\begin{Bmatrix} -\sin\beta \\ \cos\beta \end{Bmatrix}, \tag{2.5}$$

where $\bar{\mathbf{x}} = (\bar{x}, \dot{\bar{x}})^T$ and $\bar{\mathbf{y}} = (\bar{y}, \dot{\bar{y}})^T$ with

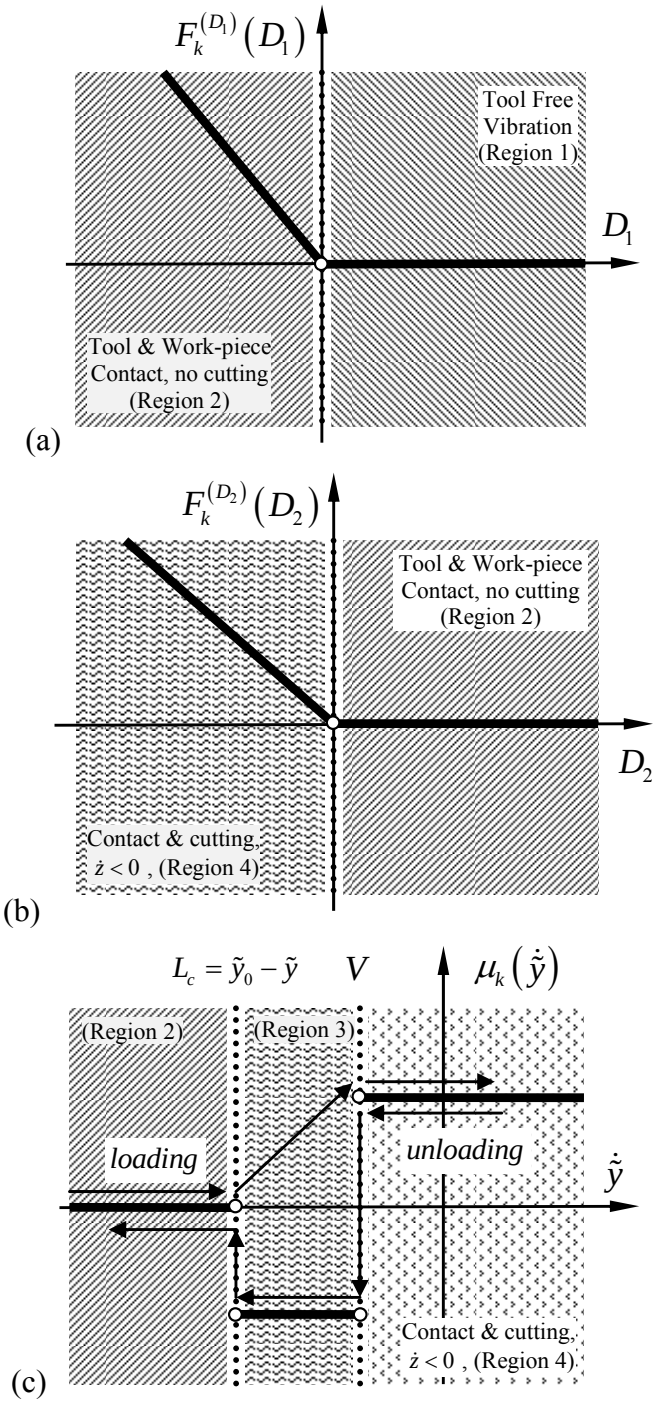

Fig. 9 Force definitions for this machine-tool system; a) region 1 to region 2 force condition, b) region 2 to region 4 force condition and c) loading and unloading paths.

$$F_{n1}\left(\overline{\mathbf{x}},\overline{\mathbf{y}}\right)=d_1\dot{\overline{x}}\sin\beta-d_1\dot{\overline{y}}\cos\beta+k_1\left(\overline{x}-\overline{x}_1^*\right)\sin\beta-k_1\left(\overline{y}-\overline{y}_1^*\right)\cos\beta; \qquad (2.6)$$

which is considered the *second region*, see Fig. 9(a,b). The forces of Eq.(2.6) express a continuous stiffness force at the point of switching. Where the forces are C^0 continuous, but C^1 discontinuous, which means the slope of the forces is discontinuous at the switching point. At this point, Eq.(2.4) is satisfied and the contact of the work-piece is defined to exert an impact force through the conservation of momentum, in the direction of normal contact, by the coefficient of restitution e_r.

For $D_1 \le 0$ and $D_2 \ge 0$, the special case may occur which reduces Eq.(2.2) to

$$(Y_{eq}+\overline{y})\sin\alpha+(X_1-X_{eq}-\overline{x})\cos\alpha=\delta_2. \qquad (2.7)$$

In this case, the machine tool will not cut the work-piece, but just slide across the surface, noted in Fig. 7(a,c). The equations of motion for this case are

$$\begin{bmatrix}1&0\\0&1\end{bmatrix}\begin{Bmatrix}\ddot{\overline{x}}\\\ddot{\overline{y}}\end{Bmatrix}+\begin{bmatrix}\overline{D}_{11}&\overline{D}_{12}\\\overline{D}_{21}&\overline{D}_{22}\end{bmatrix}\begin{Bmatrix}\dot{\overline{x}}\\\dot{\overline{y}}\end{Bmatrix}+\begin{bmatrix}\overline{K}_{11}&\overline{K}_{12}\\\overline{K}_{21}&\overline{K}_{22}\end{bmatrix}\begin{Bmatrix}\overline{x}\\\overline{y}\end{Bmatrix}=\cos\left(\Omega\overline{t}\right)\begin{Bmatrix}\overline{A}_x\\\overline{A}_y\end{Bmatrix}+\begin{Bmatrix}\overline{C}_x\\\overline{C}_y\end{Bmatrix}. \qquad (2.8)$$

For $D_1 < D_2 \le 0$, two external forces $\mathbf{F}_i\left(\overline{\mathbf{x}},\overline{\mathbf{y}}\right)$ $(i=1,2)$ will act on the tool-piece, see Fig. 7(b,d,f). The force $\mathbf{F}_1\left(\overline{\mathbf{x}},\overline{\mathbf{y}}\right)$ is given in Eq.(2.5). The supporting normal force and friction force on the left inclined surface (rake surface) acting on mass *m* provides the total force $\mathbf{F}_2\left(\overline{\mathbf{x}},\overline{\mathbf{y}}\right)$ as

$$\mathbf{F}_2\left(\overline{\mathbf{x}},\overline{\mathbf{y}}\right)=\begin{Bmatrix}F_{2x}\\F_{2y}\end{Bmatrix}=F_{n2}\left(\overline{\mathbf{x}},\overline{\mathbf{y}}\right)\begin{Bmatrix}M\left(\dot{\overline{x}},\dot{\overline{y}}\right)\\N\left(\dot{\overline{x}},\dot{\overline{y}}\right)\end{Bmatrix}, \qquad (2.9)$$

where

$$F_{n2}\left(\overline{\mathbf{x}},\overline{\mathbf{y}}\right)=d_2\dot{\overline{x}}\sin\alpha-d_2\dot{\overline{y}}\cos\alpha+k_2\left(\overline{x}-\overline{x}_2^*\right)\sin\alpha-k_2\left(\overline{y}-\overline{y}_2^*\right)\cos\alpha, \qquad (2.10)$$

and

$$\left.\begin{aligned} M\left(\dot{\bar{x}},\dot{\bar{y}}\right) &= -\left[\cos\alpha+\mu\,\mathrm{sgn}\left(\dot{\bar{z}}\right)\sin\alpha\right], \\ N\left(\dot{\bar{x}},\dot{\bar{y}}\right) &= \sin\alpha-\mu\,\mathrm{sgn}\left(\dot{\bar{z}}\right)\cos\alpha, \\ \dot{\bar{z}} &= \dot{\bar{x}}\sin\alpha+\dot{\bar{y}}\cos\alpha-\bar{V}. \end{aligned}\right\} \tag{2.11}$$

The forces of Eq.(2.9) express a continuous stiffness force at the point of switching; see Fig. 9(b). The forces are C^0 continuous, but C^1 discontinuous, which means the slope of the forces is discontinuous at the switching point. Due to the nature of friction, if $\dot{\bar{z}}<0$, the region of motion is considered as the *third region*, but if $\dot{\bar{z}}>0$, the region of motion is called the *fourth region*, see Fig. 9(c). In different regions, the governing equations are different as noted with regions one and two. Computationally motivated, the non-dimensional time $t=\Omega\bar{t}$, gives

$$\bar{\mathbf{r}}=\left(\bar{x},\bar{y}\right)^T=\left(x,y\right)^T, \tag{2.12}$$

$$\frac{d\bar{\mathbf{r}}}{d\bar{t}}=\left(\frac{d\bar{x}(t)}{d\bar{t}},\frac{d\bar{y}(t)}{d\bar{t}}\right)^T=\Omega\left(\frac{dx(t)}{d\bar{t}},\frac{dy(t)}{d\bar{t}}\right)^T, \tag{2.13}$$

$$\frac{d^2\bar{\mathbf{r}}}{d\bar{t}^2}=\left(\frac{d^2\bar{x}(t)}{d\bar{t}^2},\frac{d^2\bar{y}(t)}{d\bar{t}^2}\right)^T=\Omega^2\left(\frac{d^2x(t)}{d\bar{t}^2},\frac{d^2y(t)}{d\bar{t}^2}\right)^T. \tag{2.14}$$

Therefore, the equations of motion with the forces $\mathbf{F}_1\left(\bar{\mathbf{x}},\bar{\mathbf{y}}\right)$ and $\mathbf{F}_2\left(\bar{\mathbf{x}},\bar{\mathbf{y}}\right)$ for non-stick motion (pure cutting, no chip seizure) are,

$$\begin{bmatrix}1&0\\0&1\end{bmatrix}\begin{Bmatrix}\ddot{x}\\\ddot{y}\end{Bmatrix}+\begin{bmatrix}D_{11}^{(i)}&D_{12}^{(i)}\\D_{21}^{(i)}&D_{22}^{(i)}\end{bmatrix}\begin{Bmatrix}\dot{x}\\\dot{y}\end{Bmatrix}+\begin{bmatrix}K_{11}^{(i)}&K_{12}^{(i)}\\K_{21}^{(i)}&K_{22}^{(i)}\end{bmatrix}\begin{Bmatrix}x\\y\end{Bmatrix}=\cos(t)\begin{Bmatrix}A_x^{(i)}\\A_y^{(i)}\end{Bmatrix}+\begin{Bmatrix}C_x^{(i)}\\C_y^{(i)}\end{Bmatrix}; \tag{2.15}$$

for i = 1,2,3,4, where i denotes the parameters for each region. During the cutting process, if the chip material adheres to the tool-piece, the relative velocity on the cutting

surface (rake surface) should be zero, i.e. a velocity boundary is defined which denotes the change in direction of the frictional force exerted by the chip material on the tool rake surface,

$$\dot{x}\sin\alpha + \dot{y}\cos\alpha = V; \tag{2.16}$$

$$D_3 = \dot{z} = \dot{x}\sin\alpha + \dot{y}\cos\alpha - V\,; \tag{2.17}$$

where $V = -\bar{V}/\Omega$ ($\bar{V}$ is the chip velocity in the $\tilde{y}$-coordinate system, tool rake surface direction) and is considered the *zero region*. In order to investigate this phenomenon, a new coordinate system $(\tilde{x},\tilde{y})$ is introduced. The transformation for the two coordinates (x,y) and $(\tilde{x},\tilde{y})$ is

$$\begin{Bmatrix} x \\ y \end{Bmatrix} = \begin{bmatrix} \cos\alpha & \sin\alpha \\ -\sin\alpha & \cos\alpha \end{bmatrix} \begin{Bmatrix} \tilde{x} \\ \tilde{y} \end{Bmatrix} = \Lambda \begin{Bmatrix} \tilde{x} \\ \tilde{y} \end{Bmatrix}. \tag{2.18}$$

The corresponding velocity can be given by

$$\begin{Bmatrix} \dot{x} \\ \dot{y} \end{Bmatrix} = \Lambda \begin{Bmatrix} \dot{\tilde{x}} \\ \dot{\tilde{y}} \end{Bmatrix}, \begin{Bmatrix} \dot{\tilde{x}} \\ \dot{\tilde{y}} \end{Bmatrix} = \Lambda^{-1} \begin{Bmatrix} \dot{x} \\ \dot{y} \end{Bmatrix}. \tag{2.19}$$

From Eq.(2.18) and Eq.(2.19); Eq.(2.15) becomes

$$\begin{aligned} \begin{bmatrix} 1 & 0 \\ 0 & 1 \end{bmatrix} \begin{Bmatrix} \ddot{\tilde{x}} \\ \ddot{\tilde{y}} \end{Bmatrix} + \Lambda^{-1} \begin{bmatrix} D_{11}^{(i)} & D_{12}^{(i)} \\ D_{21}^{(i)} & D_{22}^{(i)} \end{bmatrix} \Lambda \begin{Bmatrix} \dot{\tilde{x}} \\ \dot{\tilde{y}} \end{Bmatrix} + \Lambda^{-1} \begin{bmatrix} K_{11}^{(i)} & K_{12}^{(i)} \\ K_{21}^{(i)} & K_{22}^{(i)} \end{bmatrix} \Lambda \begin{Bmatrix} \tilde{x} \\ \tilde{y} \end{Bmatrix} \\ = \cos(\Omega t)\,\Lambda^{-1} \begin{Bmatrix} A_x^{(i)} \\ A_y^{(i)} \end{Bmatrix} + \Lambda^{-1} \begin{Bmatrix} C_x^{(i)} \\ C_y^{(i)} \end{Bmatrix}. \end{aligned} \tag{2.20}$$

For stick motion (chip material adheres to the tool-piece, $\dot{z} \equiv 0$) in the $\tilde{y}$-direction, the following equations hold

$$\tilde{y} = \tilde{y}_0 - V(t - t_0), \dot{\tilde{y}} = V,\ \ddot{\tilde{y}} = 0. \tag{2.21}$$

The governing equation for stick motion in the $\tilde{x}$-direction is

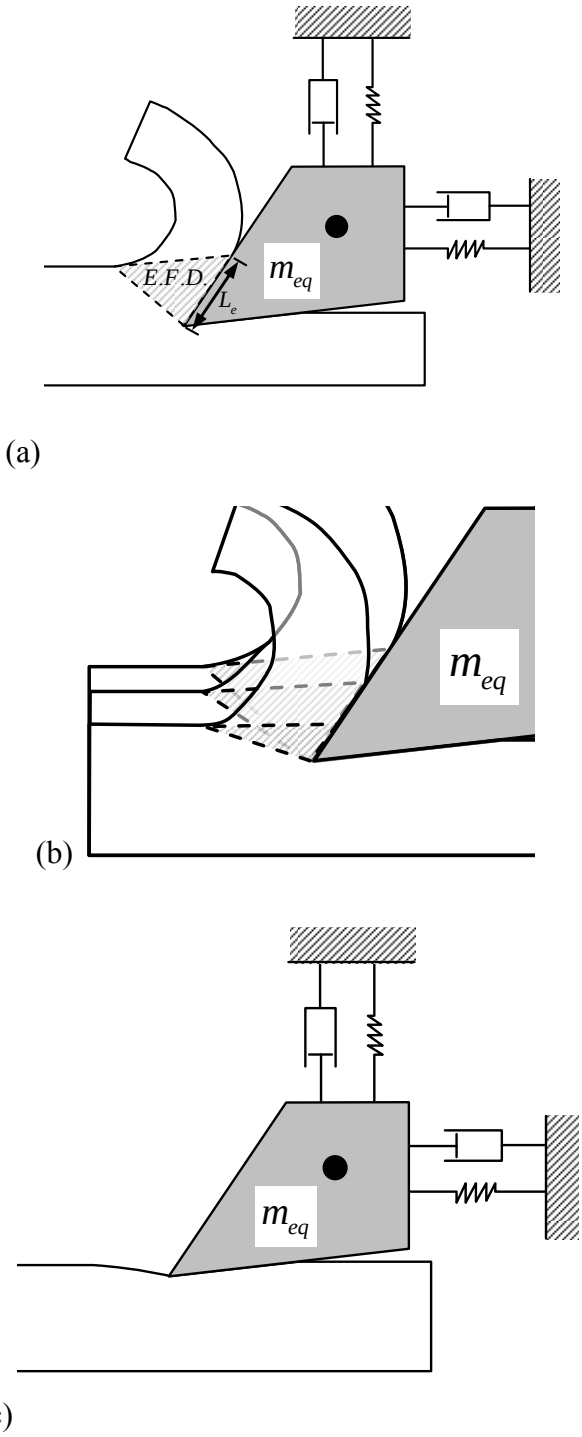

Fig. 10 Chip and tool-piece a) effective cutting force contact (region four) and b) route to loss of effective cutting force contact (region three), c) loss of effective cutting force contact (region two).

$$\ddot{\tilde{x}} + 2d\dot{\tilde{x}} + \omega^2 \tilde{x} = A_0 \cos(t) + B_0 t + C_0. \tag{2.22}$$

The undefined parameters of Eq.(2.20) and Eq.(2.22) are shown in the Appendix. There are four boundaries to consider with this problem: three displacement boundaries and one velocity boundary. Two of the displacement boundaries are due to contact with the external dynamical systems defined by $\mathbf{F}_1(\mathbf{x},\mathbf{y})$ and $\mathbf{F}_2(\mathbf{x},\mathbf{y})$ (tool and work-piece contact and onset of cutting).

The remaining displacement boundary is non-stick motion (cutting) of the system where $D_1 < D_2 \le 0$ and $\dot{z} < 0$. If the effective contact between the chip and tool-rake face is maintained the forces of the shearing action and work-piece motion will be transmitted through the tool-rake surface, see Fig. 10(a). A special case exists where the route to loss of effective chip-tool-rake surface contact occurs; see Fig. 10(b). The effective cutting force contact may vanish inducing a transition to region two, see Fig. 10(c). This effective force contact is noted by L_c; hence a displacement boundary is defined,

$$L_c = \tilde{y}_0 - \tilde{y} \tag{2.23}$$

and

$$D_4 = L_c - (\tilde{y}_0 - \tilde{y}). \tag{2.24}$$

The force conditions at the point of switching from region to region are shown in Fig. 9.

The stiffness force ($F_k^{(D_\gamma)}$ for $\gamma = 1,2,3$), when $\gamma = 3$ the friction coefficient distribution is shown, as the motion switches from *region one* to *region two* and *region two* to *region four* are shown in Fig. 9(a,b); respectively. The kinematic friction

coefficient distribution switching from *region two* to *region four* jumps past *region three* on a loading path, see Fig. 9(c). The unloading path begins in *region four* moves through *region three* and ends at *region two*. The next chapter will introduce the state, domains and boundaries such that the discontinuous systems theory can be applied.

CHAPTER III

STATE, DOMAINS AND BOUNDARY DEFINITIONS

In order to apply the discontinuous systems theory, the state with respect to each boundary needs to be defined. The machining system presented through the mechanical model of Fig. 8(b) is defined to contain four boundaries. The first boundary is the contact of the tool and work-pieces. The phase planes are partitioned to identify the discontinuities in the machine-tool system, see Fig. 11 and Fig. 12.

Definitions with Respect to Boundary 1

Boundary one is the contact measure between the tool and work-pieces. If D_1 is positive the tool and work-pieces are not in contact. The contact exists initially when $D_1 = 0$, and continues for $D_1 \le 0$. The state and vector fields for boundary 1 are defined as,

$$\mathbf{D}_1 \triangleq \left(D_1, \dot{D}_1\right)^T \text{ and } \dot{\mathbf{D}}_1 = \mathbf{F}_1 \triangleq \left(\dot{D}_1, F_{D_1}^{(i)}\left(\mathbf{D}_1, t\right)\right)^T, \tag{3.1}$$

where

$$\begin{aligned} F_{D_1}^{(i)}\left(\mathbf{D}_1, t\right) = \ddot{D}_1 &= \Omega^2\left(\ddot{x}^{(i)}\sin\beta + \ddot{y}^{(i)}\cos\beta\right) \\ &= \Omega^2\left[F_x^{(i)}\left(\mathbf{x}, \mathbf{y}, t\right)\sin\beta + F_y^{(i)}\left(\mathbf{x}, \mathbf{y}, t\right)\cos\beta\right], \end{aligned} \tag{3.2}$$

where i = 1,2,4; Fig. 11(a) and Fig. 12(a). The domains with respect to Eq.(3.1) are defined as,

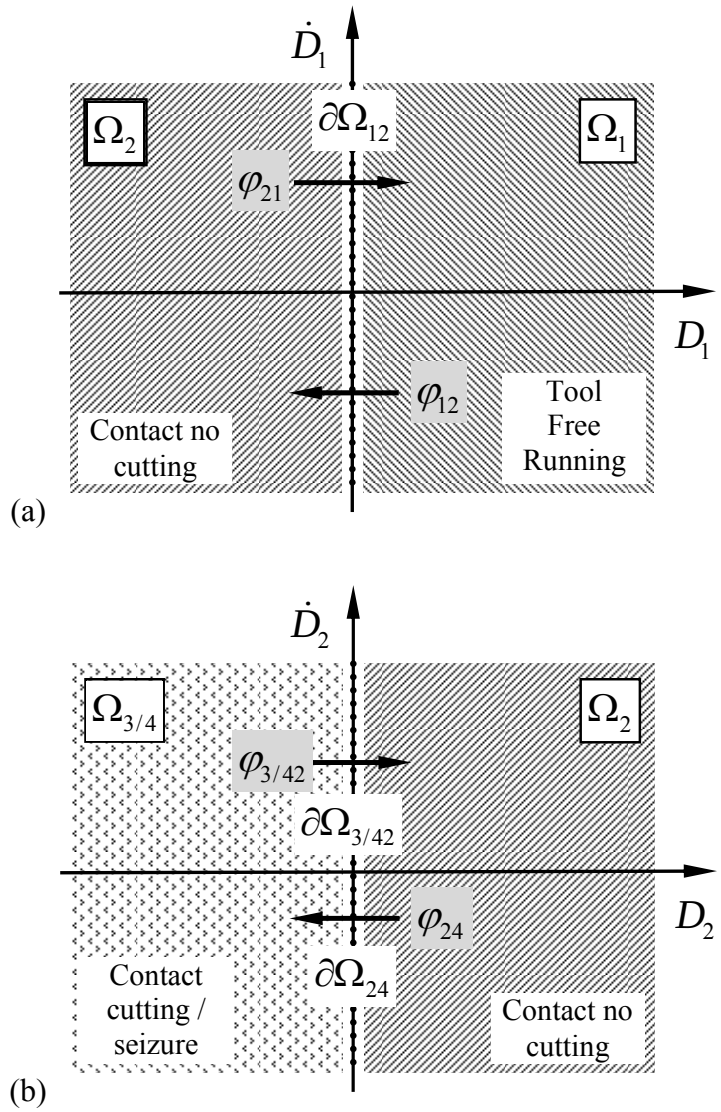

Fig. 11 Partitions in phase space for the displacement and velocity discontinuities of this machine-tool system; a) D_1 phase plane, b) D_2 phase plane.

$$\Omega_1(x,y)=\left\{(x,y)\middle|D_1(x,y)\in(0,\infty)\right\}, \tag{3.3}$$

$$\Omega_2(x,y,\dot{x},\dot{y})=\left\{(x,y)\middle|D_1(x,y)\in(-\infty,0)\right\}, \tag{3.4}$$

$$\Omega_3(x,y,\dot{x},\dot{y})=\left\{(x,y,\dot{x},\dot{y})\middle|D_1(x,y)\in(-\infty,0)\right\}, \tag{3.5}$$

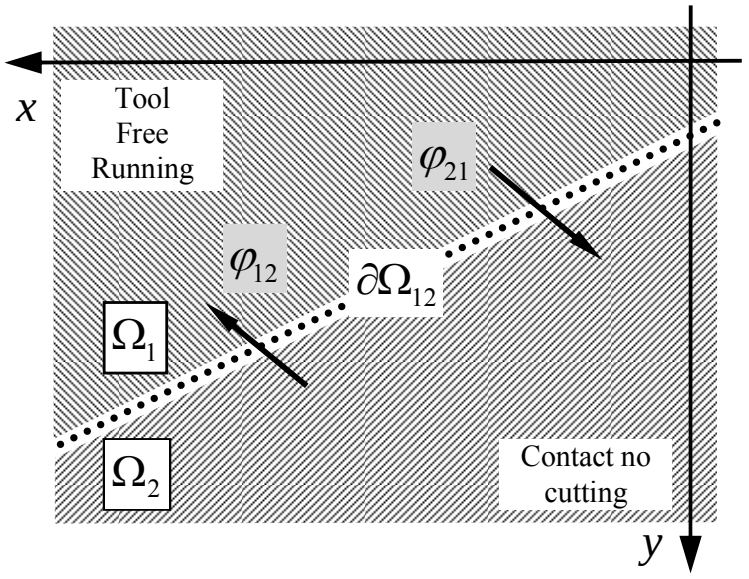

(a)

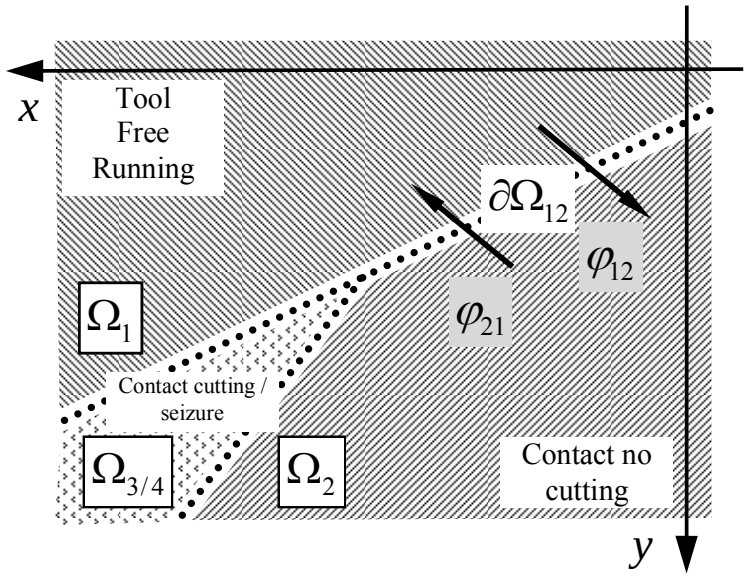

(b)

Fig. 12 Partitions in (x, y) and ($\dot{x}, \dot{y}$) space for the displacement and velocity discontinuities of this machine-tool system; boundaries a) $\partial\Omega_{12}$, b) φ_{12}.

$$\Omega_4\left(x,y,\dot{x},\dot{y}\right)=\left\{\left(x,y,\dot{x},\dot{y}\right)\middle|D_1\left(x,y\right)\in\left(-\infty,0\right)\right\}. \tag{3.6}$$

The reference domains directly correspond to the regions. Domains 2, 3 and 4 have additional constraints which will be presented in the following sections.

Definitions with Respect to Boundary 2

Boundary 2 is the cutting condition; in this case this measure is a displacement constraint, where cutting will not occur if $D_2>0$. The cutting will initiate if $D_2=0$ and continue such that $D_2\le 0$. The state and vector fields for boundary 2 are defined as,

$$\mathbf{D}_2\triangleq\left(D_2,\dot{D}_2\right)^T \text{ and } \dot{\mathbf{D}}_2=\mathbf{F}_2\triangleq\left(\dot{D}_2,F_{D_2}^{(i)}\left(\mathbf{D}_2,t\right)\right)^T, \tag{3.7}$$

where

$$\begin{aligned}F_{D_2}^{(i)}\left(\mathbf{D}_2,t\right)=\ddot{D}_2&=\Omega^2\left(\ddot{x}^{(i)}\sin\alpha+\ddot{y}^{(i)}\cos\alpha\right)\\&=\Omega^2\left[F_x^{(i)}\left(\mathbf{x},\mathbf{y},t\right)\sin\alpha+F_y^{(i)}\left(\mathbf{x},\mathbf{y},t\right)\cos\alpha\right],\end{aligned} \tag{3.8}$$

with i = 1,4; see Fig. 11(b) and Fig. 12(b). The domains with respect to Eq.(3.7) are defined as,

$$\Omega_2=\left(D_2,\dot{D}_2\right)\middle|D_2\in\left(0,\infty\right)\Big\}, \tag{3.9}$$

$$\Omega_3=\left(D_2,\dot{D}_2\right)\middle|D_2\in\left(-\infty,0\right)\Big\}, \tag{3.10}$$

$$\Omega_4=\left(D_2,\dot{D}_2\right)\middle|D_2\in\left(-\infty,0\right)\Big\}. \tag{3.11}$$

Domains 2, 3 and 4 have additional constraints which will be presented in the following sections.

Definitions with Respect to Boundary 3

Boundary 3 is the frictional discontinuity. For specific values of $\dot{\tilde{y}}$ there are different frictional forces. This is due to the direction of the friction force. If $\dot{\tilde{y}} > V$ then the friction force acts in the negative $\tilde{y}$-direction. Also, if $\dot{\tilde{y}} < V$ then the friction force acts in the positive $\tilde{y}$-direction. The state and vector fields for boundary 3 are defined as,

$$\mathbf{D}_3 = \tilde{\mathbf{y}} = \left(\tilde{y}, \dot{\tilde{y}}\right)^T \text{ and } \dot{\mathbf{D}}_3 = \dot{\tilde{\mathbf{y}}} = \mathbf{F}_{\tilde{y}}^{(\kappa)}\left(\tilde{\mathbf{x}}, \tilde{\mathbf{y}}, t\right) \triangleq \left(\dot{\tilde{y}}, F_{\tilde{y}}^{(\kappa)}\left(\tilde{\mathbf{x}}, \tilde{\mathbf{y}}, , t\right)\right)^T, \ (\kappa \in \{0,3,4\}), \quad (3.12)$$

where

$$\begin{aligned} F_{\tilde{y}}^{(i)}\left(\tilde{\mathbf{x}}, \tilde{\mathbf{y}}, t\right) &= F_{D_3}^{(i)}\left(\tilde{\mathbf{x}}, \tilde{\mathbf{y}}, t\right) = F_{D_4}^{(i)}\left(\tilde{\mathbf{x}}, \tilde{\mathbf{y}}, t\right) = \dddot{\tilde{y}}^{(i)}\left(t\right) = \dddot{x}^{(i)} \sin\alpha + \dddot{y}^{(i)} \cos\alpha \\ &= F_x^{(i)}\left(\mathbf{x}, \mathbf{y}, t\right)\sin\alpha + F_y^{(i)}\left(\mathbf{x}, \mathbf{y}, t\right)\cos\alpha; \end{aligned} \quad (3.13)$$

and $\mathbf{x} = \left(x, \dot{x}\right)^T$, $\mathbf{y} = \left(y, \dot{y}\right)^T$, $\tilde{\mathbf{x}} = \left(\tilde{x}, \dot{\tilde{x}}\right)^T$, $\tilde{\mathbf{y}} = \left(\tilde{y}, \dot{\tilde{y}}\right)^T$ with i = 3,4; see Fig. 13(a,c) and Fig. 14(b). The domains with respect to Eq.(3.7) and Eq.(3.12) are defined as,

$$\Omega_2 = \left(D_2, \dot{D}_2\right) \middle| D_2 \in \left(-\infty, \infty\right) \text{and } \left(\tilde{y}, \dot{\tilde{y}}\right) \middle| \dot{\tilde{y}} \in \left(-\infty, V\right) \Big\}; \quad (3.14)$$

$$\Omega_3 = \left(D_2, \dot{D}_2\right) \middle| D_2 \in \left(-\infty, 0\right) \text{ and } \left(\tilde{y}, \dot{\tilde{y}}\right) \middle| \dot{\tilde{y}} \in \left(-\infty, V\right) \Big\}; \quad (3.15)$$

$$\Omega_4 = \left(D_2, \dot{D}_2\right) \middle| D_2 \in \left(-\infty, 0\right) \text{ and } \left(\tilde{y}, \dot{\tilde{y}}\right) \middle| \dot{\tilde{y}} \in \left(V, \infty\right) \Big\}; \quad (3.16)$$

where

$$\left.\begin{aligned} \tilde{y} &= (x - x_0)\sin\alpha + (y - y_0)\cos\alpha, \\ \dot{\tilde{y}} &= \dot{x}\sin\left(\alpha\right) + \dot{y}\cos\left(\alpha\right). \end{aligned}\right\} \quad (3.17)$$

Domains 2 and 3 have additional constraints which will be presented in the following section.

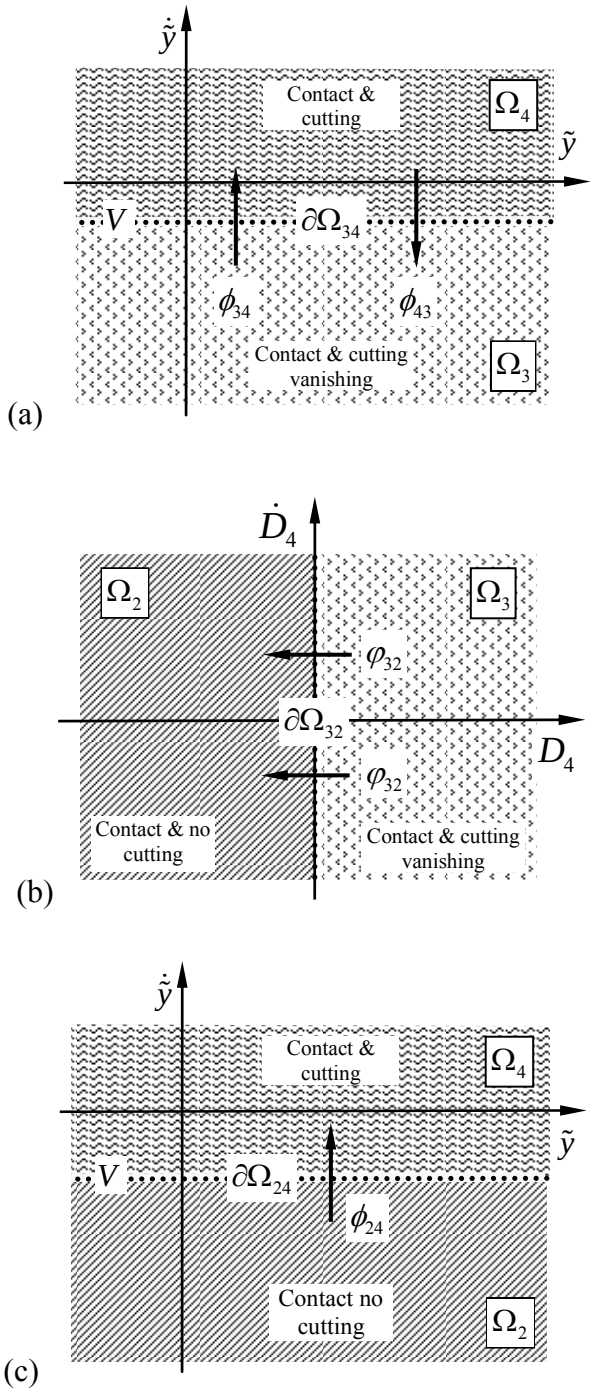

Fig. 13 Partitions in phase space for the displacement and velocity discontinuities of this machine-tool system; a) $\tilde{y}$ phase plane, b) D_4 phase plane, c) $\partial\Omega_{24}$ boundary in the $\tilde{y}$ phase plane.

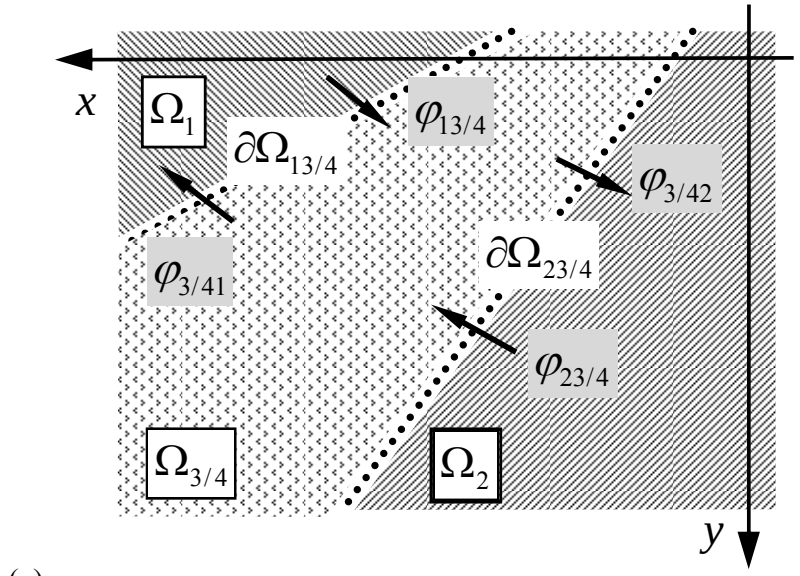

(a)

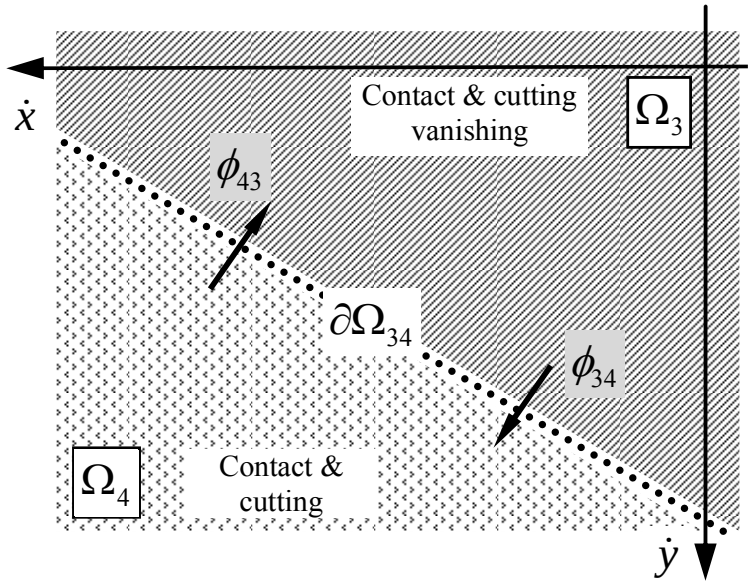

(b)

Fig. 14 Partitions in (x, y) and $(\dot{x}, \dot{y})$ space for the displacement and velocity discontinuities of this machine-tool system; boundaries (a) $\partial\Omega_{23/4}$, $\partial\Omega_{13/4}$ and (b) $\partial\Omega_{34}$.

Definitions with Respect to Boundary 4

Boundary 4 is the chip contact measure, where this determines whether the tool will continue to maintain effective force contact with the chip while $\dot{\tilde{y}} < V$. Consider the initial point where $\dot{\tilde{y}} = V$ is defined by $\tilde{y}_0$. If the tool-piece continues to maintain $\dot{\tilde{y}} < V$ to a point where the difference measure between $\tilde{y}$ and $\tilde{y}_0$ is equal to L_c, the effective force contact is lost and cutting terminates. The state and vector fields for boundary 4 are defined as,

$$\mathbf{D}_4 = \left(D_4, \dot{D}_4\right)^T \text{ and } \dot{\mathbf{D}}_4 = \mathbf{F}_{D_4}^{(\kappa)}\left(\tilde{\mathbf{x}}, \tilde{\mathbf{y}}, t\right) \triangleq \left(\dot{D}_4, F_{D_4}^{(\kappa)}\left(\tilde{\mathbf{x}}, \tilde{\mathbf{y}}, t\right)\right)^T, \ (\kappa \in \{2,3\}), \tag{3.18}$$

where

$$\begin{aligned} F_{D_4}^{(i)}\left(\tilde{\mathbf{x}}, \tilde{\mathbf{y}}, t\right) &= F_{\tilde{y}}^{(i)}\left(\tilde{\mathbf{x}}, \tilde{\mathbf{y}}, t\right) = F_{D_3}^{(i)}\left(\tilde{\mathbf{x}}, \tilde{\mathbf{y}}, t\right) = \dddot{\tilde{y}}^{(i)}\left(t\right) = \dddot{x}^{(i)} \sin\alpha + \dddot{y}^{(i)} \cos\alpha \\ &= F_x^{(i)}\left(\mathbf{x}, \mathbf{y}, t\right)\sin\alpha + F_y^{(i)}\left(\mathbf{x}, \mathbf{y}, t\right)\cos\alpha; \end{aligned} \tag{3.19}$$

with i = 2; see Fig. 13(b). The domains with respect to Eq.(3.12) and Eq.(3.18) are defined as,

$$\Omega_2 = \left(D_4, \dot{D}_4\right) \middle| D_4 \in \left(-\infty, 0\right) \text{ and } \left(\tilde{y}, \dot{\tilde{y}}\right) \middle| \dot{\tilde{y}} \in \left(-\infty, V\right) \Big\}; \tag{3.20}$$

$$\Omega_3 = \left(D_4, \dot{D}_4\right) \middle| D_4 \in \left(0, L_c\right) \text{ and } \left(\tilde{y}, \dot{\tilde{y}}\right) \middle| \dot{\tilde{y}} \in \left(-\infty, V\right) \Big\}; \tag{3.21}$$

where

$$D_4 = L_c - \left(\tilde{y}_0 - \tilde{y}\right), \ \dot{D}_4 = \dot{z} = \dot{\tilde{y}} - V. \tag{3.22}$$

A comprehensive definition of the domains and boundaries is presented in the following section.

Summary of Domain Definitions and Boundaries

The four domains considered in this study are noted to overlap in several areas and a formal comprehensive definition is necessary. Domain one is the vibration of the tool-piece without contacting the work-piece,

$$\Omega_1(x,y)=\left\{(x,y,\dot{x},\dot{y})\middle| D_1(x,y)\in(0,\infty)\right\}; \tag{3.23}$$

or

$$\Omega_1(x,y)=(x,y)\middle| y\in\left((X_{eq}+x)\tan\beta+\frac{\delta_1}{\cos\beta}+Y_1-Y_{eq},\infty\right). \tag{3.24}$$

Domain two is the contact of the tool and work-piece without cutting,

$$\Omega_2(x,y,\dot{x},\dot{y})=\begin{cases}(x,y,\dot{x},\dot{y})\middle| D_1(x,y)\in(-\infty,0)\},\\ (x,y,\dot{x},\dot{y})\middle| D_2(x,y)\in(0,\infty)\}\\ \text{or}\ \begin{cases}(x,y,\dot{x},\dot{y})\middle| D_2(x,y)\in(-\infty,\infty)\\ \text{and}\ (x,y,\dot{x},\dot{y})\middle| D_4(x,y)\in(-\infty,0)\end{cases}\\ \quad\text{if}\ (x,y,\dot{x},\dot{y})\middle|\tilde{w}(\dot{x},\dot{y})\in(-\infty,V);\end{cases}\Bigg\} \tag{3.25}$$

or

$$\Omega_2(x,y,\dot{x},\dot{y})=\begin{cases}(x,y)\middle| y\in\left(-\infty,(X_{eq}+x)\tan\beta+\frac{\delta_1}{\cos\beta}+Y_1-Y_{eq}\right),\\ (x,y)\middle| x\in\left((Y_{eq}+y)\tan\alpha-\frac{\delta_2}{\cos\alpha}+X_1-X_{eq},\infty\right),\\ (x,y)\middle| y\in\left(-\infty,y_0-(x-x_0)\tan\alpha+\frac{L_c}{\cos\alpha}\right),\\ \text{and}\ (\dot{x},\dot{y})\middle|\dot{y}\in\left(-\infty,\frac{V}{\cos\alpha}-\dot{x}\tan\alpha\right).\end{cases} \tag{3.26}$$

Domain three exists purely during route to chip vanishing ($\dot{\tilde{y}}<V$),

$$\Omega_3\left(x,y,\dot{x},\dot{y}\right)=\left\{\begin{array}{l}\left(x,y,\dot{x},\dot{y}\right)\middle|\, D_1\left(x,y\right)\in\left(-\infty,0\right)\right\},\\ \left(x,y,\dot{x},\dot{y}\right)\middle|\, D_2\left(x,y\right)\in\left(-\infty,0\right)\right\},\\ \left(x,y,\dot{x},\dot{y}\right)\middle|\, D_4\left(x,y\right)\in\left(0,L_c\right)\right\},\\ \left(x,y,\dot{x},\dot{y}\right)\middle|\, \tilde{\dot{y}}\left(\dot{x},\dot{y}\right)\in\left(-\infty,V\right)\right\};\end{array}\right\} \tag{3.27}$$

or

$$\Omega_3\left(x,y,\dot{x},\dot{y}\right)=\left\{\begin{array}{l}\left(x,y\right)\middle|\, y\in\left(-\infty,(X_{eq}+x)\tan\beta+\dfrac{\delta_1}{\cos\beta}+Y_1-Y_{eq}\right),\\ \left(x,y\right)\middle|\, y\in\left(-\infty,\dfrac{\delta_2}{\sin\alpha}+\left(x-X_1+X_{eq}\right)\tan^{-1}\alpha-Y_{eq}\right),\\ \left(x,y\right)\middle|\, y\in\left(y_0-(x-x_0)\tan\alpha+\dfrac{L_c}{\cos\alpha},y_0-(x-x_0)\tan\alpha\right),\\ \text{and }\left(\dot{x},\dot{y}\right)\middle|\, \dot{y}\in\left(-\infty,\dfrac{V}{\cos\alpha}-\dot{x}\tan\alpha\right);\end{array}\right\} \tag{3.28}$$

and domain four is defined by normal cutting ($\tilde{\dot{y}}>V$),

$$\Omega_4\left(x,y,\dot{x},\dot{y}\right)=\left\{\begin{array}{l}\left(x,y,\dot{x},\dot{y}\right)\middle|\, D_1\left(x,y\right)\in\left(-\infty,0\right),\\ \left(x,y,\dot{x},\dot{y}\right)\middle|\, D_2\left(x,y\right)\in\left(-\infty,0\right),\\ \left(x,y,\dot{x},\dot{y}\right)\middle|\, \tilde{\dot{y}}\left(\dot{x},\dot{y}\right)\in\left(V,\infty\right);\end{array}\right\} \tag{3.29}$$

or

$$\Omega_4\left(x,y,\dot{x},\dot{y}\right)=\left\{\begin{array}{l}\left(x,y\right)\middle|\, y\in\left(-\infty,(X_{eq}+x)\tan\beta+\dfrac{\delta_1}{\cos\beta}+Y_1-Y_{eq}\right),\\ \left(x,y\right)\middle|\, x\in\left(-\infty,(Y_{eq}+y)\tan\alpha-\dfrac{\delta_2}{\cos\alpha}+X_1-X_{eq}\right),\\ \text{and }\left(\dot{x},\dot{y}\right)\middle|\, \dot{y}\in\left(\dfrac{V}{\cos\alpha}-\dot{x}\tan\alpha,\infty\right).\end{array}\right\} \tag{3.30}$$

The boundary created by the domains one and two, see Fig. 11(a) and Fig. 12(a), noted in

Eq.(3.23) and Eq.(3.25) is

$$\partial\Omega_{12}\left(x,y,\dot{x},\dot{y}\right)=\left\{\left(x,y,\dot{x},\dot{y}\right)\middle|\varphi_{12}\left(x,y\right)=\varphi_{21}\left(x,y\right)=D_1\left(x,y\right)=0\right\}, \quad (3.31)$$

which is boundary one (tool and work-piece contact / impact boundary).

The boundaries created by the domains two and four, see Fig. 11(b), Fig. 12(b) and Fig. 13(c), noted in Eq.(3.25) and Eq.(3.29) is

$$\partial\Omega_{24}\left(x,y,\dot{x},\dot{y}\right)=\begin{Bmatrix}\left(x,y,\dot{x},\dot{y}\right)\middle|\varphi_{24}\left(x,y\right)=\varphi_{42}\left(x,y\right)=D_2\left(x,y\right)=0 \text{ if } \dot{\tilde{y}}\left(\dot{x},\dot{y}\right)>V,\\ \left(x,y,\dot{x},\dot{y}\right)\middle|\phi_{24}\left(\dot{x},\dot{y}\right)=\dot{\tilde{y}}\left(\dot{x},\dot{y}\right)-V=0 \text{ if } D_2\left(x,y\right)<0,\end{Bmatrix} \quad (3.32)$$

which is boundary two (onset of cutting boundary) and boundary three (chip/tool friction boundary). The boundaries created by the domains two and three, see Fig. 11(b), Fig. 12(b), Fig. 13(b) and Fig. 14(a), noted in Eq.(3.25) and Eq.(3.27) is

$$\partial\Omega_{32}=\left(x,y,\dot{x},\dot{y}\right)\middle|\varphi_{32}\left(x,y,\dot{x},\dot{y}\right)=\begin{cases}D_4\left(x,y\right)=0 \text{ if } D_2\left(x,y\right)<0,\\ D_2\left(x,y\right)=0 \text{ if } \dot{\tilde{y}}\left(\dot{x},\dot{y}\right)<V,\end{cases} \quad (3.33)$$

which is the boundary four (chip vanishing boundary) and boundary two (cutting disappearance boundary). The boundaries created by the domains three and four, see Fig. 13(a) and Fig. 14(b), noted in Eq.(3.27) and Eq.(3.29) is

$$\partial\Omega_{34}=\left(x,y,\dot{x},\dot{y}\right)\middle|\varphi_{34}\left(\dot{x},\dot{y}\right)=\varphi_{43}\left(\dot{x},\dot{y}\right)=\dot{\tilde{y}}\left(\dot{x},\dot{y}\right)-V=0 \text{ if } D_2\left(x,y\right)<0. \quad (3.34)$$

The discontinuous systems theory will be applied to this machine-tool through the state and domain definitions in the next chapter.

CHAPTER IV

INTERPRETATION OF VECTOR FIELDS

In general, the trajectory in the phase plane of any system is described by two types of motion: passable and non-passable [1,31,33,41-44,47]. For the trajectory to become passable the certain conditions with respect to the boundary and state must be met, but generally occur for all displacement boundaries. In this study there are three displacement constraints noted by boundaries 1, 2 and 4. The following section develops the criteria defining passable motion.

Passable Motion

From Luo [1,47], the passable motion is guaranteed for $t_n \subset (t_s, t_e)$ by

$$\left[\mathbf{n}^T_{\partial\Omega_{ij}} \bullet \mathbf{F}^{(i)}_{D_i}\left(\mathbf{D}_i, t_{n-}\right)\right] \times \left[\mathbf{n}^T_{\partial\Omega_{ij}} \bullet \mathbf{F}^{(j)}_{D_i}\left(\mathbf{D}_i, t_{n+}\right)\right] > 0, \tag{4.1}$$

$\left(\text{for } i \neq j \text{ and } i, j = 1,2,3,4\right)$; where the normal vector for the boundaries of Eq.(2.4), Eq.(2.7), Eq.(2.16) and Eq.(2.23) or Eq.(3.31) through Eq.(3.34) are

$$\mathbf{n}_{\partial\Omega_{12}} = \nabla\varphi_{12} = \left(\frac{\partial\varphi_{12}}{\partial D_1}, \frac{\partial\varphi_{12}}{\partial \dot{D}_1}\right)^T_{\left(D_{1m}, \dot{D}_{1m}\right)} = (1,0)^T, \tag{4.2}$$

$$\mathbf{n}_{\partial\Omega_{24}} = \begin{Bmatrix} \nabla\varphi_{24} = \left(\frac{\partial\varphi_{24}}{\partial D_2}, \frac{\partial\varphi_{24}}{\partial\dot{D}_2}\right)^T_{\left(D_{2m},\dot{D}_{2m}\right)} = \left(1,0\right)^T \ \text{if}\ \dot{\tilde{y}} > V, \\ \nabla\phi_{24} = \left(\frac{\partial\phi_{24}}{\partial\tilde{y}}, \frac{\partial\phi_{24}}{\partial\dot{\tilde{y}}}\right)^T_{\left(\tilde{y}_m,\dot{\tilde{y}}_m\right)} = \left(0,1\right)^T \ \text{if}\ D_2 < 0; \end{Bmatrix} \tag{4.3}$$

$$\mathbf{n}_{\partial\Omega_{32}} = \begin{Bmatrix} \nabla\varphi_{32} = \left(\frac{\partial\varphi_{32}}{\partial D_4}, \frac{\partial\varphi_{32}}{\partial\dot{D}_4}\right)^T_{\left(D_{4m},\dot{D}_{4m}\right)} = \left(1,0\right)^T \text{if}\ D_2 < 0, \\ \nabla\varphi_{32} = \left(\frac{\partial\varphi_{32}}{\partial D_2}, \frac{\partial\varphi_{32}}{\partial\dot{D}_2}\right)^T_{\left(D_{2m},\dot{D}_{2m}\right)} = \left(1,0\right)^T \text{if}\ \dot{\tilde{y}} < V; \end{Bmatrix} \tag{4.4}$$

$$\mathbf{n}_{\partial\Omega_{34}} = \nabla\varphi_{34} = \left(\frac{\partial\varphi_{34}}{\partial\tilde{y}}, \frac{\partial\varphi_{34}}{\partial\dot{\tilde{y}}}\right)^T_{\left(\tilde{y}_m,\dot{\tilde{y}}_m\right)} = \left(0,1\right)^T, \tag{4.5}$$

respectively. The components of Eq.(4.1), Eq.(4.2) through Eq.(4.5) give,

$$\mathbf{n}^T_{\partial\Omega_{12}} \bullet \mathbf{F}^{(j)}_{D_1}\left(\mathbf{D}_1, t_{n-}\right) = \dot{D}_1, \ \text{for}\, j = 1,2; \tag{4.6}$$

$$\begin{Bmatrix} \mathbf{n}^T_{\partial\Omega_{24}} \bullet \mathbf{F}^{(j)}_{D_2}\left(\mathbf{D}_2, t_{n-}\right) = \dot{D}_2 \ \text{if}\ \dot{\tilde{y}} > V, \\ \mathbf{n}^T_{\partial\Omega_{24}} \bullet \mathbf{F}^{(j)}_{D_3}\left(\mathbf{D}_3, t_{n-}\right) = F^{(j)}_{\tilde{y}}\left(\tilde{\mathbf{x}}, \tilde{\mathbf{y}}, , t\right) = \dddot{\tilde{y}}^{(j)}\left(t\right) \ \text{if}\ D_2 < 0, \end{Bmatrix} \ \text{for}\, j = 2,4; \tag{4.7}$$

$$\begin{Bmatrix} \mathbf{n}^T_{\partial\Omega_{32}} \bullet \mathbf{F}^{(j)}_{D_4}\left(\mathbf{D}_4, t_{n-}\right) = \dot{D}_4 = \dot{\tilde{y}} - V \ \text{if}\ \dot{\tilde{y}} < V, \\ \mathbf{n}^T_{\partial\Omega_{32}} \bullet \mathbf{F}^{(j)}_{D_2}\left(\mathbf{D}_2, t_{n-}\right) = \dot{D}_2 \ \text{if}\ D_2 < 0, \end{Bmatrix} \ \text{for}\, j = 2,3; \tag{4.8}$$

$$\mathbf{n}^T_{\partial\Omega_{34}} \bullet \mathbf{F}^{(j)}_{D_3}\left(\mathbf{D}_3, t_{n-}\right) = F^{(j)}_{\tilde{y}}\left(\tilde{\mathbf{x}}, \tilde{\mathbf{y}}, , t\right) = \dddot{\tilde{y}}^{(j)}\left(t\right), \ \ \text{for}\, j = 0,3,4; \tag{4.9}$$

respectively. Substituting Eq.(4.6) into Eq.(4.1) gives,

$$\dot{D}^{(i)}_1 \dot{D}^{(j)}_1 > 0 \ \text{on}\ \partial\Omega_{12}, \ \text{for}\ i \neq j;\ i, j = 1,2, \tag{4.10}$$

implying passable motion, for the tool and work-piece contact boundary, from domain one to domain two and vice versa. Substituting Eq.(4.7) into Eq.(4.1) gives,

$$\dot{D}_2^{(i)}\dot{D}_2^{(j)} > 0 \text{ if } \dot{\tilde{y}} > V \text{ and } F_{\tilde{y}}^{(i)}\left(\tilde{\mathbf{x}},\tilde{\mathbf{y}},,t\right)F_{\tilde{y}}^{(j)}\left(\tilde{\mathbf{x}},\tilde{\mathbf{y}},,t\right) > 0 \text{ if } D_2 < 0, \text{ on } \partial\Omega_{ij}, \qquad (4.11)$$

for $i \neq j;\ i, j = 2,4$. This implies passable motion, for the chip vanishing boundary and the chip/tool friction boundary, from domain two to domain four and vice versa. There are two conditions in Eq.(4.11) since there are two entry and exit planes to domain two and domain four with respect to boundaries 2 and 3 (see Fig. 11(b) and Fig. 13(c)). Substituting Eq.(4.8) into Eq.(4.1) gives,

$$\dot{D}_4^{(3)}\dot{D}_4^{(2)} > 0 \text{ if } \dot{\tilde{y}} < V \text{ and } \dot{D}_2^{(3)}\dot{D}_2^{(2)} > 0 \text{ if } D_2 < 0, \text{ on } \partial\Omega_{32}. \qquad (4.12)$$

This implies passable motion, for the chip vanishing boundary and the chip/tool friction boundary, from domain three to domain two only. There are two conditions in Eq.(4.12) regarding boundaries 4 and 2 (see Fig. 13(c)). Substituting Eq.(4.9) into Eq.(4.1) gives,

$$F_{\tilde{y}}^{(i)}\left(\tilde{\mathbf{x}},\tilde{\mathbf{y}},t\right)F_{\tilde{y}}^{(j)}\left(\tilde{\mathbf{x}},\tilde{\mathbf{y}},t\right) > 0 \text{ on } \partial\Omega_{ij}, \qquad (4.13)$$

for $i \neq j;\ i, j = 3,4$. This implies passable motion, for the chip/tool friction boundary, from domain three to domain four and vice versa. See Fig. 15 and Fig. 16 to observe opposing and agreeing vectors fields. The vector fields are noted by the short arrows and the actual motions are noted by long arrows.

Non-passable Motion

The non-passable motion and vanishing of the non-passable motion is guaranteed for

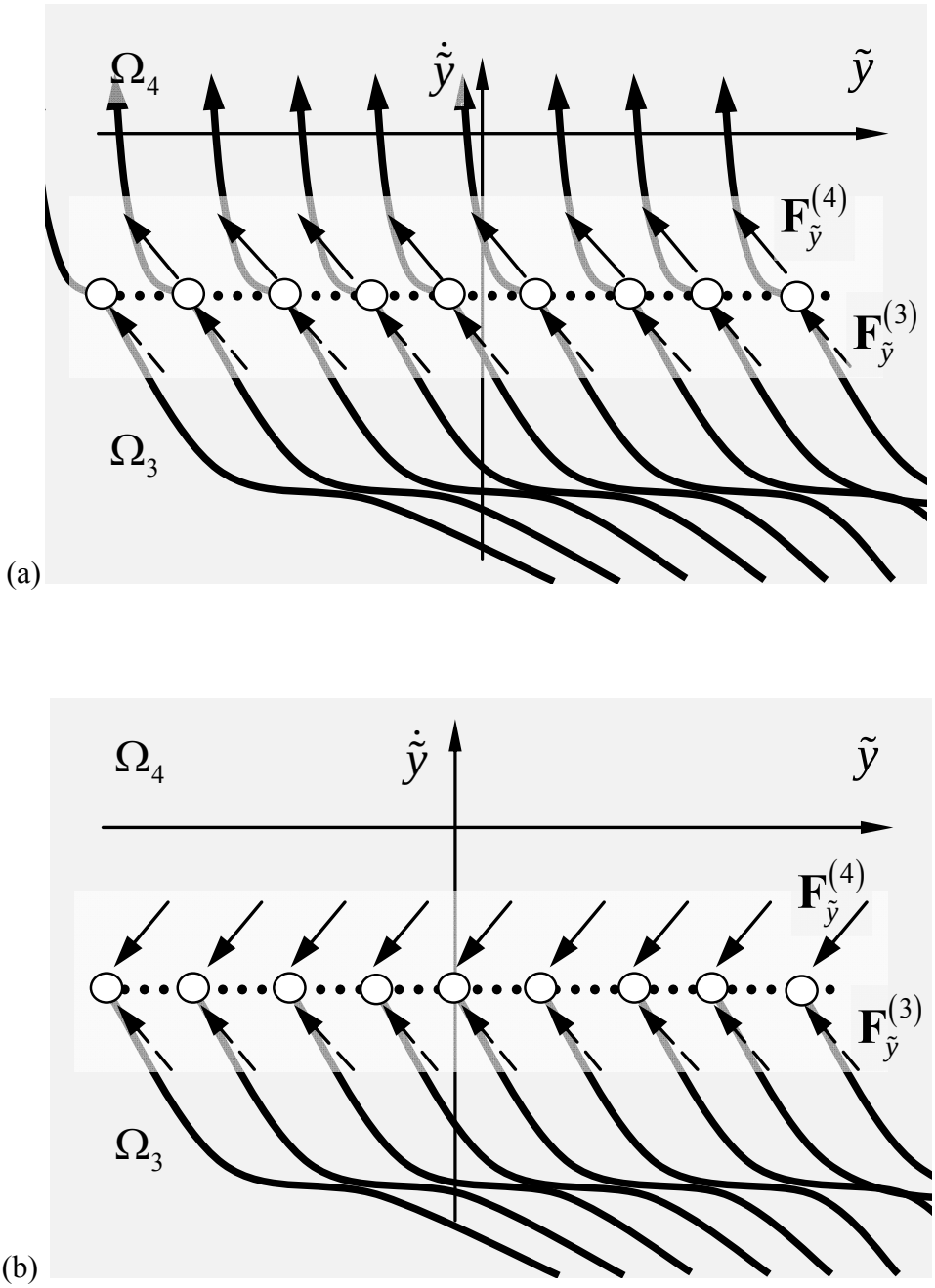

Fig. 15 Vector fields for a) passable and b) non-passable motion.

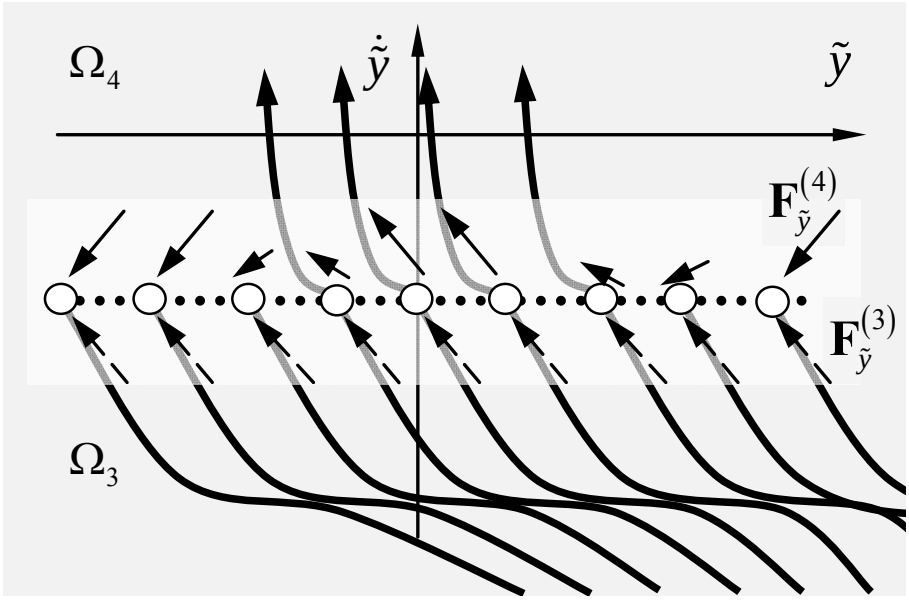

(a)

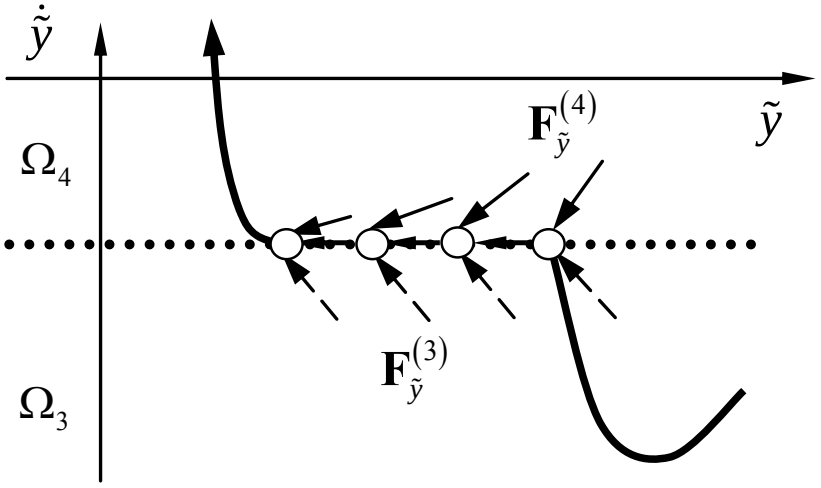

(b)

Fig. 16 Vector fields for a) passable and non-passable with appearance and vanishing points, and b) specific example of non-passable motion and vanishing point.

$t_m \in [t_i, t_{i+1})$ by

$$\left[\mathbf{n}_{\partial\Omega_{ij}}^T \bullet \mathbf{F}_{D_i}^{(i)}\left(\mathbf{D}_i, t_{m-}\right)\right] \times \left[\mathbf{n}_{\partial\Omega_{ij}}^T \bullet \mathbf{F}_{D_i}^{(j)}\left(\mathbf{D}_i, t_{m+}\right)\right] \leq 0; \tag{4.14}$$

$\left(\text{for } i \neq j \text{ and } i, j = 1,2,3,4\right)$; respectively. The only boundaries which have the possibility of a sink boundary (opposing vector fields) are the velocity boundaries. Substituting Eq.(4.8) into Eq.(4.14) gives,

$$F_{\tilde{y}}^{(2)}\left(\tilde{\mathbf{x}}, \tilde{\mathbf{y}}, , t\right) F_{\tilde{y}}^{(4)}\left(\tilde{\mathbf{x}}, \tilde{\mathbf{y}}, , t\right) \leq 0 \text{ if } D_2 < 0, \text{ on } \partial\Omega_{24}. \tag{4.15}$$

Provided Eq.(4.15) is satisfied the boundary is indeed non-passable, but regarding the machine-tool model and force conditions at the onset of cutting. When the tool returns to cutting in the positive $\tilde{y}$–direction the friction boundary is crossed at which point the contact conditions are reset to ensure a continuous stiffness force.

Since the system's equilibrium point is recalculated to accommodate the continuous stiffness force across the frictional boundary, the boundary is permanently passable. The boundary dynamics are negated due to local exceptions. Substituting Eq.(4.9) into Eq.(4.14) gives,

$$F_{\tilde{y}}^{(3)}\left(\tilde{\mathbf{x}}, \tilde{\mathbf{y}}, , t\right) F_{\tilde{y}}^{(4)}\left(\tilde{\mathbf{x}}, \tilde{\mathbf{y}}, , t\right) \leq 0, \text{ on } \partial\Omega_{34}; \tag{4.16}$$

see Fig. 15(b) to observe the opposing vector fields. There are two possible ways to interpret the inequality of Eq.(4.16). The forces producing such an effect are

$$F_{\tilde{y}}^{(i)}\left(\tilde{\mathbf{x}},\tilde{\mathbf{y}},t\right)\le 0 \text{ and } F_{\tilde{y}}^{(j)}\left(\tilde{\mathbf{x}},\tilde{\mathbf{y}},t\right)\ge 0\Big\} \text{ on } \partial\Omega_{ij}, \tag{4.17}$$

for $i \neq j;\ i, j = 3,4$ (see Fig. 16(a,b)). The forces distribution in the $\tilde{y}$ phase plane of Fig. 16(a,b) illustrate Eq.(4.17) and the onset and vanishing of the chip seizure motion.

The onset and vanishing of chip seizure motion noted in Eq.(4.17) is specifically defined as

$$F_{\tilde{y}}^{(i)}\left(\tilde{\mathbf{x}},\tilde{\mathbf{y}},t\right)=0\Big\} \text{ on } \partial\Omega_{ij}, \tag{4.18}$$

for $i, j = 3,4$ and $i \neq j$. Such a definition implies a possible grazing of boundary three (chip/tool friction boundary). This phenomenon has been extensively studied by Luo and Gegg [31] and the general theory derived can be directly applied for this machine-tool, but is not developed herein.

CHAPTER V

SWITCHING PLANES, MAPPINGS AND MAPPING STRUCTURE

Since the motion of the machine-tool can be tracked through four domains and can intersect four boundaries, simply referring to the domain traveled is not sufficient to describe the entire motion. A new notation is introduced to define the initial boundary and the final boundary in combination with the notation describing the domain traveled.

$$P_{(ij)k} \text{ for } i = 1,2,3,4;\ j = 1,2,3,4;\ \text{and } k = 0,1,2,3,4); \tag{5.1}$$

where i is the initial boundary, j is the final boundary and k is the domain traversed, see Fig. 17 and Fig. 18. The mappings describe the following cases: vibration of the tool with no contact of the work-piece (i = 1); the tool in contact with the work-piece but no cutting $(i = 2)$; the tool in contact with the work-piece with cutting where $\dot{z} < 0$ (i = 3); the tool in contact with the work-piece with cutting where $\dot{z} > 0$ (i = 4); and contact with the tool in special case where the chip/tool rake face seizure occurs, $\dot{z} \equiv 0$ (i = 0). The action of one mapping given a set of initial conditions yields a set of final conditions for this machine-tool system.

The mappings can be combined to describe the trajectory of periodic orbit in the phase plane. For example, consider the mappings $P_{(11)1}$ and $P_{(11)2}$ in series; which can be simplified using the notation $P_{21} = P_{(11)2} \circ P_{(11)1}$, where the boundary definitions are discarded and only the domains traveled remain in the notation (This notation is useful for referencing periodic motion). Through this notation, varying a system parameter

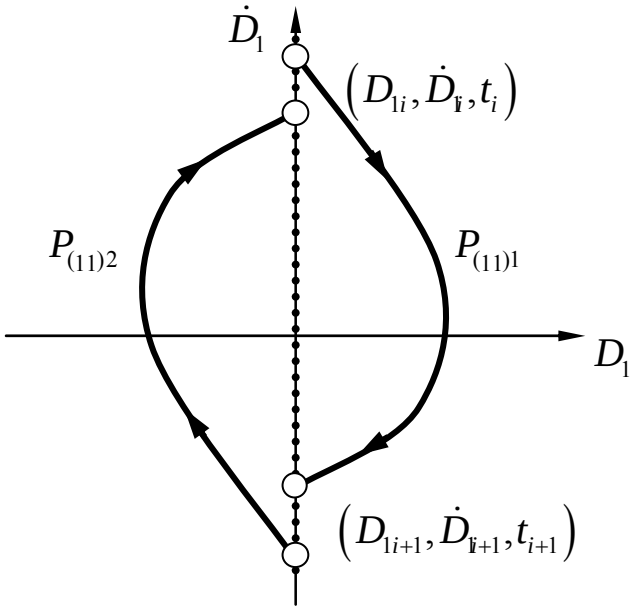

(a)

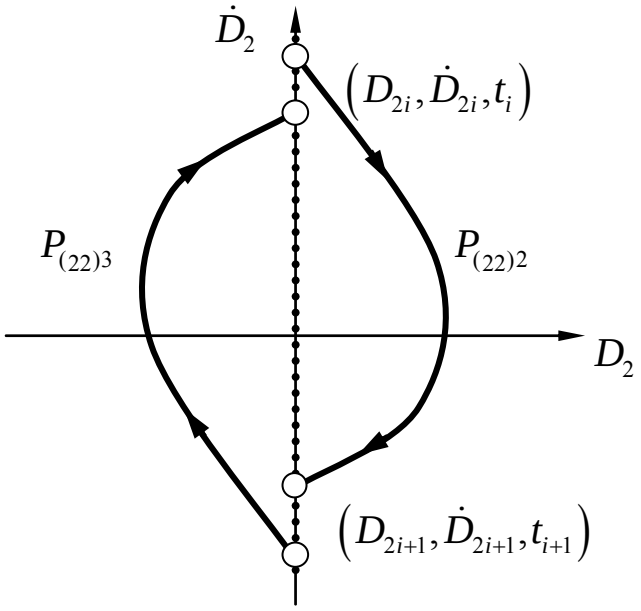

(b)

Fig. 17 Mappings according to a) $\mathbf{D}_1$, b) $\mathbf{D}_2$, phase planes.

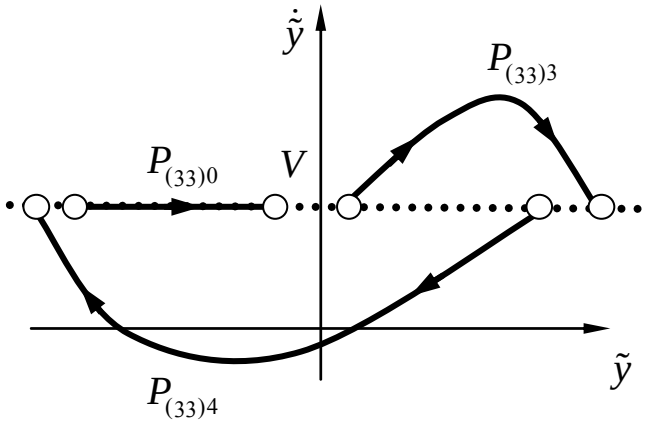

(a)

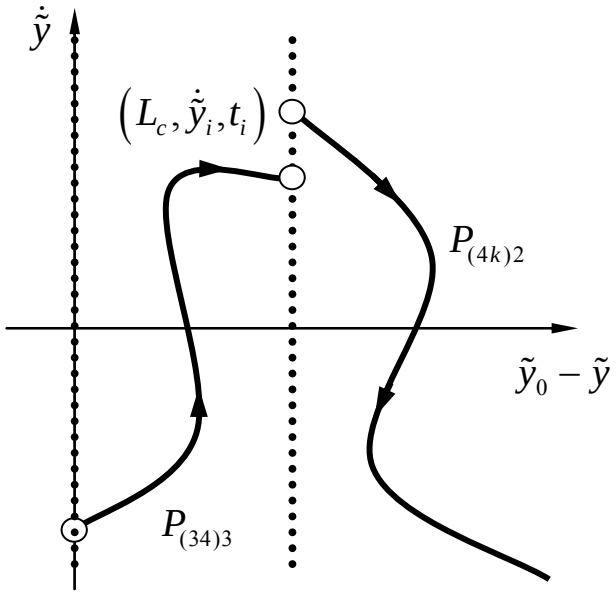

(b)

Fig. 18 Mappings according to a) $\mathbf{D}_3$, and b) $\mathbf{D}_4$, phase planes.

gives a description of how the orbits change. The following section will develop the switching sets with regard to boundary one (tool and work-piece contact / impact boundary).

Switching Planes and Mapping Notations for Transient Motions

Study of Boundary 1

The motion of the machine tool can be tracked through the phase plane by the mappings, see Fig. 17 and Fig. 18. Defining the initial and final conditions of these mappings are switching planes. The switching planes for the tool and work-piece contact / impact boundary, Eq.(2.1) (boundary one), are

$$\Xi_{D_1}^1 = \left\{ (x, y, \dot{x}, \dot{y}) \middle| D_1(x, y) = 0^+ \right\},\ \Xi_{D_1}^2 = \left\{ (x, y, \dot{x}, \dot{y}) \middle| D_1(x, y) = 0^- \right\}, \tag{5.2}$$

$$\Xi_{D_1}^3 = \left\{ (x, y, \dot{x}, \dot{y}) \middle| D_1(x, y) = 0^- \right\} \text{ if } D_2 \le 0, \tag{5.3}$$

$$\Xi_{D_1}^4 = \left\{ (x, y, \dot{x}, \dot{y}) \middle| D_1(x, y) = 0^- \right\} \text{ if } D_2 \le 0, \tag{5.4}$$

and

$$\Xi_{D_1}^0 = \left\{ (x, y, \dot{x}, \dot{y}) \middle| D_1(x, y) = 0^- \right\} \text{ if } D_2 \le 0 \text{ and } \dot{\tilde{y}} \equiv V. \tag{5.5}$$

Note that $0^- = \lim_{\delta \to 0} (0 - \delta)$ and $0^+ = \lim_{\delta \to 0} (0 + \delta)$. Motion ending at switching plane one, domain zero side, $\Xi_{D_1}^0$ is expressed as,

$$\Xi^0_{D_3} \rightarrow \Xi^0_{D_1} : P_{(31)0}. \tag{5.6}$$

The mapping of Eq.(5.6) describes some initial condition on the chip/tool friction boundary plane (switching set) mapping through domain zero (chip seizure) to boundary one (tool and work-piece contact boundary). Since the domain traversed is the zero domain the motion must start on the boundary three; hence $\Xi^0_{D_3}$. Motion beginning and ending at switching plane one, domain one side, $\Xi^1_{D_1}$ is expressed as,

$$\Xi^1_{D_1} \rightarrow \Xi^1_{D_1} : P_{(11)1}, \tag{5.7}$$

see Fig. 17(a). The mapping of Eq.(5.7) represents motion beginning on boundary one (tool and work-piece contact boundary) traversing domain one (Ω_1) (tool-piece free running) and ending on boundary one (tool and work-piece contact / impacting boundary). The motion beginning and ending at switching plane one, domain two side, $\Xi^2_{D_1}$ is expressed as,

$$\Xi^2_{D_1} \rightarrow \Xi^2_{D_1} : P_{(11)2}, \tag{5.8}$$

see Fig. 17(a).

The mapping of Eq.(5.8) describes motion through domain two (tool and work-piece contact but not cutting) and beginning and ending at boundary one. Motion beginning and ending at switching plane one, domain three side, $\Xi^3_{D_1}$ is expressed as,

$$\Xi^3_{D_1} \rightarrow \Xi^3_{D_1} : P_{(11)3}. \tag{5.9}$$

The mapping of Eq.(5.9) describes motion through domain three (tool and work-piece contact, and cutting with $\dot{\tilde{y}}(\dot{x},\dot{y}) \in (-\infty, V)$) beginning and ending on boundary one. Motion beginning and ending at switching plane one, domain four side, $\Xi^4_{D_1}$ is expressed as,

$$\Xi^4_{D_1} \to \Xi^4_{D_1} : P_{(11)4}. \tag{5.10}$$

The mapping of Eq.(5.10) describes motion through domain four (tool and work-piece contact, and cutting with $\dot{\tilde{y}}(\dot{x},\dot{y}) \in (V, \infty)$) beginning and ending on boundary one. The next section will develop the switching sets with regard to boundary two (the onset of cutting boundary).

Study of Boundary 2

The switching planes for the onset of cutting boundary, Eq.(2.2) (boundary two), are

$$\Xi^1_{D_2} = \left\{ (x, y, \dot{x}, \dot{y}) \middle| D_2(x, y) = 0^+ \right\} \text{ if } D_1 \equiv 0, \tag{5.11}$$

$$\Xi^2_{D_2} = \left\{ (x, y, \dot{x}, \dot{y}) \middle| D_2(x, y) = 0^+ \right\}, \tag{5.12}$$

$$\Xi^3_{D_2} = \left\{ (x, y, \dot{x}, \dot{y}) \middle| D_2(x, y) = 0^- \right\} \text{ if } \dot{\tilde{y}} \le V, \tag{5.13}$$

$$\Xi^4_{D_2} = \left\{ (x, y, \dot{x}, \dot{y}) \middle| D_2(x, y) = 0^- \right\} \text{ if } \dot{\tilde{y}} \ge V, \tag{5.14}$$

and

$$\Xi^0_{D_2} = \left\{ (x, y, \dot{x}, \dot{y}) \middle| D_2(x, y) = 0^- \right\} \text{ if } \dot{\tilde{y}} \equiv V. \tag{5.15}$$

The motion ending at switching plane two, domain zero side, $\Xi^0_{D_2}$ is expressed as

$$\Xi^0_{D_3} \rightarrow \Xi^0_{D_2} : P_{(32)0}. \tag{5.16}$$

The mapping of Eq.(5.16) describes motion beginning on boundary three (chip/tool friction boundary) traversing domain zero (chip/tool seizure) and ending on boundary two (onset/vanishing of cutting boundary). The motion beginning and ending at switching plane two, domain one side, $\Xi^1_{D_2}$ is expressed as

$$\Xi^1_{D_2} \rightarrow \Xi^1_{D_2} : P_{(22)1}. \tag{5.17}$$

The mapping of Eq.(5.17) describes motion beginning and ending on boundary two while traversing domain one (Ω_1) (tool free running).

Although the switching planes of Eq.(5.7) and Eq.(5.17) are different the domain traveled is domain one (Ω_1). The motion beginning and ending at switching plane two, domain two side, $\Xi^2_{D_2}$ is expressed as

$$\Xi^2_{D_2} \rightarrow \Xi^2_{D_2} : P_{(22)2}, \tag{5.18}$$

see Fig. 17(b). The mapping of Eq.(5.18) describes motion beginning and ending on boundary two while traversing domain two (Ω_2) (tool and work-piece contact with no cutting). Although the switching planes of Eq.(5.8) and Eq.(5.18) are different the domain traveled is domain two (Ω_2). The motion beginning and ending at switching plane two, domain three side, $\Xi^3_{D_2}$ is expressed as

$$\Xi^3_{D_2} \rightarrow \Xi^3_{D_2} : P_{(22)3}, \tag{5.19}$$

see Fig. 17(b).

The mapping of Eq.(5.19) describes motion beginning and ending on boundary two while traversing domain three (Ω_3) (tool and work-piece contact, and cutting with $\dot{\tilde{y}}(\dot{x},\dot{y}) \in (-\infty, V)$). Although the switching planes of Eq.(5.9) and Eq.(5.19) are different the domain traveled is domain three (Ω_3). The motion beginning and ending at switching plane two, domain four side, $\Xi^4_{D_2}$ is expressed as

$$\Xi^4_{D_2} \rightarrow \Xi^4_{D_2} : P_{(22)4}. \tag{5.20}$$

The mapping of Eq.(5.18) describes motion beginning and ending on boundary two while traversing domain four (Ω_4) (tool and work-piece contact, and cutting with $\dot{\tilde{y}}(\dot{x},\dot{y}) \in (V, \infty)$). Although the switching planes of Eq.(5.10) and Eq.(5.20) are different the domain traveled is domain four (Ω_4). The next section will develop the switching sets with regard to boundary three (chip/tool friction boundary).

Study of Boundary 3

The switching planes for chip/tool friction boundary, Eq.(2.16) (boundary three), are

$$\Xi^1_{\tilde{y}} = \left\{ \left(x, y, \dot{x}, \dot{y}\right) \middle| \dot{\tilde{y}}\left(\dot{x}, \dot{y}\right) \equiv V \right\} \text{ if } D_1 \equiv 0 \text{ and } D_2 < 0, \tag{5.21}$$

$$\Xi^2_{\tilde{y}} = \left\{ \left(x, y, \dot{x}, \dot{y}\right) \middle| \dot{\tilde{y}}\left(\dot{x}, \dot{y}\right) \equiv V \right\} \text{ if } D_2 \equiv 0, \tag{5.22}$$

$$\Xi_{\tilde{y}}^{3} = \left\{ \left(x, y, \dot{x}, \dot{y} \right) \middle| \dot{\tilde{y}}\left(\dot{x}, \dot{y} \right) = V^{-} \right\} \text{ if } D_1 < D_2 < 0, \tag{5.23}$$

$$\Xi_{\tilde{y}}^{4} = \left\{ \left(x, y, \dot{x}, \dot{y} \right) \middle| \dot{\tilde{y}}\left(\dot{x}, \dot{y} \right) = V^{+} \right\} \text{ if } D_1 < D_2 < 0, \tag{5.24}$$

and

$$\Xi_{\tilde{y}}^{0} = \left\{ \left(x, y, \dot{x}, \dot{y} \right) \middle| \dot{\tilde{y}}\left(\dot{x}, \dot{y} \right) \equiv V \right\} \text{ if } D_1 < D_2 < 0. \tag{5.25}$$

The motion beginning and ending at switching plane three, domain zero side, $\Xi_{\tilde{y}}^{0}$ is expressed as

$$\Xi_{\tilde{y}}^{0} \to \Xi_{\tilde{y}}^{0} : P_{(33)0}; \tag{5.26}$$

see Fig. 18(a). The mapping of Eq.(5.26) describes motion beginning and ending on boundary three while traversing domain zero (chip/tool seizure). Although the switching planes of Eq.(5.16) and Eq.(5.26) are different the domain traveled is domain zero. The motion beginning and ending at switching plane three, domain one side, $\Xi_{\tilde{y}}^{1}$ is expressed as

$$\Xi_{\tilde{y}}^{1} \to \Xi_{\tilde{y}}^{1} : P_{(33)1}. \tag{5.27}$$

The mapping of Eq.(5.17) describes motion beginning and ending on boundary two while traversing domain one (tool free running). Although the switching planes of Eq. (5.17) and Eq.(5.27) are different the domain traveled is domain one (Ω_1). The

motion beginning and ending at switching plane three, domain two side, $\Xi_{\tilde{y}}^{2}$ is expressed as

$$\Xi_{\tilde{y}}^{2} \rightarrow \Xi_{\tilde{y}}^{2} : P_{(33)2}. \tag{5.28}$$

The mapping of Eq.(5.28) describes motion beginning and ending on boundary three while traversing domain two (Ω_2) (tool and work-piece contact with no cutting). Although the switching planes of Eq.(5.18) and Eq.(5.28) are different the domain traveled is domain two (Ω_2).

The motion beginning and ending at $\Xi_{\tilde{y}}^{3}$ is expressed as

$$\Xi_{\tilde{y}}^{3} \rightarrow \Xi_{\tilde{y}}^{3} : P_{(33)3}; \tag{5.29}$$

see Fig. 18(a). The mapping of Eq.(5.29) describes motion beginning and ending on boundary three while traversing domain three (Ω_3) (tool and work-piece contact, and cutting with $\dot{\tilde{y}}(\dot{x}, \dot{y}) \in (-\infty, V)$). Although the switching planes of Eq.(5.19) and Eq.(5.29) are different the domain traveled is domain three (Ω_3). The motion beginning and ending at switching plane three, domain four side, $\Xi_{\tilde{y}}^{4}$ is expressed as

$$\Xi_{\tilde{y}}^{4} \rightarrow \Xi_{\tilde{y}}^{4} : P_{(33)4}; \tag{5.30}$$

see Fig. 18(a). The mapping of Eq.(5.30) describes motion beginning and ending on boundary two while traversing domain four (Ω_4) (tool and work-piece contact, and cutting with $\dot{\tilde{y}}(\dot{x}, \dot{y}) \in (V, \infty)$).

Although the switching planes of Eq.(5.20) and Eq.(5.30) are different the domain traveled is domain four (Ω_4). The next section will develop the switching sets with regard to boundary four (chip vanishing boundary).

Study of Boundary 4

The switching planes for the chip vanishing boundary, Eq.(2.23) (boundary four), are

$$\Xi^2_{D_4} = \left\{ \left(x, y, \dot{x}, \dot{y} \right) \middle| D_4\left(x, y \right) = 0^- \right\} \text{ if } D_1 < D_2 < 0, \tag{5.31}$$

$$\Xi^3_{D_4} = \left\{ \left(x, y, \dot{x}, \dot{y} \right) \middle| D_4\left(x, y \right) = 0^+ \right\} \text{ if } D_1 < D_2 < 0. \tag{5.32}$$

The motion beginning at switching plane three, domain three side, $\Xi^3_{D_3}$ and ending at switching plane four, domain three side, $\Xi^3_{D_4}$ is expressed as

$$\Xi^3_{D_3} \to \Xi^3_{D_4} : P_{(34)3}; \tag{5.33}$$

see Fig. 18(b). The mapping of Eq.(5.33) describes motion beginning on boundary three and ending on boundary four while traversing domain three (Ω_3) (tool and work-piece contact, and cutting with $\dot{\tilde{y}}(\dot{x}, \dot{y}) \in (-\infty, V)$). Although the switching planes of Eq.(5.29) and Eq.(5.33) are different the domain traveled is domain three (Ω_3). The motion beginning at $\Xi^2_{D_4}$ and ending at $\Xi^2_{D_k}$ is expressed as

$$\Xi^2_{D_4} \to \Xi^2_{D_k} : P_{(4k)2}; \tag{5.34}$$

$k = 1, 2, 3,$ see Fig. 18(b).

The mapping of Eq.(5.34) describes motion beginning on boundary four and ending on the *kth* boundary while traversing domain four (Ω_4) (tool and work-piece contact, and cutting with $\dot{\tilde{y}}(\dot{x},\dot{y}) \in (V,\infty)$). Although the switching planes of Eq.(5.30) and Eq.(5.34) are different the domain traveled is domain four (Ω_4). Motion in domains zero, one and two cannot interact with boundary four since this boundary monitors chip vanishing.

Study of Possible Combinations of the 4 Boundaries

The physical combinations of initial and final boundaries are summarized in Table 1. The possible combinations for motion include four possible initial boundaries and three possible final boundaries with five possible domains to be traveled. Certain configurations of these boundaries and domains are not physically possible; the potential motions are shown in Table 1. Consider the *jth* and *kth* initial and final boundary of a mapping where the zero domain (chip/tool seizure) is traversed,

$$\Xi^0_{D_j} \rightarrow \Xi^0_{D_k} : P_{(jk)0}. \tag{5.35}$$

The possible combinations of *j* and *k* include: $j = 1,2,3$ and $k = 1,2,3$.

Consider the *jth* and *kth* initial and final boundary of a mapping where domain one (tool free running) is traversed,

$$\Xi^1_{D_j} \rightarrow \Xi^1_{D_k} : P_{(jk)1}. \tag{5.36}$$

Table 1 Possible Switching Set Combinations and Mappings.

Initial Boundary	Final Boundary	Domain Traversed	Switching Sets: Mapping	*j*,*k*
j	k	0	$\Xi^0_{D_j} \rightarrow \Xi^0_{D_k} : P_{(jk)0}.$	$j=1,2,3;\ k=1,2,3;$
j	k	1	$\Xi^1_{D_j} \rightarrow \Xi^1_{D_k} : P_{(jk)1}.$	$j=1;\ k=1;$
j	k	2	$\Xi^2_{D_j} \rightarrow \Xi^2_{D_k} : P_{(jk)2}.$	$j=1,2,4;\ k=1,2,3;$
j	k	3	$\Xi^3_{D_j} \rightarrow \Xi^3_{D_k} : P_{(jk)3}.$	$j=1,2,3;\ k=1,2,3,4;$
j	k	4	$\Xi^4_{D_j} \rightarrow \Xi^4_{D_k} : P_{(jk)4}.$	$j=1,2,3;\ k=1,2,3;$
1	${}^1j$	k	$\Xi^k_{D_1} \rightarrow \Xi^k_{D_j} : P_{(1j)k}.$	$j=1,2,3;\ k=0,1,2,4;$
2	${}^2j$	k	$\Xi^k_{D_2} \rightarrow \Xi^k_{D_j} : P_{(2j)k}.$	$j=1,2,3;\ k=0,2,4;$
3	${}^3j$	k	$\Xi^k_{D_3} \rightarrow \Xi^k_{D_j} : P_{(3j)k}.$	$j=1,2,3;\ k=0,3,4;$
4	j	k	$\Xi^k_{D_4} \rightarrow \Xi^k_{D_j} : P_{(4j)k}.$	$j=1,2,3;\ k=2;$

Note: $D_3\left(\dot{x},\dot{y}\right) \equiv D_{\tilde{y}}\left(\dot{x},\dot{y}\right)$

1. If $j=3 \rightarrow k \neq 1;$
2. if $j=1,2,3 \rightarrow k=0,1,2,4;$
3. and $j=4;\ k=3.$

The possible combinations of j and k include: $j=1$ and $k=1$. Consider the *jth* and *kth* initial and final boundary of a mapping where domain two (tool and work-piece contact but no cutting) is traversed,

$$\Xi^2_{D_j} \rightarrow \Xi^2_{D_k} : P_{(jk)2}. \tag{5.37}$$

The possible combinations of j and k include: $j=1,2,4$ and $k=1,2,3$. Consider the *jth* and *kth* initial and final boundary of a mapping where domain three (tool and work-piece contact, with cutting and $\dot{\tilde{y}}(\dot{x},\dot{y}) \in (-\infty, V)$) is traversed,

$$\Xi^3_{D_j} \rightarrow \Xi^3_{D_k} : P_{(jk)3}. \tag{5.38}$$

The possible combinations of *j* and *k* include: $j = 1,2,3$ and $k = 1,2,3,4$.

Consider the *jth* and *kth* initial and final boundary of a mapping where domain four (tool and work-piece contact, with cutting and $\dot{\tilde{y}}(\dot{x},\dot{y}) \in (V,\infty)$) is traversed,

$$\Xi^4_{D_j} \rightarrow \Xi^4_{D_k} : P_{(jk)4}. \tag{5.39}$$

The possible combinations of j and k include: $j = 1,2,3$ and $k = 1,2,3$. Exceptions to this list exist at the intersection of two or more boundaries, which are not developed herein. The following section will discuss combinations of the switching planes with respect to initial boundaries.

Combinations with an Initial Boundary of 1

Consider the physical types of motion which exists for an initial boundary one (tool and work-piece contact / impact boundary). The switching planes previously developed are used to define such possible mappings,

$$\Xi^k_{D_1} \rightarrow \Xi^k_{D_j} : P_{(1j)k} \text{ for } j = 1,2,3 \text{ and } k = 0,1,2,3; \tag{5.40}$$

where the final boundary is *j* and the domain traversed is *k*. One exception for the *jth* term is the case where $j = 3$ then $k \neq 1$.

Combinations with an Initial Boundary of 2

Consider the physical types of motion which exist with boundary two (tool and work-piece contact and no cutting) and *j* as the initial and final boundaries, respectively. The switching planes and mappings corresponding to this motion are

$$\Xi_{D_2}^{k} \rightarrow \Xi_{D_j}^{k} : P_{(2j)k} \text{ for } j = 1,2,3 \text{ and } k = 0,2,4; \tag{5.41}$$

where the final boundary is *j* and the domain traversed is *k*. One exception for the *jth* term is the case where $j = 3$ then $k \neq 2$.

Combinations with an Initial Boundary of 3

Consider the physical types of motion which exist with boundary three (tool and work-piece contact, and cutting with $\dot{\tilde{y}}(\dot{x}, \dot{y}) \in (-\infty, V)$) and *k* as the initial and final boundaries, respectively. The switching planes and mappings corresponding to this motion are

$$\Xi_{D_3}^{k} \rightarrow \Xi_{D_j}^{k} : P_{(3j)k} \text{ for } j = 1,2,3,4 \text{ and } k = 0,3,4; \tag{5.42}$$

where the initial boundary is one, the final boundary is *j* and the domain traversed is *k*. One exception for the *jth* term is the case where $j = 4$ then $k \neq 0,4$.

Combinations with an Initial Boundary of 4

Consider the physical types of motion which exist with boundary four (tool and work-piece contact, and cutting with $\dot{\tilde{y}}(\dot{x}, \dot{y}) \in (V, \infty)$) and *k* as the initial and final boundaries, respectively. The switching planes and mappings corresponding to this motion are

$$\Xi_{D_3}^{k} \rightarrow \Xi_{D_j}^{k} : P_{(4j)k} \text{ for } j = 1,2,3 \text{ and } k = 2; \tag{5.43}$$

where the initial boundary is one, the final boundary is *j* and the domain traversed is *k*. The summary of these combinations is shown in Table 1. The next section will employ the switching planes and mapping to summarize and develop a notation for periodic

motions. Such a notation will be very useful in characterizing the orbit in the phase plane and interactions with the dynamics of the five possible domains.

Mappings for Periodic Motions

The switching sets developed in the previous sections set up the development of periodic motion. Such periodic motion can vary in initial conditions and domains traversed. The following sections will use the switching planes to introduce the ordering of mappings for the periodic motions interacting with the corresponding boundaries.

Study of Boundary 1

Consider the interaction of the motion with boundary one, the tool and work-piece contact / impact boundary, where the switching sets of Eq.(5.2). This example considers one period of motion. The ordering of switching planes to form periodic motion are

$$\begin{array}{ccc} \Xi^1_{D_1} & \overset{P_{(11)1}}{\rightarrow} & \Xi^1_{D_1} \\ \uparrow_{D_1} & & \downarrow_{D_1} \\ \Xi^2_{D_1} & \underset{P_{(11)2}}{\leftarrow} & \Xi^2_{D_1} \end{array} \quad \Rightarrow \quad P_{(11)1} \rightarrow P_{(11)2}. \tag{5.44}$$

This implies the mapping $P_{(11)2}$ acts on the final conditions of mapping $P_{(11)1}$; such an actions maps to the initial conditions of mapping $P_{(11)1}$. The mapping notation can be combined when periodic motion is discussed with the shorthand notation of the action symbol $(\circ)$ and the removal of the boundary notations.

For example the periodic motion of Eq.(5.44) is expressed as

$$P_{21} = P_{(11)2} \circ P_{(11)1}. \tag{5.45}$$

This periodic motion corresponds to the tool free running (domain one) which is directly followed by the tool-piece and work-piece contact without cutting (domain two). This motion repeats with a period $T = {}^{2\pi}\!/_{\Omega}$ equal to the eccentricity frequency (Ω). Consider the ordering of switching sets to form periodic motion of length period three $3T$,

$$\begin{array}{ccccccccccc} \Xi^1_{D_1} & \overset{P_{(11)1}}{\rightarrow} & \Xi^1_{D_1} & \overset{D_1}{\rightarrow} & \Xi^2_{D_1} & \overset{P_{(11)2}}{\rightarrow} & \Xi^2_{D_1} & \overset{D_1}{\rightarrow} & \Xi^1_{D_1} & \overset{P_{(11)1}}{\rightarrow} & \Xi^1_{D_1} \\ \uparrow_{D_1} & & & & & & & & & & \downarrow_{D_1} \\ \Xi^2_{D_1} & \underset{P_{(11)2}}{\leftarrow} & \Xi^2_{D_1} & \underset{D_1}{\leftarrow} & \Xi^1_{D_1} & \underset{P_{(11)1}}{\leftarrow} & \Xi^1_{D_1} & \underset{D_1}{\leftarrow} & \Xi^2_{D_1} & \underset{P_{(11)2}}{\leftarrow} & \Xi^2_{D_1} \end{array} \tag{5.46}$$

this can be simplified with mapping notation,

$$P_{212121} = P_{(11)2} \circ P_{(11)1} \circ P_{(11)2} \circ P_{(11)1} \circ P_{(11)2} \circ P_{(11)1}. \tag{5.47}$$

The notation is still too bulky and can be reduced by a generic form of factoring the notation; Eq.(5.47) becomes,

$$P_{(21)^3} = P_{212121}. \tag{5.48}$$

In general the *n*-period periodic motion of the P_{21} is

$$P_{(21)^n} = P_{21\ldots21}; \tag{5.49}$$

where *n* is the period of motion. Additional mappings may occur in the periodic motion interacting with boundary one. Such an interaction could include a short cutting action, implying domain four ($\dot{\tilde{y}} > V$) inclusion;

$$P_{41} = P_{(11)4} \circ P_{(11)1}, \tag{5.50}$$

domain zero (chip/tool seizure, $\dot{\tilde{y}} \equiv V$) and domain four ($\dot{\tilde{y}} > V$),

$$P_{041} = P_{(31)0} \circ P_{(13)4} \circ P_{(11)1}, \tag{5.51}$$

or domain three ($\dot{\tilde{y}} < V$) and domain four ($\dot{\tilde{y}} > V$),

$$P_{341} = P_{(31)3} \circ P_{(13)4} \circ P_{(11)1}. \tag{5.52}$$

Study of Boundary 2

Consider the interaction of the motion with boundary two, the work-piece and tool-piece contact / impact boundary, where the switching sets of Eq.(5.12) and Eq.(5.14). This example considers one period of motion. The ordering of switching sets to form periodic motion are

$$\begin{array}{ccc} \Xi^2_{D_2} & \overset{P_{(22)2}}{\rightarrow} & \Xi^2_{D_2} \\ \uparrow_{D_2} & & \downarrow_{D_2} \\ \Xi^4_{D_2} & \underset{P_{(22)4}}{\leftarrow} & \Xi^4_{D_2} \end{array} \quad \Rightarrow \quad P_{(22)2} \rightarrow P_{(22)4}. \tag{5.53}$$

The periodic motion of Eq.(5.53) is expressed as

$$P_{42} = P_{(22)4} \circ P_{(22)2}. \tag{5.54}$$

This periodic motion corresponds to the tool-piece and work-piece in contact with no cutting directly followed by the tool-piece and work-piece in contact with cutting.

This motion repeats with a period $T = 2\pi/\Omega$ equal to the eccentricity frequency (Ω). Additional mappings may occur in the periodic motion interacting with boundary two. Such an interaction could include a chip vanishing, implying domain three ($\dot{\tilde{y}} < V$) inclusion;

$$P_{342} = P_{(32)3} \circ P_{(23)4} \circ P_{(22)2}, \tag{5.55}$$

or a domain zero (chip/tool seizure, $\dot{\tilde{y}} \equiv V$),

$$P_{042} = P_{(32)0} \circ P_{(23)4} \circ P_{(22)2}. \tag{5.56}$$

Study of Boundary 3

Consider the interaction of the motion with boundary three, the chip / tool-piece rake surface friction boundary, where the switching sets of Eq.(5.23) and Eq.(5.24). This example considers one period of motion. The ordering of switching sets to form periodic motion is

$$\begin{array}{ccc} \Xi^4_{D_3} & \overset{P_{(33)4}}{\rightarrow} & \Xi^4_{D_3} \\ \uparrow_{D_3} & & \downarrow_{D_3} \\ \Xi^3_{D_3} & \underset{P_{(33)4}}{\leftarrow} & \Xi^3_{D_3} \end{array} \quad \Rightarrow \quad P_{(33)3} \rightarrow P_{(33)4}. \tag{5.57}$$

The periodic motion of Eq.(5.57) is expressed as

$$P_{34} = P_{(33)3} \circ P_{(33)4}. \tag{5.58}$$

This periodic motion corresponds to the tool-piece and work-piece in contact with cutting (domain four, $\dot{\tilde{y}} > V$) directly followed by the reduction in chip length (domain three, $\dot{\tilde{y}} < V$).

This motion repeats with a period $T = {}^{2\pi}\!/_{\Omega}$ equal to the eccentricity frequency (Ω). Additional mappings may occur in the periodic motion interacting with boundary three. Such an interaction could include domain zero (chip/tool seizure, $\dot{\tilde{y}} \equiv V$) ,

$$P_{04} = P_{(33)0} \circ P_{(33)4}, \tag{5.59}$$

and a chip vanishing motion, implying domain three ($\dot{\tilde{y}} < V$),

$$P_{034} = P_{(33)0} \circ P_{(33)3} \circ P_{(33)4}. \tag{5.60}$$

Study of Boundary 4

Consider the interaction of the motion with boundary four, the chip vanishing boundary, where the switching sets of Eq.(5.31) and Eq.(5.32). This example considers one period of motion. The ordering of switching sets to form periodic motion is

$$\begin{array}{ccccccc} \Xi^2_{D_4} & \overset{P_{(43)2}}{\rightarrow} & \Xi^2_{D_3} & \overset{D_3}{\rightarrow} & \Xi^4_{D_3} & \overset{P_{(33)4}}{\rightarrow} & \Xi^4_{D_3} \\ & \nwarrow_{D_4} & & & & \swarrow_{D_4} & \\ & & \Xi^3_{D_4} & \underset{P_{(34)3}}{\leftarrow} & \Xi^3_{D_3} & & \end{array} \quad \Rightarrow \quad P_{(43)2} \rightarrow P_{(33)4} \rightarrow P_{(34)3}. \qquad (5.61)$$

The periodic motion of Eq.(5.61) is also expressed as

$$P_{342} = P_{(34)3} \circ P_{(33)4} \circ P_{(43)2}. \qquad (5.62)$$

This periodic motion corresponds to the tool-piece and work-piece in contact without cutting (domain two) directly followed by cutting (domain four $\dot{\tilde{y}} > V$) which then crosses the frictional boundary where the chip reduces in length to zero (domain three $\dot{\tilde{y}} < V$ to boundary four).

This motion repeats with a period $T = 2\pi/\Omega$ equal to the eccentricity frequency (Ω). Additional mappings may occur in the periodic motion interacting with boundary four. Such an interaction could include a chip seizure action implying domain zero inclusion;

$$P_{3042} = P_{(34)3} \circ P_{(33)0} \circ P_{(33)4} \circ P_{(43)2}, \qquad (5.63)$$

or loss of contact (domain one, tool free running),

$$P_{1234} = P_{(11)1} \circ P_{(41)2} \circ P_{(34)3} \circ P_{(13)4}. \qquad (5.64)$$

Additional possibilities exist for interaction with the four boundaries, but are not developed herein. The next chapter will develop the connections of each mapping

through the definitions of the initial and final states, and the corresponding governing equations.

CHAPTER VI

SOLUTION STRUCTURE AND PREDICTION ROUTINE

Periodic Interrupted Cutting Motion of P_{34}

The composition of the mappings is shown in Fig. 19 to form periodic motion. This has been previously investigated for a single degree of freedom oscillator with dry friction by Luo and Gegg [42-44] and Gegg [47]. Consider one of the simplest mappings

$$P = P_3 \circ P_4. \tag{6.1}$$

Individual to each mapping are the initial and final conditions, where such a definition must be made. From Eq.(6.1), the above relation,

$$\left.\begin{aligned} P_4 &: \left(\tilde{x}_k, \dot{\tilde{x}}_k, \tilde{y}_k, V^+, t_k\right) \to \left(\tilde{x}_{k+1}, \dot{\tilde{x}}_{k+1}, \tilde{y}_{k+1}, V^+, t_{k+1}\right), \\ P_3 &: \left(\tilde{x}_{k+1}, \dot{\tilde{x}}_{k+1}, \tilde{y}_{i+1}, V^-, t_{i+1}\right) \to \left(\tilde{x}_{k+2}, \dot{\tilde{x}}_{k+2}, \tilde{y}_{i+2}, V^-, t_{i+2}\right), \end{aligned}\right\} \tag{6.2}$$

without chip seizure (domain zero, $\dot{\tilde{y}} \equiv V$) motion, $V = V^+ = V^- = -\bar{V}/\Omega$ exists.

For the periodic motion $\tilde{\mathbf{Y}}_{i+2} = P\tilde{\mathbf{Y}}_i$ where $\tilde{\mathbf{Y}}_k = \left(\tilde{x}_k, \dot{\tilde{x}}_k, \tilde{y}_k, t_k\right)^T$ during *n*-periods of excitation, we have

$$\left.\begin{aligned} &\tilde{x}_{k+2} = \tilde{x}_k, \dot{\tilde{x}}_{k+2} = \dot{\tilde{x}}_k, \\ &\tilde{y}_{k+2} = \tilde{y}_k, \ \Omega t_{k+2} = \Omega t_k + 2n\pi. \end{aligned}\right\} \tag{6.3}$$

Using the notation in Gegg et al. [33], a generalized mapping for Eq.(6.1) is

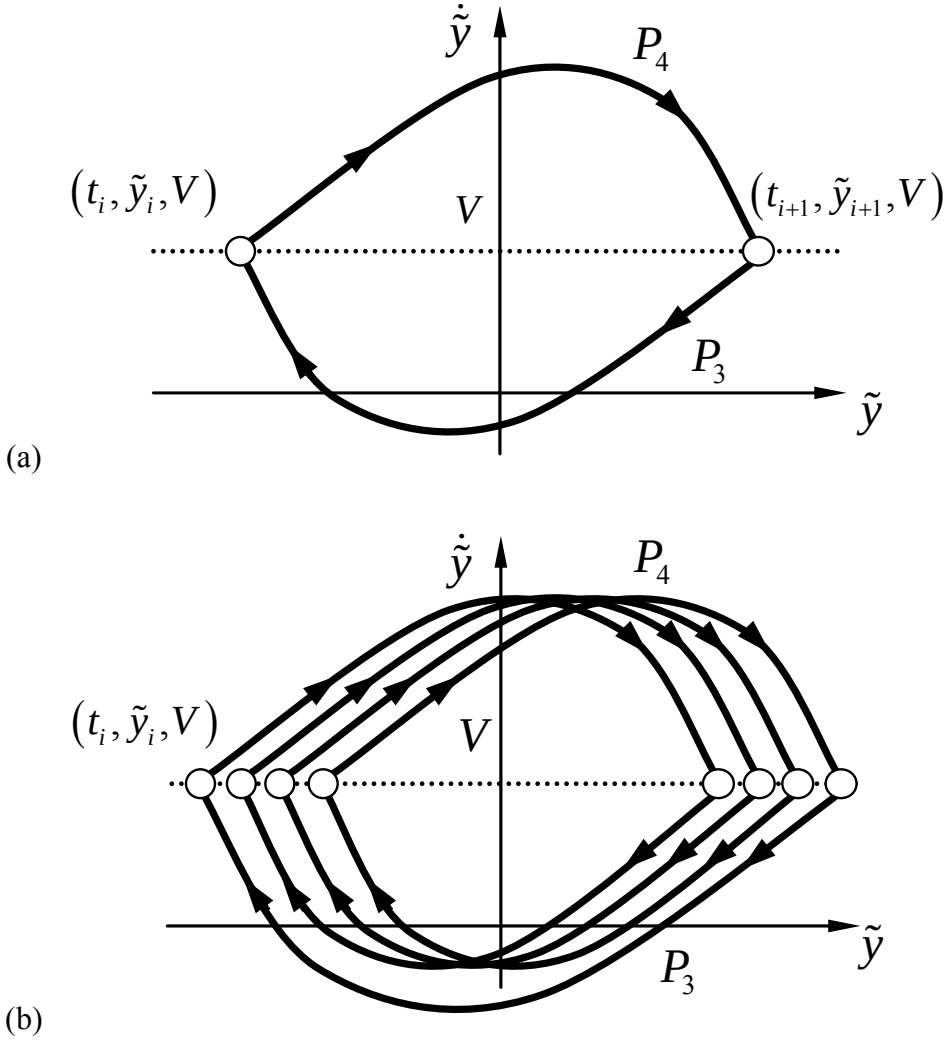

Fig. 19 Non-stick periodic motion in the absolute phase plane, (a) period one motion P_{34}, (b) period four motion $P_{(34)^4}$.

$$P = P_{(34)^m} \triangleq \underbrace{\left(P_3 \circ P_4\right) \circ \cdots \circ \left(P_3 \circ P_4\right)}_{m-\text{pairs}}. \tag{6.4}$$

The periodic motion for the foregoing mapping requires

$$\tilde{\mathbf{Y}}_{k+2m} = P\tilde{\mathbf{Y}}_k. \tag{6.5}$$

The periodicity conditions of periodic motion for the foregoing mapping are

$$\tilde{x}_{k+2m} = \tilde{x}_k, \dot{\tilde{x}}_{k+2m} = \dot{\tilde{x}}_k, \tag{6.6}$$

$$\tilde{y}_{k+2m} = \tilde{y}_k, \ \Omega t_{k+2m} = \Omega t_k + 2n\pi. \tag{6.7}$$

Such periodicity relations will be used to develop the solution structure for prediction of the motion.

The governing equations and an appropriate solving method (i.e. Newton-Raphson Method) are employed to arrive at the solution set. The governing equations of each mapping. P_κ ($\kappa \in \{3,4\}$) can be expressed by

$$\left.\begin{aligned} f_1^{(i)}\left(\tilde{\mathbf{x}}_i, \tilde{\mathbf{y}}_i, t_i, \tilde{\mathbf{x}}_{i+1}, \tilde{\mathbf{y}}_{i+1}, t_{i+1}\right) = 0, \\ f_2^{(i)}\left(\tilde{\mathbf{x}}_i, \tilde{\mathbf{y}}_i, t_i, \tilde{\mathbf{x}}_{i+1}, \tilde{\mathbf{y}}_{i+1}, t_{i+1}\right) = 0, \end{aligned}\right\} \tag{6.8}$$

$$\left.\begin{aligned} f_3^{(i)}\left(\tilde{\mathbf{x}}_i, \tilde{\mathbf{y}}_i, t_i, \tilde{\mathbf{x}}_{i+1}, \tilde{\mathbf{y}}_{i+1}, t_{i+1}\right) = 0, \\ f_4^{(i)}\left(\tilde{\mathbf{x}}_i, \tilde{\mathbf{y}}_i, t_i, \tilde{\mathbf{x}}_{i+1}, \tilde{\mathbf{y}}_{i+1}, t_{i+1}\right) = 0. \end{aligned}\right\} \tag{6.9}$$

There are many methods for solving nonlinear equations for a set of unknown variables; some methods are more suited for solving slowly with poor initial conditions and other can be very fast with good initial conditions [48-50]. However, most algorithms are sensitive to the relaxation parameter (gain used when updating the solution set). The predictions completed herein were not to simply predict with a generic solving method, but a combination of the Newton-Raphson method and a variation of this relaxation parameter.

Typically, the relaxation parameter was kept constant but in the cases where the Jacobian matrices become nearly singular the solver may fail to converge. To allow a more stable search of the solution the relaxation parameter would be ranged from 0.7 to 0.01. Notably, the solutions near such a singularity are not physically possible or the current motion vanishes. As a result of the solution set being a completely mathematical problem at this point the possibility remains that the solver may shift to physically impossible motions. This occurs since the solution structure only considers the switching points at the respective boundary and assumes the motion remains in the defined domain.

Hence; the motion must be verified physically at every convergence of the solving algorithm. Although the motion is physically verified the potential for alternate real solutions exist. This occurs since the system will achieve more than one possible steady state motion; which is ultimately caused by the defined initial conditions. The next section with develop the solution structure for periodic motion with chip seizure.

Periodic Interrupted Cutting Motion of P_{034}

Consider the mapping structure for periodic orbit with chip seizure (domain zero, $\dot{\tilde{y}} \equiv V$) motion is

$$P_{034} = P_0 \circ P_3 \circ P_4. \tag{6.10}$$

The mapping P_0 describes the starting and ending of the stick motion. The

disappearance of stick motion requires $F_{\tilde{y}}^{(i)}\left(\tilde{\mathbf{x}}_{k+1},\tilde{\mathbf{y}}_{k+1},t_{k+1}\right)=0$ and $\dot{\tilde{y}}\equiv V$, Eq.(4.18). The general mapping structure for periodic orbit with stick motion is

$$P=\underbrace{\left(P_0^{(j_{m2})}\circ P_3^{(j_{m1})}\circ P_4^{(j_{m0})}\right)\circ\cdots\circ\left(P_0^{(j_{12})}\circ P_3^{(j_{11})}\circ P_4^{(j_{10})}\right)}_{m-\text{terms}} \tag{6.11}$$

where $\left\{j_{l2},j_{l1},j_{l0}\right\}\in\left\{0,1\right\}$ and $l\in\left\{1,2,\cdots,m\right\}$. $P_n^{(0)}=1$ $P_n^{(k-1)}=P_n\circ P_n^{(k-1)}$ $(n=0,3,4)$.

For domain three and four motion, there are three possible stable motions in the two domains Ω_i $(i\in\left\{3,4\right\})$. The governing equations of mapping P_i $(i\in\left\{3,4\right\})$ are obtained from exact solutions presented in the appendix and Gegg et. al. [33]. The governing equations of mapping. P_κ $(\kappa\in\left\{0,3,4\right\})$ can be expressed by

$$\left.\begin{aligned} f_1^{(i)}\left(\tilde{\mathbf{x}}_i,\tilde{\mathbf{y}}_i,t_i,\tilde{\mathbf{x}}_{i+1},\tilde{\mathbf{y}}_{i+1},t_{i+1}\right)=0,\\ f_2^{(i)}\left(\tilde{\mathbf{x}}_i,\tilde{\mathbf{y}}_i,t_i,\tilde{\mathbf{x}}_{i+1},\tilde{\mathbf{y}}_{i+1},t_{i+1}\right)=0,\end{aligned}\right\} \tag{6.12}$$

$$\left.\begin{aligned} f_3^{(i)}\left(\tilde{\mathbf{x}}_i,\tilde{\mathbf{y}}_i,t_i,\tilde{\mathbf{x}}_{i+1},\tilde{\mathbf{y}}_{i+1},t_{i+1}\right)=0,\\ f_4^{(i)}\left(\tilde{\mathbf{x}}_i,\tilde{\mathbf{y}}_i,t_i,\tilde{\mathbf{x}}_{i+1},\tilde{\mathbf{y}}_{i+1},t_{i+1}\right)=0.\end{aligned}\right\} \tag{6.13}$$

The governing equations and an appropriate solving method (i.e. Newton-Raphson Method) are employed to arrive at the solution set. The next section will develop the solution structure for periodic motion with chip reduction (domain three, $\dot{\tilde{y}}<V$).

Periodic Interrupted Cutting Motion of P_{234}

The composition of the mappings is shown in Fig. 20(a) to form periodic motion.

Consider the mapping

$$P = P_2 \circ P_3 \circ P_4. \tag{6.14}$$

The motion expressed in Eq.(6.14) is an example of the cutting motion interrupted by the frictional boundary and loss of chip contact. From the above relation, we have

$$\left.\begin{aligned} &P_4 : \left(\tilde{x}_i, \dot{\tilde{x}}_i, \tilde{y}_i, V^+, t_i\right) \to \left(\tilde{x}_{i+1}, \dot{\tilde{x}}_{i+1}, \tilde{y}_{i+1}, V^+, t_{i+1}\right), \\ &P_3 : \left(\tilde{x}_{i+1}, \dot{\tilde{x}}_{i+1}, \tilde{y}_{i+1}, V^-, t_{i+1}\right) \to \left(\tilde{x}_{i+2}, \dot{\tilde{x}}_{i+2}, \tilde{y}_{i+1} - L_c, \dot{\tilde{y}}_{i+2}, t_{i+2}\right), \\ &P_2 : \left(\tilde{x}_{i+2}, \dot{\tilde{x}}_{i+2}, \tilde{y}_{i+1} - L_c, \dot{\tilde{y}}_{i+2}, t_{i+2}\right) \to \left(\tilde{x}_{i+3}, \dot{\tilde{x}}_{i+3}, \tilde{y}_{i+3}, V^-, t_{i+3}\right). \end{aligned}\right\} \tag{6.15}$$

without chip adhesion (stick), $V^+ = V^- = \bar{V}/\Omega$ exists.

For the periodic motion $\tilde{\mathbf{Y}}_{i+3} = P\tilde{\mathbf{Y}}_i$ where $\tilde{\mathbf{Y}}_k = \left(\tilde{x}_k, \dot{\tilde{x}}_k, \tilde{y}_k, \dot{\tilde{y}}_k, t_k\right)^T$ during N-periods of excitation, we have

$$\left.\begin{aligned} &\tilde{x}_{k+3} = \tilde{x}_k, \dot{\tilde{x}}_{k+3} = \dot{\tilde{x}}_k, \\ &\tilde{y}_{k+3} = \tilde{y}_k, \dot{\tilde{y}}_{k+3} = \dot{\tilde{y}}_k, \\ &t_{k+3} = t_k + 2N\pi. \end{aligned}\right\} \tag{6.16}$$

Using the notation in Gegg et al. (2008), a generalized mapping is

$$P = \underbrace{\left(P_2^{(j_{m2})} \circ P_3^{(j_{m1})} \circ P_4^{(j_{m0})}\right) \circ \cdots \circ \left(P_2^{(j_{12})} \circ P_3^{(j_{11})} \circ P_4^{(j_{10})}\right)}_{m-\text{terms}} \tag{6.17}$$

see Fig. 20(b). The periodic motion for the foregoing mapping requires

$$\tilde{\mathbf{Y}}_{k+3m} = P\tilde{\mathbf{Y}}_k. \tag{6.18}$$

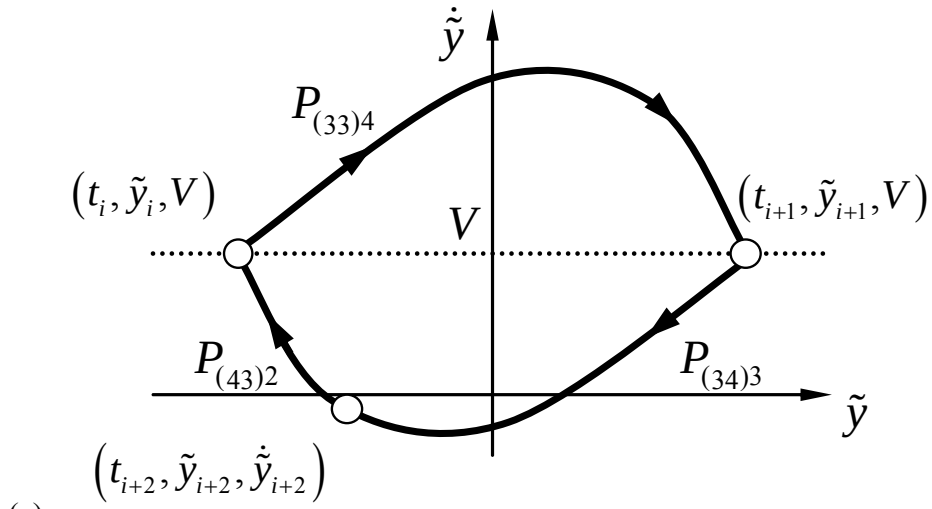

(a)

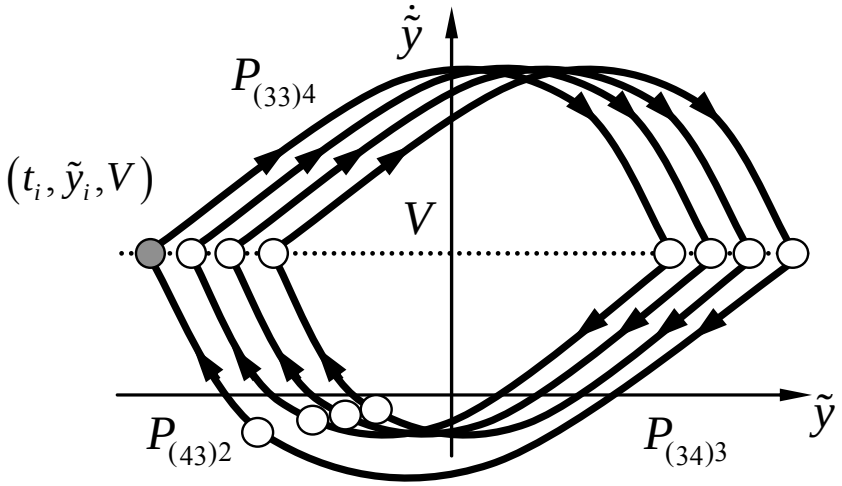

(b)

Fig. 20 Non-stick periodic motion in the absolute phase plane, (a) period one motion P_{234}, (b) period four motion $P_{(234)^4}$.

The periodicity of periodic motion for the foregoing mapping is

$$\tilde{x}_{k+3m} = \tilde{x}_k, \dot{\tilde{x}}_{k+3m} = \dot{\tilde{x}}_k, \tag{6.19}$$

$$\tilde{y}_{k+3m} = \tilde{y}_k, \dot{\tilde{y}}_{k+3m} = \dot{\tilde{y}}_k, \ t_{k+3m} = t_k + 2N\pi. \tag{6.20}$$

Similarly, the solution for $\mathbf{y}_i = \left(\tilde{y}_i, \dot{\tilde{y}}_i, t_i\right)^T$ can be determined. Consider the mapping structure for periodic orbit with stick motion is

$$P = P_{234} \triangleq P_2 \circ P_3 \circ P_4. \tag{6.21}$$

The general mapping structure for periodic orbit with stick motion is

$$P = \underbrace{\left(P_2^{(j_{m3})} \circ P_3^{(j_{m2})} \circ P_4^{(j_{m1})} \circ P_0^{(j_{m0})}\right) \circ \cdots \circ \left(P_2^{(j_{l3})} \circ P_3^{(j_{l2})} \circ P_4^{(j_{l1})} \circ P_0^{(j_{l0})}\right)}_{m-\text{terms}} \tag{6.22}$$

where $\left\{j_{l2}, j_{l1}, j_{l0}\right\} \in \left\{0,1\right\}$ and $l \in \left\{1,2,\cdots,m\right\}$. $P_n^{(0)} = 1$ $P_n^{(k-1)} = P_n \circ P_n^{(k-1)}$ $(n = 0,2,3,4)$. For non-stick motion, there are three possible stable motions in the two domains Ω_i ($i \in \left\{2,3,4\right\}$). The governing equations of mapping P_κ ($\kappa \in \left\{0,2,3,4\right\}$) are obtained from exact solutions presented in the appendix. The governing equations of mapping. P_κ ($\kappa \in \left\{0,2,3,4\right\}$) can be expressed by

$$\left.\begin{aligned} f_1^{(i)}\left(\tilde{\mathbf{x}}_i, \tilde{\mathbf{y}}_i, t_i, \tilde{\mathbf{x}}_{i+1}, \tilde{\mathbf{y}}_{i+1}, t_{i+1}\right) &= 0, \\ f_2^{(i)}\left(\tilde{\mathbf{x}}_i, \tilde{\mathbf{y}}_i, t_i, \tilde{\mathbf{x}}_{i+1}, \tilde{\mathbf{y}}_{i+1}, t_{i+1}\right) &= 0, \\ f_3^{(i)}\left(\tilde{\mathbf{x}}_i, \tilde{\mathbf{y}}_i, t_i, \tilde{\mathbf{x}}_{i+1}, \tilde{\mathbf{y}}_{i+1}, t_{i+1}\right) &= 0, \\ f_4^{(i)}\left(\tilde{\mathbf{x}}_i, \tilde{\mathbf{y}}_i, t_i, \tilde{\mathbf{x}}_{i+1}, \tilde{\mathbf{y}}_{i+1}, t_{i+1}\right) &= 0. \end{aligned}\right\} \tag{6.23}$$

where $i = 0,2,3,4$.

Such periodicity relations will be used to develop the structure for prediction of the motion by definition of the governing equations and an appropriate solving method. The next chapter will establish the significance of concentrating this study on the switching points and interruptions of cutting motions.

CHAPTER VII

NUMERICAL PREDICTIONS

The numerical predictions of the periodic chip seizure (domain zero, $\dot{\tilde{y}} \equiv V$) and cutting motions for this machine-tool system, subject to a eccentricity force, is presented over a range of external and internal parameters. The dynamical system parameters are

$$\frac{m_{eq}}{m_e} = 10^3,\ d_x = 740\,\tfrac{Ns}{mm},\ d_y = 630\,\tfrac{Ns}{mm},$$

$$k_x = k_y = 560\,\tfrac{kN}{mm},\ k_1 = 10\,\tfrac{kN}{mm},\ k_2 = 100\,\tfrac{kN}{mm},\ d_1 = d_2 = 0\,\tfrac{Ns}{\text{mm}},$$

and the external force and geometry parameters are

$$\delta_1 = \delta_2 = 10^{-3} m,\ \Omega V = -20\,\tfrac{mm}{s},\ \mu = 0.7$$

$$\alpha = \tfrac{\pi}{4}\text{rad},\ \beta = 0.1\text{rad},\ \eta = \tfrac{\pi}{4}\text{rad},$$

$$A = em_e\Omega^2,\ L_c = 10^{-3} m,\ X_1 = Y_1 = 10^{-3} m, X_{eq} = Y_{eq} = 5\times 10^{-3} m.$$

The initial contact conditions are,

$$x_1^* = 0.3941(mm),\ y_1^* = \text{-}4.4638(mm),\ x_2^* = 0.3710(mm), y_2^* = \text{-}3.2244(mm).$$

The motions for the following parameter ranges are summarized are noted in Table 2. The term bifurcation will be used throughout the description of the following results.

The definition of bifurcation according to Devaney [51,52] is “a division in two, a splitting apart, or a change”. The definition of bifurcation used here is any change in

the mapping structure; hence a change in the state along the respective boundary. The two definitions noted are similar but as the numerical results will show the term 'bifurcation' not only defines a splitting of the motion, or a change, rather a combining of solution paths or a disappearance/appearance of a new solution branch.

Numerical Prediction of Periodic Cutting and Chip Adhesion

Study of Eccentricity Excitation Amplitude (e)

The numerical predictions of the periodic chip seizure (domain zero, $\dot{\tilde{y}} \equiv V$) and cutting motions are presented over the range of eccentricity amplitude $e \in [0.0803, 0.4]$ (mm), see Fig. 21 and Fig. 22. The eccentricity frequency for this parameter range is held constant at $\Omega = 200$ $(\frac{rad}{s})$. The switching phase $\mathrm{mod}(\Omega t_i, 2\pi)$, switching displacement (y_t) versus eccentricity amplitude (e) are illustrated in Fig. 21(a,b), respectively. The most useful information is found in Fig. 22(a,b), where the switching forces ($F_{\tilde{y}}^{(3)}$ and $F_{\tilde{y}}^{(4)}$) and switching force products ($F_{\tilde{y}}^{(3)} \times F_{\tilde{y}}^{(4)}$) versus eccentricity amplitude (e) are shown. The periodic motions observed through a range of eccentricity amplitude (e) are $P_{(0(34)^m)^n}$: $(0.0803,\ 0.0870](mm)$, $P_{0(34)^2}$: $(0.0870,\ 0.1398](mm)$, $P_{(034)^3 34}$: $(0.1398,\ 0.1406](mm)$, $P_{(034)^2}$: $(0.1406,\ 0.1586](mm)$, P_{034} : $(0.1586,\ 0.1822](mm)$, P_{34} : $(0.1822,\ 0.4000](mm)$.

Table 2 Summary of Numerical Predictions.

Parameter	Boundary # Interaction	Pure Cutting	Interrupted Cutting	Fig.
$e@\Omega = 200\ (\frac{rad}{s})$	3	$e < 0.0803(mm)$	[1] $[0.0803, 0.4](mm)$	21, 22
$\Omega@e = 0.1\ (mm)$	3	$\Omega < 191.6\ (\frac{rad}{s})$	[2] $[191.6, 1k]\ (\frac{rad}{s})$	23-26
$\Omega V@\ \Omega = 200\ (\frac{rad}{s})$	3	$V > 30.1\ (\frac{mm}{s})$	[3] $[0, 30.1]\ (\frac{mm}{s})$	27, 28
$\mu@\ \Omega = 200\ (\frac{rad}{s})$	3	None	[4] $[0, 3]$	29-32
$k_2@\ \Omega = 200\ (\frac{rad}{s})$	3	None	[5] $[0, 567.6]\ (kN)$	33-36

1. $P_{(0(34)^m)^n} : (0.0803, 0.0870](mm),\ P_{0(34)^2} : (0.0870, 0.1398](mm),$
   $P_{(034)^3 34} : (0.1398, 0.1406](mm),\ P_{(034)^2} : (0.1406, 0.1586](mm),$
   $P_{34} : (0.1586, 0.4000](mm);$
2. $P_{(0(34)^m)^n} : (0.1912, 0.1916] * 10^3 (\frac{rad}{s}),\ P_{(034)^2} : (0.1916, 0.1940] * 10^3 (\frac{rad}{s}),$
   $P_{(0(34)^m)^n} : (0.1941, 0.1969] * 10^3 (\frac{rad}{s}),\ P_{0(34)^2} : (0.1970, 0.2028] * 10^3 (\frac{rad}{s}),$
   $P_{(0(34)^m)^n} : (0.2028, 0.2256] * 10^3 (\frac{rad}{s}),\ P_{34} : (0.2256, 1] * 10^3 (\frac{rad}{s});$
3. $P_{(0(34)^2)^2} : (16.66, 17.08](\frac{mm}{s}),\ P_{0(34)^2} : (17.08, 24.26](\frac{mm}{s}),\ P_{(034)^2} : (24.26, 29.14](\frac{mm}{s}),$
   $P_{034} : (29.14, 32.28](\frac{mm}{s}),\ P_{(0(34)^m)^n} : (32.28, 32.82](\frac{mm}{s});$
4. $P_{34} : (0.0000, 0.2100],\ P_{0(34)^3} : (0.2100, 0.3140],\ P_{(0(34)^m)^n} : (0.3140, 0.4380],$
   $P_{0(34)^2} : (0.4380, 0.8840],\ P_{(0(34)^m)^n} : (0.8840, 0.3000];$
5. $P_{34} : (0, 29.40](kN),\ P_{0(34)^3} : (29.40, 46.80]\ (kN),\ P_{(0(34)^m)^n} : (46.80, 74.00]\ (kN),$
   $P_{0(34)^2} : (74.00, 120.60]\ (kN),\ P_{(034)^2} : (120.60, 133.20]\ (kN),\ P_{034} : (133.20, 227.60]\ (kN),$
   $P_{(0(34)^m)^n} : (227.60, 243.80]\ (kN),\ P_{04} : (243.80, 386.20]\ (kN),$
   $P_{(04)^2} : (386.20, 405.00]\ (kN),\ P_{(04)^m} : (405.00, 415.40]\ (kN),$
   $P_{(04)^5} : (415.40, 430.00]\ (kN),\ P_{(04)^6} : (430.00, 431.20]\ (kN),$
   $P_{(0(34)^m)^n} : (431.20, 486.60]\ (kN),\ P_{(340)^2 4} : (486.60, 523.80]\ (kN),$
   $P_{(4034043)^2} : (523.80, 533.40]\ (kN),\ P_{0(40)^2 34} : (533.40, 562.00]\ (kN),$
   $P_{(0(34)^m)^n} : (562.00, 567.60]\ (kN).$

As can be observed, the periodic motion becomes simplified as the eccentricity amplitude increases. The stick-slip combination can be forced to purely slip (non-stick) motion by appropriate excitation amplitude Gegg et. al. [53]. For $e < 0.0803\ (mm)$ no motion intersects the discontinuity (or pure cutting occurs, no interruptions). The lower extreme of the eccentricity amplitude (e) range exhibits complex motions pseudo-periodic/chaotic motion. The switching phase is observed to have a dense area of switching points which originate from the onset of *chip adhesion.*

This *qualitative* observation of onset or route to unstable motion has also been observed in theory and experiment by Astakhov et. al. [10]. In such a study, the stability of a chip structure is attributed to the seizure of the work-piece chip to the tool-piece rake surface Astakhov et. al.[10]. Two chip structures contributed to this phenomenon are the continuous and fragmentary hump-backed chip. Such chip adhesion (stick or seizure) is validated to occur at $e \approx 0.1822\ (mm)$ where added complexity in motion structure appears as the eccentricity amplitude *e* decreases, see Fig. 22(a,b). The forces and force product distributions verify the onset of chip seizure (domain zero, $\dot{\tilde{y}} \equiv V$) at this point; where $F_{\tilde{y}}^{(3)} \times F_{\tilde{y}}^{(4)} = 0$. The addition of the chip seizure dynamics induces complex motions which are inherently detrimental to the surface finish of the work-piece and wear of the tool-piece.

Study of Eccentricity Excitation Frequency (Ω)

The numerical predictions of the periodic chip seizure (domain zero, $\dot{\tilde{y}} \equiv V$) and cutting motions are presented over the range of excitation frequencies $\Omega \in \left[191.6, 10^3\right]\ \left(\frac{rad}{s}\right)$,

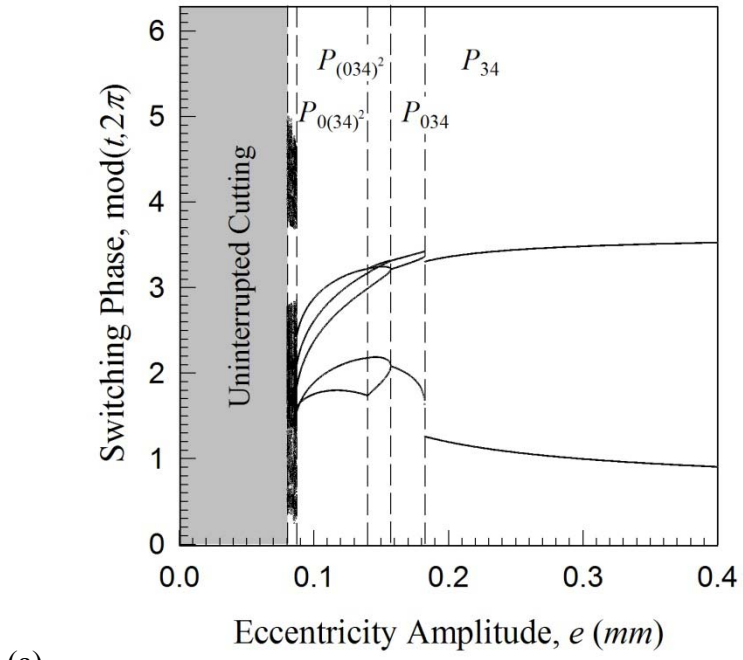

(a)

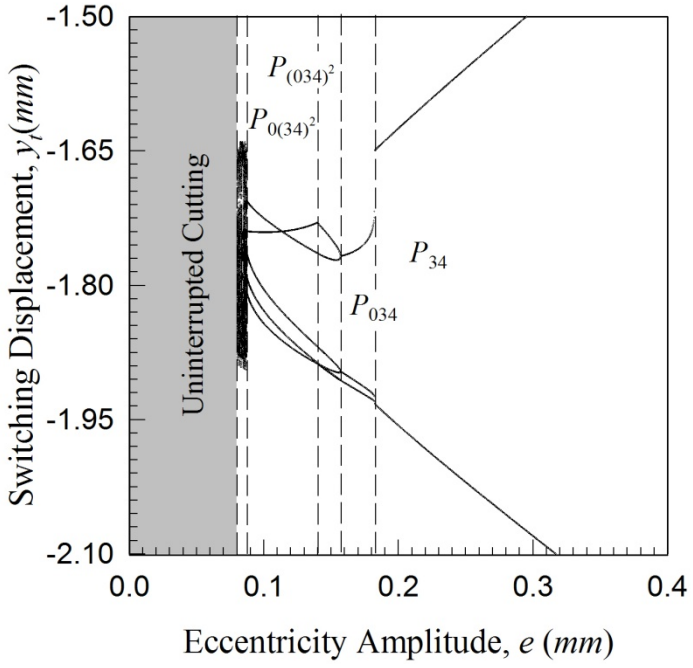

(b)

Fig. 21 Numerical prediction of (a) switching phase $\mathrm{mod}(t_i, 2\pi)$, (b) switching displacement ($y_t = \tilde{y}$) over a range of eccentricity amplitude (e); $L_c = 1(mm)$ and $\Omega = 200(\frac{rad}{s})$.

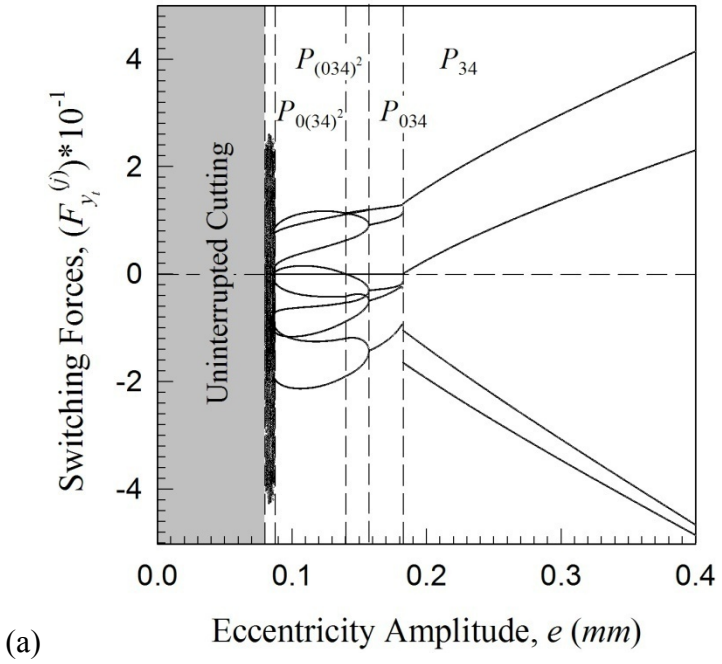

(a)

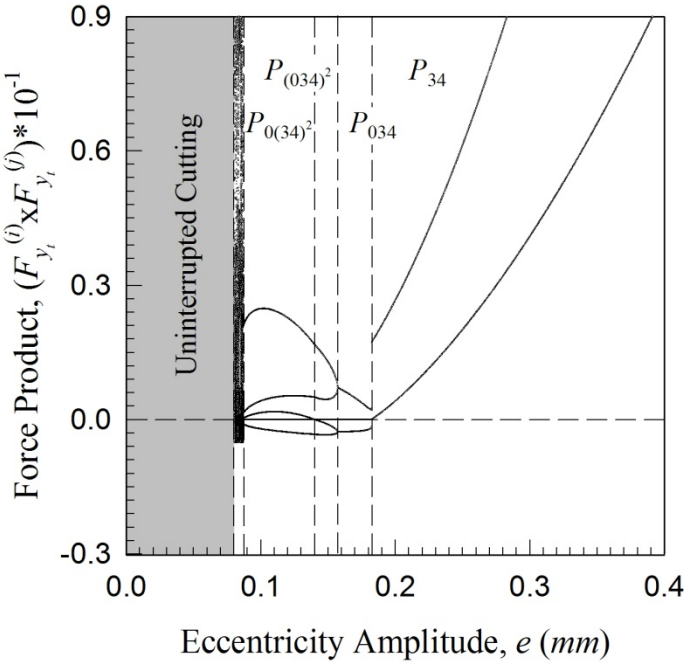

(b)

Fig. 22 Numerical prediction of (a) switching forces $(F_{y_t}^{(3)}, F_{y_t}^{(4)})$ and (b) switching force product $(F_{y_t}^{(3)} \times F_{y_t}^{(4)})$ for chip seizure and cutting periodic motions over a range of eccentricity amplitude (e); $L_c = 1(mm)$ and $\Omega = 200(\frac{rad}{s})$.

see Fig. 23 and Fig. 24. The eccentricity amplitude (e) is directly related to the eccentricity frequency (Ω); hence, $A(\Omega) = em_e\Omega^2$. The switching phase $\mathrm{mod}(\Omega t_i, 2\pi)$, switching displacement (y_t) versus excitation frequency (Ω) are illustrated in Fig. 23(a,b), respectively. The most useful information is found in Fig. 24(a,b), where the switching forces ($F_{\tilde{y}}^{(3)}$ and $F_{\tilde{y}}^{(4)}$) and switching force products ($F_{\tilde{y}}^{(3)} \times F_{\tilde{y}}^{(4)}$) versus excitation frequency (Ω) are shown. One of the simplest periodic motions is observed through a range of excitation frequency $P_{34} : (0.2256, 1] * 10^3 (\frac{rad}{s})$ for mapping structure $P_{34} = P_3 \circ P_4$.

Outside of these intervals the periodic motions are of period 1,2,3, etcetera and the interruption of cutting, chip seizure, defined by Eq.(4.17) is satisfied on the interval $P_{0(34)^2}$: $(0.1970, \ 0.2028] * 10^3 (\frac{rad}{s})$, $P_{(0(34)^m)^n}$: $(0.1941, \ 0.1969] * 10^3 (\frac{rad}{s})$, $P_{(034)^2}$ $: (0.1916, \ 0.1940] * 10^3 (\frac{rad}{s})$. For $\Omega < 191.6 \ (\frac{rad}{s})$ no motions intersect the discontinuity (or pure cutting occurs, no interruptions). The lower extreme of the eccentricity frequency (Ω) range exhibits complex motions which are presented in a detail view in Fig. 25 and Fig. 26. The switching phase is observed to have a quite dense area of switching points which originate from the more simplified motion. Since the eccentricity frequency (Ω) continues to change, the interruptions of the motions become more frequent.

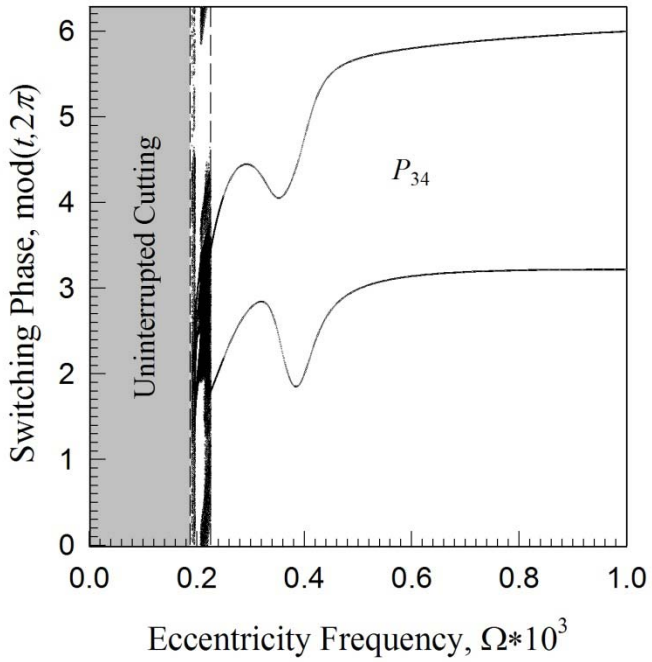

(a)

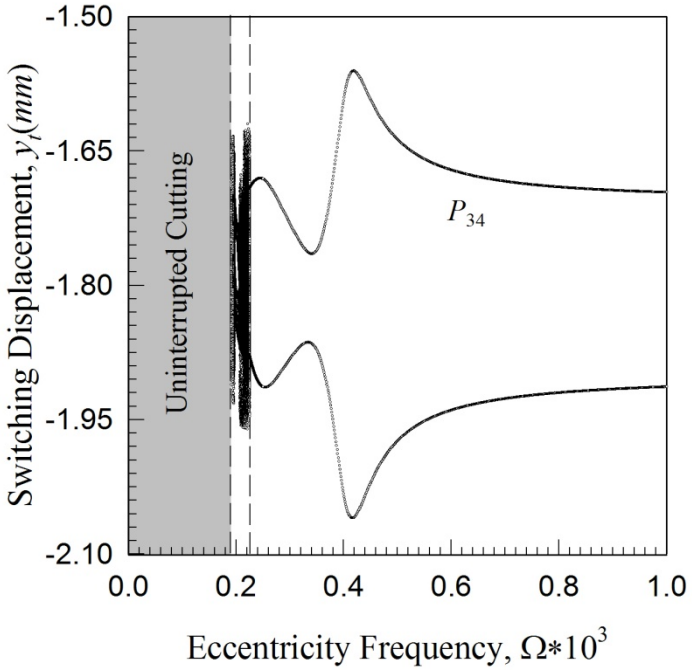

(b)

Fig. 23 Numerical prediction of (a) switching phase $\mathrm{mod}(t_i, 2\pi)$, (b) switching displacement ($y_t = \tilde{y}$) over a range of eccentricity frequency (Ω); $L_c = 1(mm)$ and $e = 0.1(mm)$.

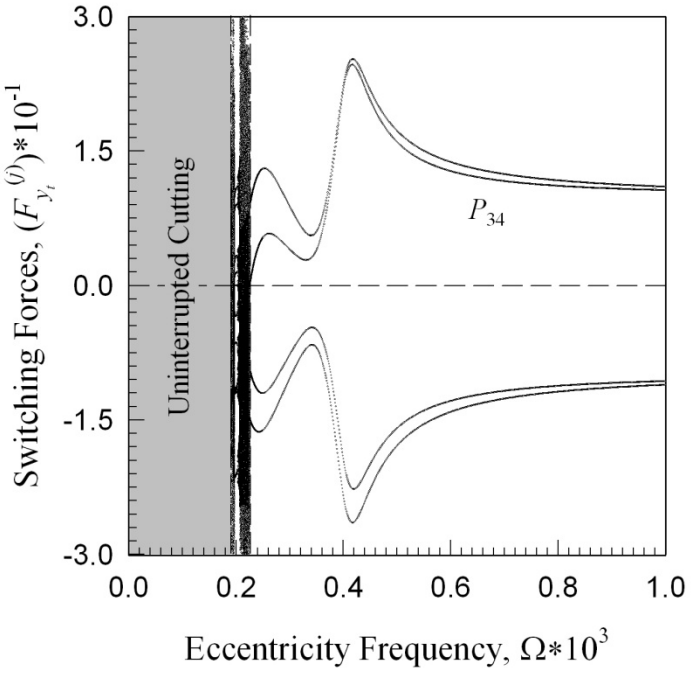

(a)

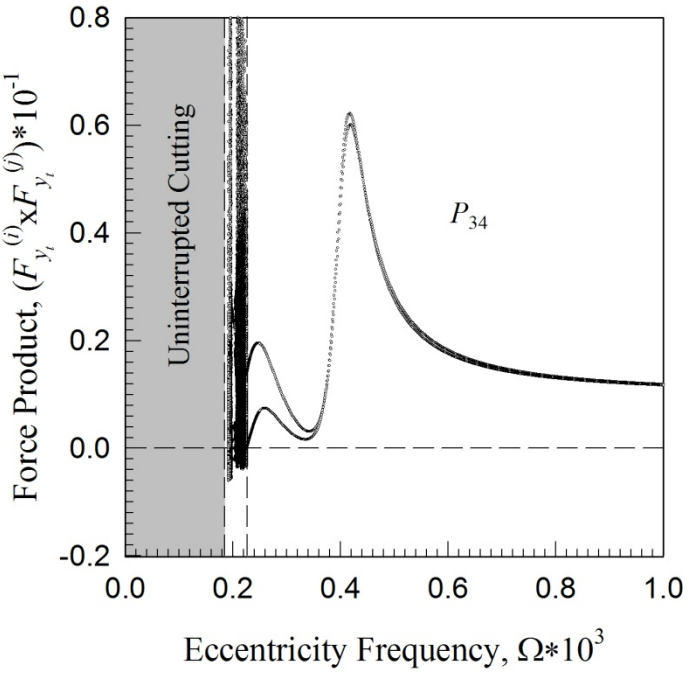

(b)

Fig. 24 Numerical prediction of (a) switching forces $(F_{y_t}^{(3)}, F_{y_t}^{(4)})$ and (b) switching force product $(F_{y_t}^{(3)} \times F_{y_t}^{(4)})$ for chip seizure and cutting periodic motions over a range of eccentricity frequency (Ω); $L_c = 1(mm)$ and $e = 0.1(mm)$.

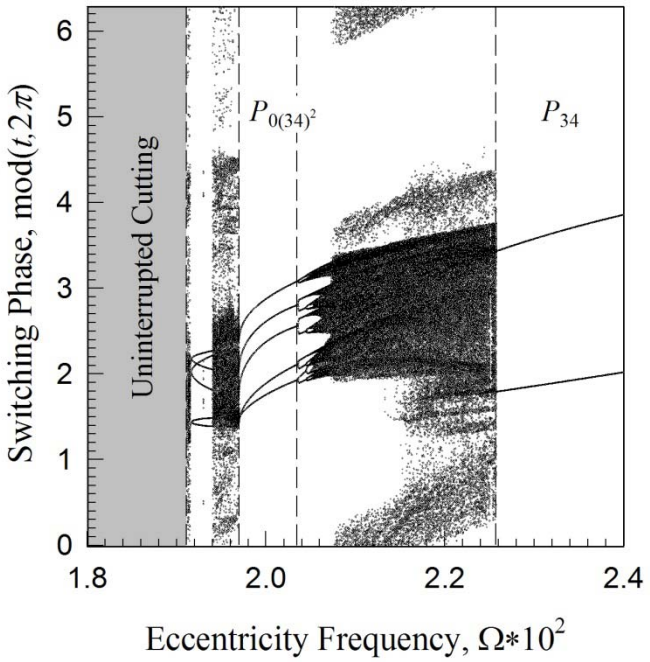

(a)

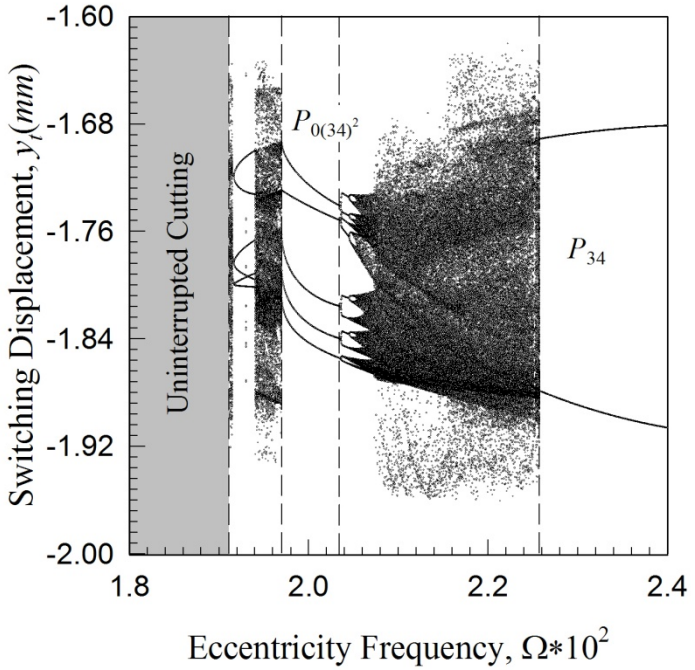

(b)

Fig. 25 Numerical prediction (detail view) of (a) switching phase $\mathrm{mod}(t_i, 2\pi)$, (b) switching displacement ($y_t = \tilde{y}$) over a range of eccentricity frequency (Ω); $L_c = 1(mm)$ and $e = 0.1(mm)$.

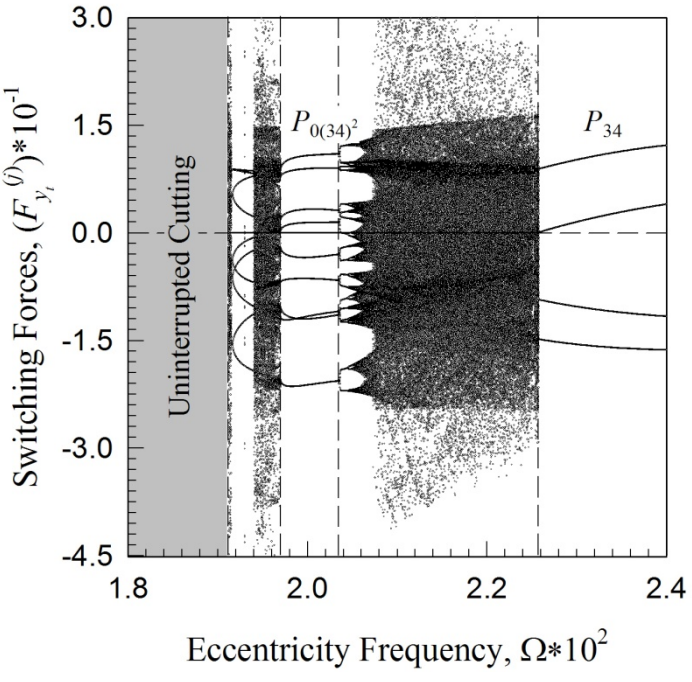

(a)

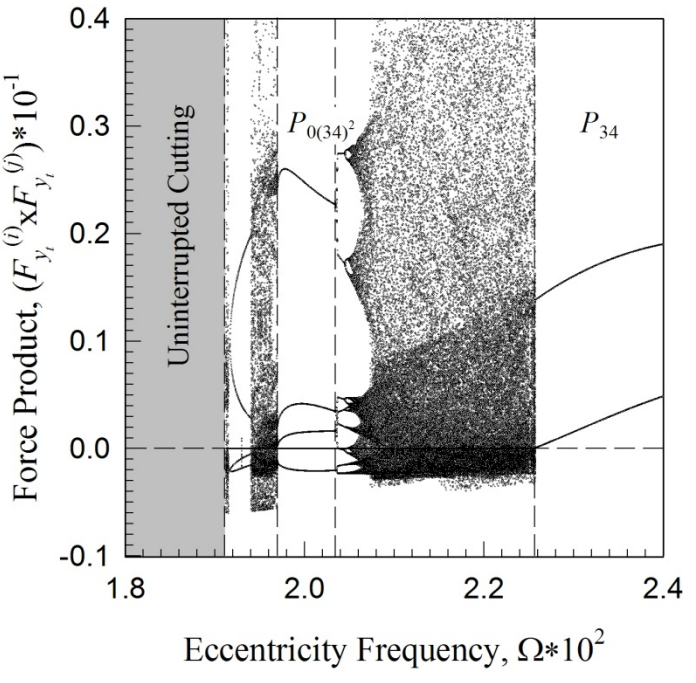

(b)

Fig. 26 Numerical prediction (detail view) of (a) switching forces $(F_{y_t}^{(3)}, F_{y_t}^{(4)})$ and (b) switching force product $(F_{y_t}^{(3)} \times F_{y_t}^{(4)})$ for chip seizure and cutting periodic motions over a range of eccentricity frequency (Ω); $L_c = 1(mm)$ and $e = 0.1(mm)$.

Hence, the motions are complicated due to the interaction with *chip seizure*. This *qualitative* observation has also been observed in theory and experiment by Astakhov et. al. [10]. Such chip seizure (domain zero, $\dot{\tilde{y}} \equiv V$) is validated to occur at $\Omega \approx 225.6$ ($\frac{rad}{s}$) where added complexity in the motion structure appears, see Fig. 26(a,b). The forces and force product distributions show the onset of chip seizure (domain zero, $\dot{\tilde{y}} \equiv V$) at this point. The addition of the chip seizure dynamics induces very complex motion which is inherently detrimental to the surface finish of the work-piece and wear of the tool-piece. The transients associated with the entry of the tool into the cutting process are critical in the amount of tool wear, Chandrasekaran and Thoors [54]. The bifurcations observed in Fig. 23 through Fig. 26 produce transient effects which lead to such wear.

Study of Chip Velocity (ΩV)

The numerical predictions of the periodic chip seizure (domain zero, $\dot{\tilde{y}} \equiv V$) and cutting motions are presented over the range of chip velocity $\Omega V \in [0, 32.82]$ ($\frac{mm}{s}$), see Fig. 27 and Fig. 28. The eccentricity amplitude (e) is set to 0.1 (mm) for remaining numerical predictions; hence, $A(\Omega) = m_e \Omega^2 / 10$. The switching phase $\mathrm{mod}(\Omega t_i, 2\pi)$, switching displacement (y_t) versus chip velocity (ΩV) are illustrated in Fig. 27(a,b), respectively. The most useful information is found in Fig. 28(a,b), where the switching forces ($F_{\tilde{y}}^{(3)}$ and $F_{\tilde{y}}^{(4)}$) and switching force products ($F_{\tilde{y}}^{(3)} \times F_{\tilde{y}}^{(4)}$) versus chip velocity (ΩV) are shown. The distribution of motions over the range of chip velocity (ΩV) for each

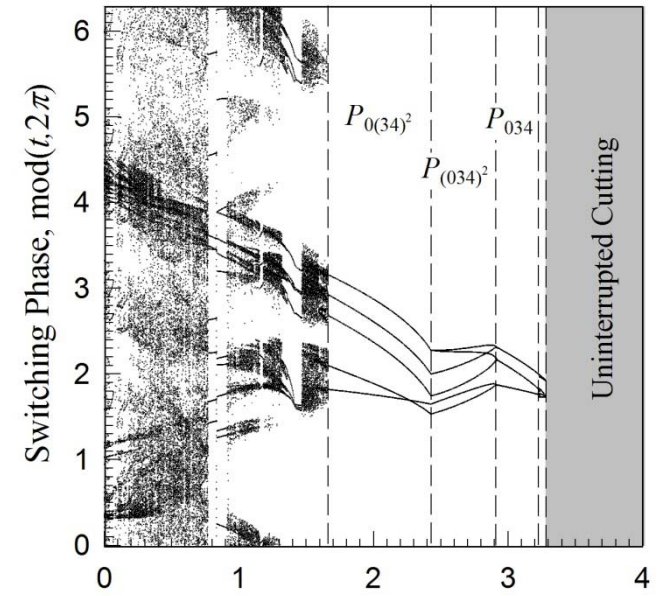

(a)

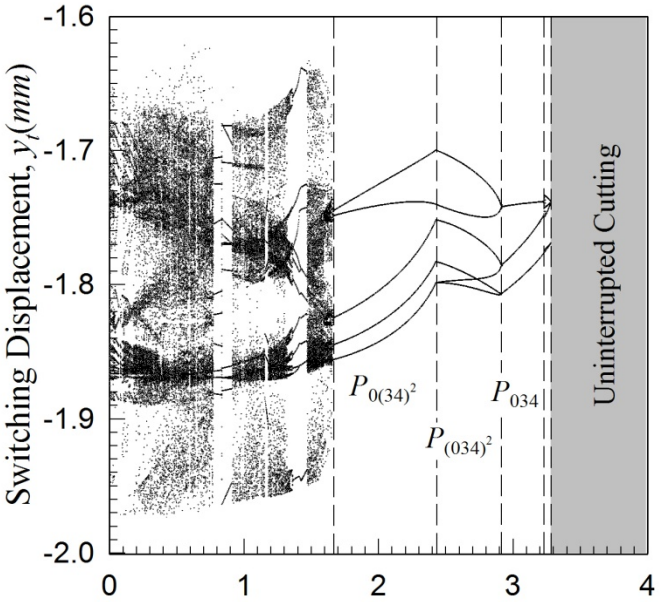

(b)

Fig. 27 Numerical prediction (detail view) of (a) switching phase $\mathrm{mod}(t_i, 2\pi)$, (b) switching displacement ($y_t = \tilde{y}$) over a range of chip velocity (ΩV); $L_c = 1(mm)$ and $\Omega = 200(\frac{rad}{s})$.

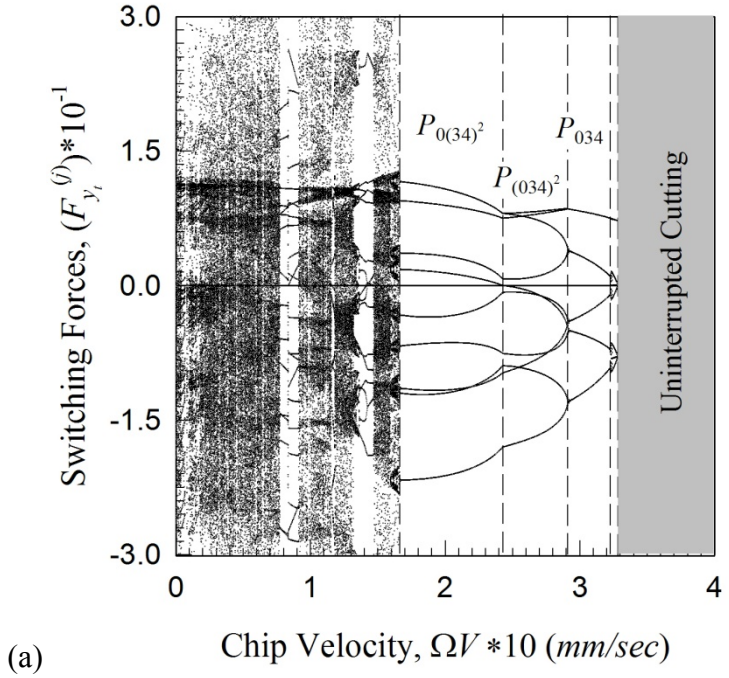

(a)

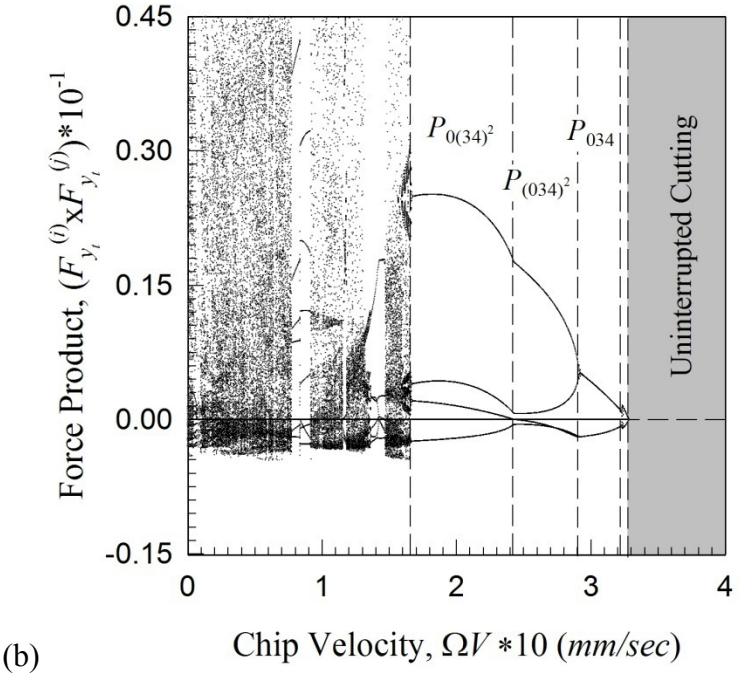

(b)

Fig. 28 Numerical prediction (detail view) of (a) switching forces $(F_{y_t}^{(3)}, F_{y_t}^{(4)})$ and (b) switching force product $(F_{y_t}^{(3)} \times F_{y_t}^{(4)})$ for chip seizure and cutting periodic motions over a range of chip velocity (ΩV); $L_c = 1(mm)$ and $\Omega = 200(\frac{rad}{s})$.

mapping; $P_{(0(34)^2)^2}: \left(16.66,\ 17.08\right]\ (\frac{mm}{s})$, $P_{0(34)^2}: \left(17.08,\ 24.26\right]\ (\frac{mm}{s})$, $P_{(034)^2}: \left(24.26,\ 29.14\right]\ (\frac{mm}{s})$, $P_{034}: \left(29.14,\ 32.28\right]\ (\frac{mm}{s})$, $P_{(0(34)^m)^n}: \left(32.28,\ 32.82\right]\ (\frac{mm}{s})$.

There are no interruptions of the motion for $\Omega V > 32.82\ (\frac{mm}{s})$; hence the motions are not studied. Observe the chip seizure bifurcation at $\Omega V \approx 24.26\ (\frac{mm}{s})$, and the grazing (tangential or saddle-node) bifurcations at $\Omega V \approx 17.08,\ 29.14\ (\frac{mm}{s})$. The frequency of loss of contact/cutting is directly related to the cutting velocity in a machine-tool Chandiramani and Pothala [28]. The interruption frequency of the periodic motion is directly related to the eccentricity frequency (Ω) and chip velocity (ΩV) in this study and is verified herein. The tool life of cutting motions varies inversely with both the interruption frequency and cutting velocity Chou and Evans [55].

The range of velocities considered herein show the complexity of the motions which not only increase the cutting velocity and interruption frequency, but create material build up on the tool rake surface (further increasing wear during major shear of this material).

Study of Friction Coefficient (μ)

The numerical predictions of the periodic chip seizure and cutting motions are presented over the range of chip / tool friction coefficient $\mu \in \left[0, 3.0\right]$, see Fig. 29 and Fig. 30. The friction coefficient range associated with interrupted machining range from 0.33 to 2 Chandrasekaran and Thoors [54]. The switching phase $\mathrm{mod}\left(\Omega t_i, 2\pi\right)$, switching

displacement (y_t) versus chip stiffness $\left(k_2\right)$ are illustrated in Fig. 29(a,b), respectively. The most useful information is found in Fig. 30(a,b), where the switching forces ($F_{\tilde{y}}^{(3)}$ and $F_{\tilde{y}}^{(4)}$) and switching force products ($F_{\tilde{y}}^{(3)} \times F_{\tilde{y}}^{(4)}$) versus chip/tool friction coefficient $\left(\mu\right)$ are shown. The periodic motion is summarized by the mapping specific to the ranges noted as P_{34}: $\left(0.0000,\ \ 0.2100\right]$, $P_{0(34)^3}$: $\left(0.2100,\ \ 0.3140\right]$, $P_{(0(34)^m)^n}$: $\left(0.3140,\ \ 0.4380\right]$, $P_{0(34)^2}$: $\left(0.4380,\ \ 0.8840\right]$, $P_{(0(34)^m)^n}$: $\left(0.8840,\ \ 0.3000\right]$. For $\mu > 3.0$ the motion is not studied.

The lower extreme of the chip stiffness range exhibits *semi-stable* interrupted cutting (no chip seizure) periodic motions transitioning to *chip seizure* periodic motions which are presented in a detail view in Fig. 31 and Fig. 32. The switching phase is observed to have a dense area of switching point which originates from the more simplified motions. Hence, the motions are complicated due to the introduction of *chip seizure*. There are two chip seizure bifurcations well defined at $\mu = 0.210,\ 0.884$ and the grazing bifurcation at $\mu = 0.314$. Hence, the lower boundary for the semi-stable periodic motion is defined at $\mu = 0.210$ for this machine-tool system.

The friction coefficient on the chip/tool rake surface governs the stick-slip boundary for a machine-tool Maity and Das [56]. A phenomenon termed chatter is well known in manufacturing process and is in part a result of dry friction due to the velocity dependent nature Vela-Martinez [17].

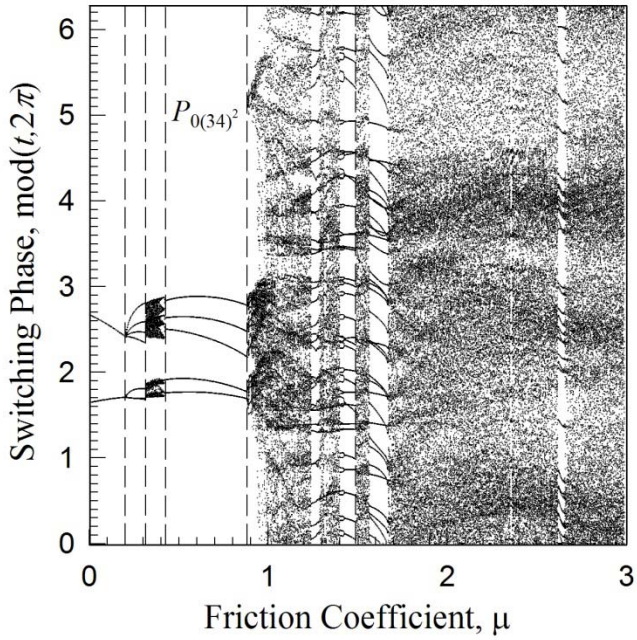

(a)

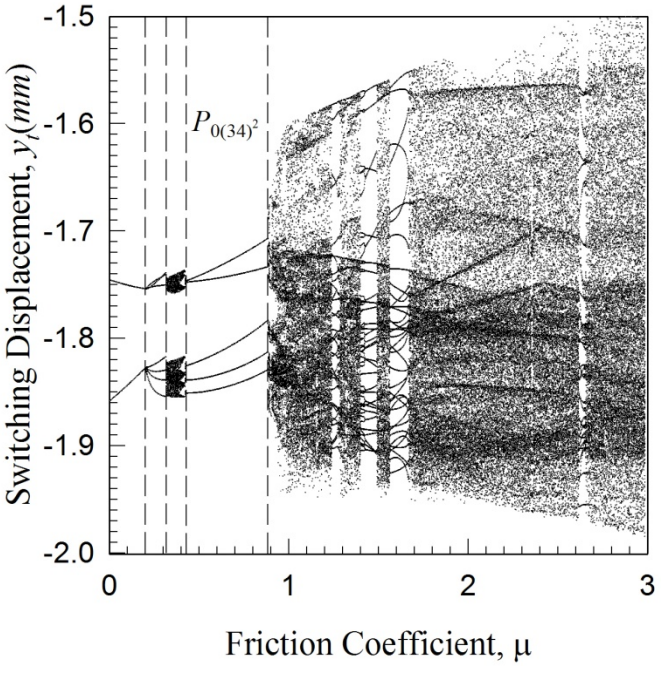

(b)

Fig. 29 Numerical prediction of (a) switching phase $\mathrm{mod}(t_i, 2\pi)$, (b) switching displacement ($y_t = \tilde{y}$) over a range of chip / tool friction coefficient (μ); $L_c = 1(mm)$ and $\Omega = 200(\frac{rad}{s})$.

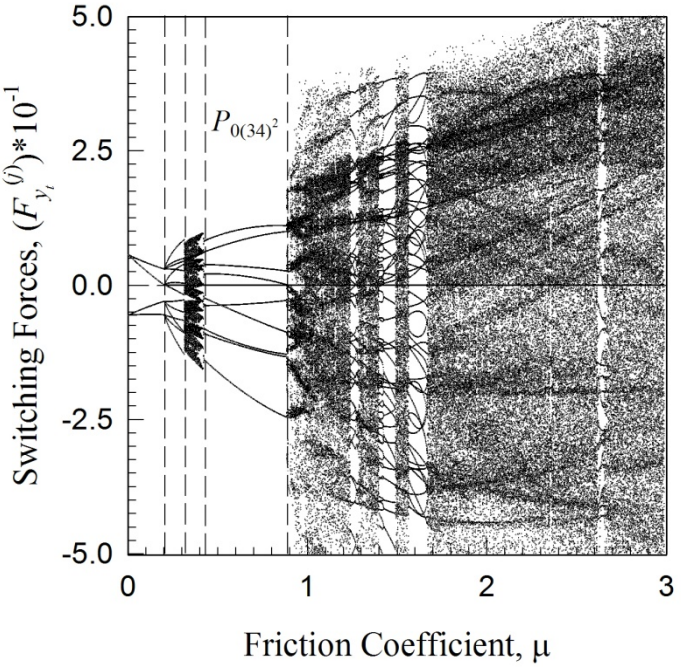

(a)

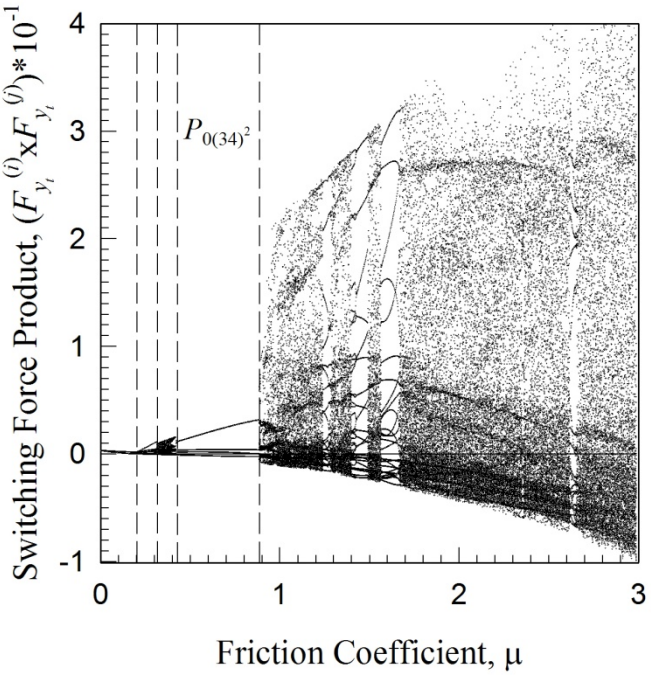

(b)

Fig. 30 Numerical prediction of (a) switching forces $(F_{y_t}^{(3)}, F_{y_t}^{(4)})$ and (b) switching force product $(F_{y_t}^{(3)} \times F_{y_t}^{(4)})$ for chip seizure and cutting periodic motions over a range of chip / tool friction coefficient (μ); $L_c = 1(mm)$ and $\Omega = 200(\frac{rad}{s})$.

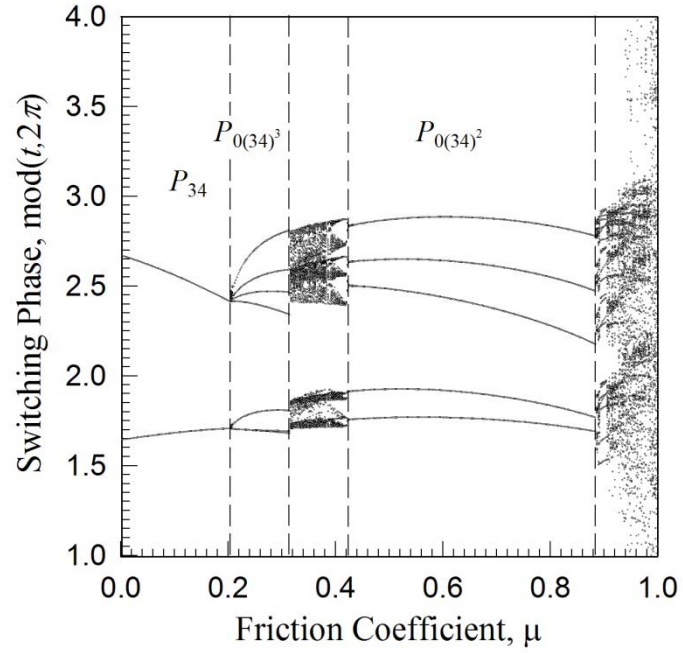

(a)

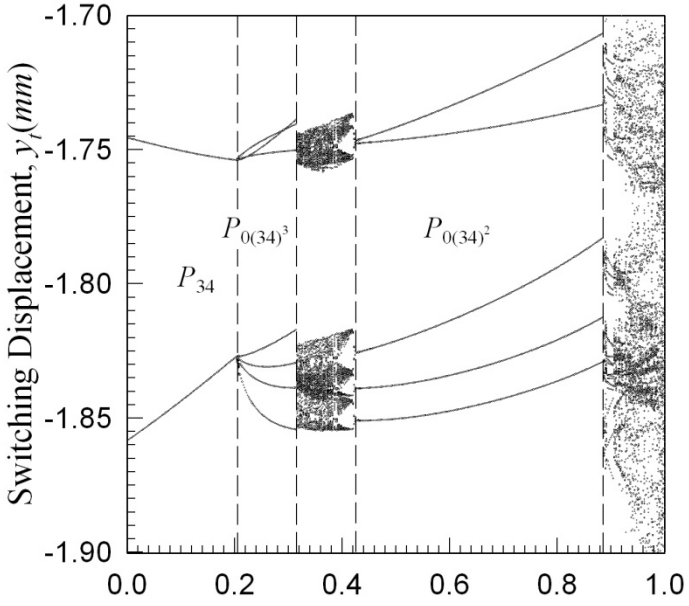

(b)

Fig. 31 Numerical prediction (detail view) of (a) switching phase $\mathrm{mod}(t_i, 2\pi)$, (b) switching displacement ($y_t = \tilde{y}$) over a range of chip / tool friction coefficient (μ); $L_c = 1(mm)$ and $\Omega = 200(\frac{rad}{s})$.

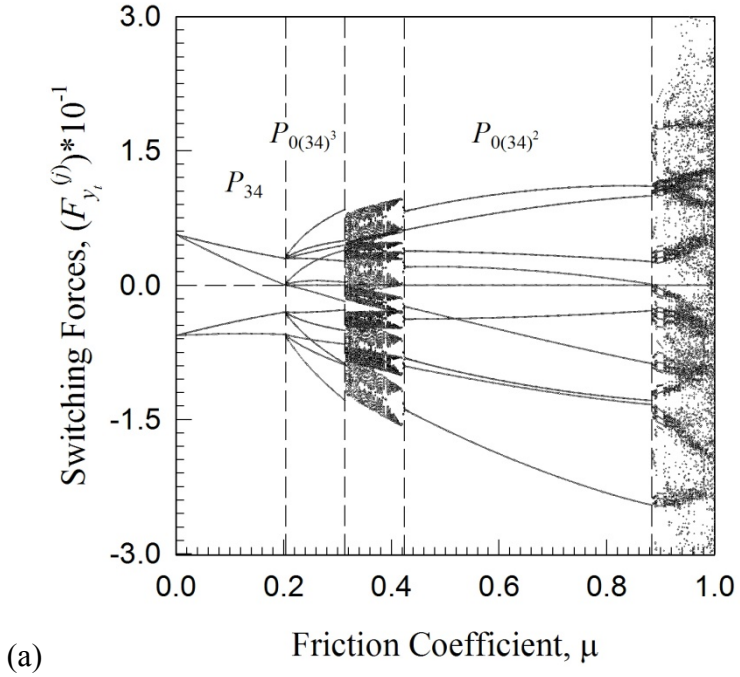

(a)

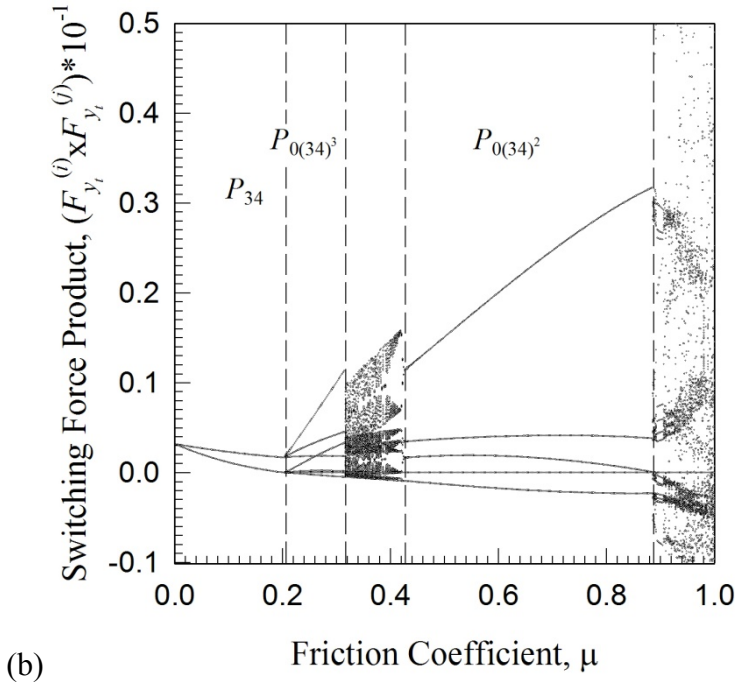

(b)

Fig. 32 Numerical prediction (detail view) of (a) switching forces $(F_{y_t}^{(3)}, F_{y_t}^{(4)})$ and (b) switching force product $(F_{y_t}^{(3)} \times F_{y_t}^{(4)})$ for stick and non-stick periodic motions over a range of chip / tool friction coefficient (μ); $L_c = 1(mm)$ and $\Omega = 200(\frac{rad}{s})$.

Study of Chip Stiffness Coefficient (k_2)

The numerical predictions of the periodic chip seizure and cutting motions are presented over the range of chip stiffness $k_2 \in \left[191.6, 10^3\right]$ $(\frac{kN}{mm})$, see Fig. 33 and Fig. 34. The switching phase $\mathrm{mod}\left(\Omega t_i, 2\pi\right)$, switching displacement (y_t) versus chip stiffness $\left(k_2\right)$ are illustrated in Fig. 33(a,b), respectively. The most useful information is found in Fig. 34(a,b), where the switching forces ($F_{\tilde{y}}^{(3)}$ and $F_{\tilde{y}}^{(4)}$) and switching force products ($F_{\tilde{y}}^{(3)} \times F_{\tilde{y}}^{(4)}$) versus chip stiffness $\left(k_2\right)$ are shown. The periodic motion is summarized by the mapping specific to the ranges noted as P_{34}: $\left(0,\ 29.40\right]$ $(\frac{kN}{mm})$, $P_{0(34)^3}$: $\left(29.40,\ 46.80\right]$ $(\frac{kN}{mm})$, $P_{(0(34)^m)^n}$: $\left(46.80,\ 74.00\right]$ $(\frac{kN}{mm})$, $P_{0(34)^2}$: $\left(74.00,\ 120.60\right]$ $(\frac{kN}{mm})$, $P_{(034)^2}$: $\left(120.60,\ 133.20\right]$ $(\frac{kN}{mm})$, P_{034}: $\left(133.20,\ 227.60\right]$ $(\frac{kN}{mm})$, $P_{(0(34)^m)^n}$: $\left(227.60,\ 243.80\right]$ $(\frac{kN}{mm})$, P_{04}: $\left(243.80,\ 386.20\right]$ $(\frac{kN}{mm})$, $P_{(04)^2}$: $\left(386.20,\ 405.00\right]$ $(\frac{kN}{mm})$, $P_{(04)^m}$: $\left(405.00,\ 415.40\right]$ $(\frac{kN}{mm})$, $P_{(04)^5}$: $\left(415.40,\ 430.00\right]$ $(\frac{kN}{mm})$, $P_{(04)^6}$: $\left(430.00,\ 431.20\right]$ $(\frac{kN}{mm})$, $P_{(0(34)^m)^n}$: $\left(431.20,\ 486.60\right]$ $(\frac{kN}{mm})$, $P_{(340)^2 4}$: $\left(486.60,\ 523.80\right]$ $(\frac{kN}{mm})$, $P_{(4034043)^2}$: $\left(523.80,\ 533.40\right]$ $(\frac{kN}{mm})$, $P_{0(40)^2 34}$: $\left(533.40,\ 562.00\right]$ $(\frac{kN}{mm})$, $P_{(0(34)^m)^n}$: $\left(562.00,\ 567.60\right]$ $(\frac{kN}{mm})$. For $e > 567.60$ $(\frac{kN}{mm})$ the motion is not studied.

The lower extreme of the chip stiffness range exhibits complex motions which are presented in a detail view in Fig. 35 and Fig. 36. The motion is quite simple until a chip seizure bifurcation occurs at $k_2 = 29.40,\ 120.60$ $(\frac{kN}{mm})$ and induces complicated motions. Hence, the motions are complicated due to the interaction with *chip seizure*.

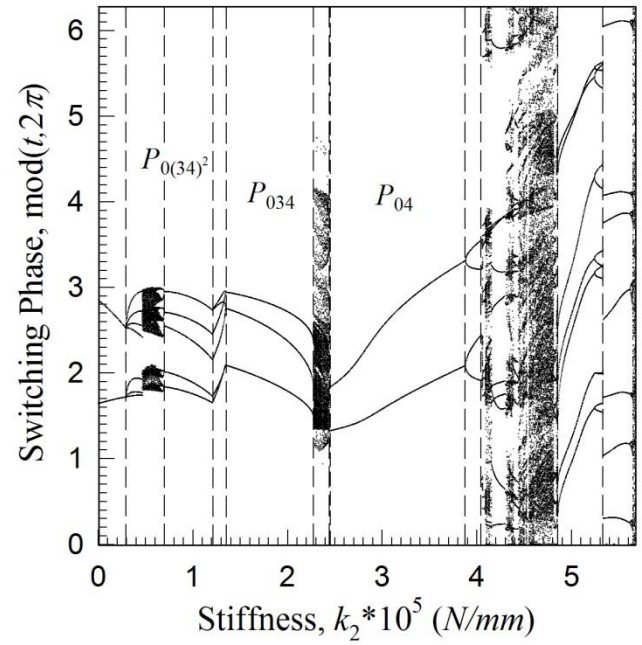

(a)

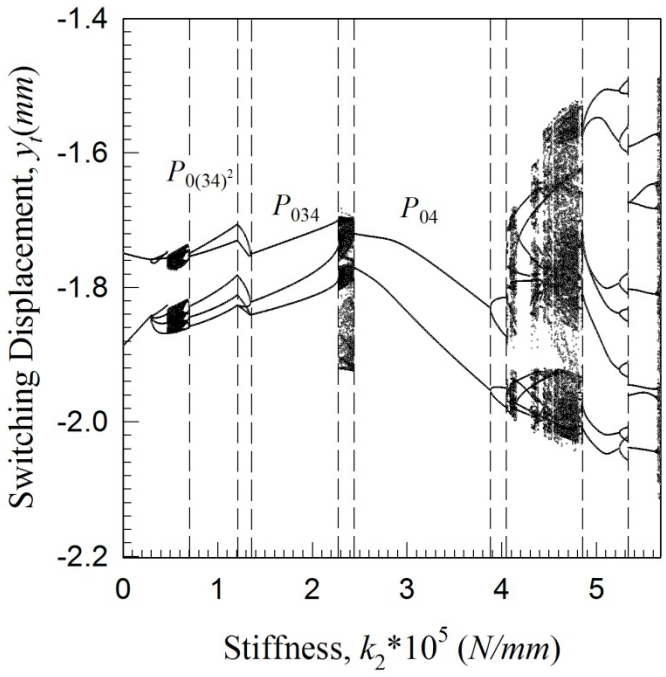

(b)

Fig. 33 Numerical prediction of (a) switching phase $\mathrm{mod}(t_i, 2\pi)$, (b) switching displacement ($y_t = \tilde{y}$) over a range of chip stiffness coefficient (k_2); $L_c = 1(mm)$ and $\Omega = 200(\frac{rad}{s})$.

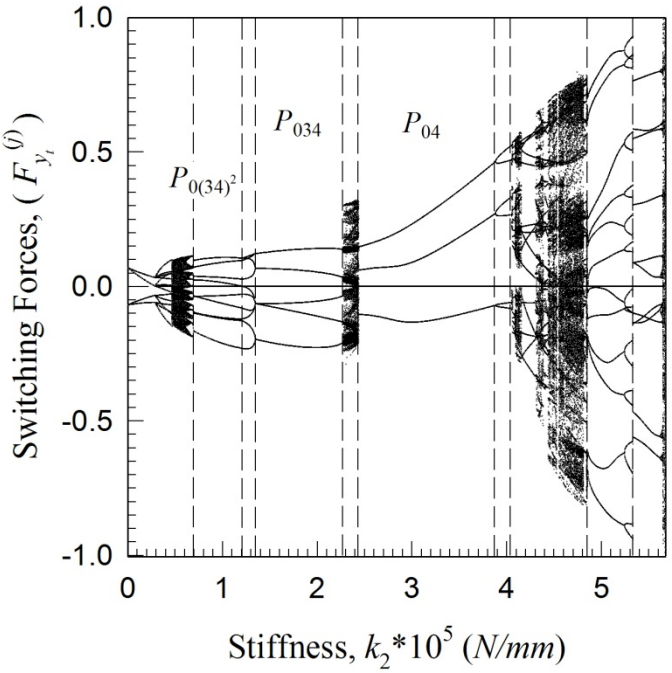

(a)

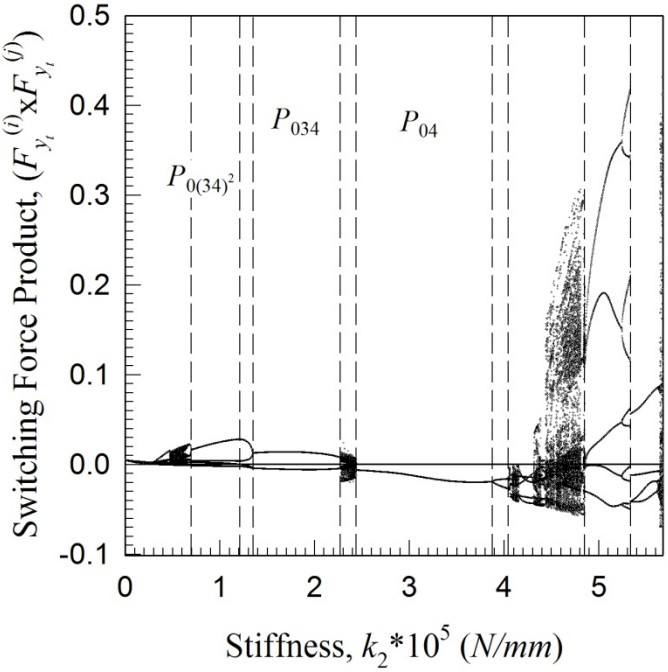

(b)

Fig. 34 Numerical prediction of (a) switching forces $(F_{y_t}^{(3)}, F_{y_t}^{(4)})$ and (b) switching force product $(F_{y_t}^{(3)} \times F_{y_t}^{(4)})$ for stick and non-stick periodic motions over a range of chip stiffness coefficient (k_2); $L_c = 1(mm)$ and $\Omega = 200(\frac{rad}{s})$.

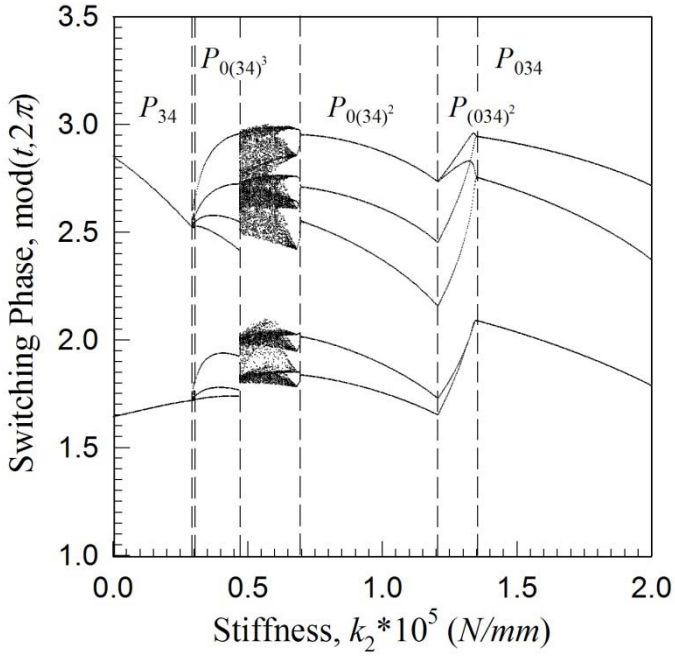

(a)

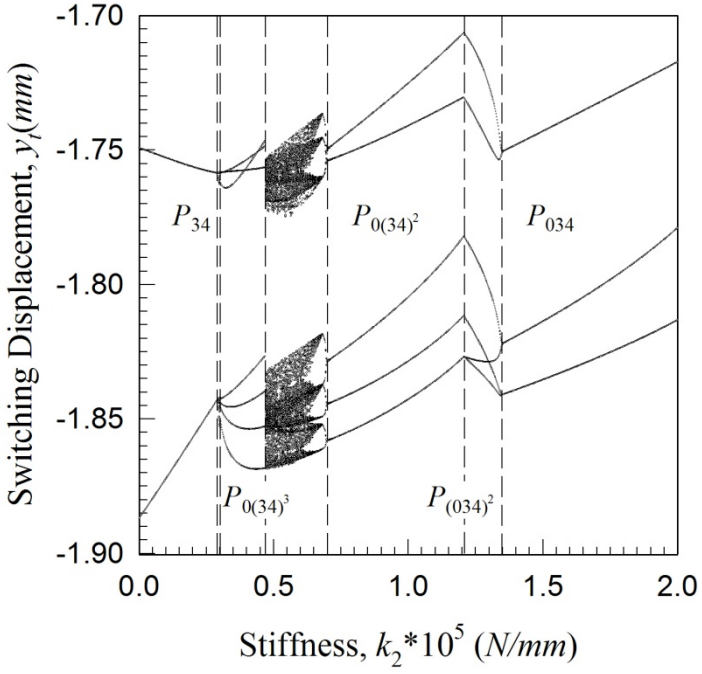

(b)

Fig. 35 Numerical prediction (detail view) of (a) switching phase $\mathrm{mod}(t_i, 2\pi)$, (b) switching displacement ($y_t = \tilde{y}$) over a range of chip stiffness coefficient (k_2); $L_c = 1(mm)$ and $\Omega = 200(\frac{rad}{s})$.

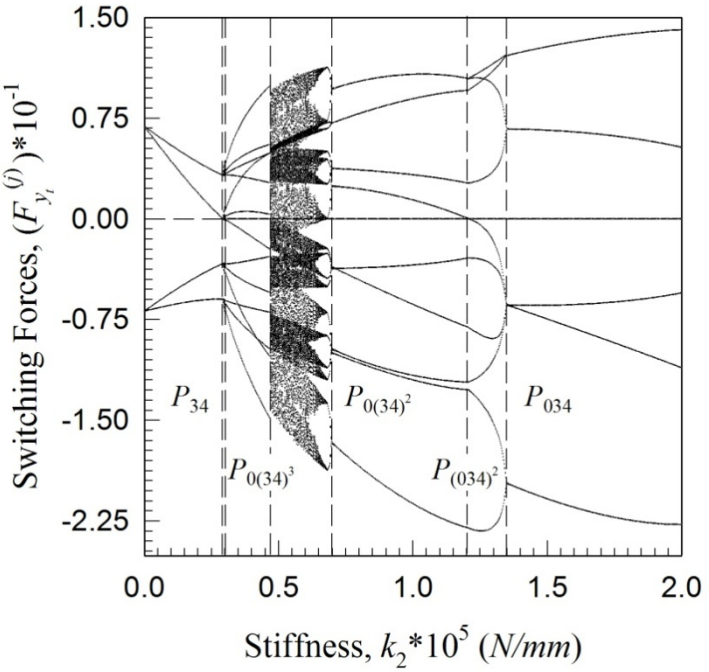

(a)

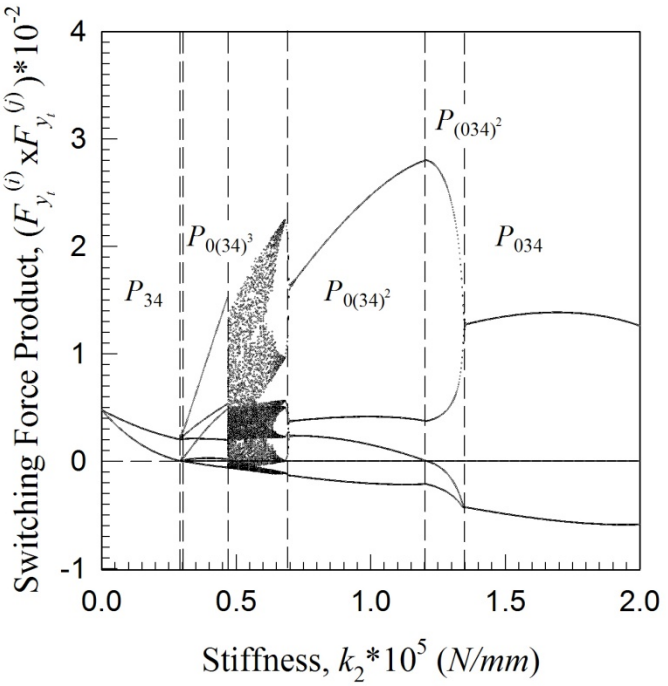

(b)

Fig. 36 Numerical prediction (detail view) of (a) switching forces $(F_{y_t}^{(3)}, F_{y_t}^{(4)})$ and (b) switching force product $(F_{y_t}^{(3)} \times F_{y_t}^{(4)})$ for stick and non-stick periodic motions over a range of chip stiffness coefficient (k_2); $L_c = 1(mm)$ and $\Omega = 200(\frac{rad}{s})$.

The forces and force product distributions show the onset of chip seizure at this point, see Fig. 36(a,b); respectively. The grazing bifurcations occur at $k_2 = 46.80,\ 74.00,\ 133.20\ (\frac{kN}{mm})$ which further attributes to the complexity of the motions. As a result of varying the chip stiffness the natural frequencies of the machine-tool system vary and may move towards one or more of the exciting frequencies; hence, the system may experience more near interruption (grazing bifurcations) possibilities due to the added energy.

The excitation amplitude and frequency in discontinuous systems widely affect the appearance and disappearance of grazing bifurcations Gegg et. al. [57]. The verification of these numerical predictions will be completed in part as a sample in the next chapter.

CHAPTER VIII

VERIFICATION OF NUMERICAL PREDICTIONS

The numerical simulation of the periodic chip seizure and cutting motion for this machine-tool system subject to an eccentricity force is presented in Fig. 37-Fig. 40. The dynamical system parameters are

$$\frac{m_e}{m_{eq}} = 10^3,\ d_x = 740\,\tfrac{Ns}{mm},\ d_y = 630\,\tfrac{Ns}{mm},$$

$$k_x = k_y = 560\,\tfrac{kN}{mm},\ k_1 = 10^3\,\tfrac{kN}{mm},\ k_2 = 10^2\,\tfrac{kN}{mm},\ d_1 = d_2 = 0\,\tfrac{Ns}{\text{mm}},$$

and the external force and geometry parameters are

$$\delta_1 = \delta_2 = 10^{-3} m,\ \Omega V = -20\,\tfrac{mm}{s},\ \mu = 0.7$$

$$\alpha = \tfrac{\pi}{4}\text{rad},\ \beta = 0.1\text{rad},\ \eta = \tfrac{\pi}{4}\text{rad},$$

$$A = em_e\Omega^2,\ L_c = 10^{-3} m,\ X_1 = Y_1 = 10^{-3} m, X_{eq} = Y_{eq} = 5\times 10^{-3} m.$$

A regular cutting periodic motion is illustrated in Fig. 37 for $\Omega = 228$ $(\tfrac{rad}{s})$. The simulations to verify the predictions of Fig. 23 and Fig. 24 are completed via the closed form solution. The initial conditions for this motion are shown in Table 3. In Fig. 37(a), the trajectory of the periodic motion relative to the mapping structure P_{34} is illustrated.

The switching points are noted by circular symbols ($\circ$). The motion in domain (Ω_3) is labeled by mapping P_3. Following intersection of the frictional boundary, the

Table 3: Initial Conditions for Simulations of Numerical Predictions.

Ω	$L_c(mm)$	x_t	y_t	$\dot{x}_t$	$\dot{y}_t$	Ωt_{bar}	Mapping	Fig.
228	1	2.2174	-1.8845	-2.2468	-20	3.5086	P_{34}	37, 38
200	1	2.2751	-1.8427	-5.5565	-20	2.8721	$P_{0(34)^2}$	39, 40

motion then moves into domain (Ω_4) (labeled by mapping P_4). To verify the switching ability of motion on the boundary, the forces ($F_{\tilde{y}}^{(3)}$ and $F_{\tilde{y}}^{(4)}$) versus displacement (y_t) and velocity ($\dot{y}_t$) is presented in Fig. 37(b) and Fig. 38(a), respectively. The switching ability condition is observed on the boundary. Finally, the forces ($F_{\tilde{y}}^{(3)}$ and $F_{\tilde{y}}^{(4)}$) time history for this motion is shown in Fig. 38(b). An interrupted cutting periodic motion is illustrated in Fig. 39 and Fig. 40 for $\Omega = 200$ ($\frac{rad}{s}$). In Fig. 39(a), the trajectory of the periodic motion relative to the mapping structure $P_{0(34)^2}$ is illustrated. The switching points are noted by circular symbols ($\circ$). The motion in domain four (Ω_4) and three (Ω_3) is one portion of the total response which is followed by motion in domain four (Ω_4) and three (Ω_3) then domain zero (chip seizure, labeled by mapping P_0) to complete the period 3 (3*T*) motion.

To verify the switching ability of motion on the boundary, the forces switching ability conditions are observed on the boundary. Finally, the forces ($F_{\tilde{y}}^{(3)}$ and $F_{\tilde{y}}^{(4)}$) ($F_{\tilde{y}}^{(3)}$ and $F_{\tilde{y}}^{(4)}$) versus displacement (y_t) and velocity ($\dot{y}_t$) is presented in Fig. 39(b) and

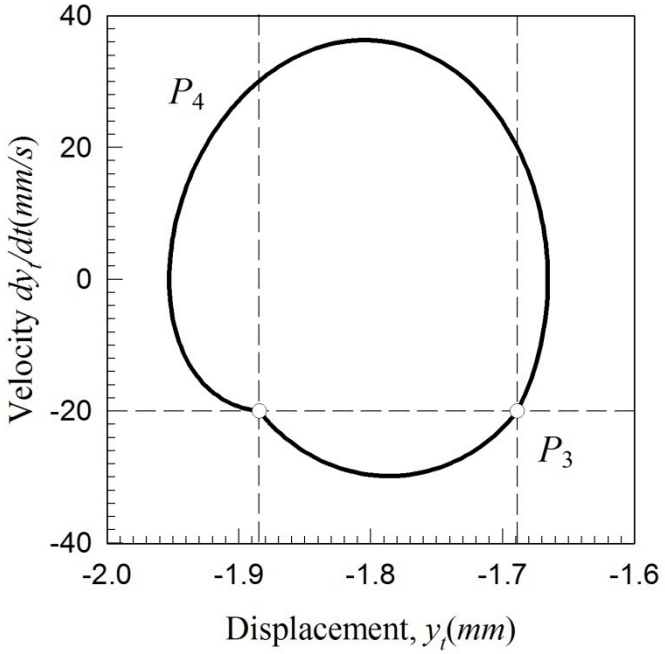

(a)

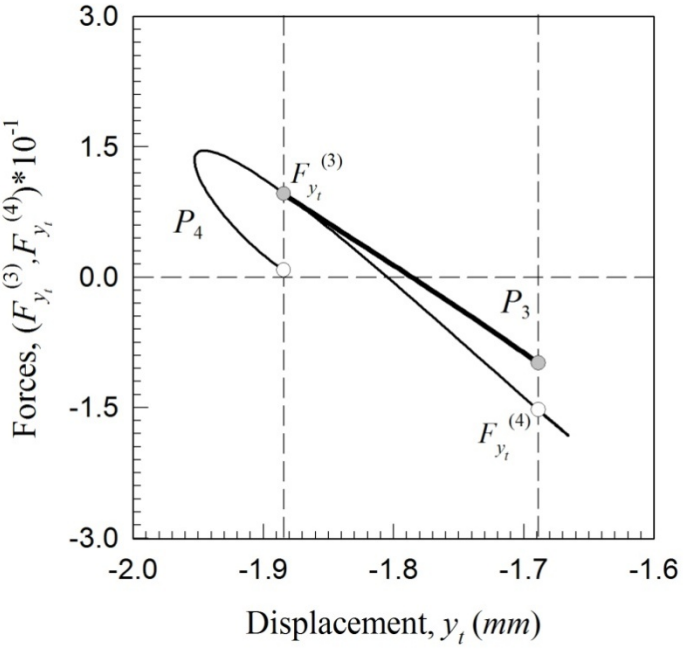

(b)

Fig. 37 Non-stick periodic motion (P_{34}): (a) phase trajectory in phase plane $(y_t, \dot{y}_t)$, (b) forces $(F_{y_t}^{(3)}, F_{y_t}^{(4)})$ versus $(y_t = \tilde{y})$; $L_c = 1(mm)$ and $\Omega = 228(\frac{rad}{s})$.

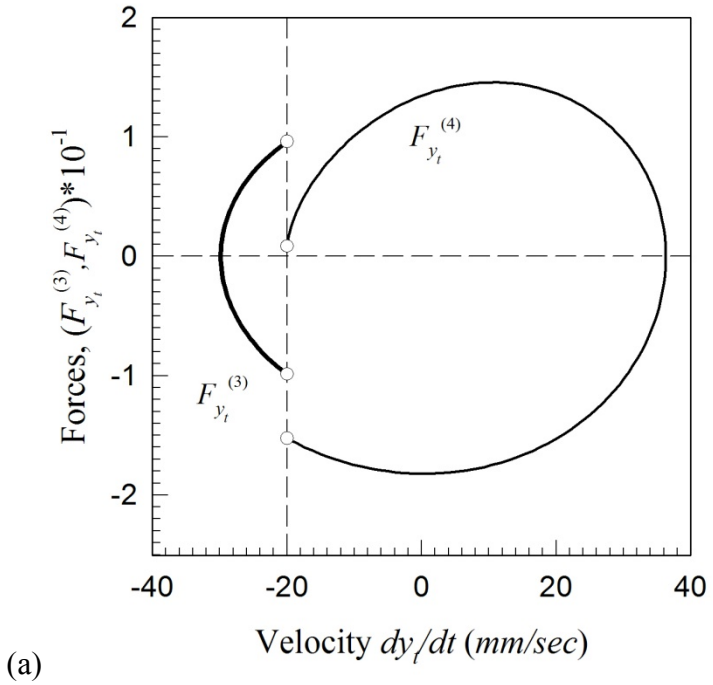

(a)

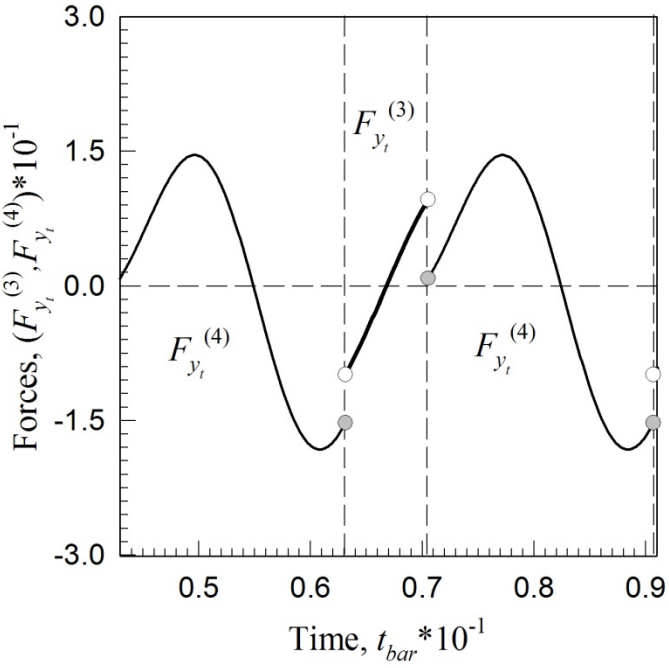

(b)

Fig. 38 Non-stick periodic motion (P_{34}): (a) force $(F_{y_t}^{(3)}, F_{y_t}^{(4)})$ versus $(\dot{y}_t = \dot{\tilde{y}})$ and (b) forces $(F_{y_t}^{(3)}, F_{y_t}^{(4)})$ time history; $L_c = 1(mm)$ and $\Omega = 228(\frac{rad}{s})$.

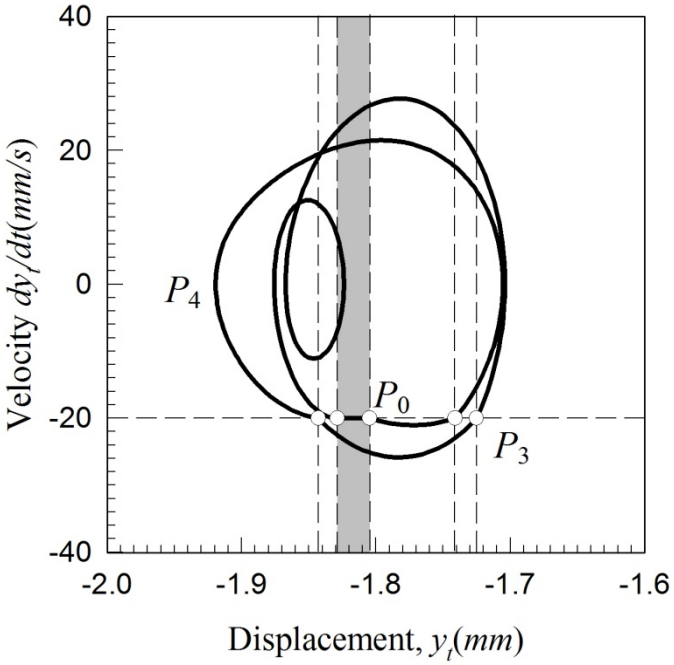

(a)

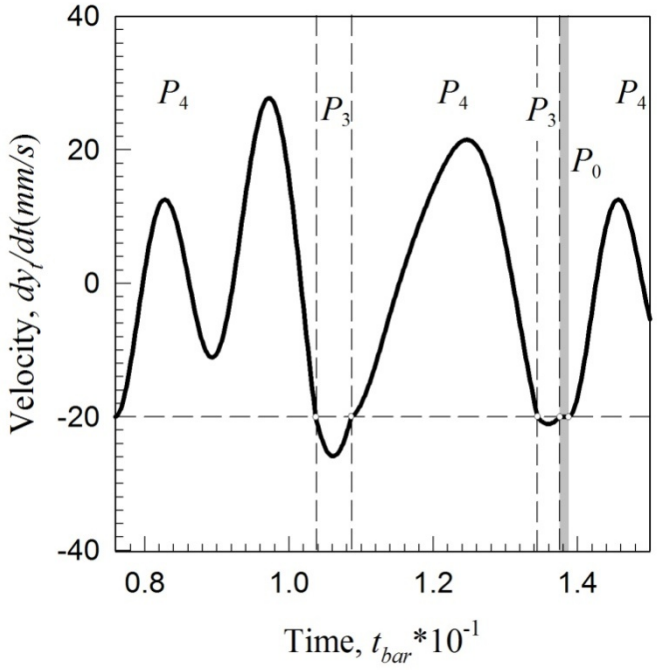

(b)

Fig. 39 Non-stick periodic motion ($P_{0(34)^2}$): (a) phase trajectory in phase plane $(y_t, \dot{y}_t)$, b) velocity $(\dot{y}_t = \dot{\tilde{y}})$ time history; $L_c = 1(mm)$ and $\Omega = 200(\frac{rad}{s})$.

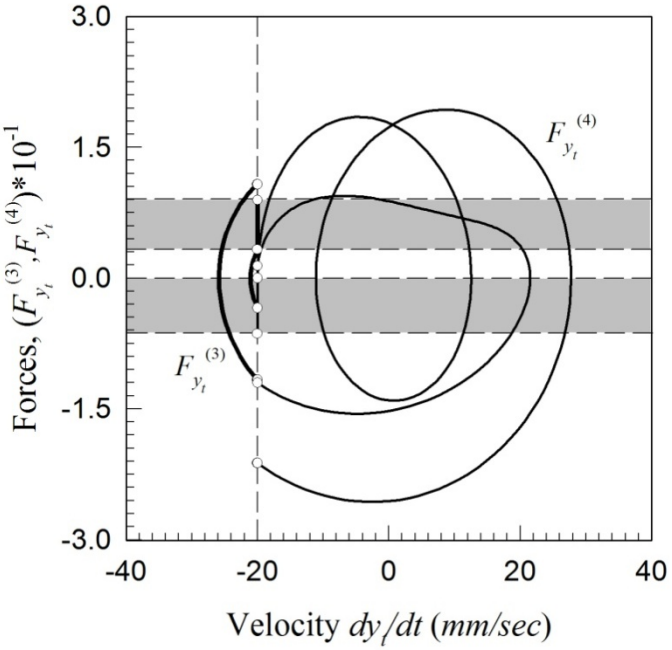

(a)

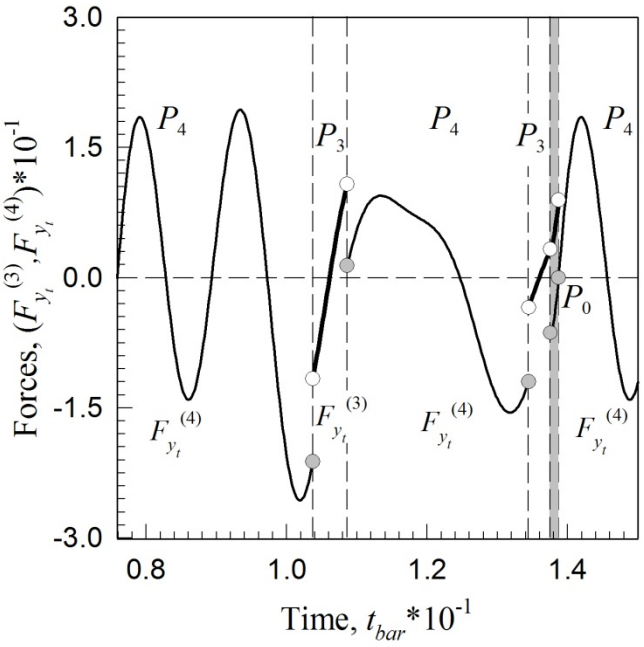

(b)

Fig. 40 Non-stick periodic motion ($P_{0(34)^2}$): (a) force $(F_{y_t}^{(3)}, F_{y_t}^{(4)})$ versus $(\dot{y}_t = \dot{\tilde{y}})$ and (b) forces $(F_{y_t}^{(3)} \times F_{y_t}^{(4)})$ time history; $L_c = 1(mm)$ and $\Omega = 200(\frac{rad}{s})$.

Fig. 40(a). The time history for this motion is shown in Fig. 40(b). Observe in Fig. 40(a,b) the P_0 vanishes with $F_{\tilde{y}}^{(4)} = F_{y_t}^{(4)} = 0$. The differences between the orbits of Fig. 38(a) and Fig. 40(a) depend on the period of the orbit and the existence of the chip seizure.

As observed in Fig. 37(a) the additional loop in the center of the phase will move towards the frictional boundary with a variation of the excitation frequency (Ω). Through the reduction of the excitation frequency (Ω) the orbit associated with chip seizure induces higher order periodic motions. Hence, an investigation of the semi-stable periodic motion over a parameter range is necessary to characterize the effects that interactions with the chip/tool friction boundary and the chip vanishing boundary will have on the complexity/stability of the motions. The next chapter is dedicated to the analytical prediction of semi-stable motions and the boundaries of such motions.

CHAPTER IX

ANALYTICAL PREDICTIONS

Analytical Prediction of Periodic Motions Interacting with Boundary 3

Given the set of equations in Eq.(6.8) and Eq.(6.9) and a proper initial solution set the system of equations defining the interrupted cutting periodic motion can be solved through traditional numerical techniques. The cutting motion is affected by various parameters of the machine-tool system. The following are the results of the prediction routine described in Chapter VI (Solution Structure and Prediction Routine). A summary of the specific mappings and parameter ranges are in Table 4. The first parameter studied is the absolute amplitude of the excitation force (normalized eccentricity amplitude).

Study of Excitation Amplitude (A)

The numerical and analytical predictions of the interrupted periodic cutting motions for this machine-tool system with an excitation force, is presented over the range of excitation amplitude $A \in [322.5, 1k]$. The dynamical system parameters are

$$d_x = 74 \tfrac{Ns}{mm},\ d_y = 63 \tfrac{Ns}{mm},$$

$$k_x = k_y = 56 \tfrac{kN}{mm},\ k_1 = 0.1 \tfrac{MN}{mm}, k_2 = 10 \tfrac{kN}{mm},\ d_1 = d_2 = 0 \tfrac{Ns}{\text{mm}},$$

and the external force and geometry parameters are

$$\delta_1 = \delta_2 = 10^{-3} m,\ \mu = 0.7,\ L_c = 1.0 \times 10^{-3} m,\ \Omega V = 20 \tfrac{mm}{s},$$

Table 4 Summary of Numerical and Analytical Prediction of P_{34}.

Range of Parameter	Boundary # Interaction	Pure Cutting	Interrupted Cutting	Fig.
$A@\Omega = 200(\frac{rad}{s})$	3	$A < 322.5$	$[322.5, 1k]$	41, 42
$A@\Omega = 400(\frac{rad}{s})$	3	$A < 319.0$	$[319.0, 1k]$	43, 44
$\Omega@A = 500$	3	see note	$[379.0, 484.4](\frac{rad}{s})$	45, 46
$\Omega V @\ \Omega = 200(\frac{rad}{s})$	3	$\Omega V > 30.1(\frac{mm}{s})$	$[0, 30.1](\frac{mm}{s})$	47, 48
$\Omega V @\Omega = 400(\frac{rad}{s})$	3	$\Omega V > 31.2(\frac{mm}{s})$	$[0, 31.2](\frac{mm}{s})$	49, 50
$\mu @\ \Omega = 200(\frac{rad}{s})$	3	None	$[0, 3]$	51, 52
$\mu @\ \Omega = 400(\frac{rad}{s})$	3	None	$[0, 3]$	53, 54
$k_2 @\ \Omega = 200(\frac{rad}{s})$	3	None	$[0, 100](\frac{kN}{mm})$	55, 56
$k_2 @\ \Omega = 400(\frac{rad}{s})$	3	$k_2 > 24.25(\frac{kN}{mm})$	$[0, 24.25](\frac{kN}{mm})$	57, 58

Note: $\Omega < 379.0(\frac{rad}{s})$ and $\Omega > 484.4(\frac{rad}{s})$.

$$\alpha = \tfrac{\pi}{4}\text{rad},\ \beta = 0.1\text{rad},\ \eta = \tfrac{\pi}{4}\text{rad},$$

$$X_1 = Y_1 = 10^{-3}m, X_{eq} = Y_{eq} = 5\times 10^{-3}m.$$

The switching phase $\text{mod}(\Omega t_i, 2\pi)$, switching displacement (y_t) versus excitation amplitude ($A = A_F/m$) are illustrated in Fig. 41(a,b) for $\Omega = 200\ (\frac{rad}{s})$, respectively. The numerical and analytical predictions are illustrated by the solid black line ($-$) and triangular symbol (∇) in Fig. 41; respectively. The most useful information is found in

Fig. 42(a,b), where the switching forces ($F_{\tilde{y}}^{(3)}$ and $F_{\tilde{y}}^{(4)}$) and switching force products $(F_{\tilde{y}}^{(3)} \times F_{\tilde{y}}^{(4)})$ versus excitation amplitude (A) are shown.

The dominant motion thru the range of excitation amplitude $A \in [322.5, 1k]$ is $P_{34} = P_3 \circ P_4$. For $A < 322.5$ the chip travels along the tool rake face faster than the tool; hence, pure cutting occurs. The predictions are completed via the closed form solution to Eq.(2.20). The contact conditions are,

$$x_1^* = 0.3941 \times 10^{-3} m,\ y_1^* = -4.4638 \times 10^{-3} m,\ x_2^* = 0.2720 \times 10^{-3} m, y_2^* = -2.9126 \times 10^{-3} m.$$

Additional interruptions are noted with an excitation frequency of $\Omega = 400$ ($\frac{rad}{s}$). The switching phase $\mathrm{mod}(\Omega t_i, 2\pi)$, switching displacement (y_t) versus excitation amplitude (A) are illustrated in Fig. 43(a,b), respectively. Figure Fig. 44(a,b), illustrates the switching forces $(F_{\tilde{y}}^{(3)}$ and $F_{\tilde{y}}^{(4)})$ and switching force products $(F_{\tilde{y}}^{(3)} \times F_{\tilde{y}}^{(4)})$ versus excitation amplitude (A) are shown. The periodic motions observed thru a range of excitation amplitude $A \in [319, 1k]$ are $P_{34} = P_3 \circ P_4$. For $A < 319$ the chip velocity travels along the tool rake face faster than the tool; hence, pure cutting occurs and no interruptions altered the dynamics of the cutting process. At this point, the grazing of the chip/tool friction boundary occurs and creates a potentially unstable orbit for the machine-tool. The excitation amplitude and frequency in discontinuous systems widely affect the appearance and disappearance of grazing bifurcations Gegg et. al. [31]. The excitation frequency (Ω) will be studied in the next section for the effects on the $P_{34} = P_3 \circ P_4$ motion. The chip stiffness coefficient (Ω) will be studied in the next section.

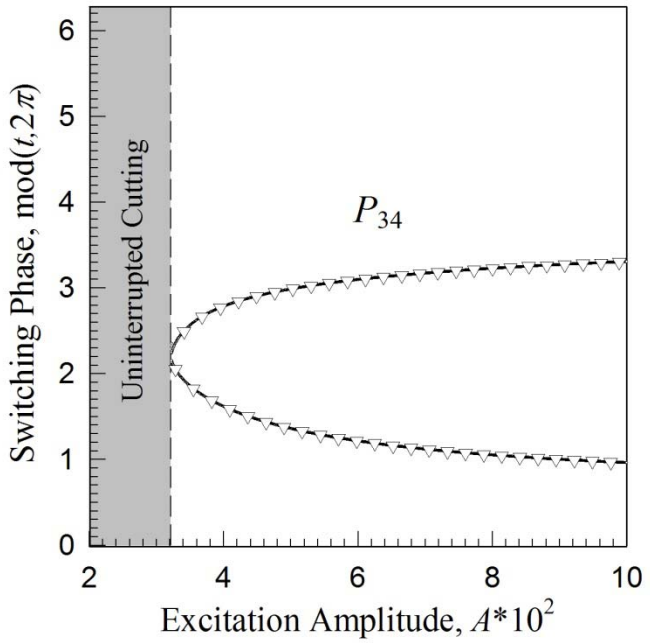

(a)

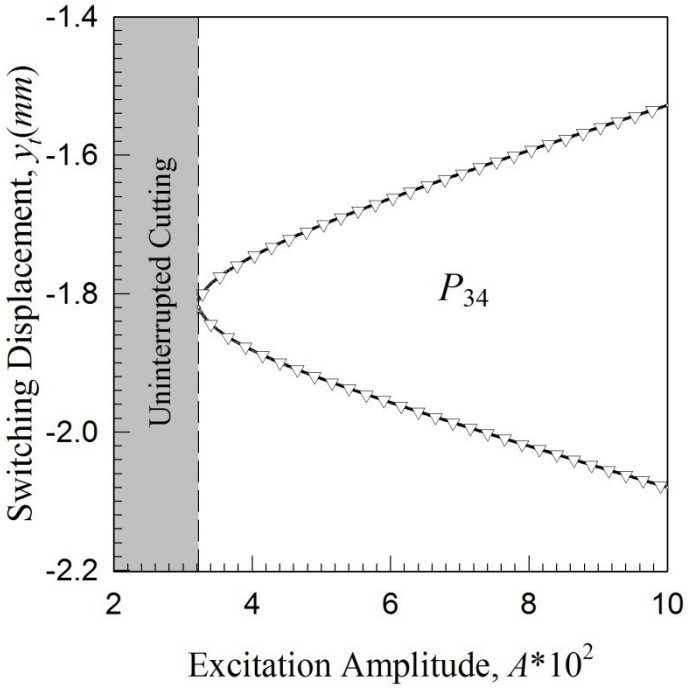

(b)

Fig. 41 Numerical and analytical predictions of (a) switching phase $\mathrm{mod}(t_i, 2\pi)$, (b) switching displacement $(y_t = \tilde{y})$ for interrupted periodic motions over a range of excitation amplitude (A); $L_c = 1(mm)$ and $\Omega = 200(\frac{rad}{s})$.

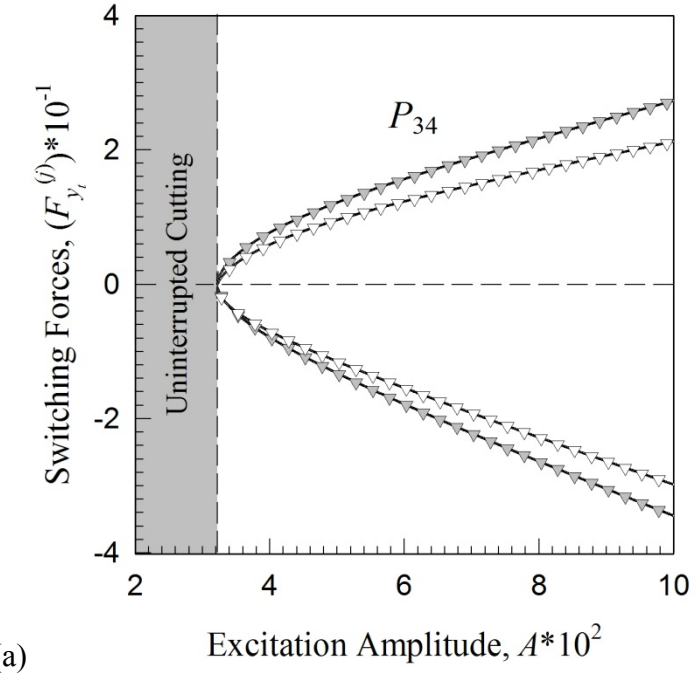

(a)

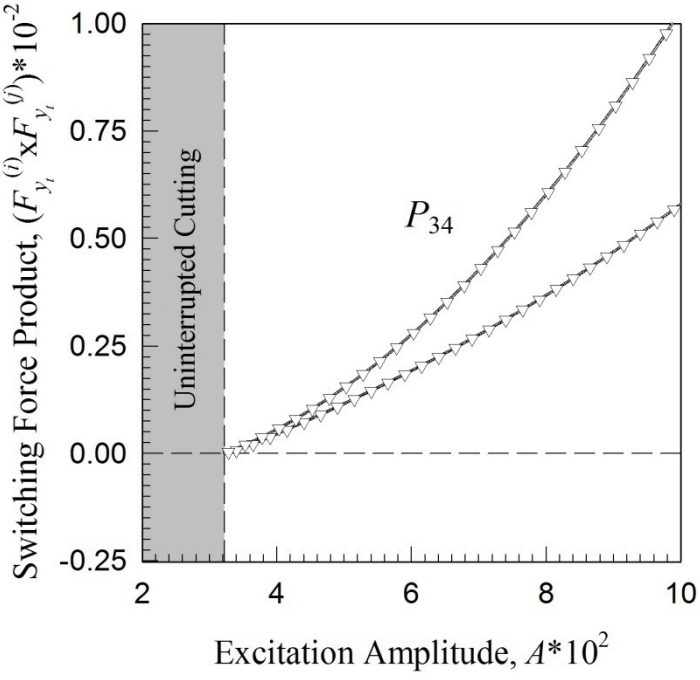

(b)

Fig. 42 Numerical and analytical predictions of (a) switching forces $(F_{y_t}^{(3)}, F_{y_t}^{(4)})$ and (b) switching force product $(F_{y_t}^{(3)} \times F_{y_t}^{(4)})$ for interrupted periodic motions over a range of excitation amplitude (A); $L_c = 1(mm)$ and $\Omega = 200(\frac{rad}{s})$.

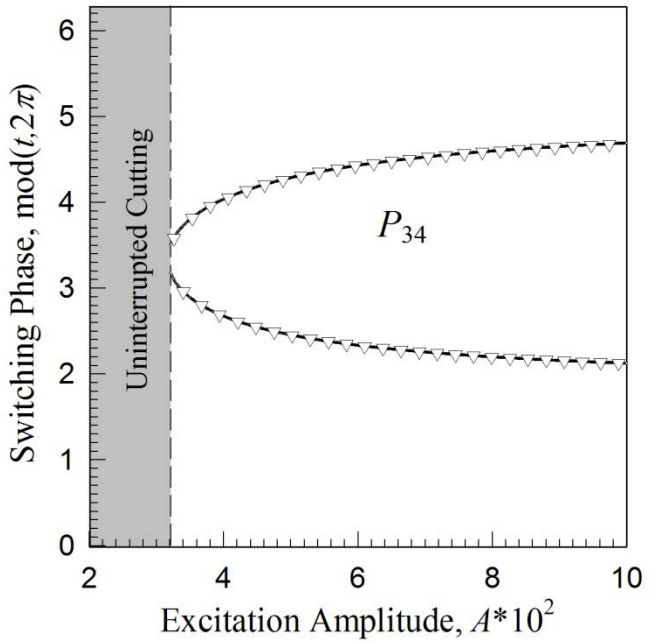

(a)

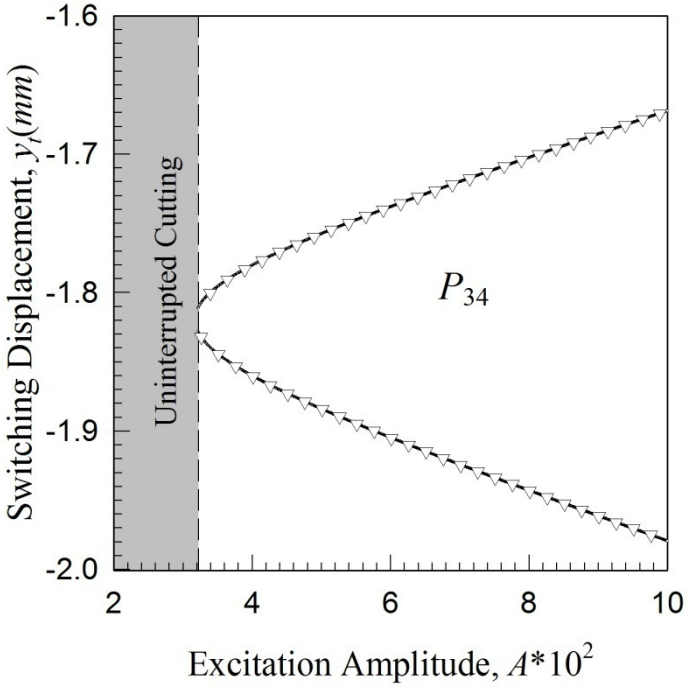

(b)

Fig. 43 Numerical and analytical predictions of (a) switching phase $\mathrm{mod}(t_i, 2\pi)$, (b) switching displacement $(y_t = \tilde{y})$ for interrupted periodic motions over a range of excitation amplitudes (A); $L_c = 1(mm)$ and $\Omega = 400(\frac{rad}{s})$.

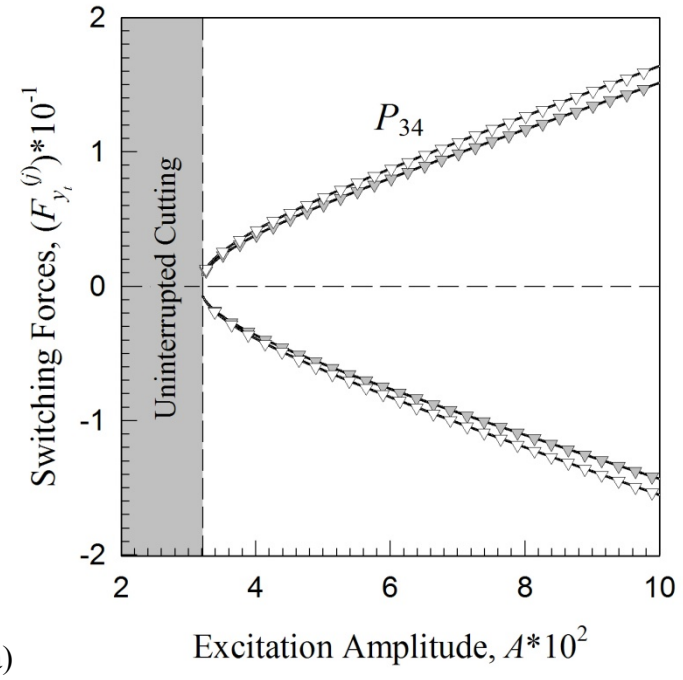

(a)

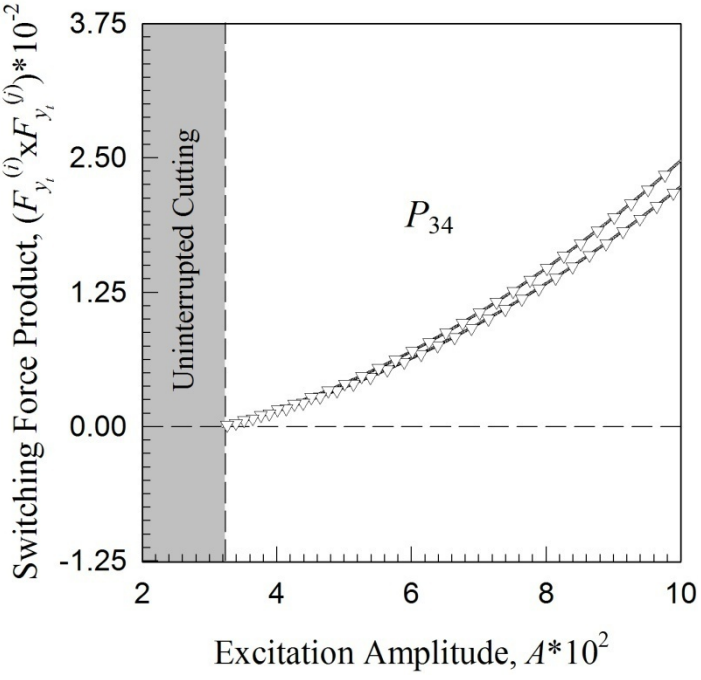

(b)

Fig. 44 Numerical and analytical predictions of (a) switching forces $(F_{y_t}^{(3)}, F_{y_t}^{(4)})$ and (b) switching force product $(F_{y_t}^{(3)} \times F_{y_t}^{(4)})$ for interrupted periodic motions over a range of excitation amplitudes (A); $L_c = 1(mm)$ and $\Omega = 400(\frac{rad}{s})$.

Study of Excitation Frequency (Ω)

The numerical and analytical predictions of the interrupted periodic cutting motions for this machine-tool system with an excitation force, is presented over the range of excitation frequencies $\Omega \in [379.0, 484.4]$ $(\frac{rad}{s})$. The external force and geometry parameters are

$$A = 500,\ \Omega V = 20 \frac{mm}{s},\ \mu = 0.7,\ k_2 = 100 \frac{kN}{mm}.$$

The switching phase $\mathrm{mod}(\Omega t_i, 2\pi)$, switching displacement (y_t) versus excitation frequency (Ω) are illustrated in Fig. 45(a,b), respectively. The most useful information is found in Fig. 46(a,b), where the switching forces ($F_{\tilde{y}}^{(3)}$ and $F_{\tilde{y}}^{(4)}$) and switching force products ($F_{\tilde{y}}^{(3)} \times F_{\tilde{y}}^{(4)}$) versus excitation frequency (Ω) are shown. The periodic motions observed thru a range of excitation frequencies $\Omega \in [379.0, 484.4]$ $(\frac{rad}{s})$ is $P_{34} = P_3 \circ P_4$.

In the neighborhood outside of the interval $\Omega \in [379.0, 484.4]$ $(\frac{rad}{s})$ the periodic motions do not intersect the discontinuity (or pure cutting occurs, no interruptions). There are two points where the grazing motion is well defined, $\Omega = 397.0,\ 484.4$ $(\frac{rad}{s})$. Such a phenomenon is verified by the forces products trending toward zero. The chip seizure motion is also a possibility at these points. The chip velocity (ΩV) will be studied in the next section.

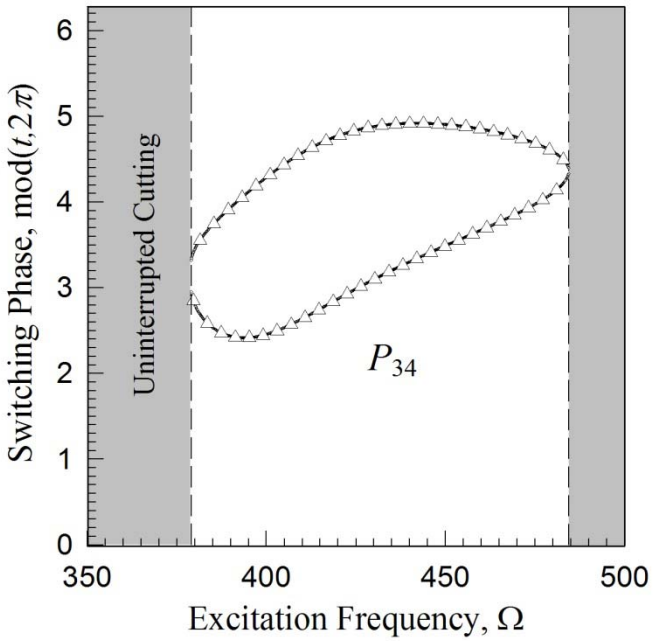

(a)

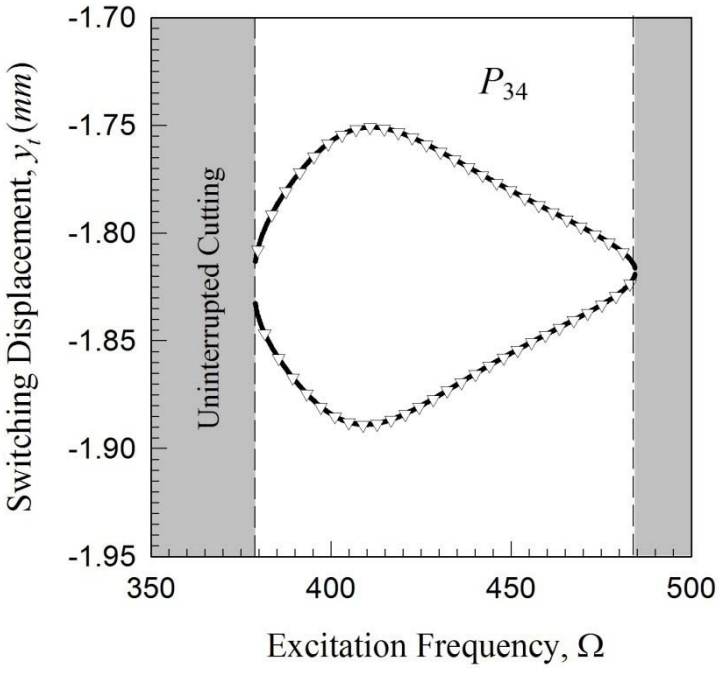

(b)

Fig. 45 Numerical and analytical predictions of (a) switching phase $\mathrm{mod}(t_i, 2\pi)$, (b) switching displacement $(y_t = \tilde{y})$ for interrupted periodic motions over a range of excitation frequencies (Ω); $L_c = 1(mm)$ and $A = 500$.

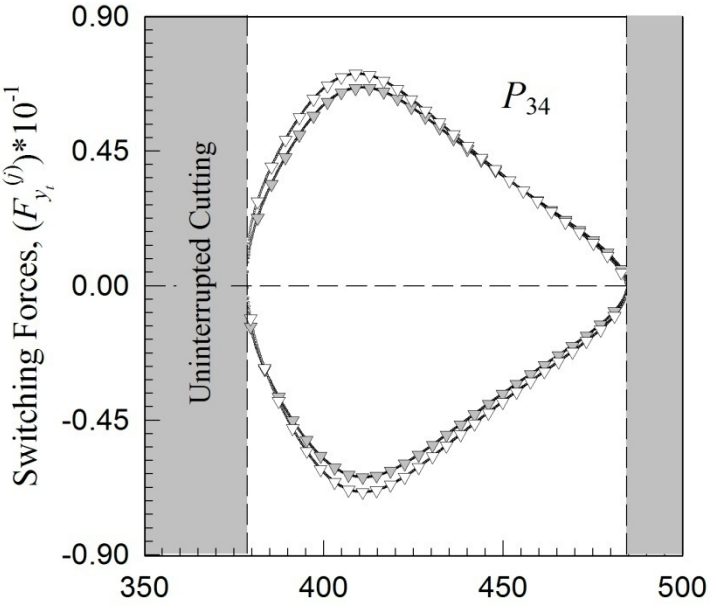

(a)

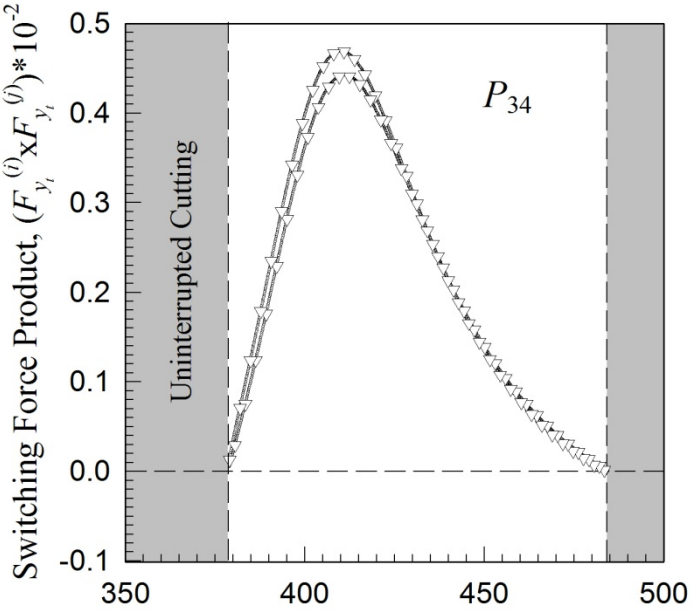

(b)

Fig. 46 Numerical and analytical predictions of (a) switching forces $(F_{y_t}^{(3)}, F_{y_t}^{(4)})$ and (b) switching force product $(F_{y_t}^{(3)} \times F_{y_t}^{(4)})$ for interrupted periodic motions over a range of excitation frequencies (Ω); $L_c = 1(mm)$ and $A = 500$.

Study of Chip Velocity (ΩV)

The numerical and analytical predictions of the interrupted periodic cutting motions for this machine-tool system with an excitation force, is presented over the range of chip velocities $\Omega V \in [0, 30.1]$ $(\frac{mm}{s})$. The external force parameters are

$$A = 500,\ \mu = 0.7,\ k_2 = 10\,\frac{kN}{mm}.$$

The switching phase $\mathrm{mod}(\Omega t_i, 2\pi)$, switching displacement (y_t) versus chip velocity (ΩV) are illustrated in Fig. 47(a,b) for $\Omega = 200$ $(\frac{rad}{s})$, respectively. The most useful information is found in Fig. 48(a,b), where the switching forces $(F_{\tilde{y}}^{(3)}$ and $F_{\tilde{y}}^{(4)})$ and switching force products $(F_{\tilde{y}}^{(3)} \times F_{\tilde{y}}^{(4)})$ versus chip velocity (ΩV) are shown. One of the simplest periodic motions is observed thru a range of chip velocities $\Omega V \in [0, 30.1]$ $(\frac{mm}{s})$ for mapping structure $P_{34} = P_3 \circ P_4$. For $\Omega V > 30.1$ $(\frac{mm}{s})$ the periodic motions do not intersect the discontinuity (or pure cutting occurs, no interruptions); hence the velocity grazing boundary is noted at this point.

Additional interruptions are noted with an excitation frequency of $\Omega = 400$ $(\frac{rad}{s})$. The switching phase $\mathrm{mod}(\Omega t_i, 2\pi)$, switching displacement (y_t) versus chip velocity (ΩV) are illustrated in Fig. 49(a,b), respectively. The most useful information is found in Fig. 50(a,b), where the switching forces $(F_{\tilde{y}}^{(3)}$ and $F_{\tilde{y}}^{(4)})$ and switching force products $(F_{\tilde{y}}^{(3)} \times F_{\tilde{y}}^{(4)})$ versus chip velocity (ΩV) are shown. One of the simplest periodic

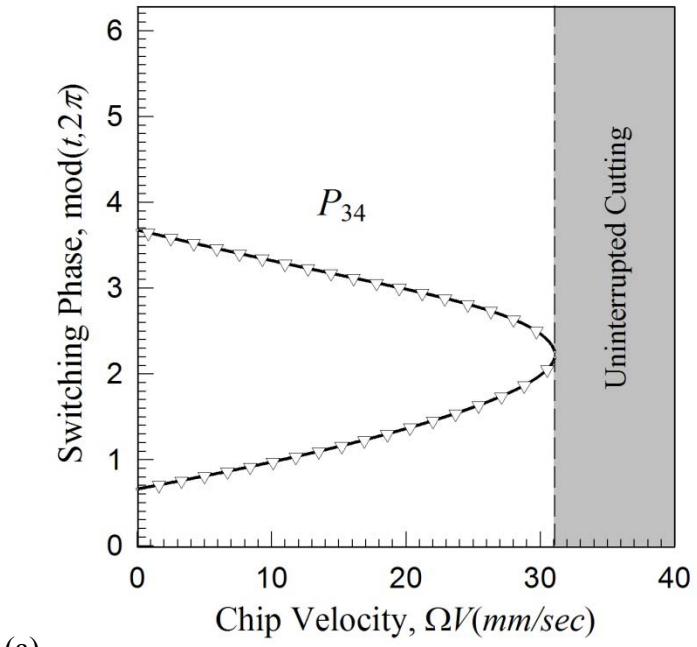

(a)

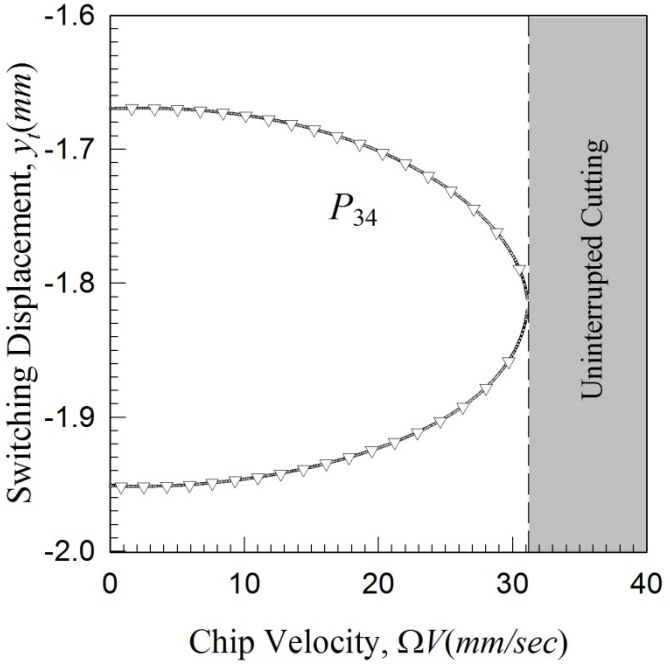

(b)

Fig. 47 Numerical and analytical predictions of (a) switching phase $\mathrm{mod}(t_i, 2\pi)$, (b) switching displacement $(y_t = \tilde{y})$ for interrupted periodic motions over a range of chip velocities (ΩV); $L_c = 1(mm)$ and $\Omega = 200(\frac{rad}{s})$.

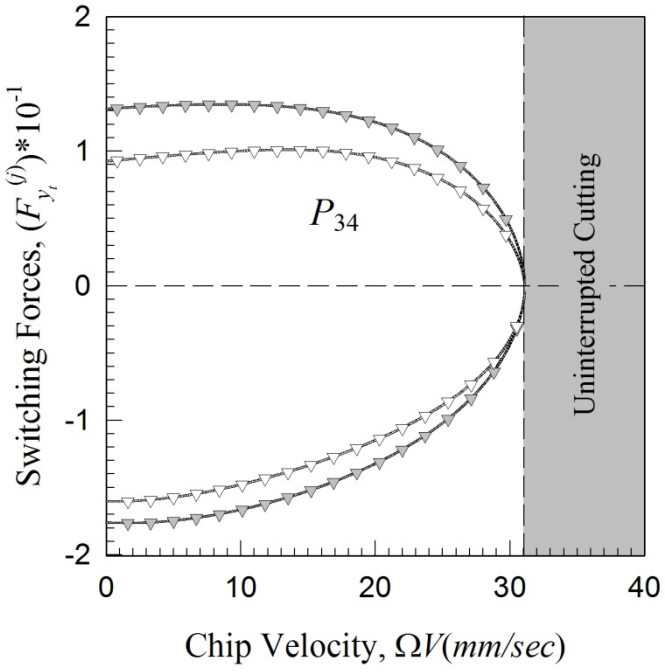

(a)

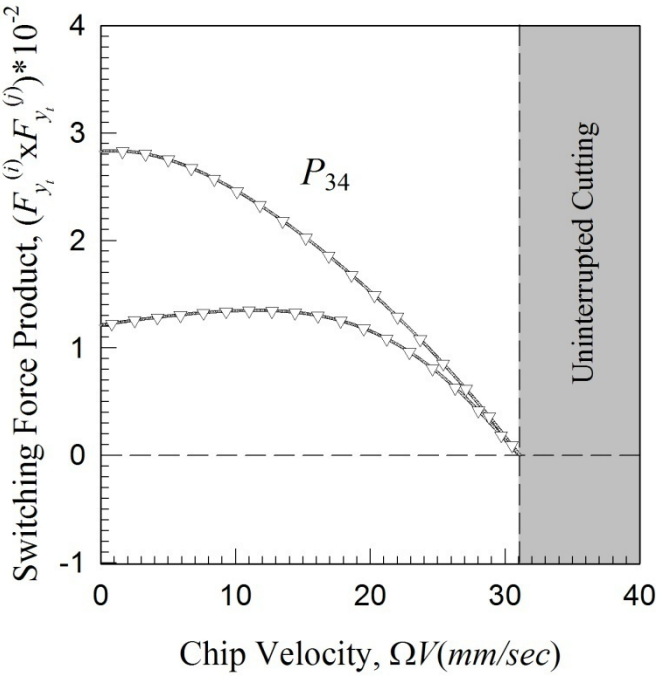

(b)

Fig. 48 Numerical and analytical predictions of (a) switching forces $(F_{y_t}^{(3)}, F_{y_t}^{(4)})$ and (b) switching force product $(F_{y_t}^{(3)} \times F_{y_t}^{(4)})$ for interrupted periodic motions over a range of chip velocities (ΩV); $L_c = 1(mm)$ and $\Omega = 200(\frac{rad}{s})$.

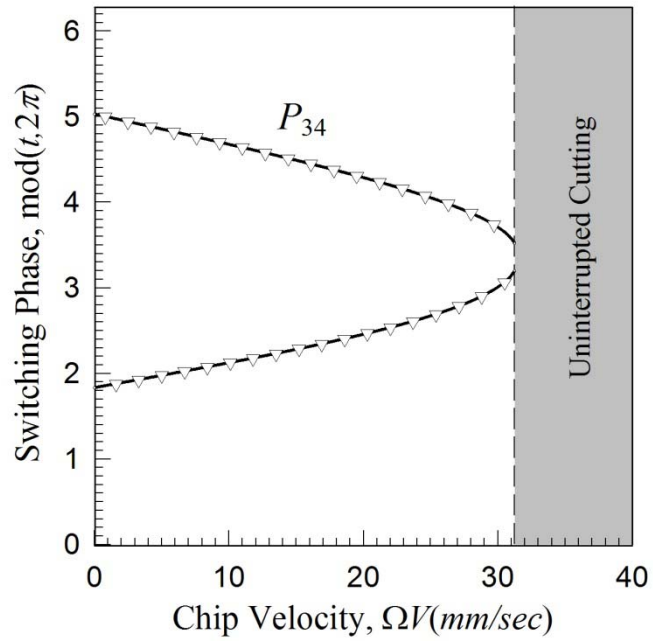

(a)

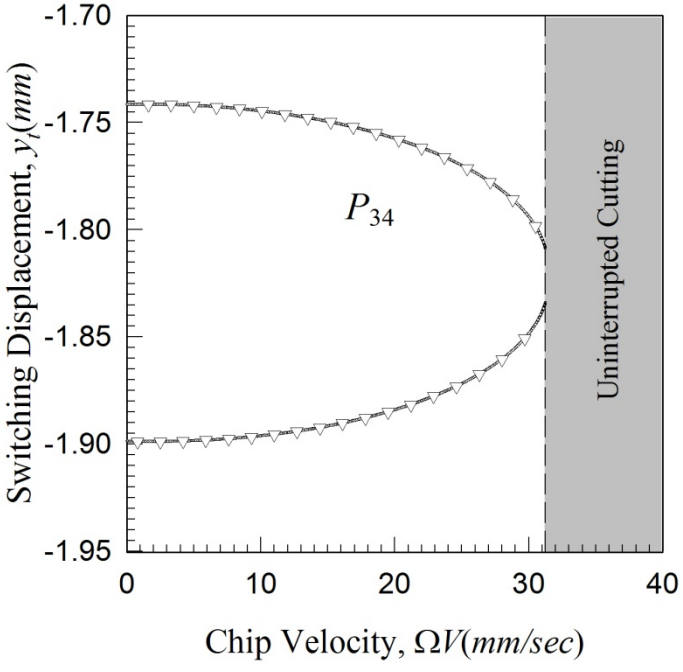

(b)

Fig. 49 Numerical and analytical predictions of (a) switching phase $\mathrm{mod}(t_i, 2\pi)$, (b) switching displacement $(y_t = \tilde{y})$ for interrupted periodic motions over a range of chip velocities (ΩV); $L_c = 1(mm)$ and $\Omega = 400(\frac{rad}{s})$.

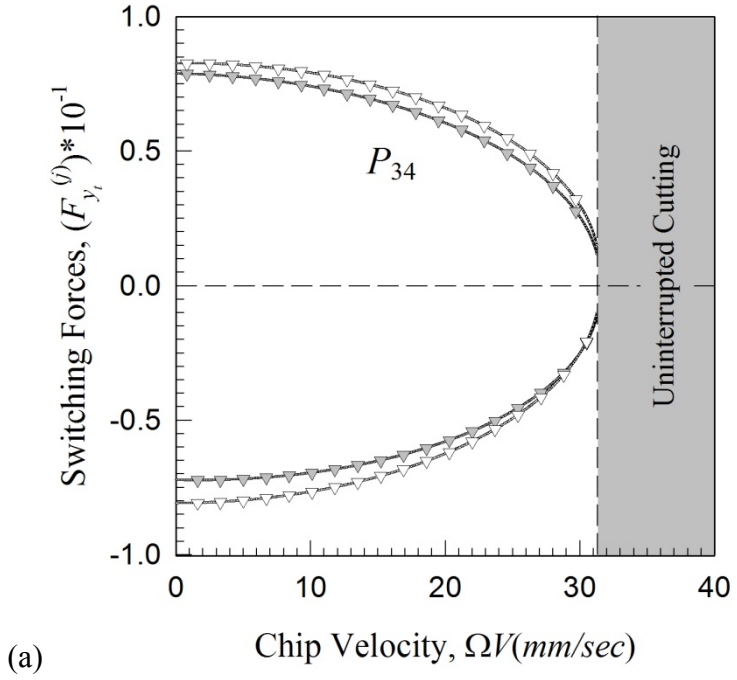

(a)

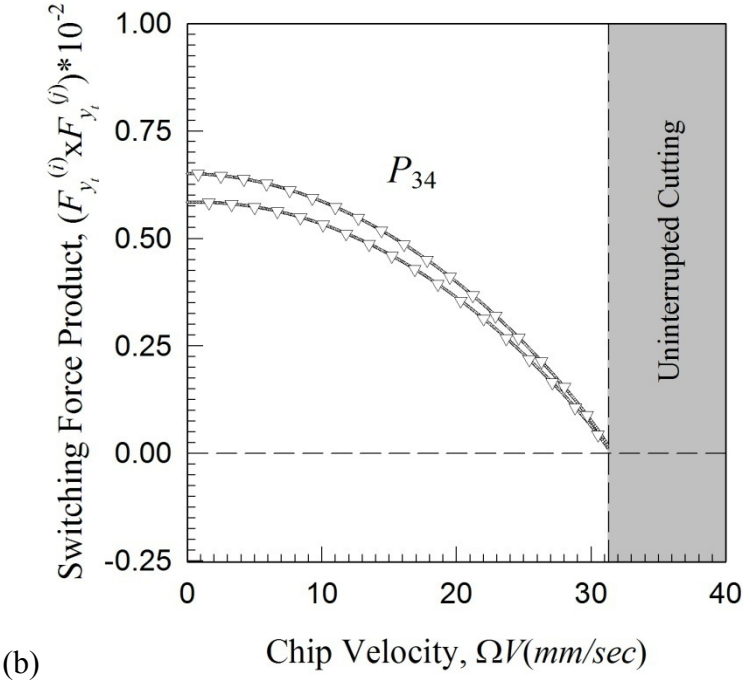

(b)

Fig. 50 Numerical and analytical predictions of (a) switching forces $(F_{y_t}^{(3)}, F_{y_t}^{(4)})$ and (b) switching force product $(F_{y_t}^{(3)} \times F_{y_t}^{(4)})$ for interrupted periodic motions over a range of chip velocities (ΩV); $L_c = 1(mm)$ and $\Omega = 400(\frac{rad}{s})$.

motions is observed thru a range of chip velocities $(\Omega V) \in [0, 31.2]$ $(\frac{mm}{s})$ for mapping structure $P_{34} = P_3 \circ P_4$. For $(\Omega V) > 31.2$ $(\frac{mm}{s})$ the periodic motions do not intersect the discontinuity (or pure cutting occurs, no interruptions).

The frequency of loss of contact/cutting is directly related to the cutting velocity in a machine-tool Chandiramani and Pothala [28]. The contribution of these results relates the percentage of the orbit interrupted to the chip velocity and interruption boundary with respect to the chip velocity. The chip/tool friction coefficient (μ) will be studied in the next section.

Study of Friction Coefficient (μ)

The numerical and analytical predictions of the interrupted periodic cutting motions for this machine-tool system with an excitation force, is presented over the range of friction coefficients $\mu \in [0, 3]$. The external force parameters are

$$A = 500,\ \Omega V = 20 \frac{mm}{s},\ k_2 = 10 \frac{kN}{mm}.$$

The switching phase $\mathrm{mod}(\Omega t_i, 2\pi)$, switching displacement $(y_t = \tilde{y})$ versus friction coefficient (μ) are illustrated in Fig. 51(a,b) for $\Omega = 200$ $(\frac{rad}{s})$, respectively. The most useful information is found in Fig. 52(a,b), where the switching forces $(F_{\tilde{y}}^{(3)}$ and $F_{\tilde{y}}^{(4)})$ and switching force products $(F_{\tilde{y}}^{(3)} \times F_{\tilde{y}}^{(4)})$ versus friction coefficient (μ) are shown. The periodic motions observed thru a range of the friction coefficient $\mu \in [0, 3]$ is $P_{34} = P_3 \circ P_4$.

Additional interruptions are noted with an excitation frequency of $\Omega = 400$ ($\frac{rad}{s}$). The switching phase $\mathrm{mod}(\Omega t_i, 2\pi)$, switching displacement (y_t) versus friction coefficient (μ) are illustrated in Fig. 53(a,b), respectively. The most useful information is found in Fig. 54(c,d), where the switching forces ($F_{\tilde{y}}^{(3)}$ and $F_{\tilde{y}}^{(4)}$) and switching force products ($F_{\tilde{y}}^{(3)} \times F_{\tilde{y}}^{(4)}$) versus friction coefficient (μ) are shown. One of the simplest periodic motions is observed through a range of friction coefficient $\mu \in [0,3]$ for mapping structure $P_{34} = P_3 \circ P_4$. The chip/tool friction coefficient (μ) appears to have little effect on the switching phase $\mathrm{mod}(\Omega t_i, 2\pi)$ and displacement ($y_t = \tilde{y}$). However, the switching forces ($F_{\tilde{y}}^{(3)}$ and $F_{\tilde{y}}^{(4)}$) and switching force products ($F_{\tilde{y}}^{(3)} \times F_{\tilde{y}}^{(4)}$) increase towards a more passable motion for $\Omega = 200$ ($\frac{rad}{s}$) and decrease towards a possible chip seizure motion for $\Omega = 400$ ($\frac{rad}{s}$).

This implies the excitation frequency (Ω) and the chip/tool friction coefficient (Ω) directly affect the degree of passability of this machine-tool system. The chip stiffness coefficient (k_2) will be studied in the next section.

Study of Chip Stiffness (k_2)

The numerical and analytical predictions of the interrupted periodic cutting motions for this machine-tool system with an excitation force, is presented over the range of stiffness coefficients $k_2 \in [0,100k]$ ($\frac{N}{mm}$). The external force parameters are

$$A = 500,\ \Omega V = 20\frac{mm}{s},\ \mu = 0.7.$$

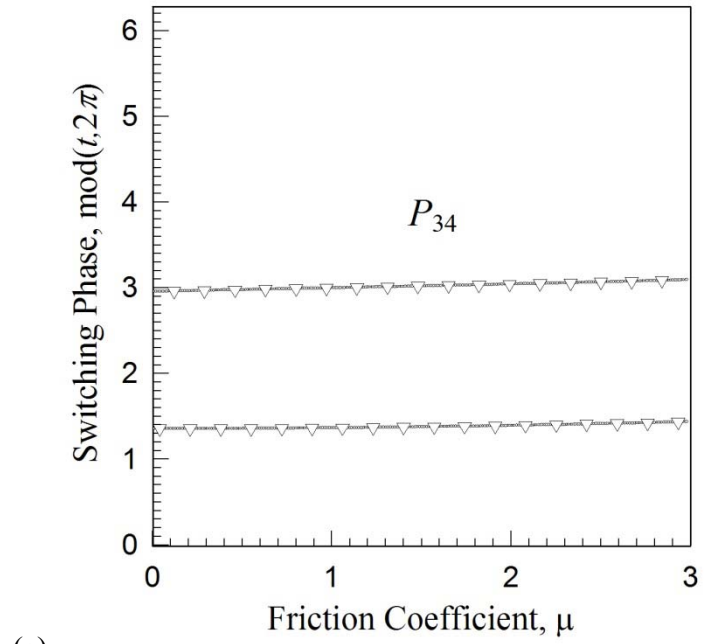

(a)

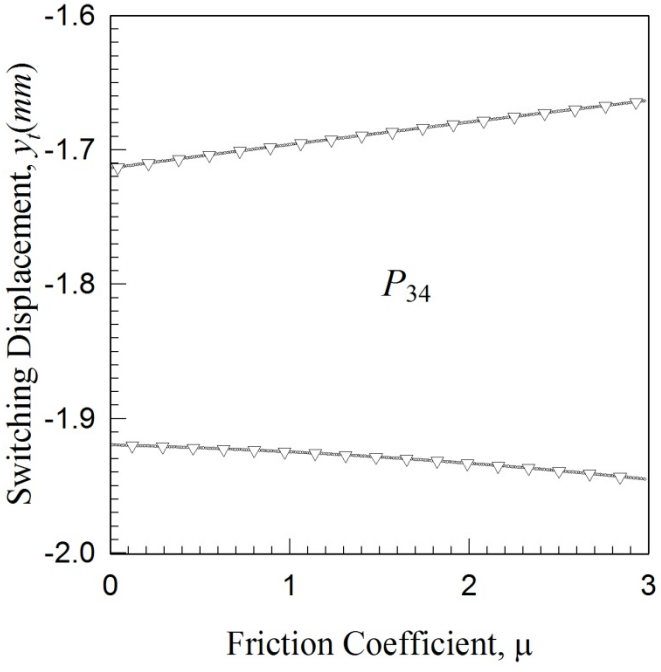

(b)

Fig. 51 Numerical and analytical predictions of (a) switching phase $\mathrm{mod}(t_i, 2\pi)$, (b) switching displacement $(y_t = \tilde{y})$ for interrupted periodic motions over a range of friction coefficient (μ); $L_c = 1(mm)$ and $\Omega = 200(\frac{rad}{s})$.

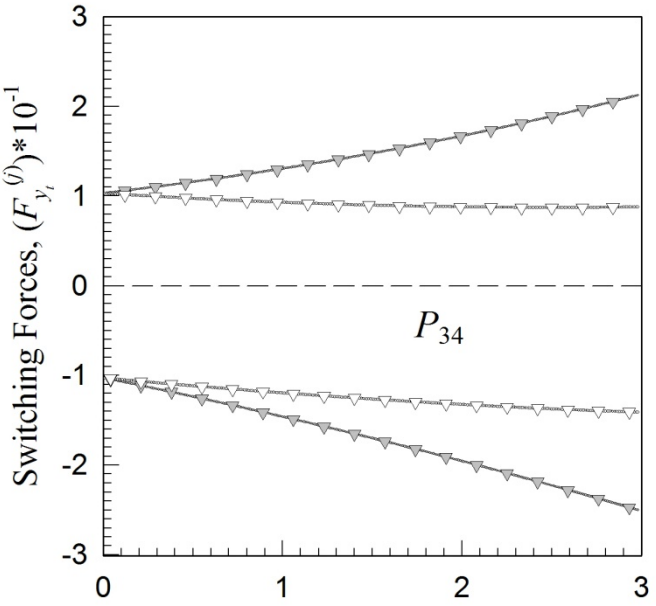

(a)

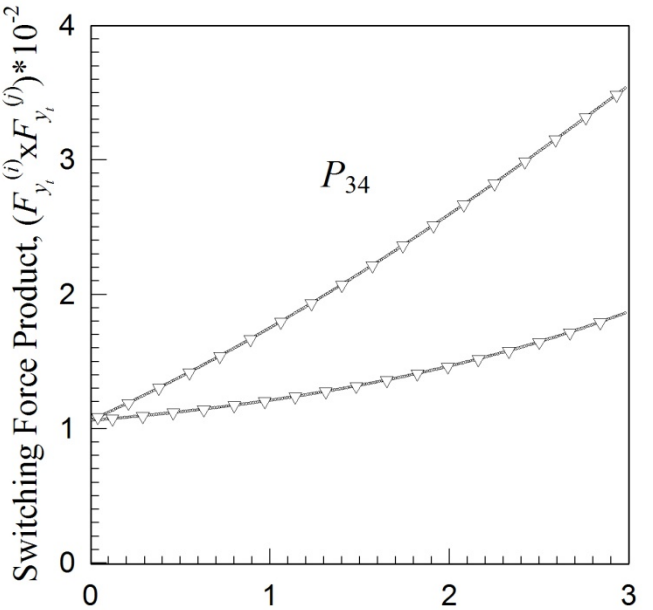

(b)

Fig. 52 Numerical and Analytical predictions of (a) switching forces $(F_{y_t}^{(3)}, F_{y_t}^{(4)})$ and (b) switching force product $(F_{y_t}^{(3)} \times F_{y_t}^{(4)})$ for interrupted periodic motions over a range of friction coefficient (μ); $L_c = 1(mm)$ and $\Omega = 200(\frac{rad}{s})$.

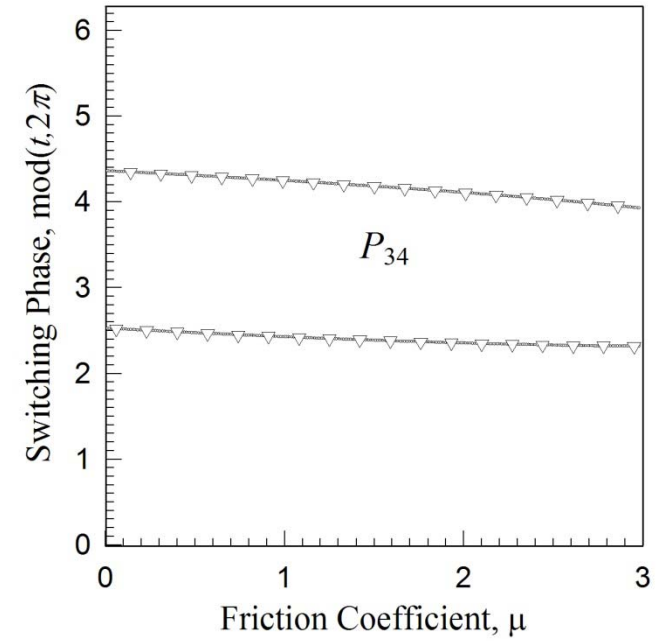

(a)

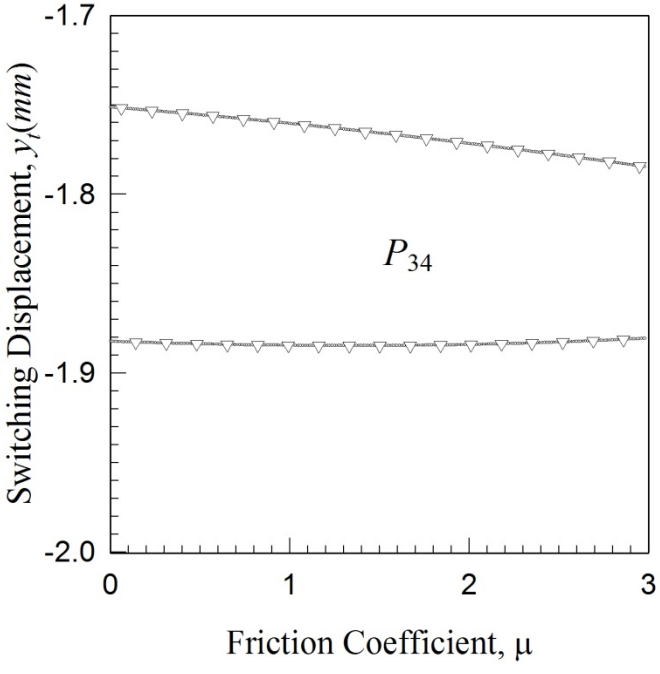

(b)

Fig. 53 Numerical and Analytical predictions of (a) switching phase $\mathrm{mod}(t_i, 2\pi)$, (b) switching displacement $(y_t = \tilde{y})$ for interrupted periodic motions over a range of friction coefficient (μ); $L_c = 1(mm)$ and $\Omega = 400(\frac{rad}{s})$.

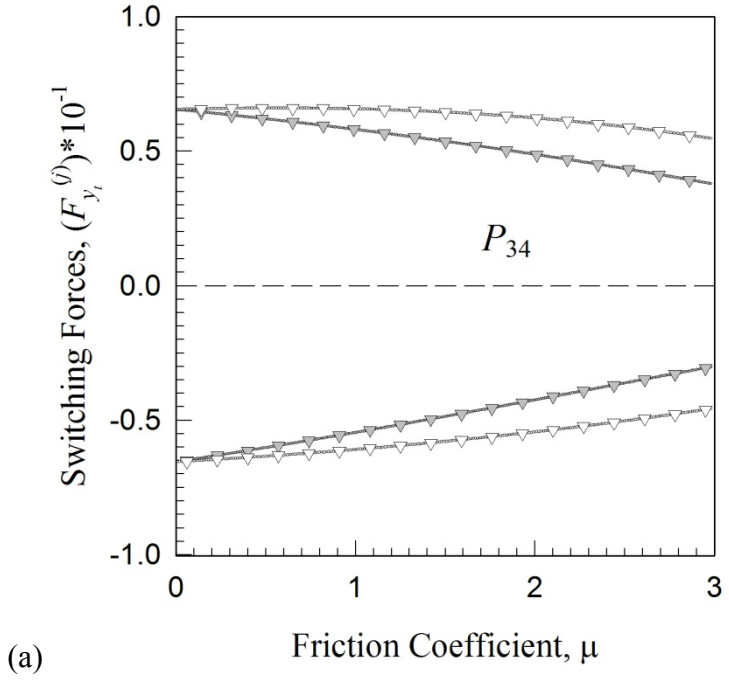

(a)

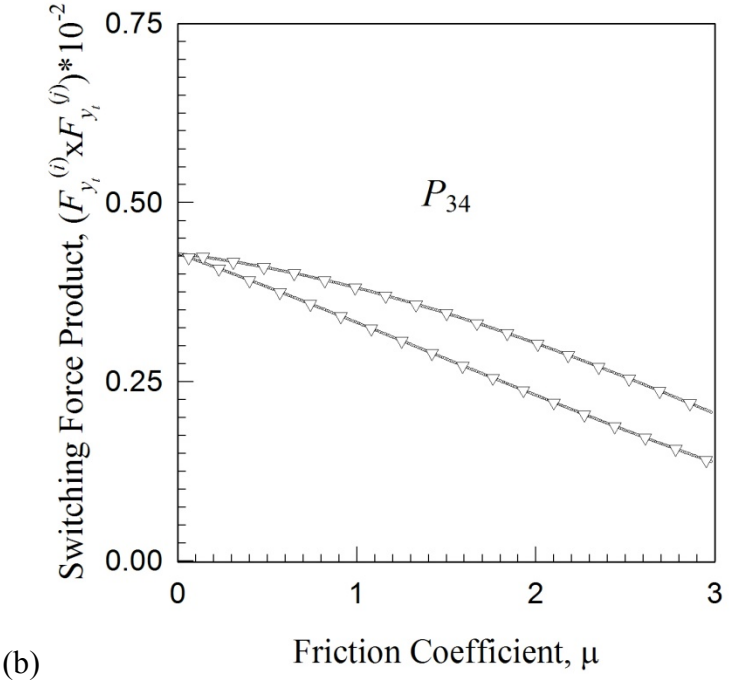

(b)

Fig. 54 Numerical and analytical predictions of (c) switching forces $(F_{y_t}^{(3)}, F_{y_t}^{(4)})$ and (d) switching force product $(F_{y_t}^{(3)} \times F_{y_t}^{(4)})$ for interrupted periodic motions over a range of friction coefficient (μ); $L_c = 1(mm)$ and $\Omega = 400(\frac{rad}{s})$.

The switching phase $\mathrm{mod}(\Omega t_i, 2\pi)$, switching displacement (y_t) versus chip stiffness coefficient (k_2) are illustrated in Fig. 55(a,b) for $\Omega = 200$ ($\frac{rad}{s}$), respectively. The most useful information is found in Fig. 56(a,b), where the switching forces ($F_{\tilde{y}}^{(3)}$ and $F_{\tilde{y}}^{(4)}$) and switching force products ($F_{\tilde{y}}^{(3)} \times F_{\tilde{y}}^{(4)}$) versus stiffness coefficient (k_2) are shown. One of the simplest periodic motions is observed through a range of stiffness $k_2 \in [0, 100k]$ ($\frac{N}{mm}$) for mapping structure $P_{34} = P_3 \circ P_4$.

Additional interruptions are noted with an excitation frequency of $\Omega = 400$ ($\frac{rad}{s}$). The switching phase $\mathrm{mod}(\Omega t_i, 2\pi)$, switching displacement (y_t) versus stiffness coefficient (k_2) are illustrated in Fig. 57(a,b), respectively. The most useful information is found in Fig. 58(a,b), where the switching forces ($F_{\tilde{y}}^{(3)}$ and $F_{\tilde{y}}^{(4)}$) and switching force products ($F_{\tilde{y}}^{(3)} \times F_{\tilde{y}}^{(4)}$) versus stiffness coefficient (k_2) are shown. One of the simplest periodic motions is observed through a range of stiffness $k_2 \in [0, 24.25k]$ ($\frac{N}{mm}$) for mapping structure $P_{34} = P_3 \circ P_4$. The transition between cutting and ploughing action is affected by the stick-slip friction phenomenon Simoneau and Elbestawi [14].

The increasing stiffness coefficient leads to such a conclusion, but the trend of potential stick-slip interruptions are noted to be sensitive to chip resistance and excitation frequency. A claim can be directly made that for high excitation frequencies (at or above the highest natural frequency) the stick-slip phenomenon is more likely to occur due to the grazing bifurcations of the chip/tool friction boundary. This can be attributed to the increase chip resistance which prevents motion in the direction of the chip shearing

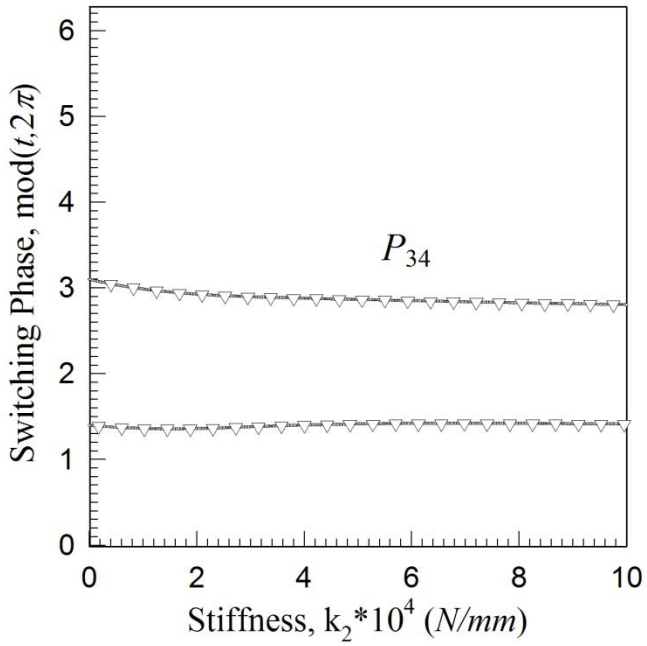

(a)

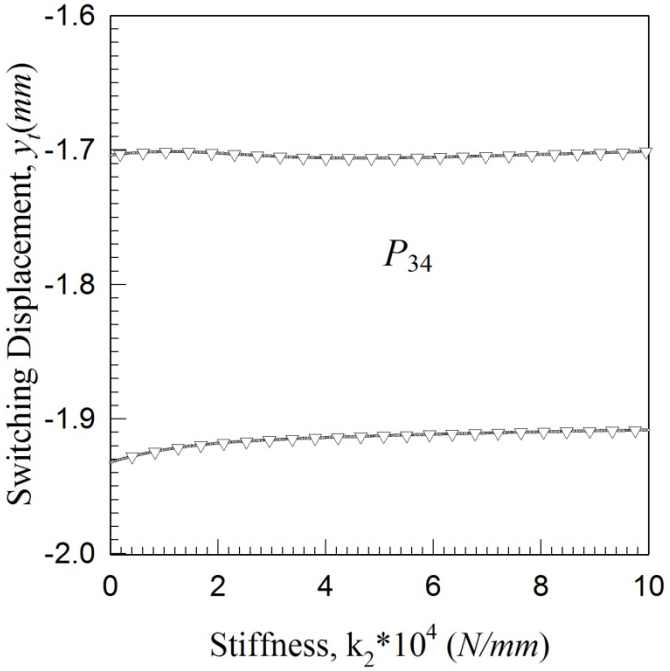

(b)

Fig. 55 Numerical and analytical predictions of (a) switching phase $\mathrm{mod}(t_i, 2\pi)$, (b) switching displacement $(y_t = \tilde{y})$ for interrupted periodic motions over a range of stiffness coefficient (k_2); $L_c = 1(mm)$ and $\Omega = 200(\frac{rad}{s})$.

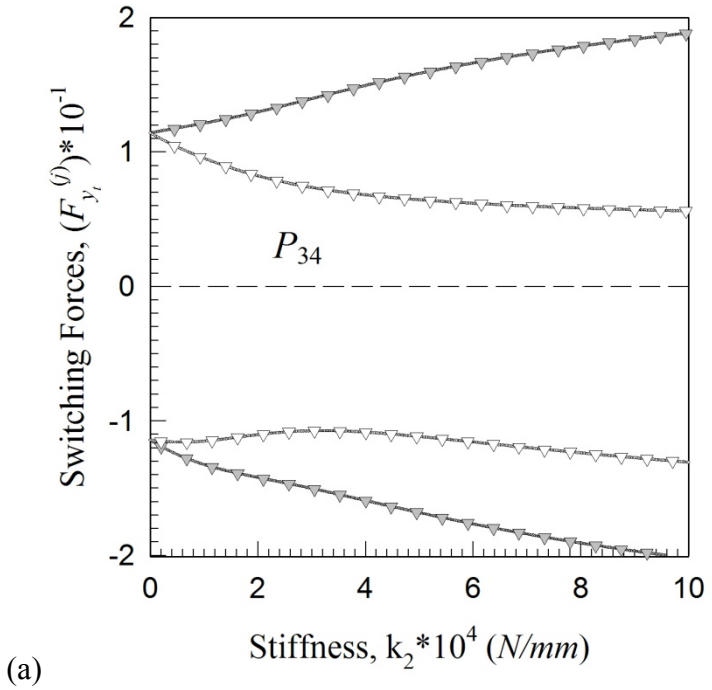

(a)

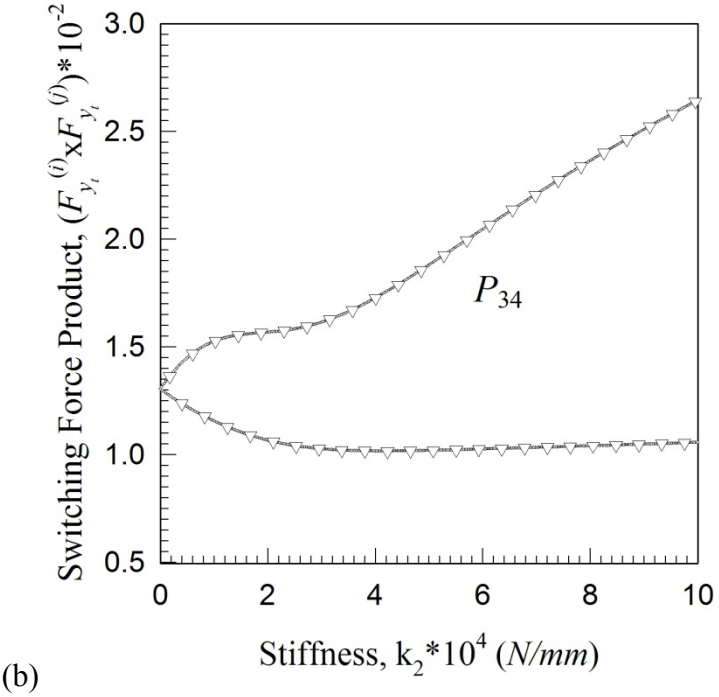

(b)

Fig. 56 Numerical and analytical predictions of (a) switching forces $(F_{y_t}^{(3)}, F_{y_t}^{(4)})$ and (b) switching force product $(F_{y_t}^{(3)} \times F_{y_t}^{(4)})$ for interrupted periodic motions over a range of stiffness coefficient (k_2); $L_c = 1(mm)$ and $\Omega = 200(\frac{rad}{s})$.

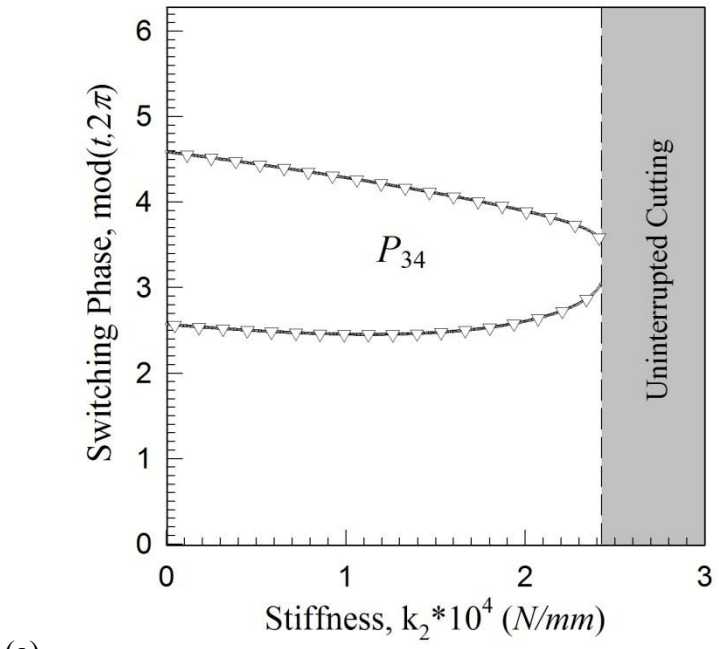

(a)

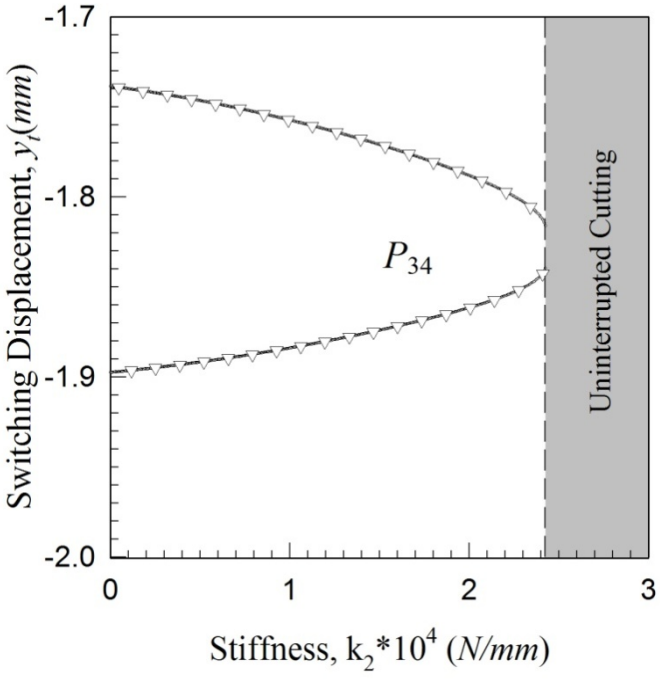

(b)

Fig. 57 Numerical and analytical predictions of (a) switching phase $\mathrm{mod}(t_i, 2\pi)$, (b) switching displacement $(y_t = \tilde{y})$ for interrupted periodic motions over a range of stiffness coefficient (k_2); $L_c = 1(mm)$ and $\Omega = 400(\frac{rad}{s})$.

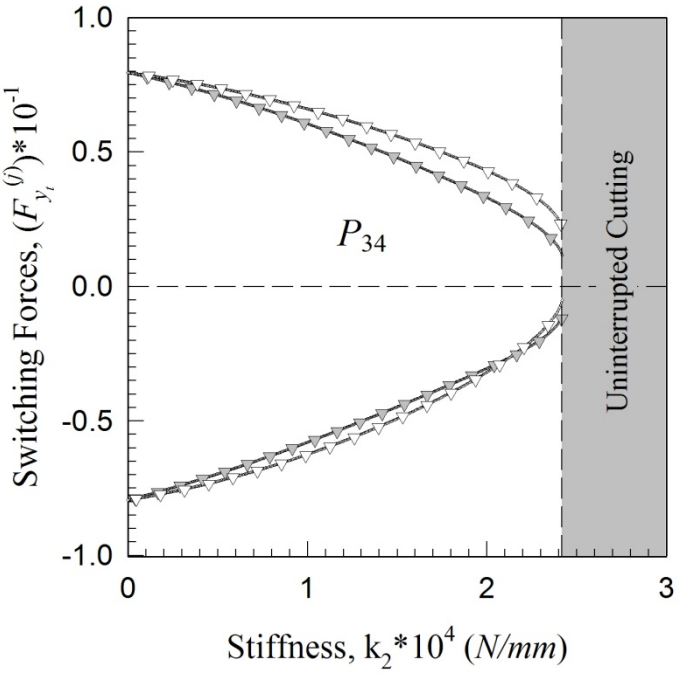

(a)

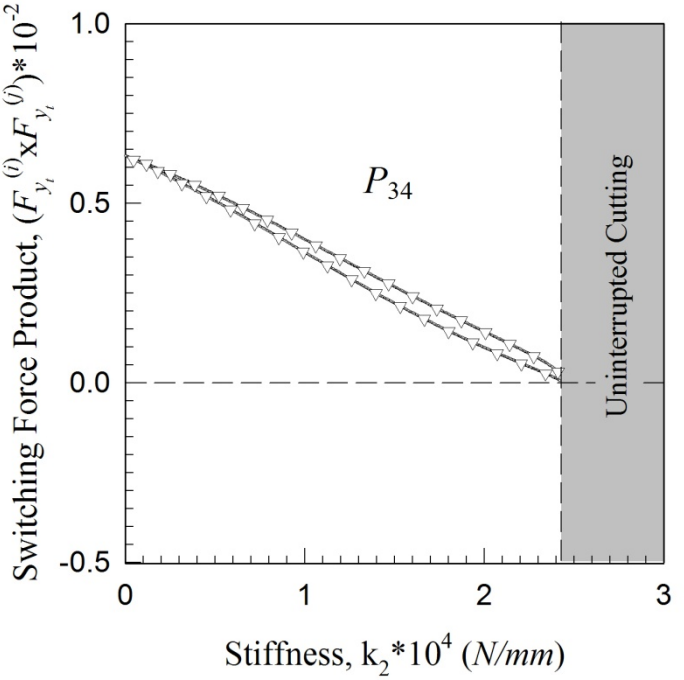

(b)

Fig. 58 Numerical and analytical predictions of (a) switching forces $(F_{y_t}^{(3)}, F_{y_t}^{(4)})$ and (b) switching force product $(F_{y_t}^{(3)} \times F_{y_t}^{(4)})$ for interrupted periodic motions over a range of stiffness coefficient (k_2); $L_c = 1(mm)$ and $\Omega = 400(\frac{rad}{s})$.

direction; hence, a reduction in the change of the friction force during interaction with the chip/tool friction boundary (boundary three).

Analytical Prediction of Periodic Motions Interacting with Boundaries 3 and 4

Given the set of equations in Eq.(6.8) and Eq.(6.9) and a proper initial solution set the system of equations defining the interrupted cutting periodic motion can be solved through traditional numerical techniques. The dynamical system parameters are

$$\frac{m_e}{m} = 10^3,\ d_x = 74\tfrac{Ns}{mm},\ d_y = 63\tfrac{Ns}{mm},$$

$$k_x = k_y = 56\tfrac{kN}{mm},\ k_1 = 0.1\tfrac{MN}{mm}, k_2 = 10\tfrac{kN}{mm},\ d_1 = d_2 = 0\tfrac{Ns}{\text{mm}},$$

and the external force and geometry parameters are

$$\delta_1 = \delta_2 = 10^{-3} m,\ \mu = 0.7,\ L_c = 1.0\times10^{-4} m,\ \Omega V = 20\tfrac{mm}{s},$$

$$\alpha = \tfrac{\pi}{4}\text{rad},\ \beta = 0.1\text{rad},\ \eta = \tfrac{\pi}{4}\text{rad},$$

$$X_1 = Y_1 = 10^{-3} m, X_{eq} = Y_{eq} = 5\times10^{-3} m.$$

The summary of the parameters and their respective characteristics are noted in Table 5.

Study of Eccentricity Amplitude (e)

Consider the variation of the motion throughout the range of eccentricity amplitude $e \in [0.0805, 0.2000]$ (mm) for $\Omega = 250$ $(\frac{rad}{s})$, see Fig. 59 and Fig. 60. The switching phase $\text{mod}(t_i, 2\pi)$ and switching displacement $(\tilde{y}_i)$ versus the eccentricity amplitude (e)

Table 5 Summary of Numerical and Analytical Predictions of P_{234}.

Range of Parameter	Boundary Interactions	Pure Cutting	Interrupted Cutting	Fig.
$e@\Omega = 250(\frac{rad}{s})$	3,4	$e < 0.0805$	[1] $[0.0805, 0.2]$	59, 60
$e@\Omega = 400(\frac{rad}{s})$	3,4	$e < 0.0203$	[2] $[0.0203, 0.2]$	61, 62
$\Omega@e = 0.1(mm)$	3,4	$\Omega < 191.5$	[3] $[0.1915k, 1k]$	63, 64
$\Omega@e = 0.05(mm)$	3,4	$\Omega < 0.221k$ $0.286k < \Omega < 0.366k$	[4] $[0.2210k, 0.2860k]$ $[0.3660k, 1k]$	65, 66
$\Omega V@\Omega = 250(\frac{rad}{s})$	3,4	$V > 50.41$	[5] $[0, 50.41]$	67, 68
$\Omega V@\Omega = 340(\frac{rad}{s})$	3,4	$V > 28.62$	[6] $[0, 28.62]$	69, 70
$\mu@\Omega = 250(\frac{rad}{s})$	3,4	n.a.	[7] $[0, 3.0]$	71, 72
$\mu@\Omega = 400(\frac{rad}{s})$	3,4	n.a.	[7] $[0, 3.0]$	73, 74
$k_2@\Omega = 250(\frac{rad}{s})$	3,4	n.a.	[8] $[0, 500k]$	75, 76
$k_2@\Omega = 400(\frac{rad}{s})$	3,4	n.a.	[8] $[0, 500k]$	77, 78
$L_c@\Omega = 250(\frac{rad}{s})$	3,4	n.a.	[9] $[0.0, 1.0]$	79, 80
$L_c@\Omega = 400(\frac{rad}{s})$	3,4	n.a.	[10] $[0.0, 1.0]$	81, 82

1. $P_{34} : (0.0805, 0.0870](mm)$ and $P_{234} : (0.0870, 0.2000](mm)$;
2. $P_{34} : (0.0203, 0.0295](mm)$ and $P_{234} : (0.0295, 0.2000](mm)$;
3. $P_{34} \in (0.1910k, 0.1945k](\frac{rad}{s})$ and $P_{234} \in (0.1945k, 1k](\frac{rad}{s})$;
4. $P_{34} \in (0.2315k, 0.2773k](\frac{rad}{s})$ and $(0.3660k, 0.3780k](\frac{rad}{s})$,
   $P_{(034)^n} \in (0.2773k, 0.2860k](\frac{rad}{s})$ and $[0.2210k, 0.2315k)(\frac{rad}{s})$,
   and $P_{234} \in (0.3780k, 1k](\frac{rad}{s})$;
5. $P_{234} : (0.00, 48.90](\frac{mm}{s})$ and $P_{34} : (48.90, 51.41](\frac{mm}{s})$;
6. $P_{234} : (0.00, 23.90](\frac{mm}{s})$ and $P_{34} : (23.90, 28.62](\frac{mm}{s})$;
7. $P_{234} : [0, 3.0](\frac{mm}{s})$;
8. $P_{234} : [0, 500k](\frac{N}{mm})$;
9. $P_{234} : [0.0, 0.488)(mm)$ and $P_{34} : [0.488, 1.0](mm)$;
10. $P_{234} : [0.0, 0.455)(mm)$ and $P_{34} : [0.455, 1.0](mm)$.

are presented to show the expanding orbit of the motion for the mappings P_{34} : $\left(0.0805,\ 0.0870\right]$ (mm) and P_{234} : $\left(0.0870,\ 0.2000\right]$ (mm), see Fig. 59(a,b); respectively. The switching points during this periodic interrupted cutting motion allows for a very clear and concise tool for determining the point of bifurcation of the motion to include the dynamics of reducing chip length (P_2). Traditional analysis, such as floquet multiplier method, cannot predict or establish criterion to define such a transition Gegg [47]. Observe how the measure switching displacement $(\tilde{y}_i)$ of Fig. 41(b) grows with respect to increasing eccentricity amplitude (e); indeed this is intuitive to linear systems.

The validation of the predictions are shown in Fig. 60(a,b) by the switching forces and switching force products versus eccentricity amplitude (e). Since the force products are shown to be greater than zero over the entire range $e \in \left[0.0805,\ 0.2000\right]$ (mm); the motions are experimentally and theoretically verified. In effort to identify the effects of both the eccentricity amplitude (e) and frequency (Ω), the eccentricity frequency (Ω) will be adjusted appropriately. Consider the variation of the motion throughout the range of eccentricity amplitude $e \in \left[0.0203, 0.2000\right]$ (mm) for $\Omega = 400$ $(\frac{rad}{s})$, see Fig. 61 and Fig. 62. The switching phase $\mathrm{mod}(t_i, 2\pi)$ and switching displacement $(\tilde{y}_i)$ versus the eccentricity amplitude (e) are presented to show the expanding orbit of the motion for the mappings P_{34} : $\left(0.0203,\ 0.0295\right]$ (mm) and P_{234} : $\left(0.0295,\ 0.2000\right]$ (mm), see Fig. 61(a,b); respectively.

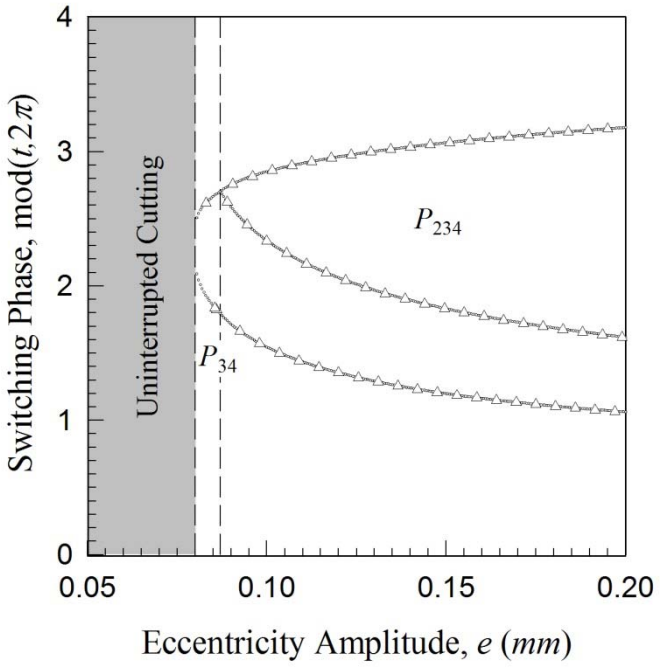

(a)

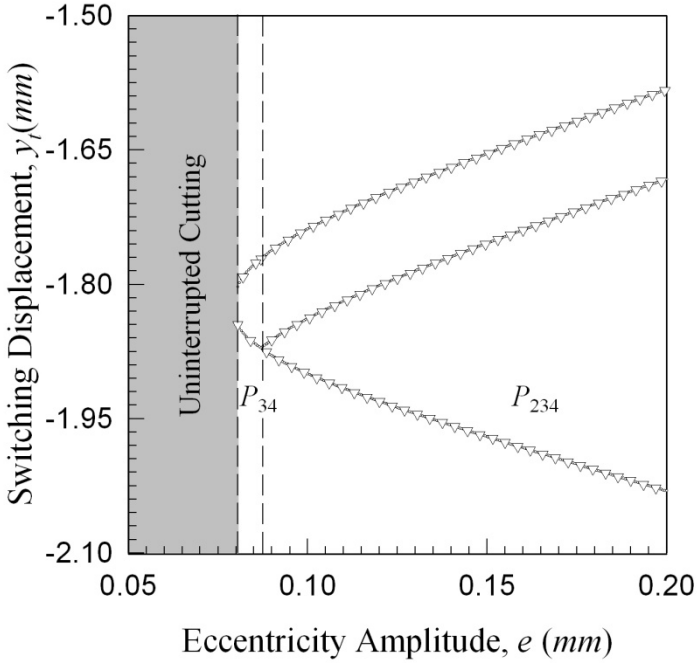

(b)

Fig. 59 Numerical and analytical predictions of (a) switching phase $\mathrm{mod}(t_i, 2\pi)$, (b) switching displacement $(y_t = \tilde{y})$ for interrupted periodic motions over a range of eccentricity amplitude (e); $L_c = 0.1(mm)$ and $\Omega = 250(\frac{rad}{s})$.

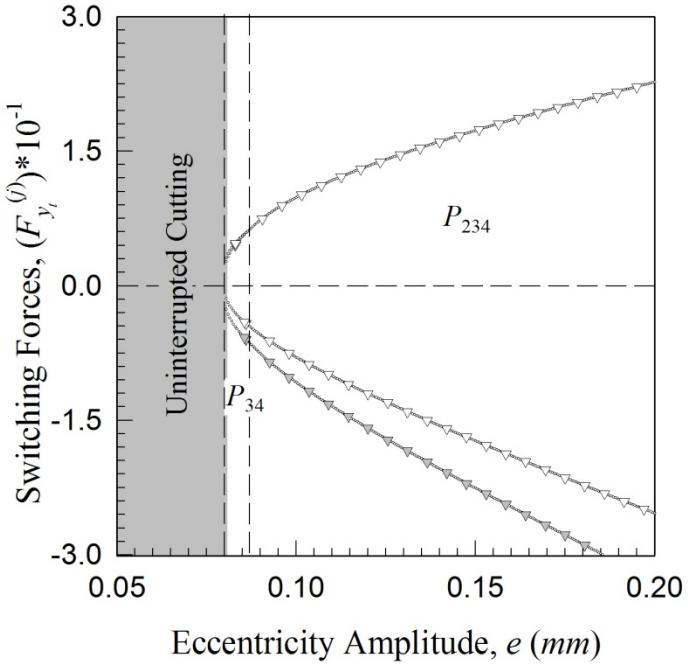

(a)

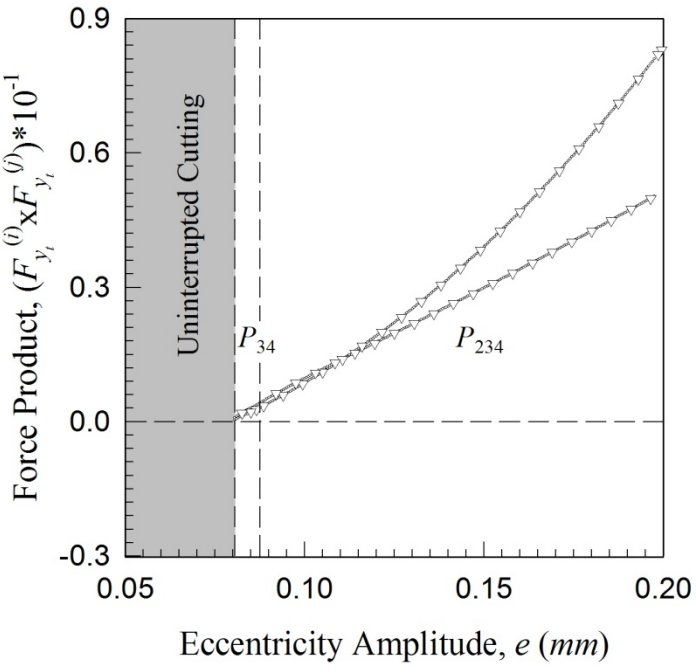

(b)

Fig. 60 Numerical and analytical predictions of (a) switching forces $(F_{y_t}^{(3)}, F_{y_t}^{(4)})$ and (b) switching force product $(F_{y_t}^{(3)} \times F_{y_t}^{(4)})$ for interrupted periodic motions over a range of eccentricity amplitude (e); $L_c = 0.1(mm)$ and $\Omega = 250(\frac{rad}{s})$.

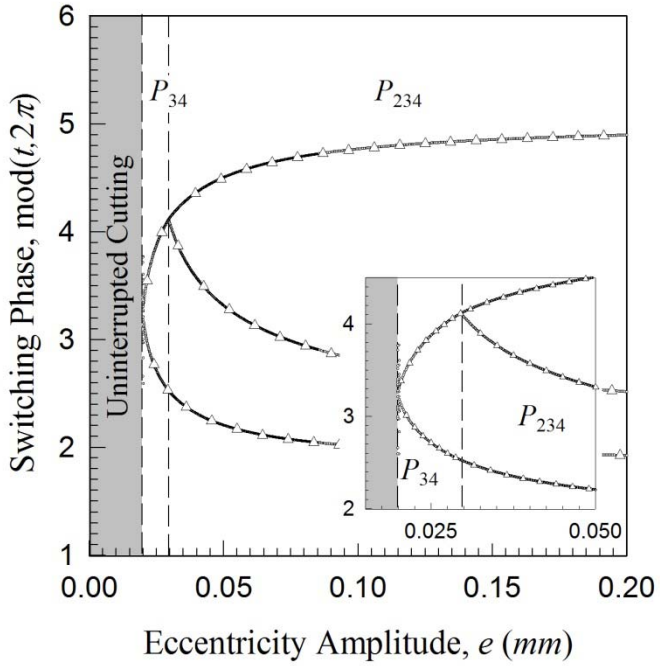

(a)

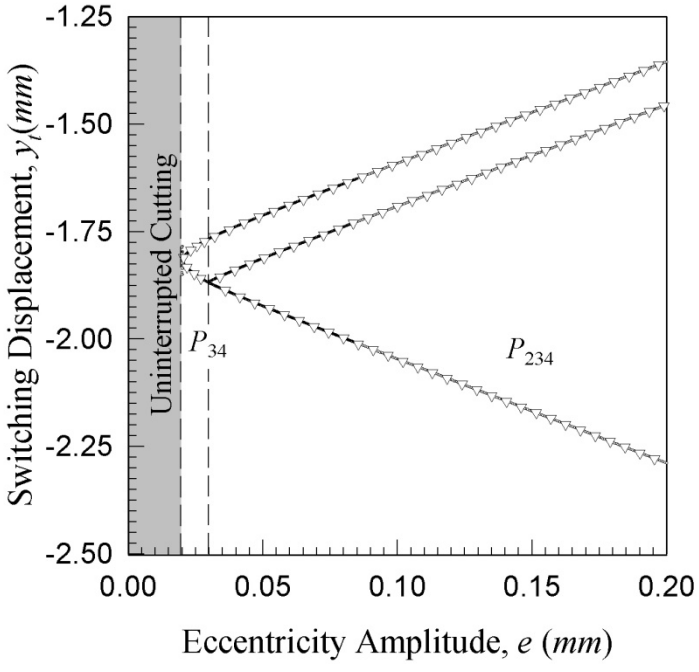

(b)

Fig. 61 Numerical and analytical predictions of (a) switching phase $\mathrm{mod}(t_i, 2\pi)$, (b) switching displacement $(y_t = \tilde{y})$ for interrupted periodic motions over a range of eccentricity amplitudes (e); $L_c = 0.1(mm)$ and $\Omega = 400(\frac{rad}{s})$.

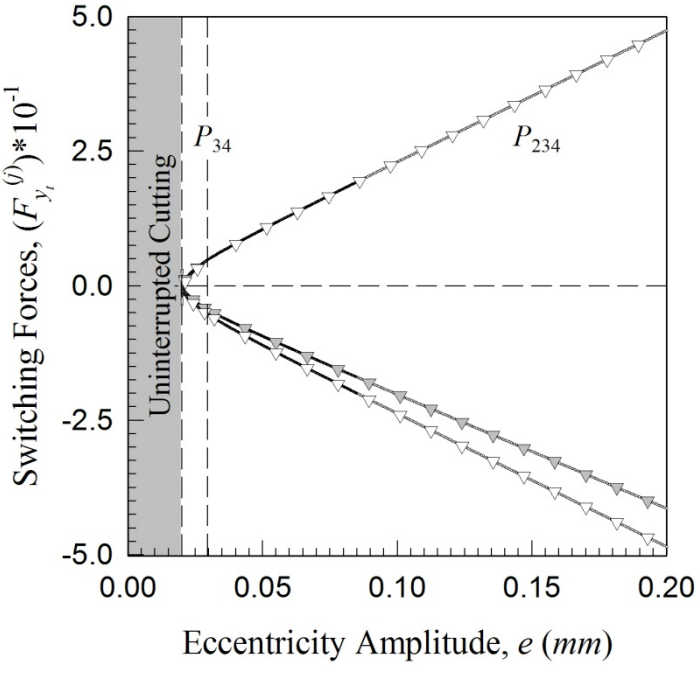

(a)

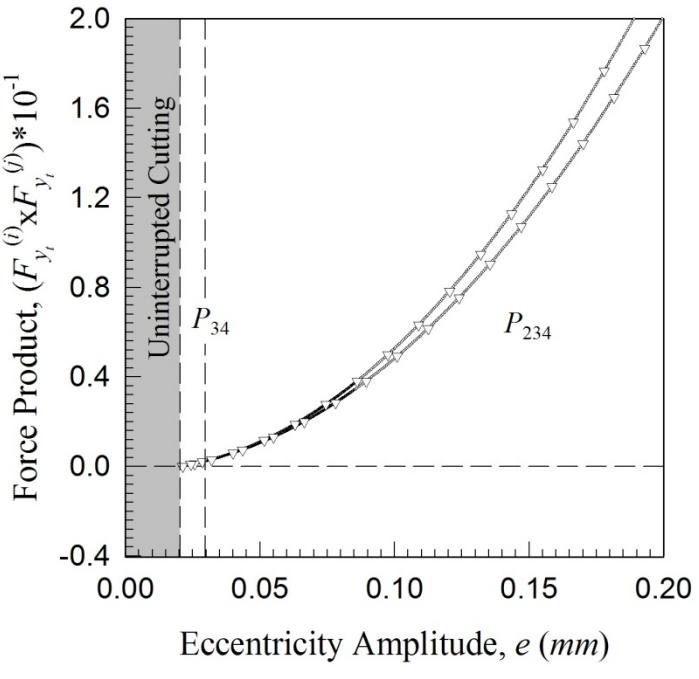

(b)

Fig. 62 Numerical and analytical predictions of (a) switching forces $(F_{y_t}^{(3)}, F_{y_t}^{(4)})$ and (b) switching force product $(F_{y_t}^{(3)} \times F_{y_t}^{(4)})$ for interrupted periodic motions over a range of eccentricity amplitudes (e); $L_c = 0.1(mm)$ and $\Omega = 400(\frac{rad}{s})$.

Observe how the measure switching displacement $(\tilde{y}_i)$ of Fig. 61(b) grows with respect to increasing eccentricity amplitude (e); indeed this is intuitive to linear systems. The validation of the predictions are shown in Fig. 62(a,b) by the switching forces and switching force products versus eccentricity amplitude (e). Since the force products are shown to be greater than zero over the entire range $e \in [0.0203,\ 0.2000]$ (mm); the motions are experimentally and theoretically verified. The change of eccentricity frequency seems to affect the magnitude of the switching characteristics and the grazing bifurcation of chip/tool friction boundary is notably lower in amplitude for the higher eccentricity frequency $e \approx 0.0203$ for $\Omega = 400$ $(\frac{rad}{s})$ and $e \approx 0.0805$ for $\Omega = 250$ $(\frac{rad}{s})$, see Fig. 61 and Fig. 62. The eccentricity frequency (Ω) will be studied in the next section.

Study of Eccentricity Frequency (Ω)

Consider the variation of the motion throughout the range of eccentricity frequency $\Omega \in [0.1915k,\ 1k]$ $(\frac{rad}{s})$ for $e = 0.100$ (mm), see Fig. 63 and Fig. 64. The switching phase $\mathrm{mod}(t_i, 2\pi)$ and switching displacement $(y_t = \tilde{y}_i)$ versus the eccentricity frequency (Ω) are presented to show the expanding orbit of the motion for the mappings P_{34}: $(0.1910k, 0.1945k]$ $(\frac{rad}{s})$ and P_{234}: $(0.1945k, 1k]$ $(\frac{rad}{s})$, see Fig. 63(a,b); respectively. Observe how the measure switching displacement $(y_t = \tilde{y}_i)$ of Fig. 63(b) grows with respect to increasing eccentricity frequency (Ω). The validation of the predictions are shown in Fig. 64(a,b) by the switching forces and switching force products versus eccentricity frequency (Ω). Since the force products are shown to be greater than zero

over the entire range $\Omega \in \left[0.1915k, 1k\right]$ $(\frac{rad}{s})$; the motions are numerically and theoretically verified.

The grazing bifurcation of the chip/tool friction boundary is noted to appear near $\Omega = 0.1915k$ $(\frac{rad}{s})$. By observation the reduction of amplitude between the natural frequency peaks may lead to pure cutting motions if the excitation of the system is reduced. Such an occurrence is discovered by reducing the eccentricity amplitude for the next frequency range. Consider the variation of the motion throughout the range of eccentricity frequency $\Omega \in \left[0.2210k, 1k\right](\frac{rad}{s})$ for $e = 0.050\ (mm)$, see Fig. 65 and Fig. 66. The switching phase $\text{mod}(t_i, 2\pi)$ and switching displacement $(y_t = \tilde{y}_i)$ versus the eccentricity frequency (Ω) are presented to show the expanding orbit of the motion for the mappings $P_{(034)^n} \in \left[0.2210k,\ 0.2315k\right)$ $(\frac{rad}{s})$, $P_{34} \in \left(0.2315k,\ 0.2773k\right]$ $(\frac{rad}{s})$, $P_{(034)^n} \in \left(0.2773k, 0.2860k\right]$ $(\frac{rad}{s})$, $P_{34} \in \left(0.3660k, 0.3780k\right]$ $(\frac{rad}{s})$, $P_{234} \in \left(0.3780k,\ 1k\right]$ $(\frac{rad}{s})$; see Fig. 65(a,b); respectively.

The span of eccentricity frequency $\Omega \in \left(0.2860k,\ 0.3660k\right]$ $(\frac{rad}{s})$ has no motion interacting with the chip/tool friction boundary. Observe how the switching displacement $(y_t = \tilde{y}_i)$ of Fig. 65(b) grows with respect to increasing eccentricity frequency (Ω). The validation of the predictions are shown in Fig. 66(a,b) by the switching forces and switching force products versus eccentricity frequency (Ω). Since the force products are shown to be greater than zero over the range $\Omega \in \left[0.3660k, 1k\right]$ $(\frac{rad}{s})$; the motions numerically verify the theory. However, the grazing and

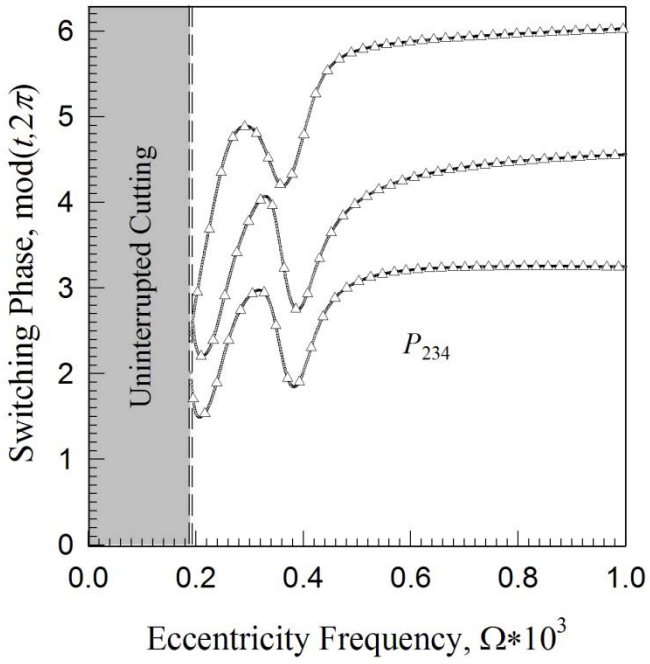

(a)

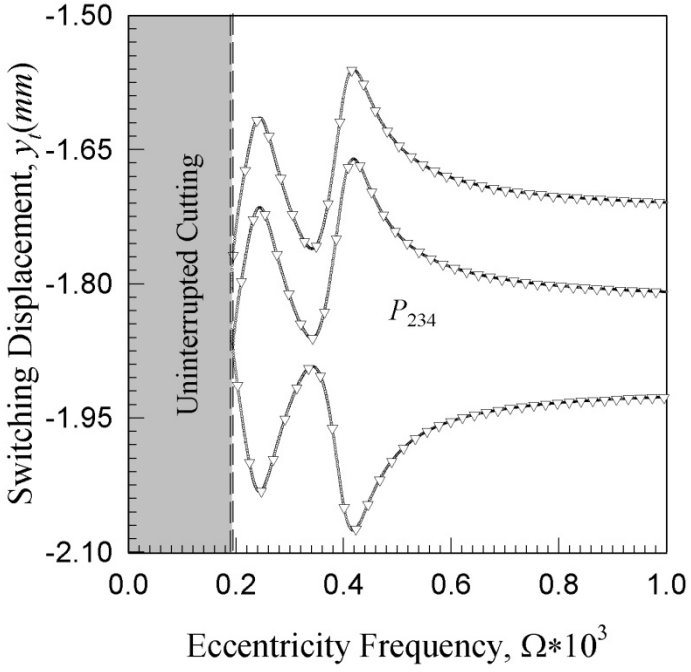

(b)

Fig. 63 Numerical and analytical predictions of (a) switching phase $\mathrm{mod}(t_i, 2\pi)$, (b) switching displacement $(y_t = \tilde{y})$ for interrupted periodic motions over a range of eccentricity frequencies (Ω); $L_c = 0.1(mm)$ and $e = 0.1(mm)$.

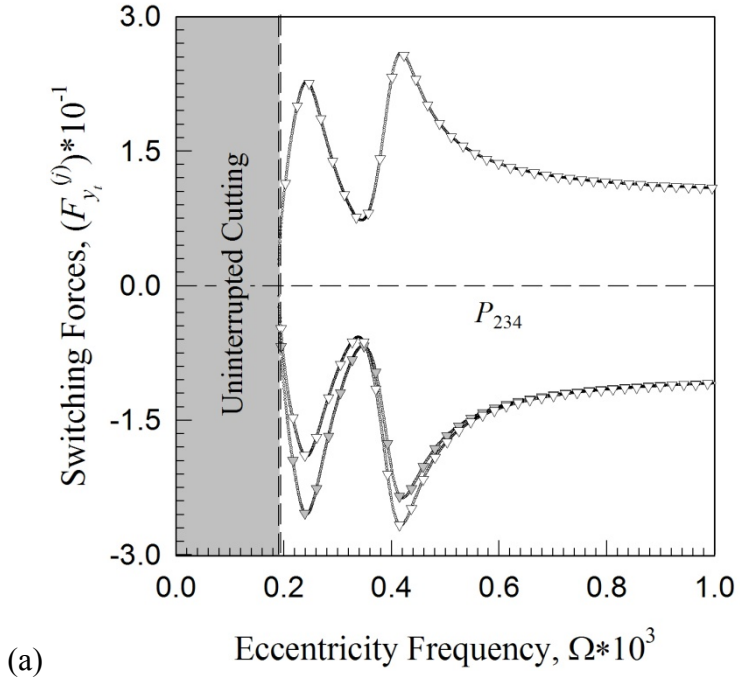

(a)

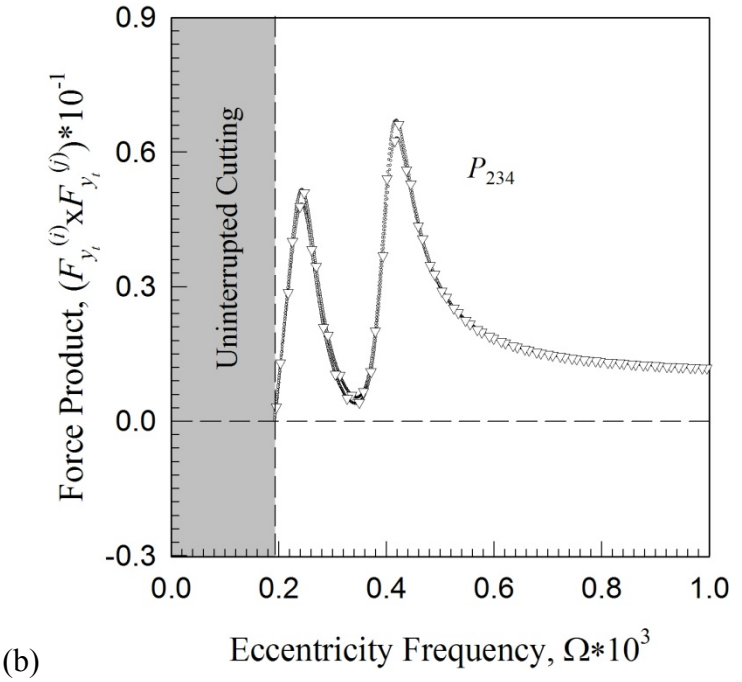

(b)

Fig. 64 Numerical and analytical predictions of (a) switching forces $(F_{y_t}^{(3)}, F_{y_t}^{(4)})$ and (b) switching force product $(F_{y_t}^{(3)} \times F_{y_t}^{(4)})$ for interrupted periodic motions over a range of eccentricity frequencies (Ω); $L_c = 0.1(mm)$ and $e = 0.1(mm)$.

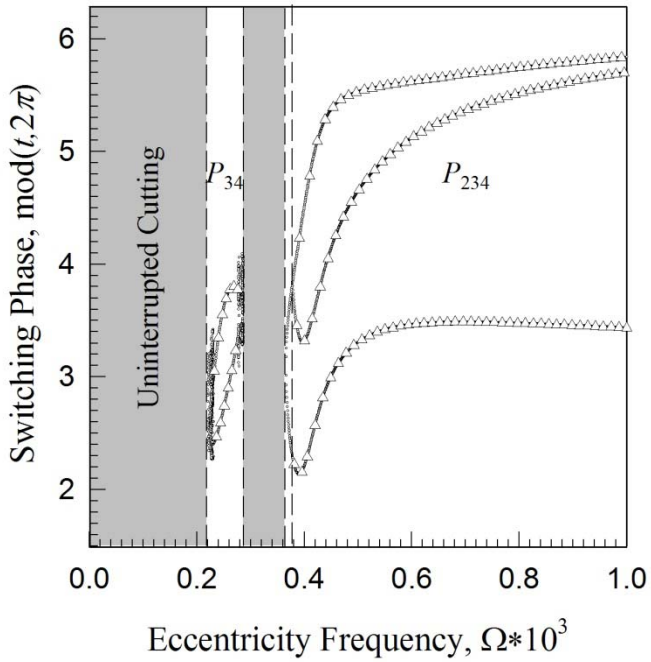

(a)

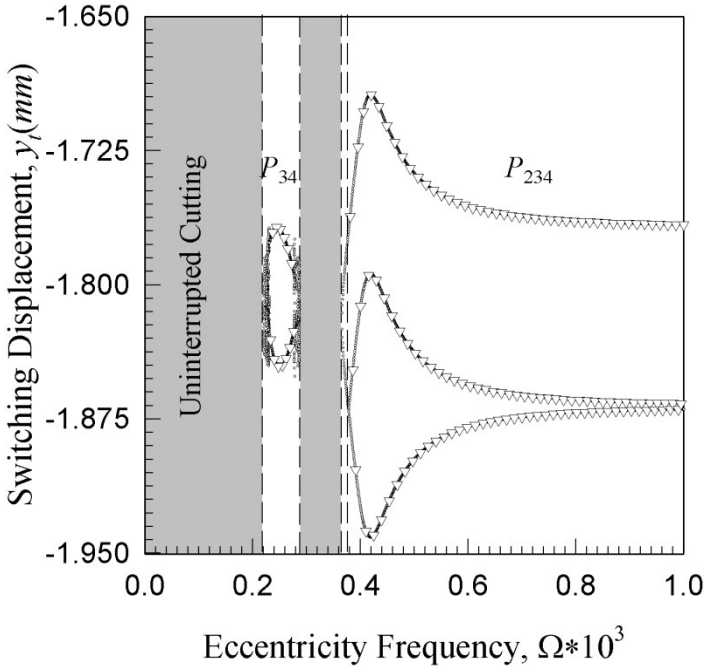

(b)

Fig. 65 Numerical and analytical predictions of (a) switching phase $\mathrm{mod}(t_i, 2\pi)$, (b) switching displacement $(y_t = \tilde{y})$ for interrupted periodic motions over a range of eccentricity frequencies (Ω); $L_c = 0.1(mm)$ and $e = 0.05(mm)$.

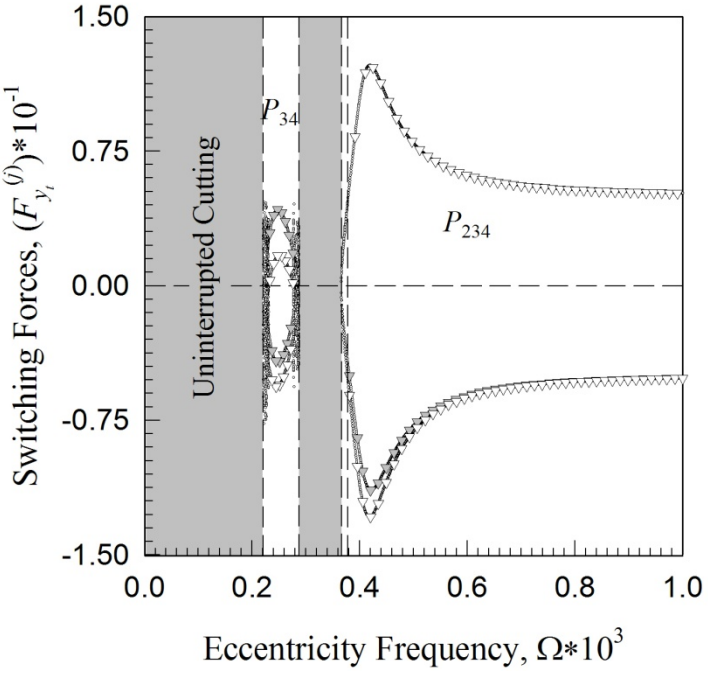

(a)

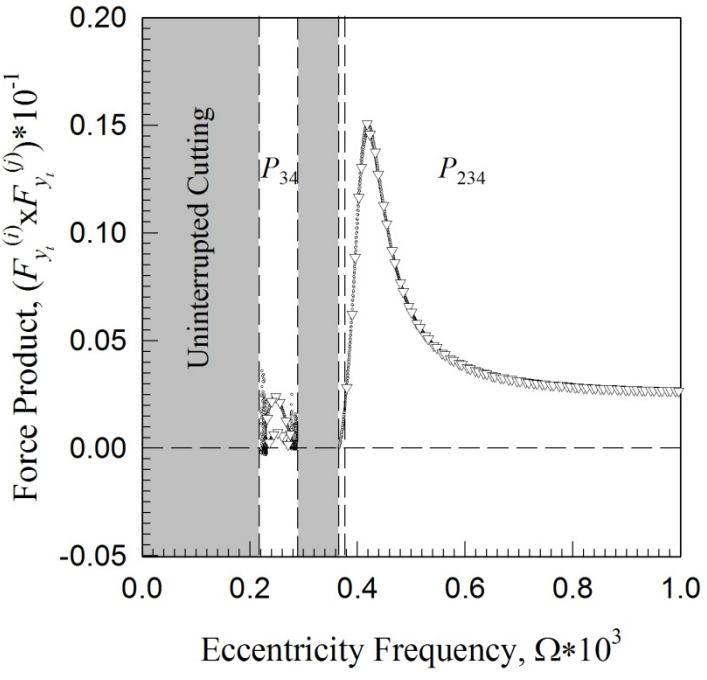

(b)

Fig. 66 Numerical and analytical predictions of (a) switching forces $(F_{y_t}^{(3)}, F_{y_t}^{(4)})$ and (b) switching force product $(F_{y_t}^{(3)} \times F_{y_t}^{(4)})$ for interrupted periodic motions over a range of eccentricity frequencies (Ω); $L_c = 0.1(mm)$ and $e = 0.05(mm)$.

chip seizure bifurcations occur in the neighborhood of $\Omega \approx 0.2210k$, $0.2860k$ and $0.3660k$ $(\frac{rad}{s})$.

Depending on the excitation amplitude (e) and frequency (Ω) of the external or self excitation, the *parameter boundary* of stick-slip (chip seizure-cutting motion) becomes bifurcated at $\Omega \approx 0.2210k$ $(\frac{rad}{s})$ and $0.2860k$ $(\frac{rad}{s})$ for $e = 0.050$ (mm) and $\Omega \approx 0.1910k$ $(\frac{rad}{s})$ for $e = 0.100$ (mm). A parameter boundary is a type of boundary defined in parameter space (dynamical system parameters) which defines the transition point from one type of motion to another. In this case the parameter boundary describes the transition from pure cutting motion to stick-slip motion with respect to eccentricity frequency and amplitude (Ω, A), respectively. This can be observed in the results presented in Fig. 63, Fig. 64, Fig. 65 and Fig. 66. The chip vanishing *parameter boundary* is also shown in these results at $\Omega \approx 0.3780k$ $(\frac{rad}{s})$ for $e = 0.050$ (mm) and $\Omega \approx 0.1945k$ $(\frac{rad}{s})$ for $e = 0.100$ (mm). A range of the chip velocity (ΩV) will be studied in the next section.

Study of Chip Velocity (ΩV)

Consider the variation of the motion throughout the range of chip velocity $\Omega V \in [0.00, 51.41]$ $(\frac{mm}{s})$ for $e = 0.100$ (mm), see Fig. 67 and Fig. 68. The switching phase $\mathrm{mod}(t_i, 2\pi)$ and switching displacement $(y_t = \tilde{y}_i)$ versus the chip velocity (ΩV) are presented to show the expanding orbit of the motion for the mappings P_{234}: $(0.00, 48.90]$ $(\frac{mm}{s})$ and P_{34}: $(48.90, 51.41]$ $(\frac{mm}{s})$, see Fig. 67(a,b); respectively. Observe

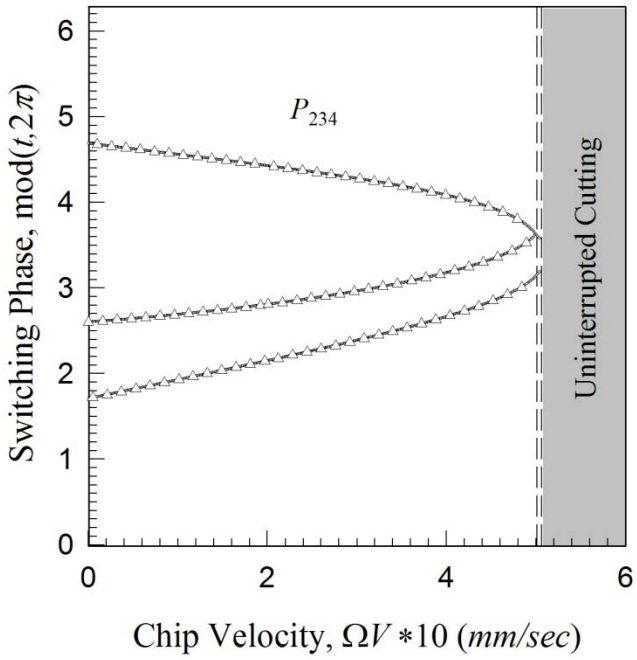

(a)

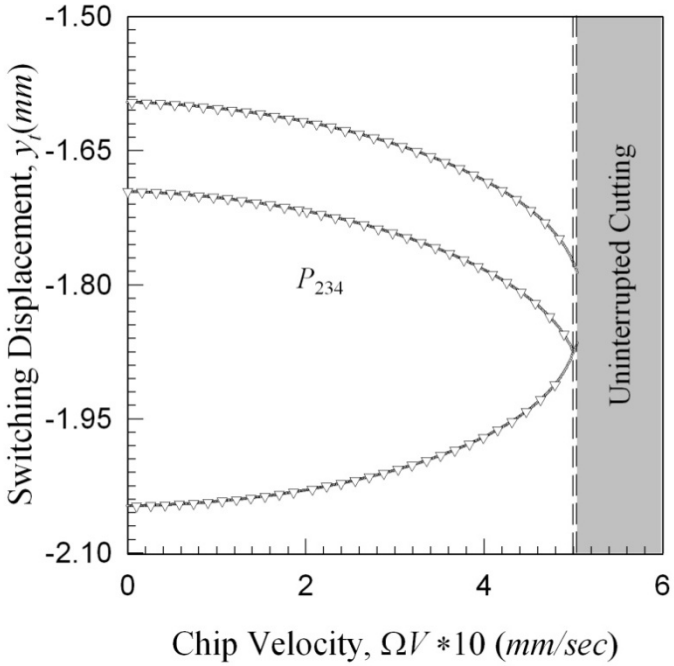

(b)

Fig. 67 Numerical and analytical predictions of (a) switching phase $\mathrm{mod}(t_i, 2\pi)$, (b) switching displacement $(y_t = \tilde{y})$ for interrupted periodic motions over a range of chip velocity (ΩV); $L_c = 0.1(mm)$ and $\Omega = 250(\frac{rad}{s})$.

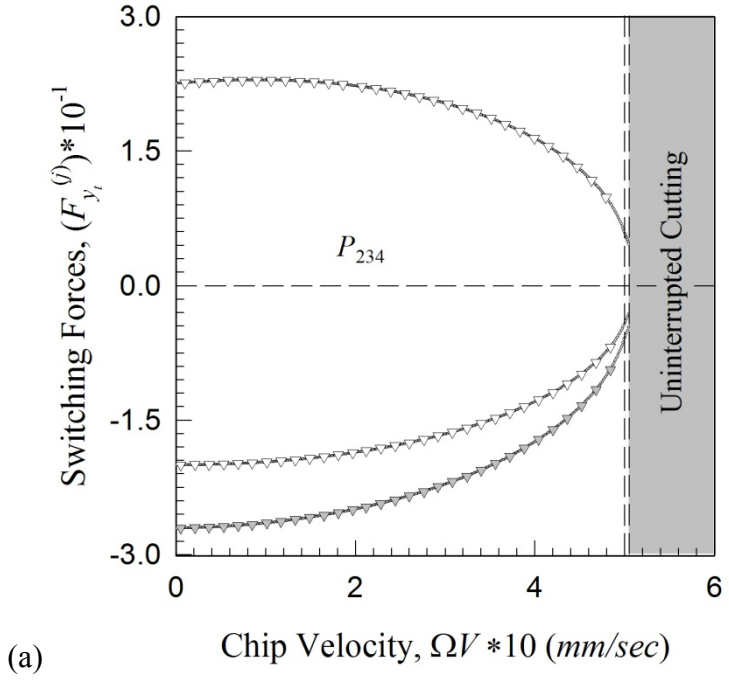

(a)

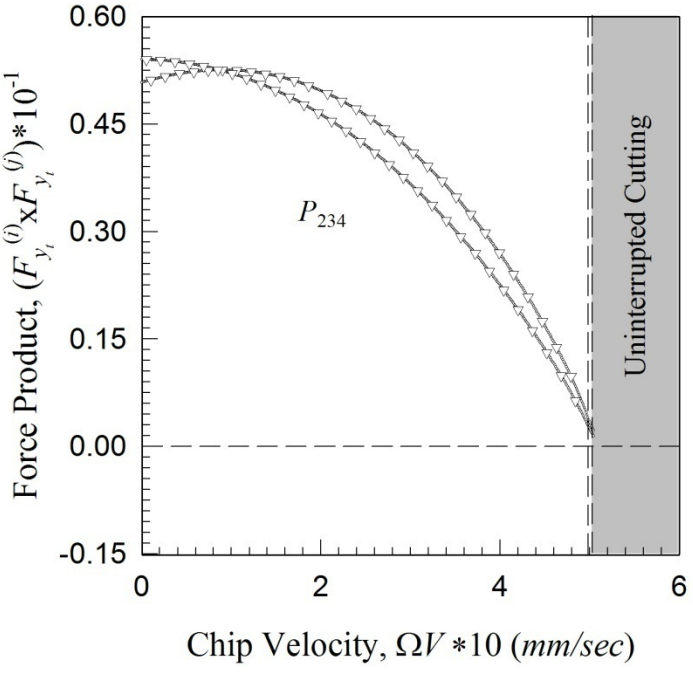

(b)

Fig. 68 Numerical and analytical predictions of (a) switching forces $(F_{y_t}^{(3)}, F_{y_t}^{(4)})$ and (b) switching force product $(F_{y_t}^{(3)} \times F_{y_t}^{(4)})$ for interrupted periodic motions over a range of chip velocity (ΩV); $L_c = 0.1(mm)$ and $\Omega = 250(\frac{rad}{s})$.

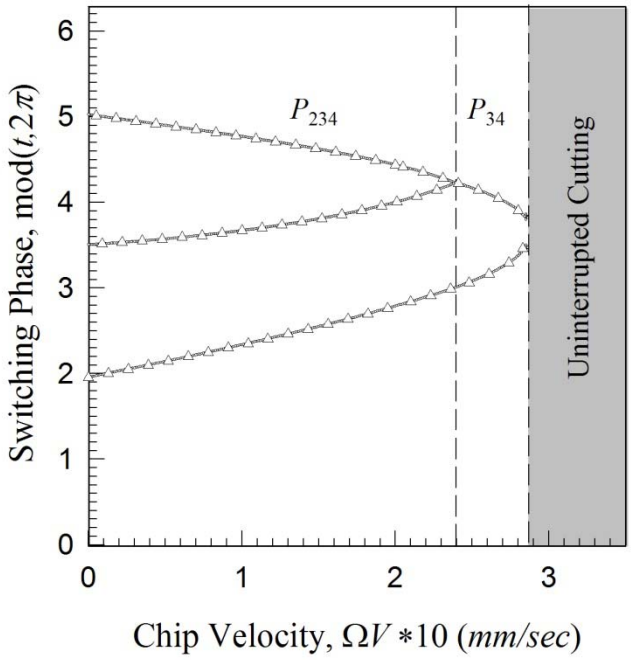

(a)

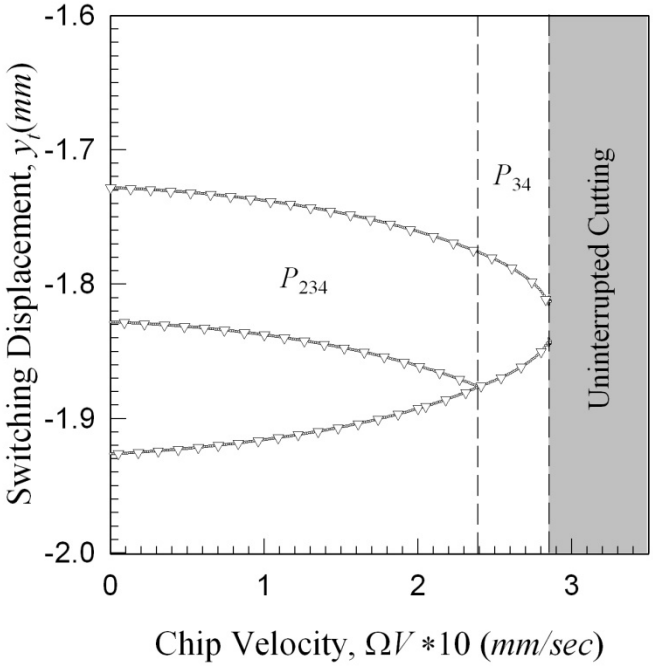

(b)

Fig. 69 Numerical and analytical predictions of (a) switching phase $\mathrm{mod}(t_i, 2\pi)$, (b) switching displacement $(y_t = \tilde{y})$ for interrupted periodic motions over a range of chip velocity (ΩV); $L_c = 0.1(mm)$ and $\Omega = 340(\frac{rad}{s})$.

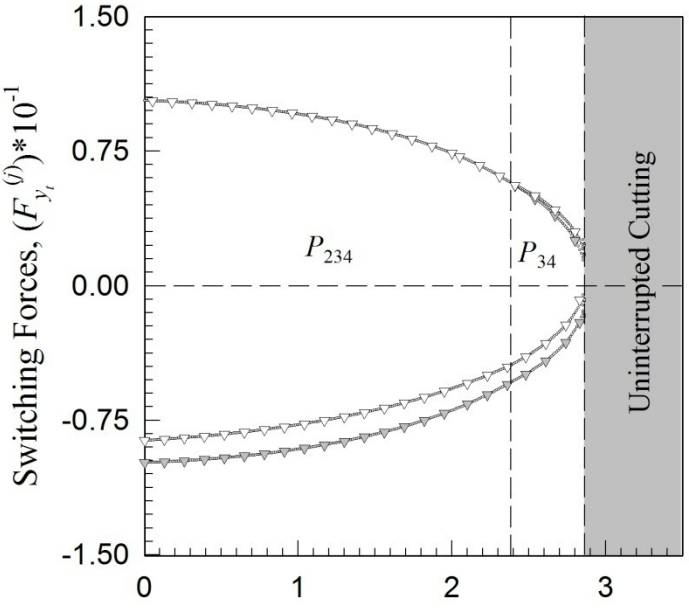

(a)

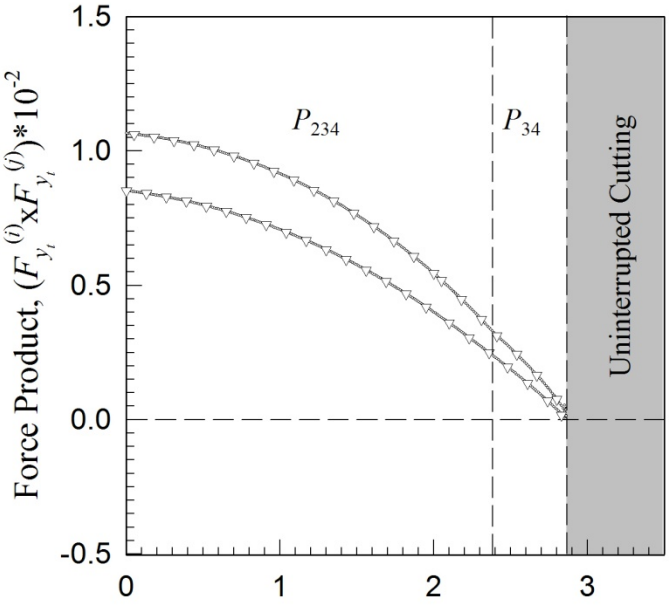

(b)

Fig. 70 Numerical and analytical predictions of (a) switching forces $(F_{y_t}^{(3)}, F_{y_t}^{(4)})$ and (b) switching force product $(F_{y_t}^{(3)} \times F_{y_t}^{(4)})$ for interrupted periodic motions over a range of chip velocity (ΩV); $L_c = 0.1(mm)$ and $\Omega = 340(\frac{rad}{s})$.

how the measure switching displacement $(\tilde{y}_i)$ of Fig. 67(b) decreases with respect to increasing chip velocity (ΩV). The validation of the predictions are shown in Fig. 68(a,b) by the switching forces and switching force products versus chip velocity (ΩV). Since the force products are shown to be greater than zero over the entire range $\Omega V \in [0.00, 51.41](\frac{mm}{s})$; the passability of the motions are numerically and theoretically verified.

Consider the variation of the motion throughout the range of chip velocity $\Omega V \in [0.00, 28.62]$ $(\frac{mm}{s})$ for $\Omega = 340$ $(\frac{rad}{s})$, see Fig. 69 and Fig. 70. The switching phase $\mathrm{mod}(t_i, 2\pi)$ and switching displacement $(\tilde{y}_i)$ versus the chip velocity (ΩV) are presented to show the expanding orbit of the motion for the mappings P_{234}: $(0.00, 23.90]$ $(\frac{mm}{s})$ and P_{34}: $(23.90, 28.62]$ $(\frac{mm}{s})$, see Fig. 69(a,b); respectively. Observe how the measure switching displacement $(y_t = \tilde{y}_i)$ of Fig. 69(b) also decreases with respect to increasing chip velocity (ΩV). The validation of the predictions are shown in Fig. 70(a,b) by the switching forces and switching force products versus chip velocity (ΩV). Since the force products are shown to be greater than zero over the entire range $\Omega V \in [0.00, 28.62](\frac{mm}{s})$; the passability of the motions are numerically and theoretically verified.

The velocity range was similarly investigated with stochastic and deterministic cutting resistances exhibit similar distributions, but the stochastic input yields more chaotic results Wiercigroch and Cheng [24]. The onset of seizure is denoted by a critical cutting speed which is dependent on a force measurement with respect to the real and

apparent contact area of the interfacing surfaces Gekonade and Subramanian [58]. This also implies the *parameter boundary* of chip seizure/grazing bifurcation and chip vanishing varies with respect to chip velocity (ΩV). Such a chip seizure/grazing bifurcation *parameter boundary*, regarding the above results, is defined at $\Omega V \approx 51.41$ $(\frac{mm}{s})$ for $\Omega = 250$ $(\frac{rad}{s})$ and $\Omega V \approx 28.62$ $(\frac{mm}{s})$ for $\Omega = 340$ $(\frac{rad}{s})$. The chip/tool friction coefficient (μ) will be studied in the next section.

Study of Friction Coefficient (μ)

Consider the variation of the motion throughout the range of chip/tool friction coefficient $\mu \in [0.0, 3.0]$ for $e = 0.100$ (mm) and $\Omega = 250$ $(\frac{rad}{s})$, see Fig. 71 and Fig. 72. The switching phase $\text{mod}(t_i, 2\pi)$ and switching displacement $(y_t = \tilde{y}_i)$ versus the chip/tool friction coefficient (μ) are presented to show the expanding orbit of the motion for the mappings $P_{234} : (0.0, 3.0]$, see Fig. 71(a,b); respectively. Observe how the measure switching displacement $(y_t = \tilde{y}_i)$ of Fig. 71(b) grows with respect to increasing chip/tool friction coefficient (μ). The validation of the predictions are shown in Fig. 72(a,b) by the switching forces and switching force products versus chip/tool friction coefficient (μ). Since the force products are shown to be greater than zero over the entire range $\mu \in [0.0, 3.0]$; the passability of the motions are numerically and theoretically verified.

The chip/tool friction coefficient seems to only slightly increase the force product and has no evident trend toward stick-slip in a reasonable range of the friction coefficient. The friction coefficient range associated with interrupted machining range from 0.33 to 2 Chandrasekaran and Thoors [54]. Consider the variation of the

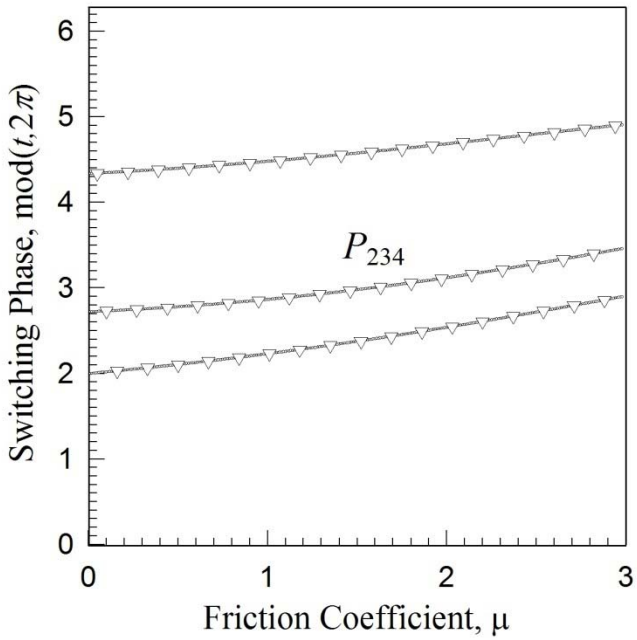

(a)

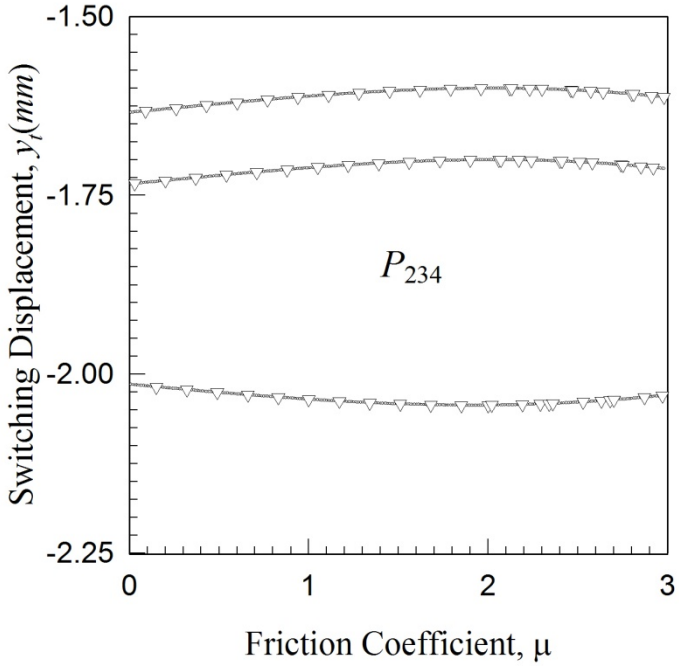

(b)

Fig. 71 Numerical and analytical predictions of (a) switching phase $\mathrm{mod}(t_i, 2\pi)$, (b) switching displacement $(y_t = \tilde{y})$ for interrupted periodic motions over a range of chip friction coefficients (μ); $L_c = 0.1(mm)$ and $\Omega = 250(\frac{rad}{s})$.

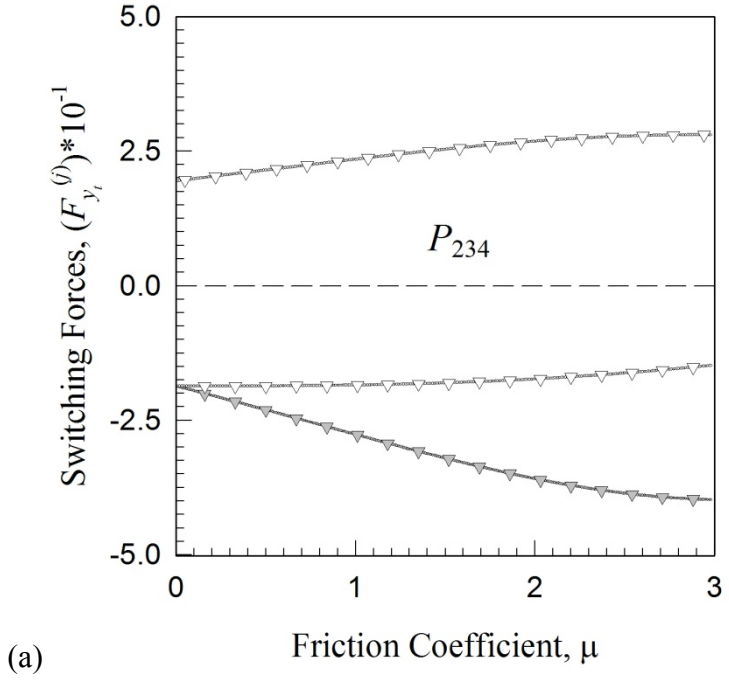

(a)

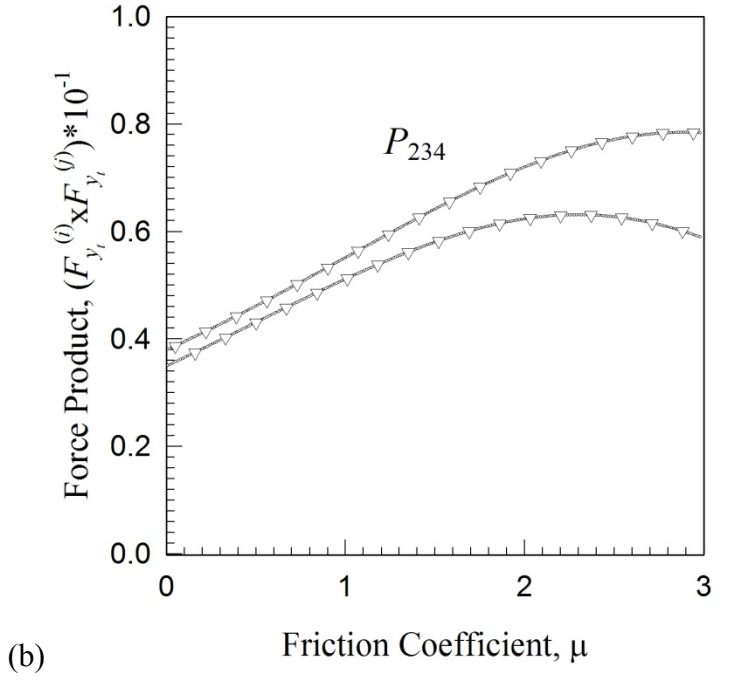

(b)

Fig. 72 Numerical and analytical predictions of (a) switching forces $(F_{y_t}^{(3)}, F_{y_t}^{(4)})$ and (b) switching force product $(F_{y_t}^{(3)} \times F_{y_t}^{(4)})$ for interrupted periodic motions over a range of chip friction coefficients (μ); $L_c = 0.1(mm)$ and $\Omega = 250(\frac{rad}{s})$.

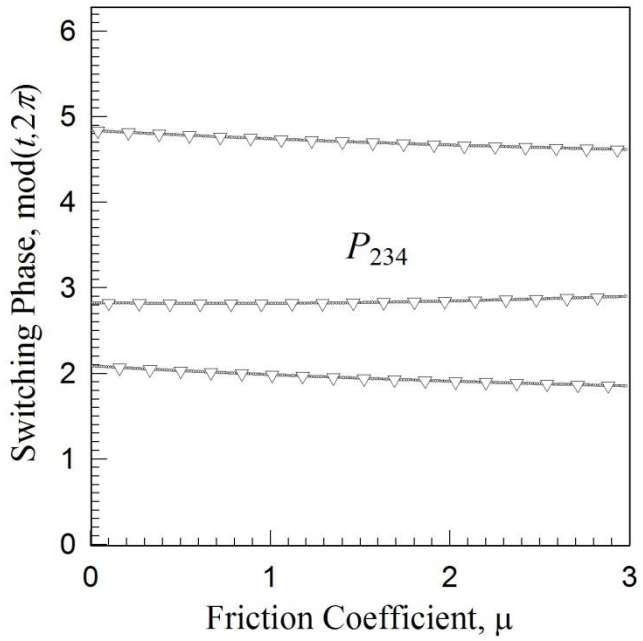

(a)

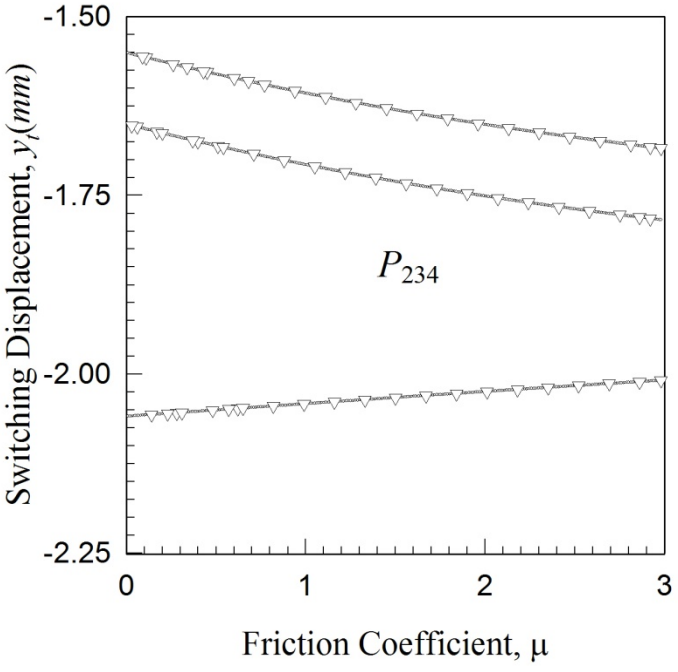

(b)

Fig. 73 Numerical and analytical predictions of (a) switching phase $\mathrm{mod}(t_i, 2\pi)$, (b) switching displacement $(y_t = \tilde{y})$ for interrupted periodic motions over a range of chip friction coefficients (μ); $L_c = 0.1(mm)$ and $\Omega = 400(\frac{rad}{s})$.

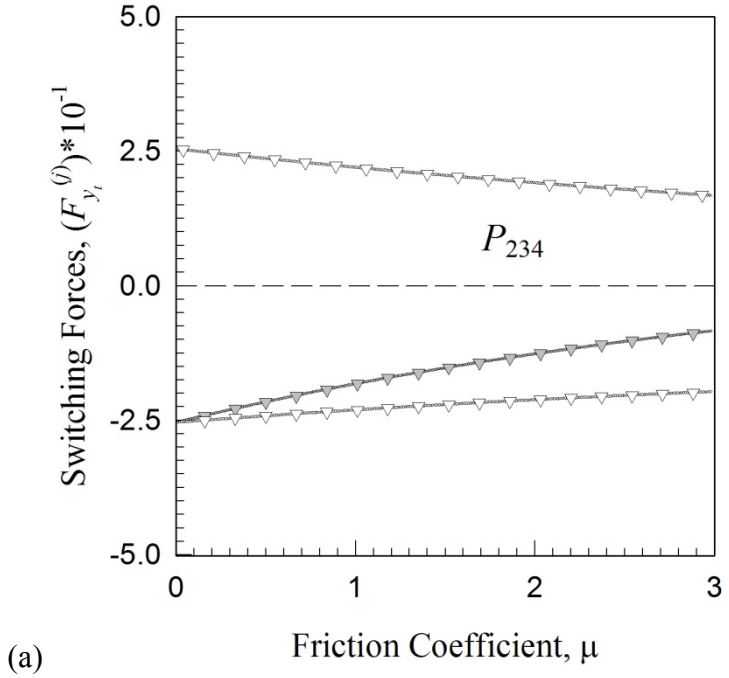

(a)

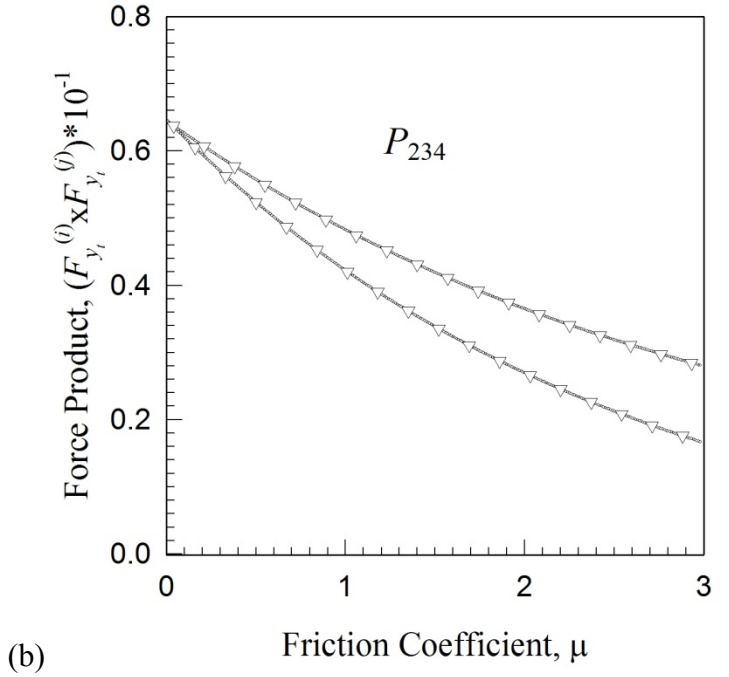

(b)

Fig. 74 Numerical and analytical predictions of (a) switching forces $(F_{y_t}^{(3)}, F_{y_t}^{(4)})$ and (b) switching force product $(F_{y_t}^{(3)} \times F_{y_t}^{(4)})$ for interrupted periodic motions over a range of chip friction coefficients (μ); $L_c = 0.1(mm)$ and $\Omega = 400(\frac{rad}{s})$.

motion throughout the range of chip/tool friction coefficient $\mu \in [0.0, 3.0]$ for $e = 0.100$ (mm) and $\Omega = 400$ $(\frac{rad}{s})$, see Fig. 73 and Fig. 74. The switching phase $\text{mod}(t_i, 2\pi)$ and switching displacement $(\tilde{y}_i)$ versus the chip/tool friction coefficient (μ) are presented to show the expanding orbit of the motion for the mappings $P_{234} : (0.0, 3.0]$, see Fig. 73(a,b); respectively. Observe how the measure switching displacement $(\tilde{y}_i)$ of Fig. 73(b) grows with respect to increasing chip/tool friction coefficient (μ).

The validation of the predictions are shown in Fig. 74(a,b) by the switching forces and switching force products versus chip/tool friction coefficient (μ). Since the force products are shown to be greater than zero over the entire range $\mu \in [0.0, 3.0]$; the passability of the motions are numerically and theoretically verified. Although, the force products remain greater than zero, the trend is towards a possibility of the stick-slip for $\Omega = 400$ $(\frac{rad}{s})$ which is quite different from the results for $\Omega = 250$ $(\frac{rad}{s})$. This implies a *parameter boundary* for the chip/tool friction coefficient (μ) and eccentricity frequency (Ω), but the current operating conditions do not exhibit such a boundary. Perhaps studying the chip/tool friction coefficient (μ) at a higher eccentricity frequency (Ω) would reveal this boundary. The chip stiffness (k_2) will be studied in the next section.

Study of Chip Stiffness (k_2)

Consider the variation of the motion throughout the range of chip stiffness coefficient $k_2 \in [0, 500k]$ $(\frac{N}{mm})$ for $e = 0.100$ (mm) and $\Omega = 250$ $(\frac{rad}{s})$, see Fig. 75. The switching

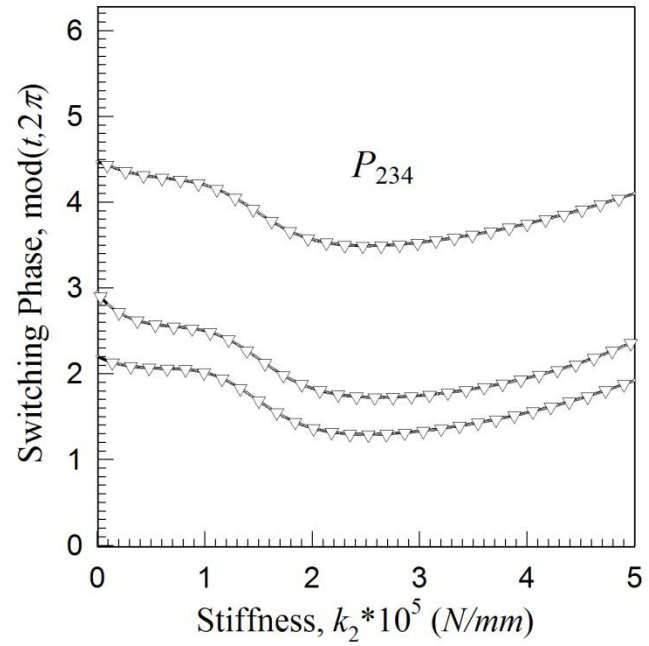

(a)

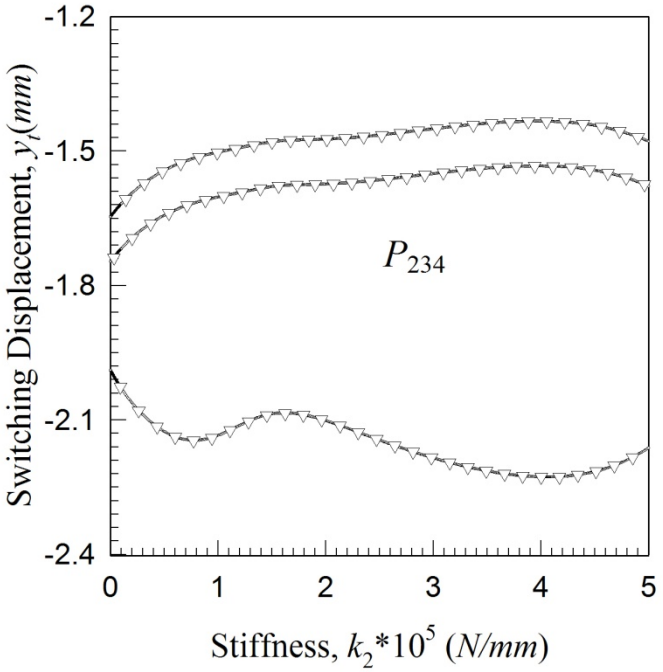

(b)

Fig. 75 Numerical and analytical predictions of (a) switching phase $\mathrm{mod}(t_i, 2\pi)$, (b) switching displacement $(y_t = \tilde{y})$ for interrupted periodic motions over a range of chip stiffness coefficients (k_2); $L_c = 0.1(mm)$ and $\Omega = 250(\frac{rad}{s})$.

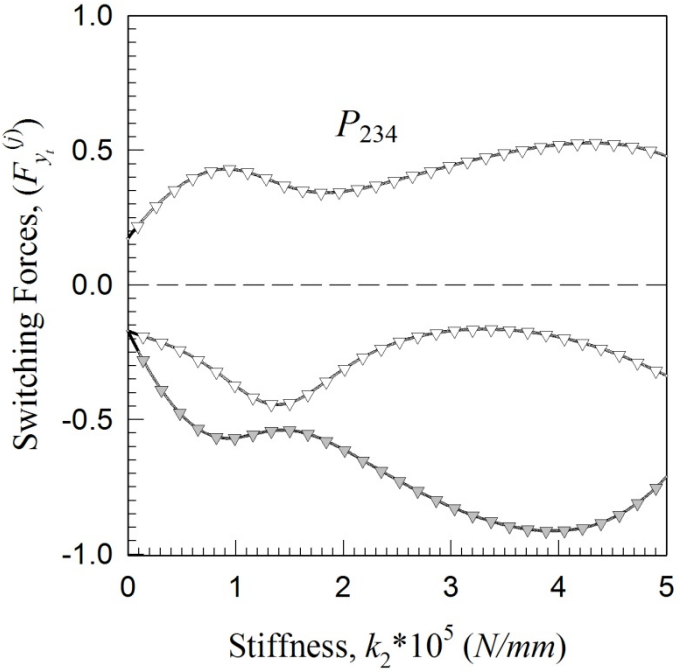

(a)

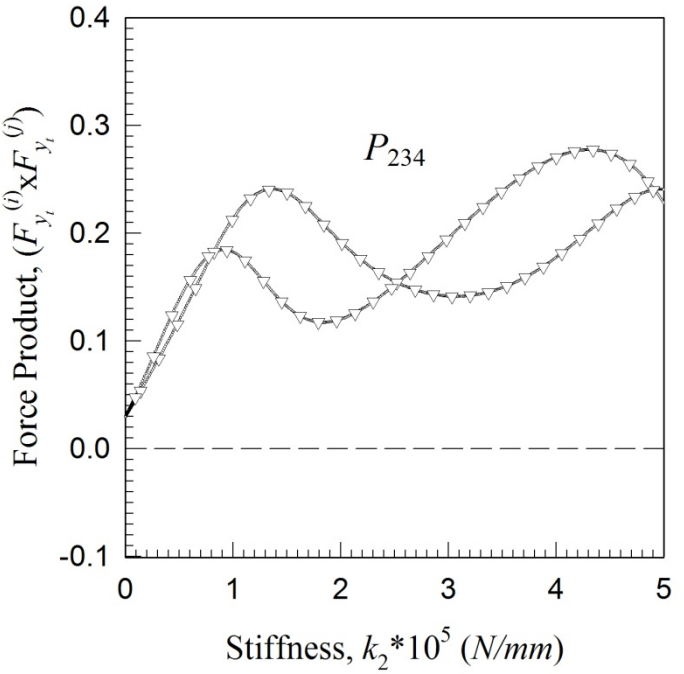

(b)

Fig. 76 Numerical and analytical predictions of (a) switching forces $(F_{y_t}^{(3)}, F_{y_t}^{(4)})$ and (b) switching force product $(F_{y_t}^{(3)} \times F_{y_t}^{(4)})$ for interrupted periodic motions over a range of chip stiffness coefficients (k_2); $L_c = 0.1(mm)$ and $\Omega = 250(\frac{rad}{s})$.

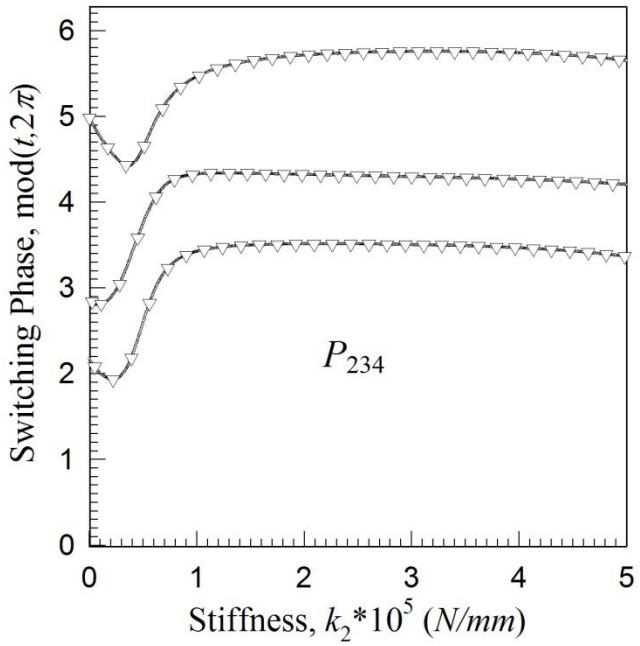

(a)

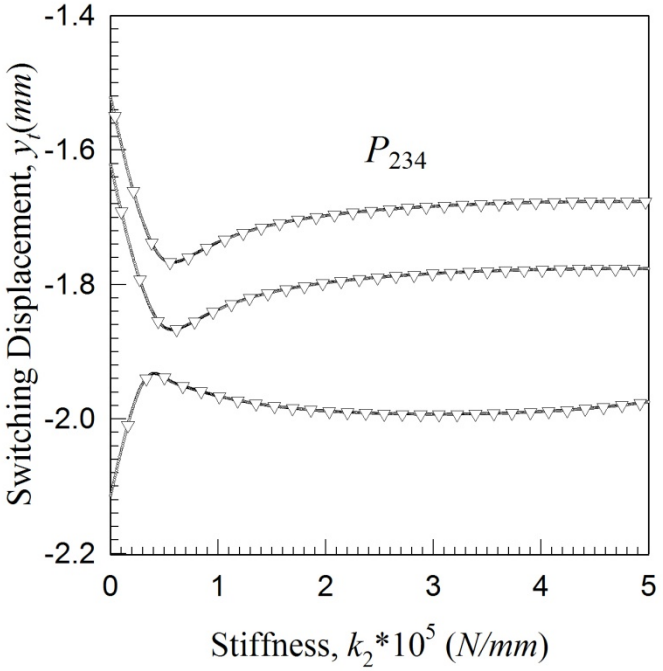

(b)

Fig. 77 Numerical and analytical predictions of (a) switching phase $\mathrm{mod}(t_i, 2\pi)$, (b) switching displacement $(y_t = \tilde{y})$ for interrupted periodic motions over a range of chip stiffness coefficients (k_2); $L_c = 0.1(mm)$ and $\Omega = 400(\frac{rad}{s})$.

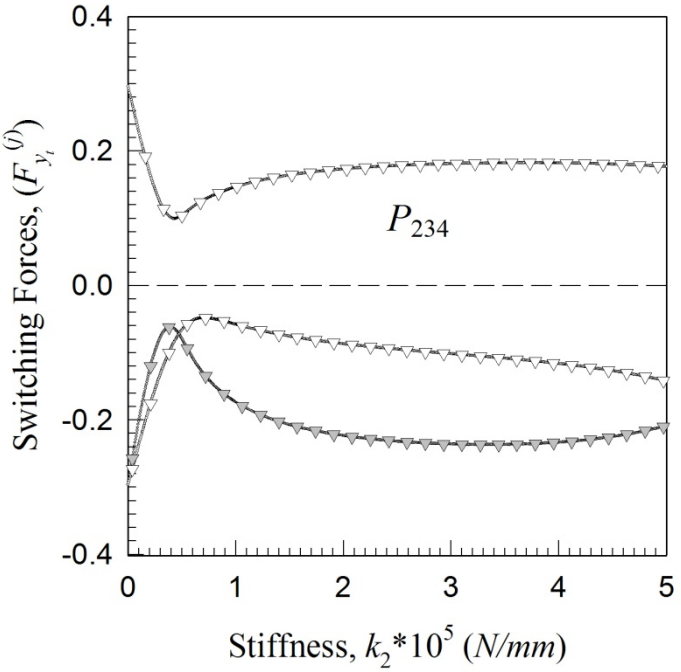

(a)

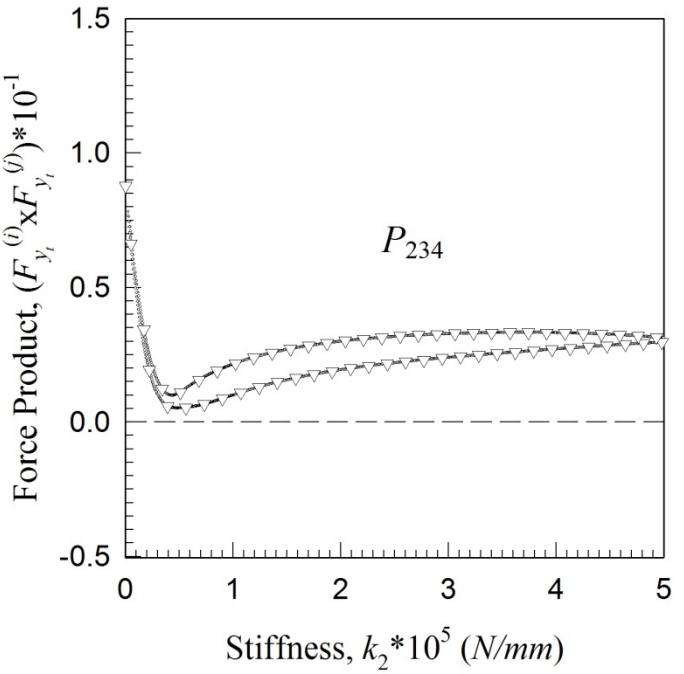

(b)

Fig. 78 Numerical and analytical predictions of (a) switching forces $(F_{y_t}^{(3)}, F_{y_t}^{(4)})$ and (b) switching force product $(F_{y_t}^{(3)} \times F_{y_t}^{(4)})$ for interrupted periodic motions over a range of chip stiffness coefficients (k_2); $L_c = 0.1(mm)$ and $\Omega = 400(\frac{rad}{s})$.

phase $\text{mod}(t_i, 2\pi)$ and switching displacement $(y_t = \tilde{y}_i)$ versus the chip stiffness (k_2) are presented to show the varying orbit of the motion for the mappings P_{234} : $[0,500k]$ $(\frac{N}{mm})$, see Fig. 75(a,b); respectively. Observe how the switching displacement $(\tilde{y}_i)$ of Fig. 75(b) grows with respect to increasing chip stiffness coefficient (k_2). The validation of the predictions are shown in Fig. 76(a,b) by the switching forces and switching force products versus chip stiffness coefficient (k_2). Since the force products are shown to be greater than zero over the entire range $k_2 \in [0,500k]$ $(\frac{N}{mm})$; the passability of the motions are numerically and theoretically verified.

The switching force products express no current concern for the appearance of chip seizure. Consider the variation of the motion throughout the range of chip stiffness coefficient $k_2 \in [0,500k]$ $(\frac{N}{mm})$ for $e = 0.100$ (mm) $\Omega = 400$ $(\frac{rad}{s})$, see Fig. 77. The switching phase $\text{mod}(t_i, 2\pi)$ and switching displacement $(\tilde{y}_i)$ versus the chip stiffness coefficient (k_2) are presented to show the apparent phase shifting or crossing of a single or group of natural frequencies for the mappings P_{234} : $[0,500k]$ $(\frac{N}{mm})$, see Fig. 77(a,b); respectively. This can also be described as the movement of the natural frequencies of the system, due to the ranging of the chip stiffness coefficient (k_2), toward and eventually over, and past the eccentricity frequency (Ω). Indeed the excitation of the system appears to be in part in the $\tilde{x}$-direction, since the $\tilde{y}$-direction switching points (see Fig. 77(b)) are reducing in amplitude.

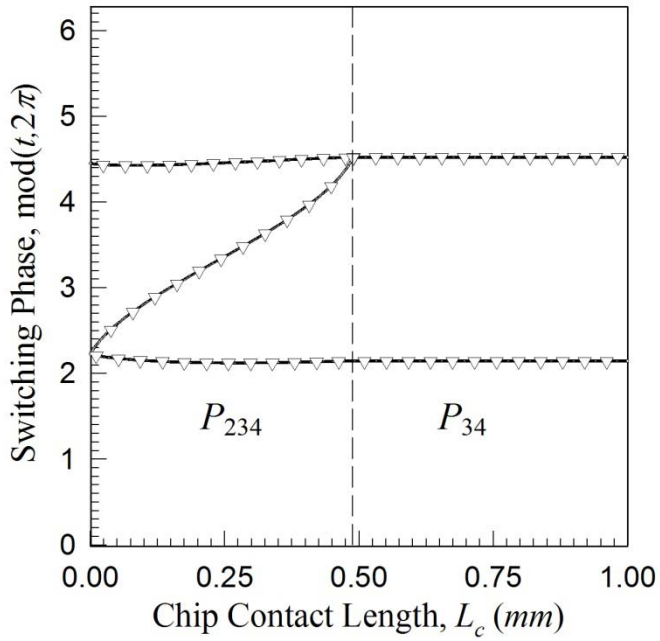

(a)

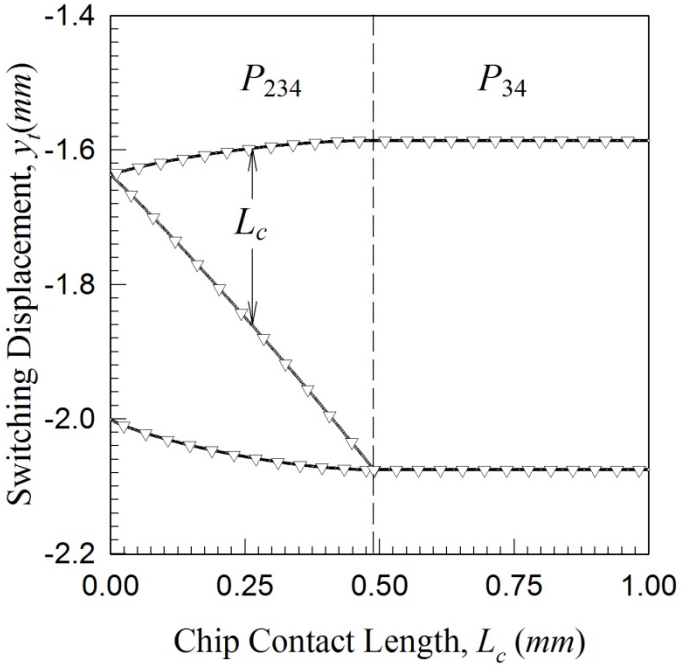

(b)

Fig. 79 Numerical and analytical predictions of (a) switching phase $\mathrm{mod}(t_i, 2\pi)$, (b) switching displacement $(y_t = \tilde{y})$ for interrupted periodic motions over a range of chip contact length (L_c); $e = 0.1(mm)$ and $\Omega = 250(\frac{rad}{s})$.

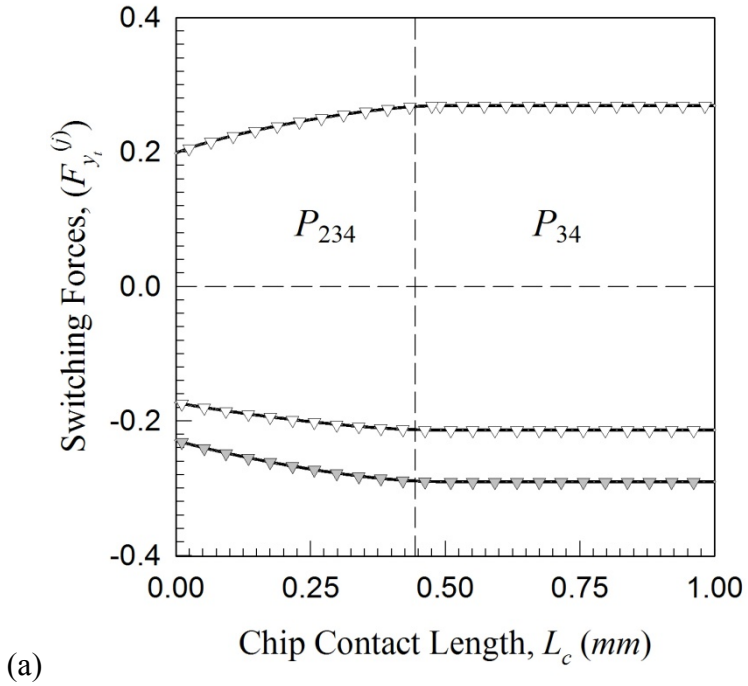

(a)

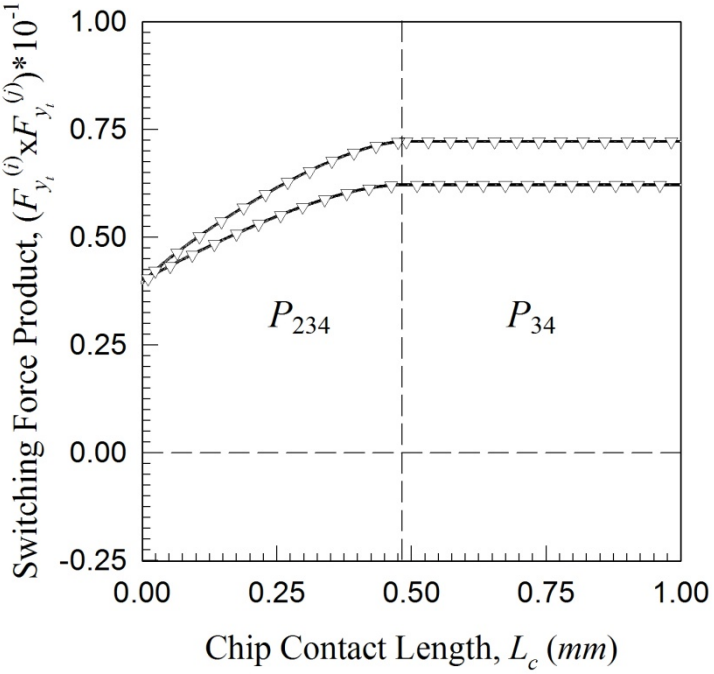

(b)

Fig. 80 Numerical and analytical predictions of (a) switching forces $(F_{y_t}^{(3)}, F_{y_t}^{(4)})$ and (b) switching force product $(F_{y_t}^{(3)} \times F_{y_t}^{(4)})$ for interrupted periodic motions over a range of chip contact length (L_c); $e = 0.1(mm)$ and $\Omega = 250(\frac{rad}{s})$.

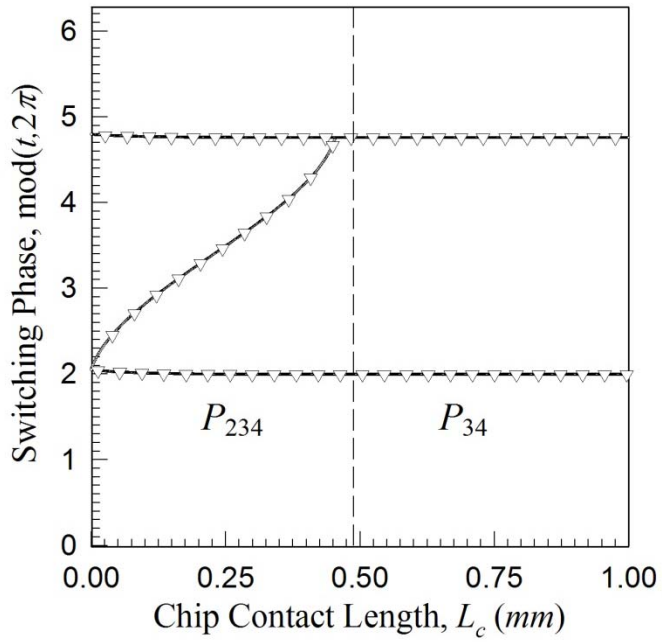

(a)

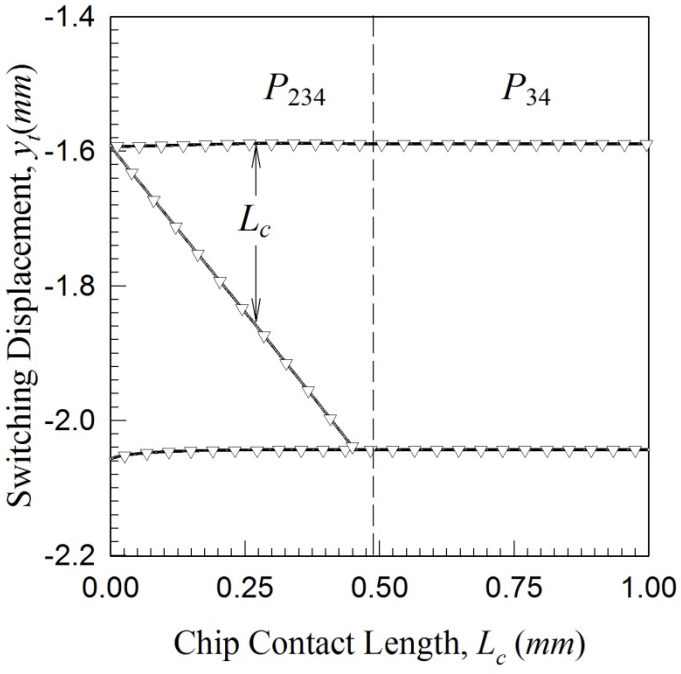

(b)

Fig. 81 Numerical and analytical predictions of (a) switching phase $\mathrm{mod}(t_i, 2\pi)$, (b) switching displacement $(y_t = \tilde{y})$ for interrupted periodic motions over a range of chip contact length (L_c); $e = 0.1(mm)$ and $\Omega = 400(\frac{rad}{s})$.

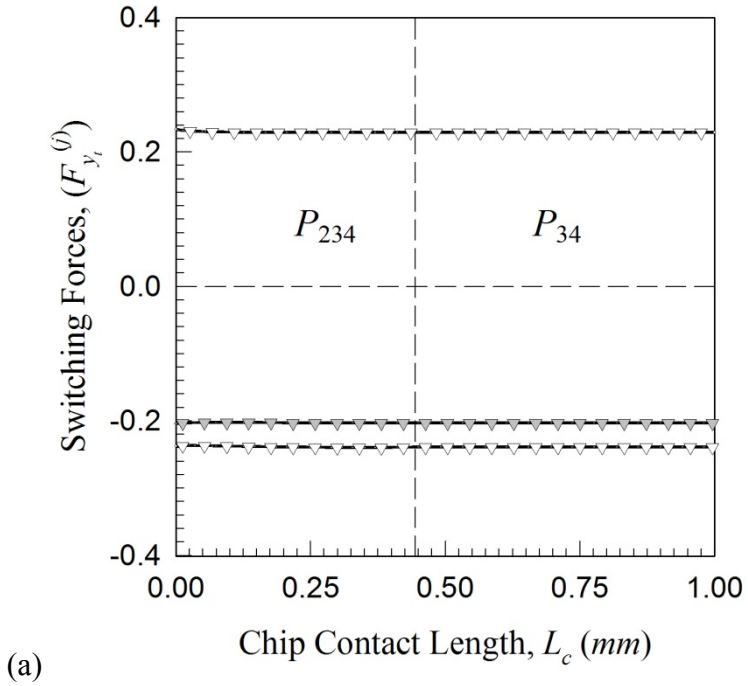

(a)

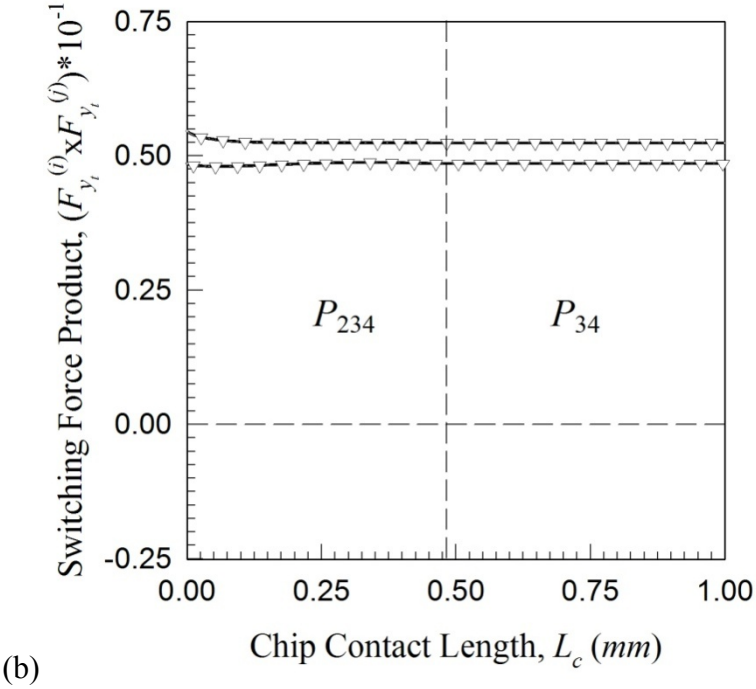

(b)

Fig. 82 Numerical and analytical predictions of (a) switching forces $(F_{y_t}^{(3)}, F_{y_t}^{(4)})$ and (b) switching force product $(F_{y_t}^{(3)} \times F_{y_t}^{(4)})$ for interrupted periodic motions over a range of chip contact length (L_c); $e = 0.1(mm)$ and $\Omega = 400(\frac{rad}{s})$.

The switching forces and force products also reflect the reduction in amplitude as the eccentricity frequency (Ω) is approached, see Fig. 78(a,b). Since the force products are shown to be greater than zero over the entire range $k_2 \in [0, 500k](\frac{N}{mm})$; the motions are numerically and theoretically verified to be passable through the friction boundary. The chip contact length (L_c) will be studied in the next section.

Study of Chip Contact Length (L_c)

Consider the variation of the motion throughout the range of chip stiffness coefficient $L_c \in [0.0, 1.0]$ (mm) for $e = 0.100$ (mm) and $\Omega = 250$ $(\frac{rad}{s})$, see Fig. 79. The switching phase $\text{mod}(t_i, 2\pi)$ and switching displacement $(y_t = \tilde{y}_i)$ versus the chip contact length (L_c) are presented to show the varying orbit of the motion for the mappings P_{234}: $[0.0, 0.488)$ (mm) and P_{34}: $[0.488, 1.0]$ (mm), see Fig. 79(a,b); respectively. Observe how the switching displacement $(\tilde{y}_i)$ of Fig. 79(b) grows with respect to increasing chip contact length (L_c). The validation of the predictions are shown in Fig. 80(a,b) by the switching forces and switching force products versus chip contact length (L_c). Since the force products are shown to be greater than zero over the entire range $L_c \in [0.0, 1.0]$ (mm); the motions are numerically and theoretically verified.

Consider the variation of the motion throughout the range of chip contact length $L_c \in [0.0, 1.0]$ (mm) for $e = 0.100$ (mm) and $\Omega = 400$ $(\frac{rad}{s})$, see Fig. 81. The switching phase $\text{mod}(t_i, 2\pi)$ and switching displacement $(y_t = \tilde{y}_i)$ versus the chip

contact length (L_c) are presented for the mappings $P_{234}: [0.0, 0.455)$ (mm) and $P_{34}: [0.455, 1.0]$ (mm), see Fig. 81(a,b); respectively. Since the force products are shown to be greater than zero over the entire range $L_c \in [0.0, 1.0](mm)$; the motions are numerically and theoretically verified to be passable through the friction boundary. The switching force products appear to affect only in the range of $L_c < 0.488$ (mm) for $\Omega = 250$ $(\frac{rad}{s})$. The grazing bifurcation parameter boundary for these two studies is defined at $L_c \approx 0.488$ (mm) for $\Omega = 250$ $(\frac{rad}{s})$ and $L_c \approx 0.455$ $(\frac{mm}{s})$ for $\Omega = 400$ $(\frac{rad}{s})$. The next chapter will verify each of the analytical predictions with one or two sample from each parameter range for the mappings P_{34} and P_{234}.

CHAPTER X

VERIFICATION OF ANALYTICAL PREDICTIONS

Numerical Simulations of Periodic Motions Interacting with Boundary 3

Eccentricity Amplitude (e)

The numerical simulation of the interrupted periodic motion for this machine-tool, subject to an eccentricity force, is presented in Fig. 83-Fig. 86. The dynamical system parameters are

$$d_x = 74\,\tfrac{Ns}{mm},\ d_y = 63\,\tfrac{Ns}{mm},$$

$$k_x = k_y = 56\,\tfrac{kN}{mm},\ k_1 = 0.1\,\tfrac{MN}{mm}, k_2 = 10\,\tfrac{kN}{mm},\ d_1 = d_2 = 0\,\tfrac{Ns}{\text{mm}},$$

and the external force and geometry parameters are

$$\delta_1 = \delta_2 = 10^{-3} m,\ \mu = 0.7,\ L_c = 1.0\times 10^{-3} m,\ \Omega V = 20\,\tfrac{mm}{s},$$

$$\alpha = \tfrac{\pi}{4}\text{rad},\ \beta = 0.1\text{rad},\ \eta = \tfrac{\pi}{4}\text{rad},$$

$$X_1 = Y_1 = 10^{-3} m, X_{eq} = Y_{eq} = 5\times 10^{-3} m.$$

The simulations to verify the predictions of Fig. 41 and Fig. 42 are completed via the closed form solution for $\Omega = 200\ (\tfrac{rad}{s})$ and $A = 350, 500,$ see Fig. 83 and Fig. 84. The initial conditions for this motion are shown in Table 6. In Fig. 83(a), the trajectory of the periodic motion relative to the mapping structure P_{34} is illustrated.

The switching points are noted by circular symbols ($\circ$). The motion in domain (Ω_3) is labeled by mapping P_3 (dark and light gray shaded areas). Following

Table 6 Initial Conditions for Simulations Interacting with Boundary 3.

$\Omega(\frac{rad}{s})$	A	x_t	y_t	$\dot{x}_t$	$\dot{y}_t$	Ωt_{bar}	Mapping	Fig.
250	350	2.2591	-1.7780	-10.4344	-20	1.8573	P_{34}	83, 84
250	500	2.3016	-1.7013	-7.3116	-20	1.3605	P_{34}	83, 84
400	350	2.2007	-1.7574	34.7040	-20	2.4539	P_{34}	85, 86
400	500	2.2371	-1.7956	24.4697	-20	2.8900	P_{34}	85, 86
385	500	2.3132	-1.8570	3.9301	-20	3.7305	P_{34}	87, 88
480	500	2.2343	-1.8280	8.2446	-20	4.5851	P_{34}	87, 88
$\Omega(\frac{rad}{s})$	$\Omega V(\frac{mm}{s})$	x_t	y_t	$\dot{x}_t$	$\dot{y}_t$	Ωt_{bar}	Mapping	Fig.
200	20	2.1775	-1.9230	-15.6561	-20	2.9863	P_{34}	89, 90
200	30	2.2218	-1.8533	-17.6011	-30	2.4668	P_{34}	89, 90
400	20	2.3152	-1.8840	0.5433	-20	4.2851	P_{34}	91, 92
400	30	2.3009	-1.8486	19.1903	-30	3.7060	P_{34}	91, 92
$\Omega(\frac{rad}{s})$	$k_2(\frac{kN}{mm})$	x_t	y_t	$\dot{x}_t$	$\dot{y}_t$	Ωt_{bar}	Mapping	Fig.
400	10	2.2007	-1.7574	34.7040	-20	2.4539	P_{34}	93, 94
400	22.5	2.2610	-1.7998	28.6839	-20	2.7651	P_{34}	93, 94

intersection of the chip/tool friction boundary, the motion then moves into domain (Ω_4) (labeled by mapping P_4). To verify the switching ability of motion on the chip/tool friction boundary, the forces ($F_{\dot{y}}^{(3)}$ and $F_{\dot{y}}^{(4)}$) versus velocity $(\dot{y}_t = \dot{\tilde{y}})$ is presented in Fig. 83(b). The switching ability conditions are observed on the boundary. Finally, the displacement ($y_t = \tilde{y}$) and velocity ($\dot{y}_t = \dot{\tilde{y}}$) time histories for this motion is shown in

Fig. 84(a, b). The shaded and dark shaded areas illustrate the motion in domain three (chip reduction, $\dot{\tilde{y}} < V$).

The simulations to verify the predictions of Fig. 43 and Fig. 44 are completed via the closed form solution for $\Omega = 400$ ($\frac{rad}{s}$) and $A = 350, 500,$ see Fig. 85 and Fig. 86. In Fig. 85(a), the trajectory of the periodic motion relative to the mapping structure P_{34} is illustrated. The motion in domain (Ω_3) is labeled by mapping P_3 (dark and light gray shaded areas). Following intersection of the frictional boundary, the motion then moves into domain (Ω_4) (labeled by mapping P_4). To verify the switching ability of motion on the boundary, the forces ($F_{\tilde{y}}^{(3)}$ and $F_{\tilde{y}}^{(4)}$) versus velocity ($\dot{y}_t = \dot{\tilde{y}}$) is presented in Fig. 85(b).

The switching ability conditions are observed on the boundary. Finally, the displacement ($y_t = \tilde{y}$) and velocity ($\dot{y}_t = \dot{\tilde{y}}$) time histories for this motion is shown in Fig. 86(a, b). The shaded and dark shaded areas illustrate the motion in domain three (chip reduction, $\dot{\tilde{y}} < V$). The simulations for the variation of excitation amplitudes illustrate the intuitive understanding of the response of linear systems with respect to an exciting amplitude. The simulations will be completed for $\Omega = 385$ and 480 ($\frac{rad}{s}$) in the next section.

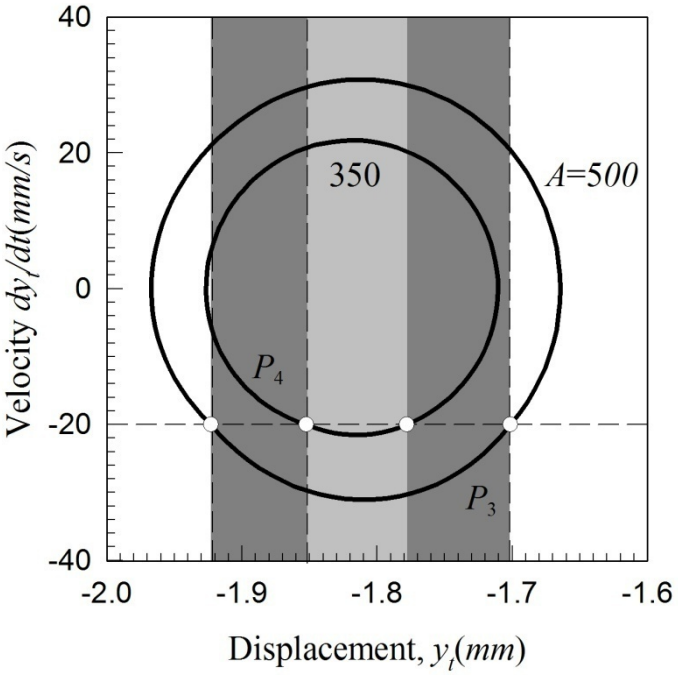

(a)

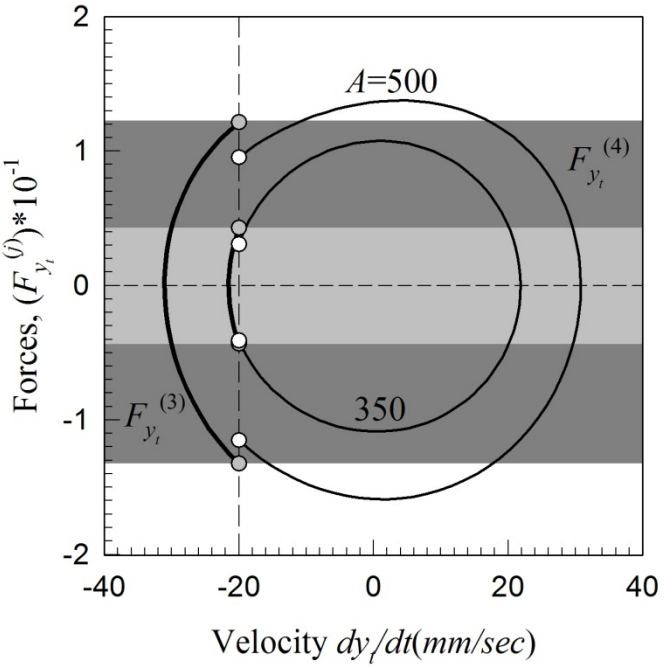

(b)

Fig. 83 Verification of non-stick periodic motion (P_{34}): (a) phase trajectory in phase plane $(y_t, \dot{y}_t)$, (b) forces $(F_{y_t}^{(3)}, F_{y_t}^{(4)})$ versus $(\dot{y}_t = \dot{\tilde{y}})$, $L_c = 1(mm)$, $A = 350, 500$ and $\Omega = 250(\frac{rad}{s})$.

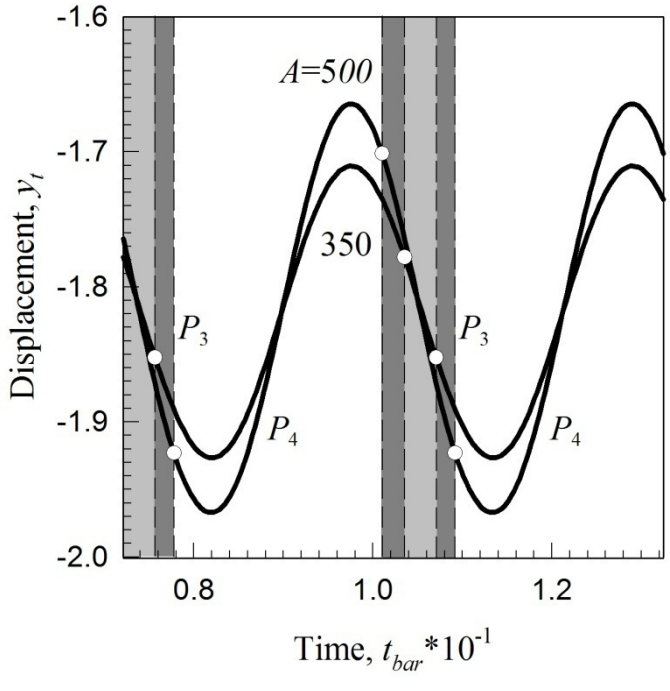

(a)

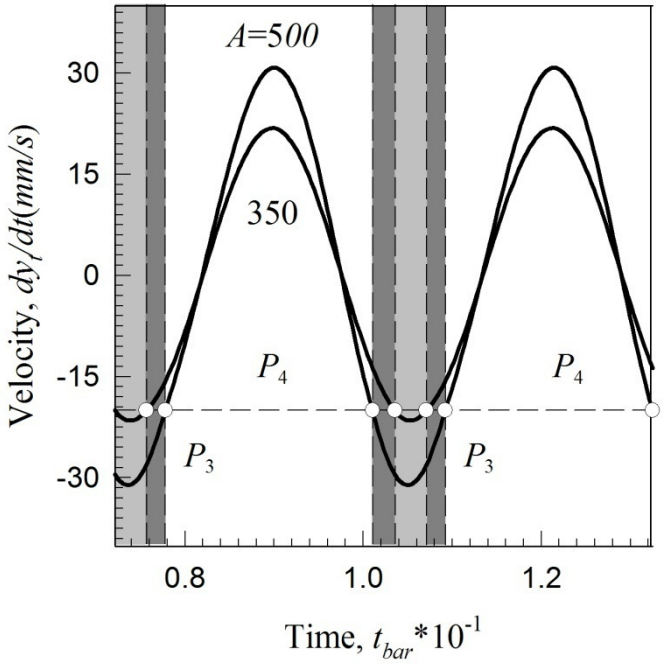

(b)

Fig. 84 Verification of non-stick periodic motion (P_{34}): (a) displacement ($y_t = \tilde{y}$) time history and (b) velocity ($\dot{y}_t = \dot{\tilde{y}}$) time history; $L_c = 1(mm)$, $A = 350, 500$ and $\Omega = 250(\frac{rad}{s})$.

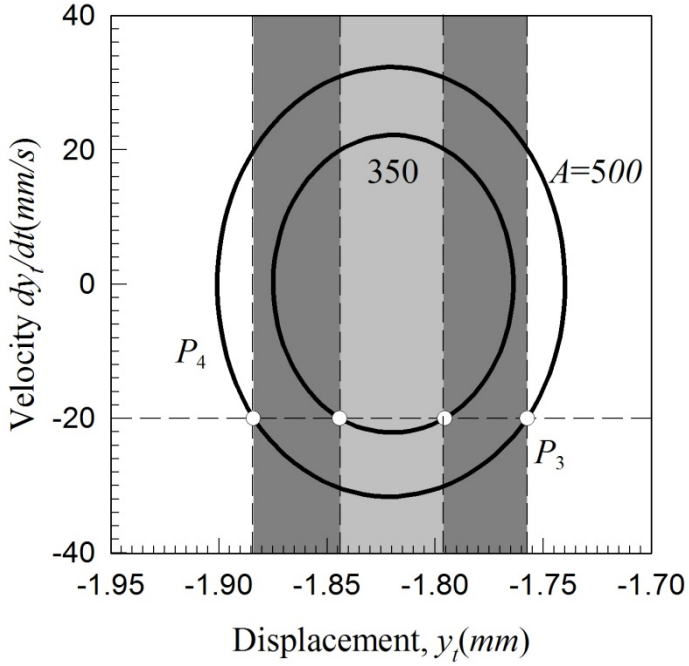

(a)

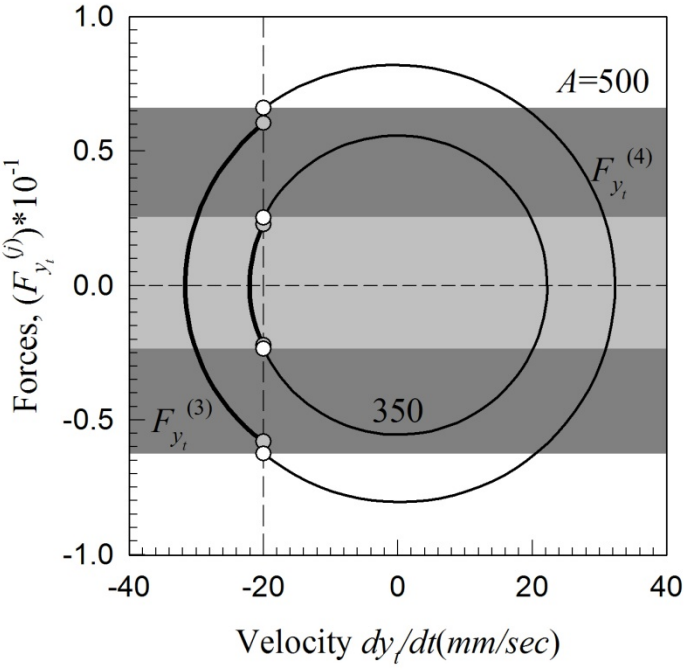

(b)

Fig. 85 Verification of non-stick periodic motion (P_{34}): (a) phase trajectory in phase plane $(y_t, \dot{y}_t)$, (b) forces $(F_{y_t}^{(3)}, F_{y_t}^{(4)})$ versus $(\dot{y}_t = \dot{\tilde{y}})$, $L_c = 1(mm)$, $A = 350, 500$ and $\Omega = 400(\frac{rad}{s})$.

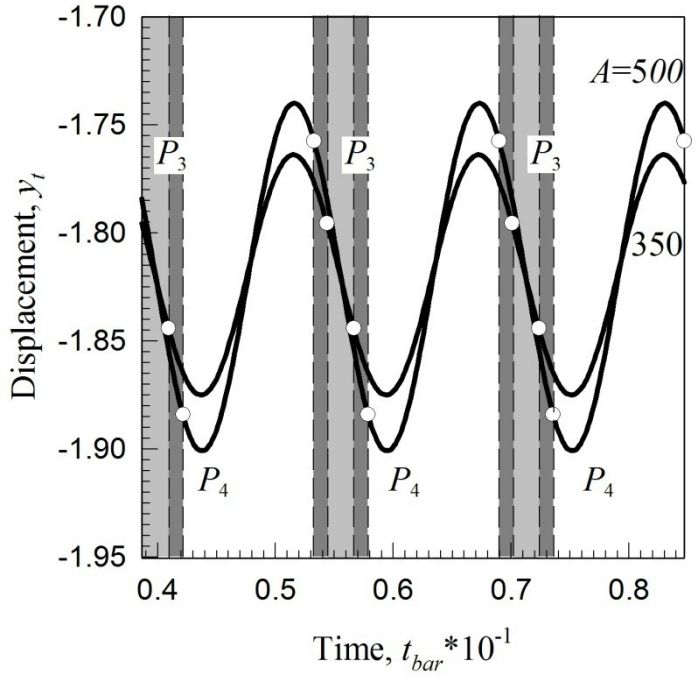

(a)

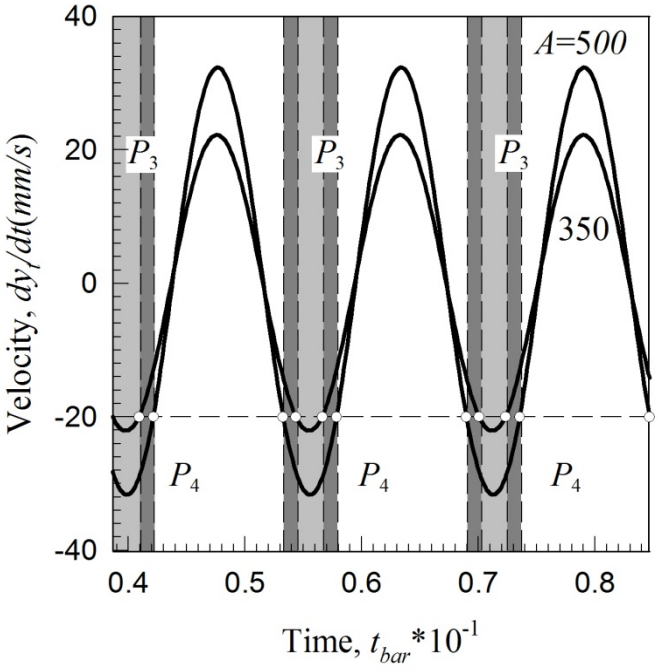

(b)

Fig. 86 Verification of non-stick periodic motion (P_{34}): (a) displacement ($y_t = \tilde{y}$) time history and (b) velocity ($\dot{y}_t = \dot{\tilde{y}}$) time history; $L_c = 1(mm)$, $A = 350, 500$ and $\Omega = 400(\frac{rad}{s})$.

Excitation Frequency (Ω)

The numerical simulation of the interrupted periodic motion for this machine-tool, subject to an eccentricity force, is presented in Fig. 87 and Fig. 88. The remaining parameters are

$$A = 500,\ \Omega V = -20\,\tfrac{mm}{s} \text{ and } \mu = 0.7.$$

The simulations to verify the predictions of Fig. 45 and Fig. 46 are completed via the closed form solutions for $\Omega = 385, 480$ $(\tfrac{rad}{s})$. The initial conditions for this motion are shown in Table 6. In Fig. 87(a,b), the trajectory of the periodic motion relative to the mapping structure P_{34} is illustrated. The motion in domain (Ω_3) is labeled by mapping P_3 (dark and light gray shaded areas). Following intersection of the frictional boundary, the motion then moves into domain (Ω_4) (labeled by mapping P_4).

To verify the switching ability of motion on the boundary, the forces ($F_{\tilde{y}}^{(3)}$ and $F_{\tilde{y}}^{(4)}$) versus velocity $(\dot{y}_t = \dot{\tilde{y}})$ is presented in Fig. 87(b). The switching ability conditions are observed on the boundary. Finally, the displacement $(y_t = \tilde{y})$ and velocity $(\dot{y}_t = \dot{\tilde{y}})$ time histories for this motion is shown in Fig. 88(a-b). The amplitude of the orbit in the phase plane not only varies from $\Omega = 385$ to $\Omega = 480$, but the time the motion is affected by the domain three (chip reduction, $\dot{\tilde{y}} < V$) parameters is notably longer. The simulations will be completed for $\Omega V = 20$ and 30 $(\tfrac{mm}{s})$ in the next section.

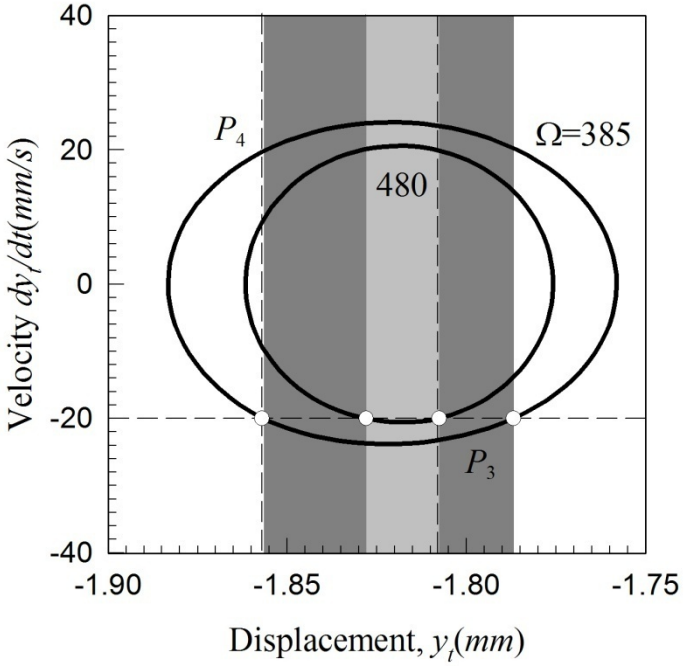

(a)

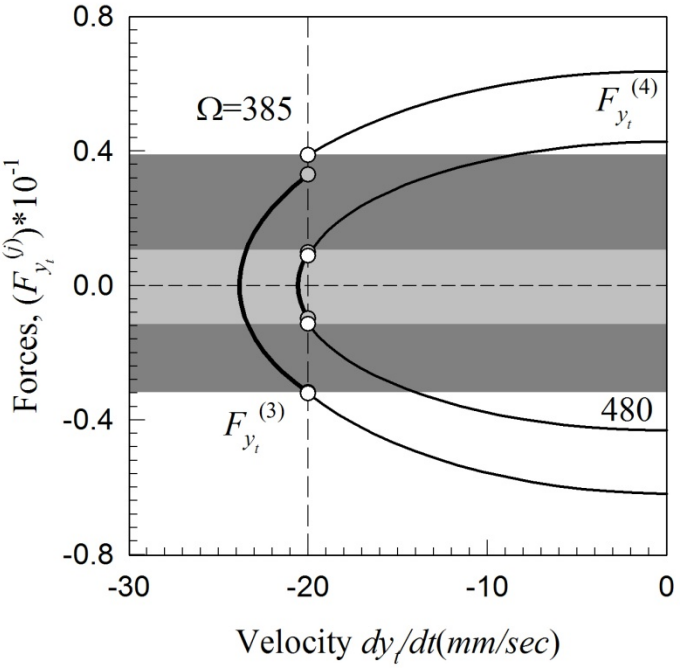

(b)

Fig. 87 Verification of non-stick periodic motion (P_{34}): (a) phase trajectory in phase plane $(y_t, \dot{y}_t)$, (b) forces $(F_{y_t}^{(3)}, F_{y_t}^{(4)})$ versus $(\dot{y}_t = \dot{\tilde{y}})$; $L_c = 1(mm)$, $A = 500$ and $\Omega = 385, 480(\frac{rad}{s})$.

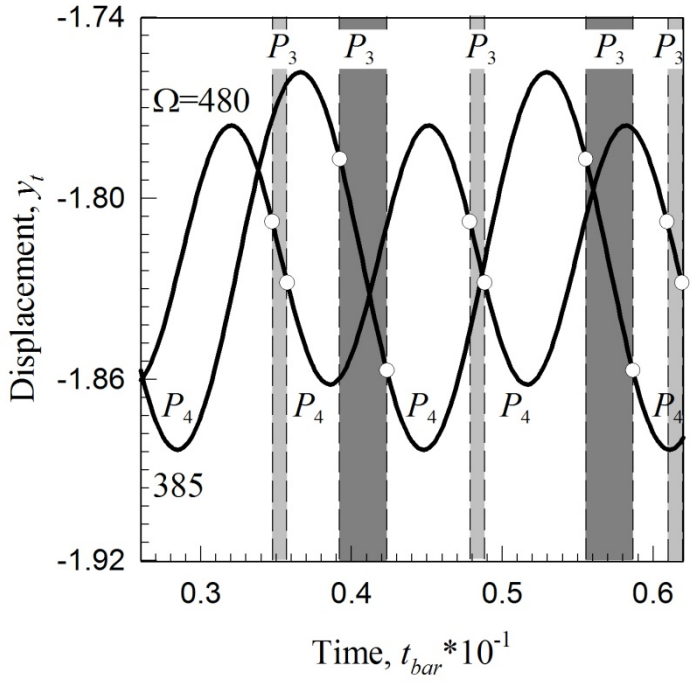

(a)

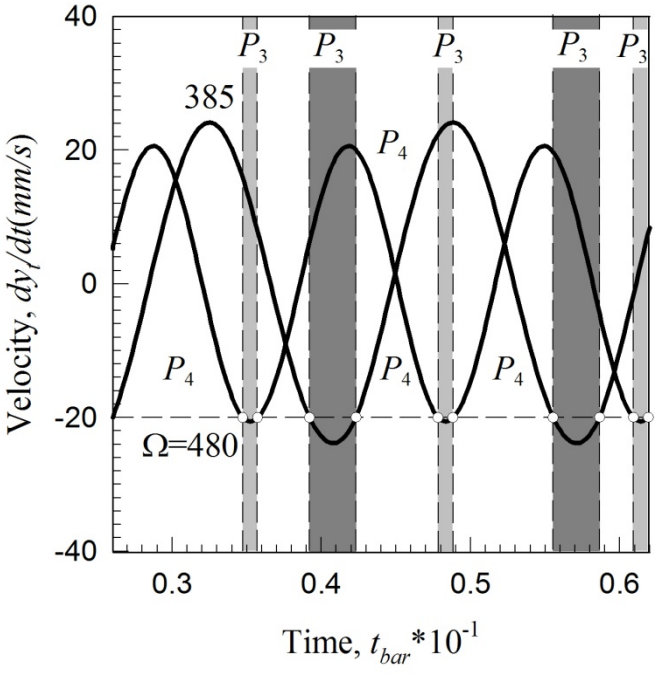

(b)

Fig. 88 Verification of non-stick periodic motion (P_{34}): (a) displacement ($y_t = \tilde{y}$) time history and (b) velocity ($\dot{y}_t = \dot{\tilde{y}}$) time history; $L_c = 1(mm)$, $A = 500$ and $\Omega = 385, 480(\frac{rad}{s})$.

Chip Velocity (ΩV)

The numerical simulation of the interrupted periodic motion for this machine-tool, subject to an eccentricity force, is presented in Fig. 89 through Fig. 92. The remaining parameters are

$$A = 500,\ \Omega = 200\,\tfrac{rad}{s} \text{ and } \mu = 0.7.$$

The simulations to verify the predictions of Fig. 89 and Fig. 90 and are completed via the closed form solutions for $\Omega V = 20.0,\ 30.0\ \ (\tfrac{mm}{s})$. In Fig. 89(a), the trajectory of the periodic motion relative to the mapping structure P_{34} is illustrated. The motion in domain (Ω_3) is labeled by mapping P_3 (dark and light gray shaded areas).

Following intersection of the frictional boundary, the motion then moves into domain (Ω_4) (labeled by mapping P_4). To verify the switching ability of motion on the boundary, the forces ($F_{\tilde{y}}^{(3)}$ and $F_{\tilde{y}}^{(4)}$) versus velocity ($\dot{y}_t = \dot{\tilde{y}}$) is presented in Fig. 89(b). The motion can be observed to intersect the frictional boundary with forces implying pass-ability. Finally, the displacement ($y_t = \tilde{y}$) and velocity ($\dot{y}_t = \dot{\tilde{y}}$) time histories for this motion is shown in Fig. 90(a-b). The simulations to verify the predictions of Fig. 91 and Fig. 92 are completed via the closed form solution for $\Omega = 400\ \ (\tfrac{rad}{s})$, see Fig. 91 and Fig. 92.

In Fig. 91(a), the trajectory of the periodic motion relative to the mapping structure P_{34} is illustrated. The motion in domain (Ω_3) is labeled by mapping P_3 (dark

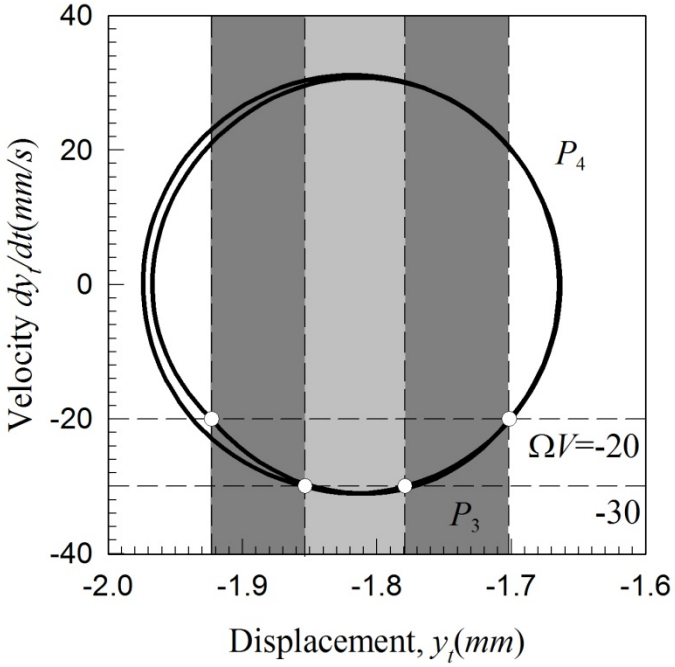

(a)

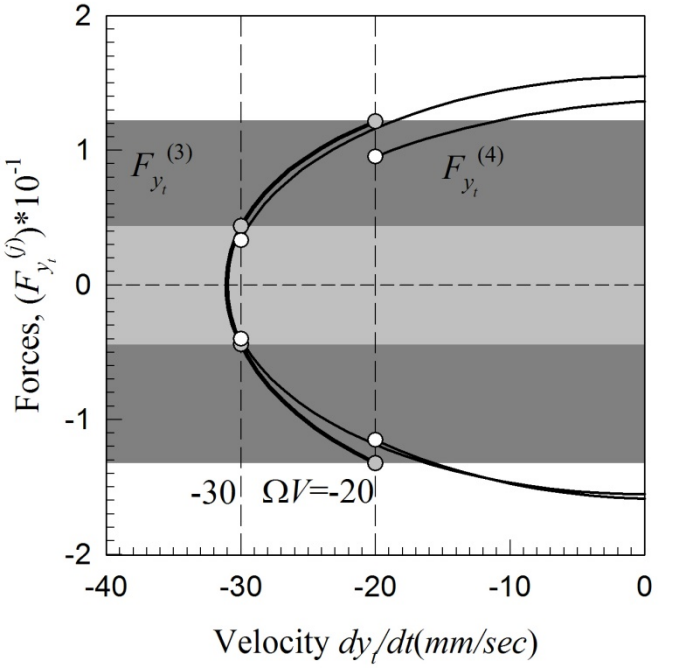

(b)

Fig. 89 Verification of non-stick periodic motion (P_{34}): (a) phase trajectory in phase plane $(y_t, \dot{y}_t)$, (b) forces $(F_{y_t}^{(3)}, F_{y_t}^{(4)})$ versus $(\dot{y}_t = \dot{\tilde{y}})$, $L_c = 1(mm)$, $\Omega V = -20, -30(\frac{mm}{s})$ and $\Omega = 200(\frac{rad}{s})$.

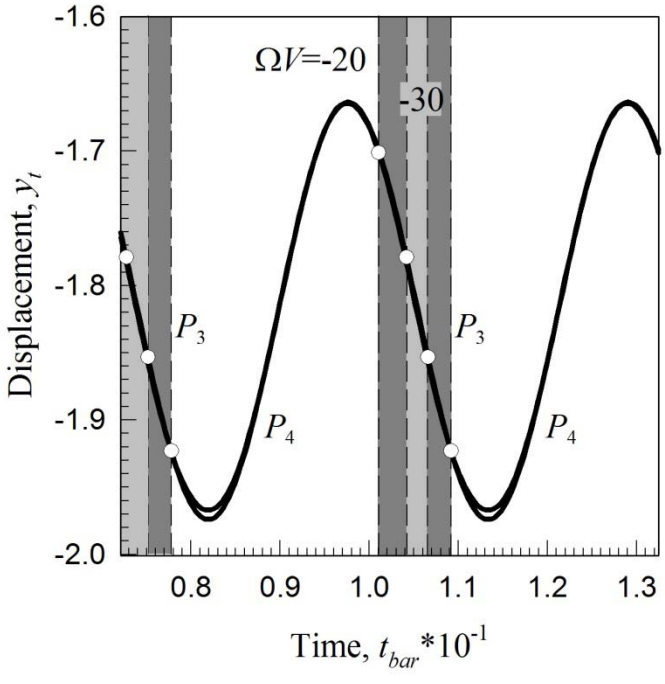

(a)

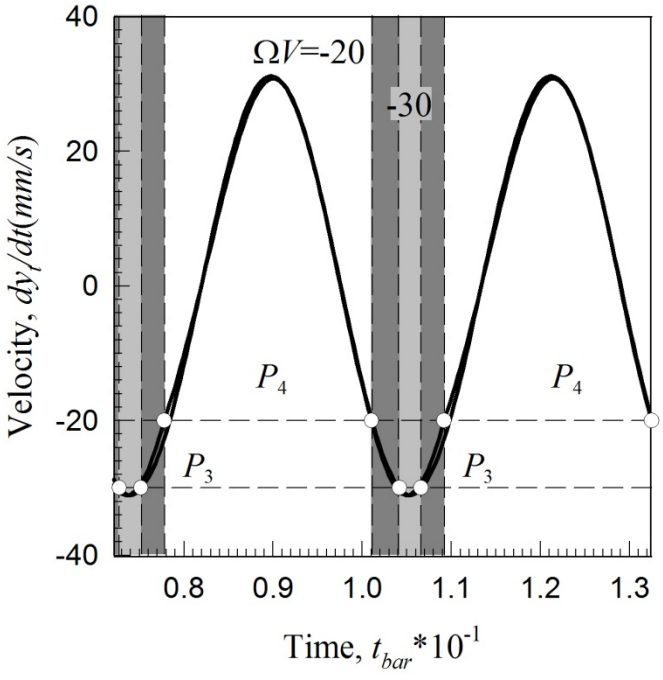

(b)

Fig. 90 Verification of non-stick periodic motion (P_{34}): (a) displacement ($y_t = \tilde{y}$) time history and (b) velocity ($\dot{y}_t = \dot{\tilde{y}}$) time history; $L_c = 1(mm)$, $\Omega V = -20, -30(\frac{mm}{s})$ and $\Omega = 200(\frac{rad}{s})$.

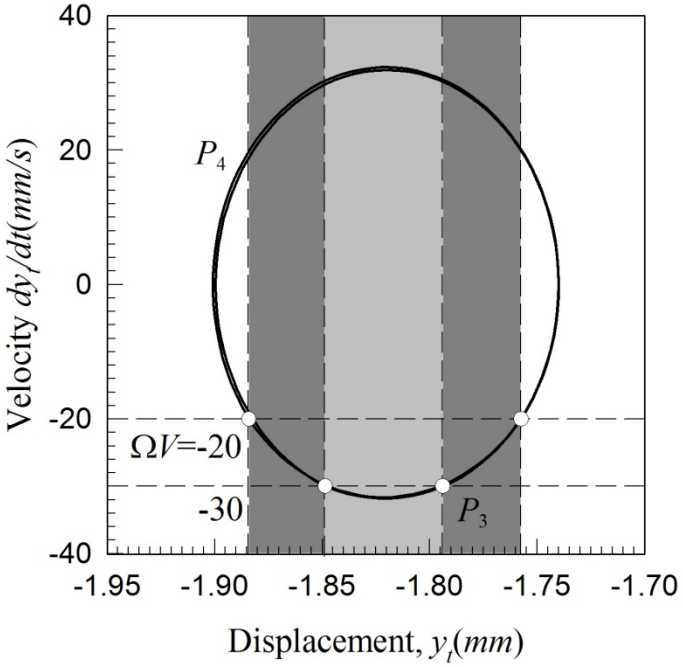

(a)

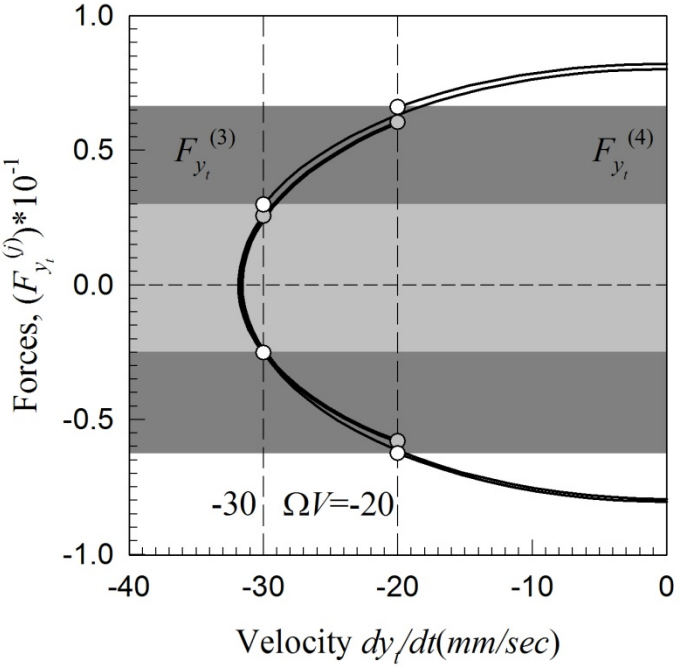

(b)

Fig. 91 Verification of non-stick periodic motion (P_{34}): (a) phase trajectory in phase plane $(y_t, \dot{y}_t)$, (b) forces $(F_{y_t}^{(3)}, F_{y_t}^{(4)})$ versus $(\dot{y}_t = \dot{\tilde{y}})$, $L_c = 1(mm)$, $\Omega V = -20, -30(\frac{mm}{s})$ and $\Omega = 400(\frac{rad}{s})$.

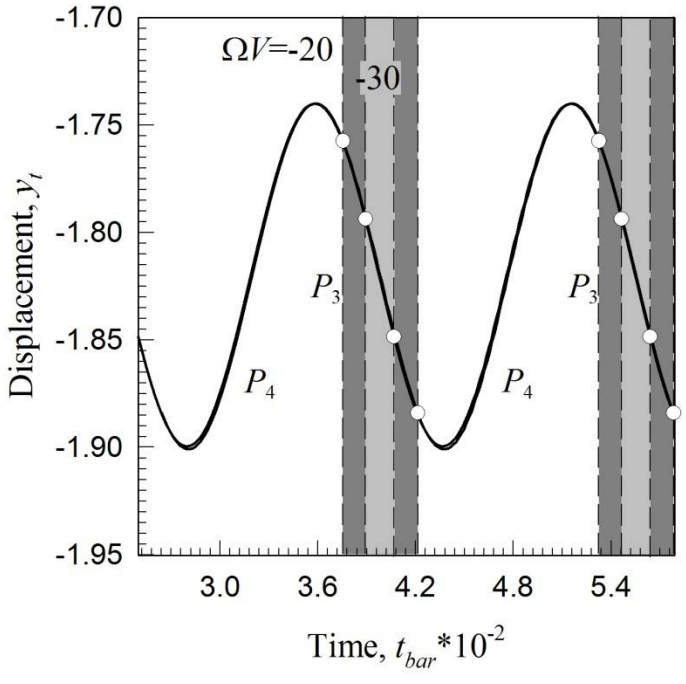

(a)

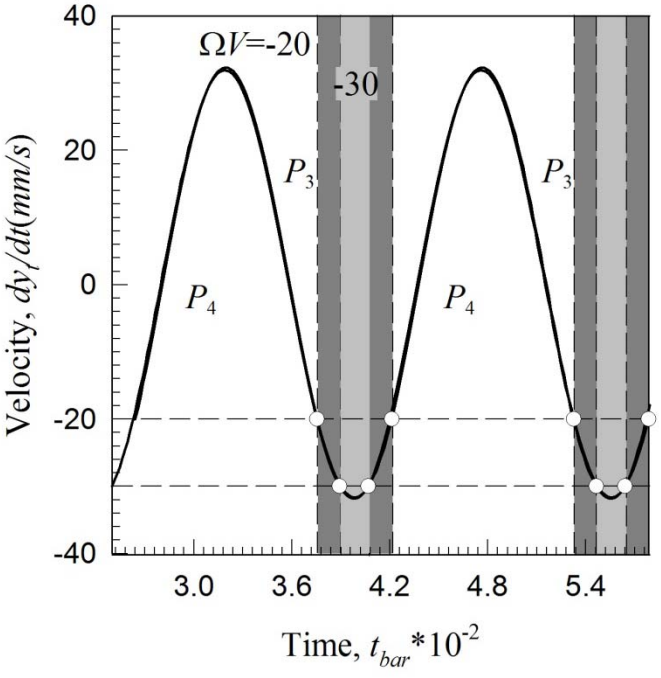

(b)

Fig. 92 Verification of non-stick periodic motion (P_{34}): (a) displacement ($y_t = \tilde{y}$) time history and (b) velocity ($\dot{y}_t = \dot{\tilde{y}}$) time history; $L_c = 1(mm)$, $\Omega V = -20, -30(\frac{mm}{s})$ and $\Omega = 400(\frac{rad}{s})$.

and light gray shaded areas). Following intersection of the frictional boundary, the motion then moves into domain (Ω_4) (labeled by mapping P_4). To verify the switching ability of motion on the boundary, the forces ($F_{\tilde{y}}^{(3)}$ and $F_{\tilde{y}}^{(4)}$) versus velocity ($\dot{y}_t = \dot{\tilde{y}}$) is presented in Fig. 91(b). The switching ability conditions are observed on the boundary. Finally, the displacement ($y_t = \tilde{y}$) and velocity ($\dot{y}_t = \dot{\tilde{y}}$) time histories for this motion is shown in Fig. 92(a-b).

The grazing phenomenon is expected to occur if the chip velocity continues to decrease; such cases are seen for both $\Omega = 200,\ 400$ $(\frac{rad}{s})$. The simulations will be completed for $k_2 = 10k$ and $22.5k$ (N) in the next section.

Chip Stiffness Coefficient (k_2)

The numerical simulation of the interrupted periodic motion for this machine-tool, subject to an eccentricity force, is presented in Fig. 93 and Fig. 94. The remaining parameters are

$$A = 500,\ \Omega = 200\ (\tfrac{rad}{s}) \text{ and } \mu = 0.7.$$

A regular cutting periodic motion is illustrated in Fig. 93 and Fig. 94 for $\Omega = 400$ $(\frac{rad}{s})$. The simulations to verify the predictions of Fig. 57 and Fig. 58 are completed via the closed form solution. The initial conditions for this motion are shown in Table 6. In Fig. 93(a), the trajectory of the periodic motion relative to the mapping structure P_{34} is illustrated.

The switching points are noted by circular symbols ($\circ$). The motion in domain

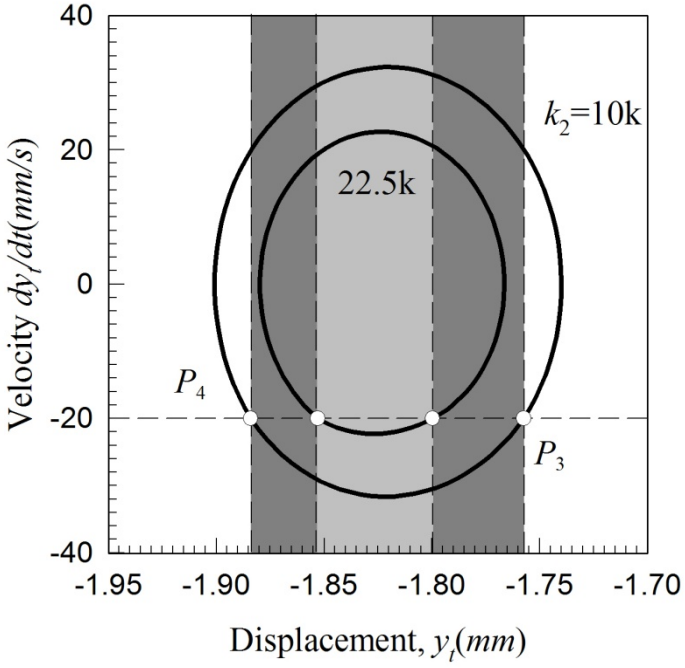

(a)

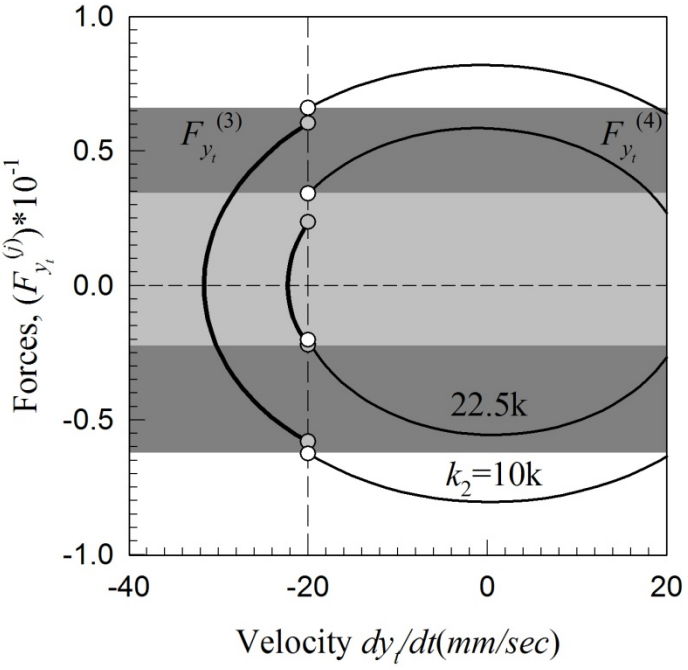

(b)

Fig. 93 Verification of non-stick periodic motion (P_{34}): (a) phase trajectory in phase plane $(y_t, \dot{y}_t)$, (b) forces $(F_{y_t}^{(3)}, F_{y_t}^{(4)})$ versus $(\dot{y}_t = \dot{\tilde{y}})$, $L_c = 1(mm)$, $k_2 = 10k, 22.5k(\frac{N}{mm})$ and $\Omega = 400(\frac{rad}{s})$.

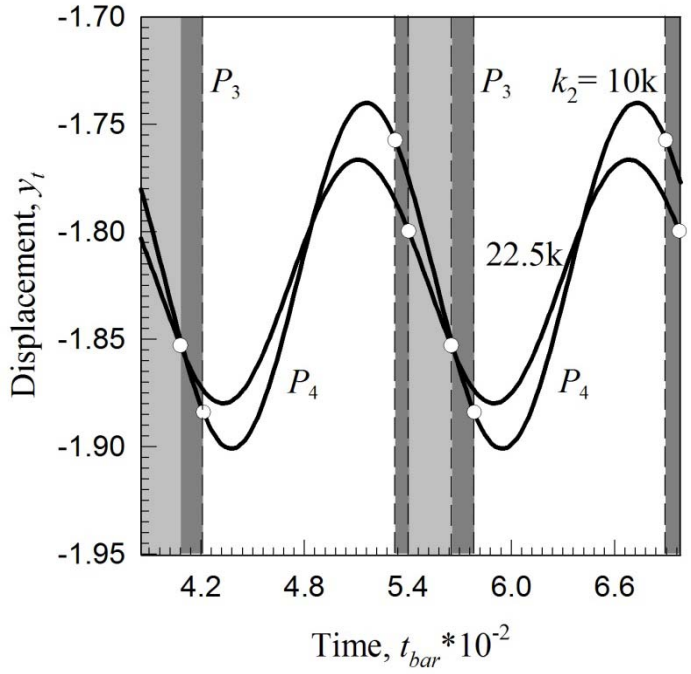

(a)

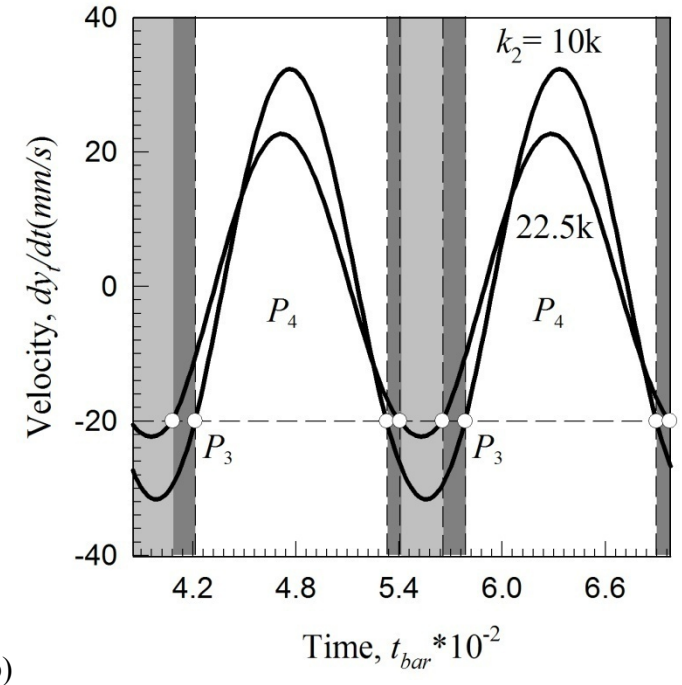

(b)

Fig. 94 Verification of non-stick periodic motion (P_{34}): (a) displacement ($y_t = \tilde{y}$) time history and (b) velocity ($\dot{y}_t = \dot{\tilde{y}}$) time history; $L_c = 1(mm)$, $k_2 = 10k, 22.5k(\frac{N}{mm})$ and $\Omega = 400(\frac{rad}{s})$.

(Ω_3) is labeled by mapping P_3 (dark and light gray shaded areas). Following intersection of the frictional boundary, the motion then moves into domain (Ω_4) (labeled by mapping P_4). To verify the switching ability of motion on the boundary, the forces ($F_{\tilde{y}}^{(3)}$ and $F_{\tilde{y}}^{(4)}$) versus velocity ($\dot{y}_t = \dot{\tilde{y}}$) is presented in Fig. 93(b). The switching ability conditions are observed on the boundary. Finally, the displacement ($y_t = \tilde{y}$) and velocity ($\dot{y}_t = \dot{\tilde{y}}$) time histories for this motion is shown in Fig. 94(a-b).

The motion for $\Omega = 200\ (\frac{rad}{s})$ will not be simulated since from the parameter range the amplitude is unchanging and provides no useful insight to complications with the boundaries. The next section will simulate the interrupted cutting motions with the mapping P_{234}.

Numerical Simulations of Periodic Motions Interacting with Boundaries 3 and 4

Further validation of the analytical predictions is the simulation of the motions by exact solutions presented in the appendix. Consider the dynamical system parameters,

$$\frac{m_e}{m} = 10^3,\ d_x = 74\,\tfrac{Ns}{mm},\ d_y = 63\,\tfrac{Ns}{mm},$$

$$k_x = k_y = 56\,\tfrac{kN}{mm},\ k_1 = 0.1\,\tfrac{MN}{mm}, k_2 = 10\,\tfrac{kN}{mm},\ d_1 = d_2 = 0\,\tfrac{Ns}{\text{mm}},$$

and the external force and geometry parameters are

$$\delta_1 = \delta_2 = 10^{-3} m,\ \mu = 0.7,\ L_c = 1.0\times10^{-4} m,\ \Omega V = 20\,\tfrac{mm}{s},$$

Table 7 Initial Conditions for Simulations of Numerical and Analytical Predictions, D_3 and D_4.

$\Omega(\frac{rad}{s})$	e	x_t	y_t	$\dot{x}_t$	$\dot{y}_t$	Ωt_{bar}	Mapping	Fig.
200	0.085	2.2534	-1.7784	-9.7667	-20	1.8532	P_{34}	95-97
200	0.100	2.1921	-1.9000	-13.2679	-20	2.8487	P_{234}	98-100
400	0.025	2.2915	-1.8503	10.2050	-20	3.8727	P_{34}	101
400	0.040	2.3370	-1.8977	-3.3785	-20	4.3672	P_{234}	101
340	0.100	2.2816	-1.8926	-54.3393	-20	4.4369	P_{234}	102
400	0.100	2.4738	-2.0466	-44.5792	-20	4.7672	P_{234}	102
$\Omega(\frac{rad}{s})$	$\Omega V(\frac{mm}{s})$	x_t	y_t	$\dot{x}_t$	$\dot{y}_t$	Ωt_{bar}	Mapping	Fig.
250	-20	2.3800	-1.6177	-7.2599	-20	2.1500	P_{234}	103
250	-40	2.3490	-1.6834	-23.8214	-40	2.6652	P_{234}	103
340	-20	2.3820	-1.7608	22.9631	-20	2.7871	P_{234}	104
340	-25	2.3939	-1.7815	6.4147	-25	3.0785	P_{34}	104
$\Omega(\frac{rad}{s})$	μ	x_t	y_t	$\dot{x}_t$	$\dot{y}_t$	Ωt_{bar}	Mapping	Fig.
250	0.1	2.1031	-2.0164	-2.5535	-20	4.3452	P_{234}	105
250	2.0	2.0970	-2.0432	-3.1071	-20	4.6817	P_{234}	105
400	0.1	2.5012	-2.0570	-4.9865	-20	4.8280	P_{234}	106
400	2.0	2.4255	-2.0242	-3.4997	-20	4.6685	P_{234}	106
$\Omega(\frac{rad}{s})$	$k_2(\frac{kN}{mm})$	x_t	y_t	$\dot{x}_t$	$\dot{y}_t$	Ωt_{bar}	Mapping	Fig.
250	150	2.2205	-2.0868	-5.4724	-20	3.8750	P_{234}	107 †
250	400	2.1584	-2.2271	-3.0433	-20	3.7479	P_{234}	107 †
400	50	2.3210	-1.9386	-5.8520	-20	4.6282	P_{234}	108
400	500	2.2021	-1.9748	-6.0114	-20	5.6501	P_{234}	108
$\Omega(\frac{rad}{s})$	$L_c(mm)$	x_t	y_t	$\dot{x}_t$	$\dot{y}_t$	Ωt_{bar}	Mapping	Fig.
250	0.1	2.0980	-2.0295	-2.7926	-20	4.4271	P_{234}	109
250	0.4	2.0581	-2.0723	-2.9239	-20	4.4998	P_{234}	109

† Route to grazing / chip seizure motion.

$$\alpha = \tfrac{\pi}{4}\text{rad},\ \beta = 0.1\text{rad},\ \eta = \tfrac{\pi}{4}\text{rad},$$

$$A = e\frac{m_e}{m}, X_1 = Y_1 = 10^{-3}m, X_{eq} = Y_{eq} = 5\times 10^{-3}m.$$

Eccentricity Amplitude (e)

The specific motion first illustrated corresponds to the mapping P_{34} with initial conditions and eccentricity amplitude (e) and frequency (Ω); noted in Table 7, $e = 0.0850\ (mm)$ and $\Omega = 200\ (\frac{rad}{s})$; respectively (see Fig. 95 through Fig. 97). The phase plane corresponding to the measure $(y_t = \tilde{y})$ illustrating the interaction with the friction boundary, $\dot{\tilde{y}} = V = -20\ (\frac{mm}{s})$, see Fig. 95(a). The forces versus the displacement $(y_t = \tilde{y})$ validates the passage of motion through the friction boundary, $\dot{\tilde{y}} = V$, see Fig. 95(b). The forces time history provides an intuitive relation to understand what the forces are at the specific time the motion intersects the friction boundary, $(\dot{\tilde{y}} = V)$, see Fig. 96(a). The displacement $(y_t = \tilde{y})$ time history show in Fig. 96(b) shows no effect by the interaction of the friction boundary.

An alternative view point is the forces versus the velocity $(\dot{y}_t = \dot{\tilde{y}})$, which shows the effects of the changing friction forces at the boundary, see Fig. 97(a). The velocity time history of the particle is shown directly with the friction boundary, $(\dot{\tilde{y}} = V)$, see Fig. 97(b). Although this periodic motion experiences interrupted cutting, the interaction with the friction boundary is not the only concern. The interaction with the chip vanishing boundary (boundary four) must be studied. Consider the periodic interrupted cutting motion defined by the mapping P_{234} with initial conditions, eccentricity

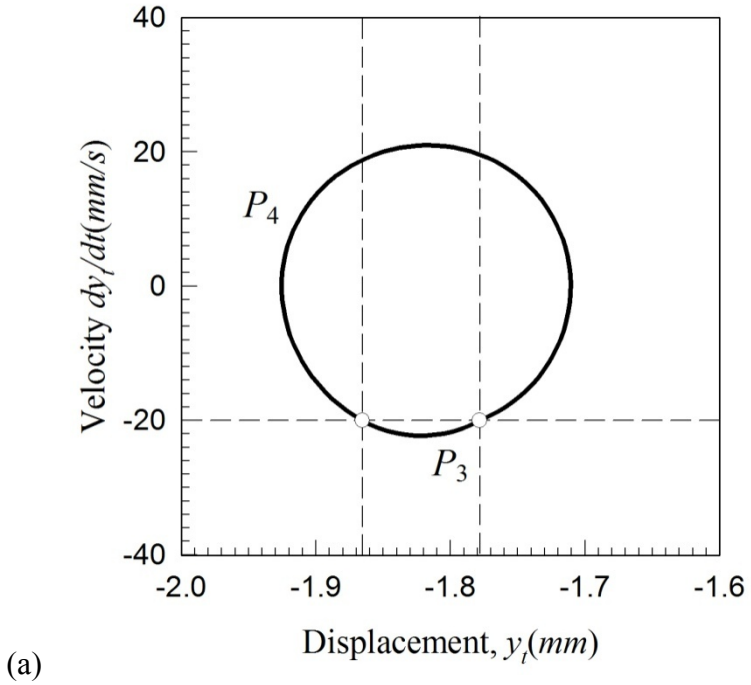

(a)

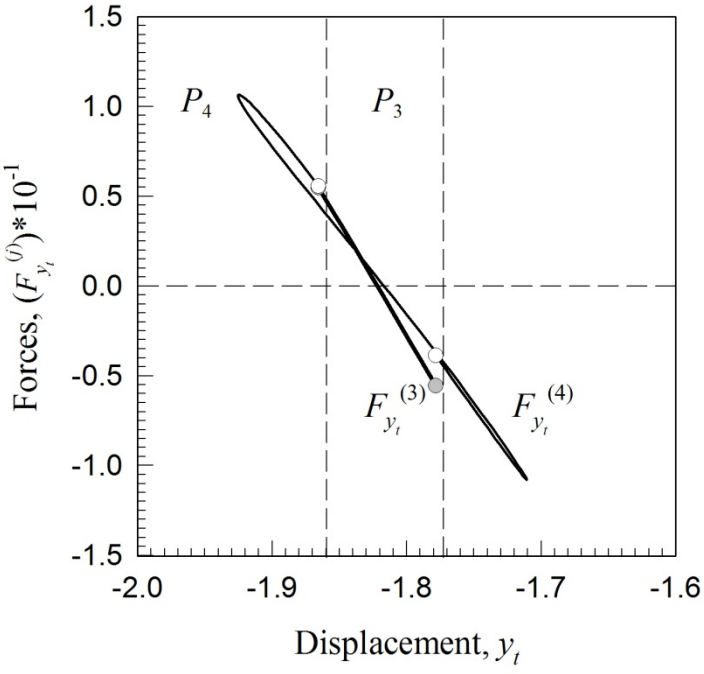

(b)

Fig. 95 Verification of non-stick periodic motion (P_{34}): (a) phase trajectory in phase plane $(y_t, \dot{y}_t)$, b) forces $(F_{y_t}^{(3)}, F_{y_t}^{(4)})$ versus $(y_t = \tilde{y})$, $L_c = 0.1(mm)$, $e = 0.085(mm)$ and $\Omega = 250(\frac{rad}{s})$.

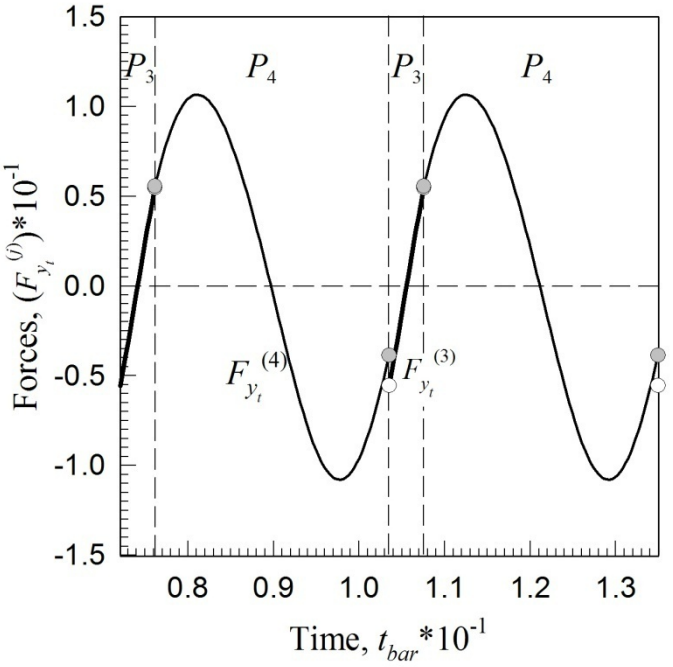

(a)

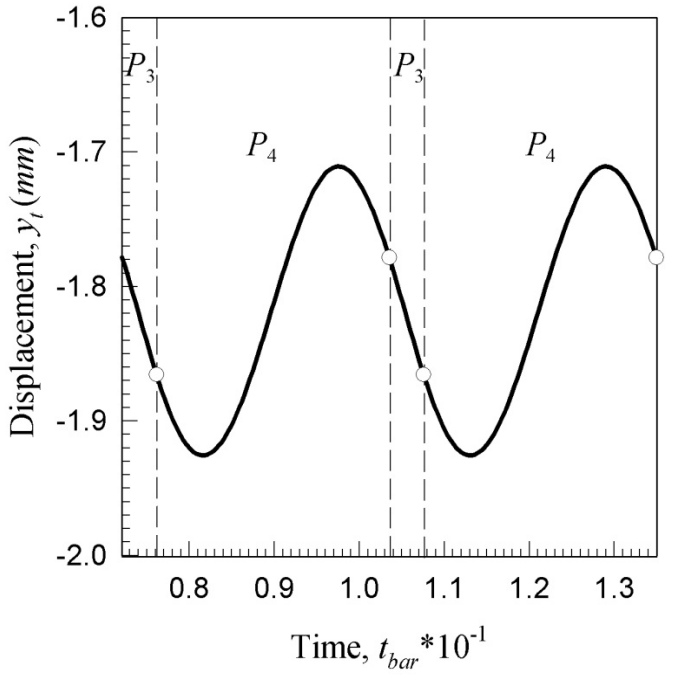

(b)

Fig. 96 Verification of non-stick periodic motion (P_{34}): (a) forces $(F_{y_t}^{(3)}, F_{y_t}^{(4)})$ time history and (b) displacement $(y_t = \tilde{y})$ time history $L_c = 0.1(mm)$, $e = 0.085(mm)$ and $\Omega = 250(\frac{rad}{s})$.

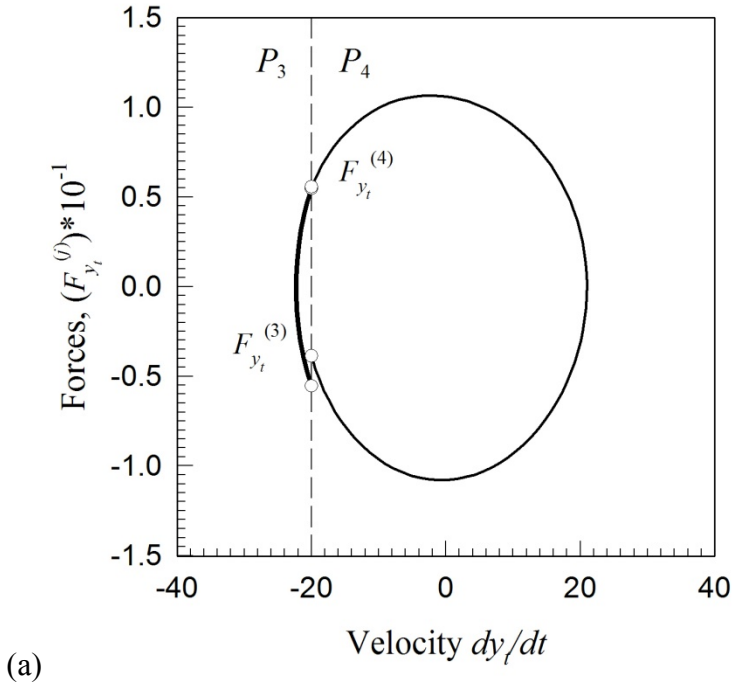

(a)

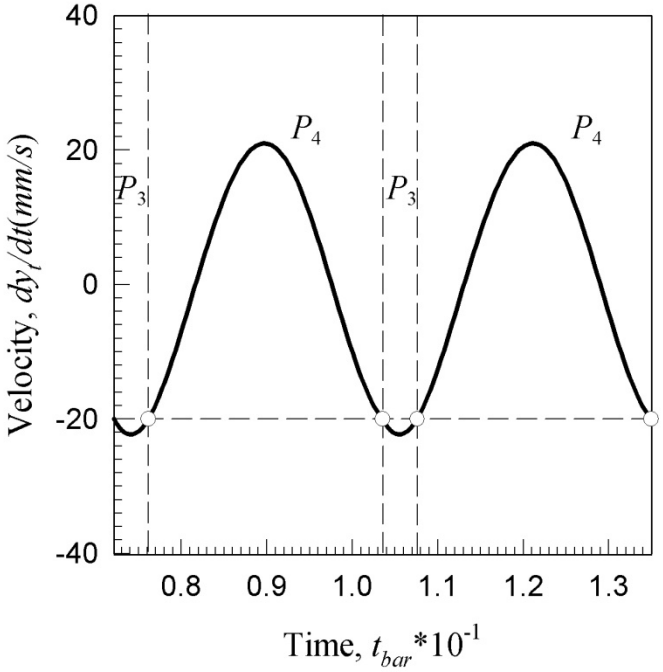

(b)

Fig. 97 Verification of non-stick periodic motion (P_{34}): (a) forces $(F_{y_t}^{(3)}, F_{y_t}^{(4)})$ versus $(\dot{y}_t)$ and (b) velocity $(\dot{y}_t = \dot{\tilde{y}})$ time history $L_c = 0.1(mm)$, $e = 0.085(mm)$ and $\Omega = 250(\frac{rad}{s})$.

amplitude (e) and frequency (Ω); noted in Table 7, $e = 0.100\ (mm)$ and $\Omega = 200\ (\frac{rad}{s})$; respectively (see Fig. 98 through Fig. 100).

Observe the motion through the phase plane where the P_3 is followed by the mapping P_2 (tool and work-piece contact but no cutting), see Fig. 98(a). The P_2 (light gray shaded area) motion results from the chip length decreasing to zero. Similar studies of this occurrence by Woon et. al. [15] illustrate the effects on the orbit of the interrupted cutting motions. This can be verified by the forces $(F_{\tilde{y}}^{(i)})$ versus displacement $(y_t = \tilde{y})$ for each of the mappings, see Fig. 98(b). The forces $(F_{\tilde{y}}^{(i)})$ time history clearly shows the growth and reduction of the forces, see Fig. 99(a). The displacement $(y_t = \tilde{y})$ appears to have no affects related to the P_2 interruption, besides the change of force at the onset of the P_2 motion, see Fig. 99(b). Such affects could in turn delay the return of the cutting action.

This change in forces $(F_{\tilde{y}}^{(i)})$ can be verified to change with the velocity $(\dot{y}_t = \dot{\tilde{y}})$ in Fig. 100(a). The velocity $(\dot{y}_t = \dot{\tilde{y}})$ time history for this periodic motion is shown to illustrate the state when the motion switches to the new dynamics for each of the specific motions, see Fig. 100(b). Consider the periodic interrupted cutting motion defined by the mapping P_{34} and P_{234} with initial conditions, eccentricity amplitude and frequency; noted in Table 7, $e = 0.025,\ 0.040\ (mm)$ and $\Omega = 400\ (\frac{rad}{s})$; respectively (see Fig. 101). Observe the motion through the phase plane where for $e = 0.040\ (mm)$ the P_3 mapping is followed by the mapping P_2 (tool and work-piece contact but no cutting), see

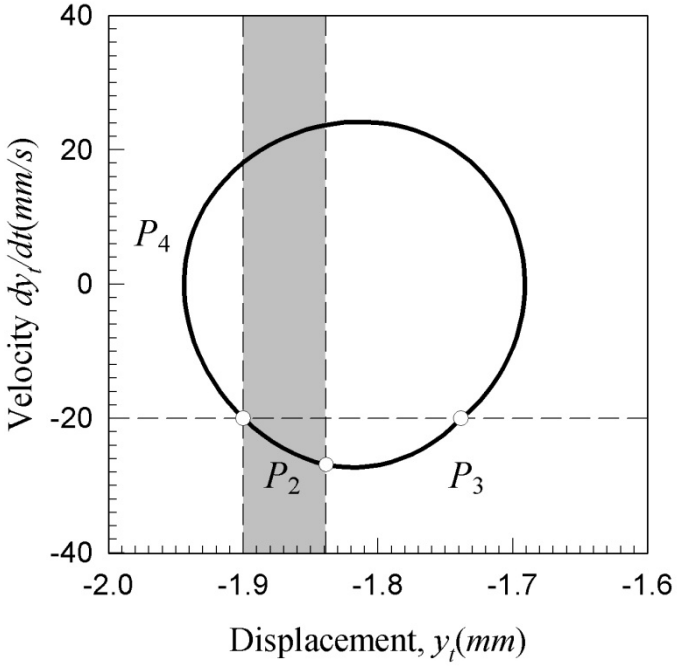

(a)

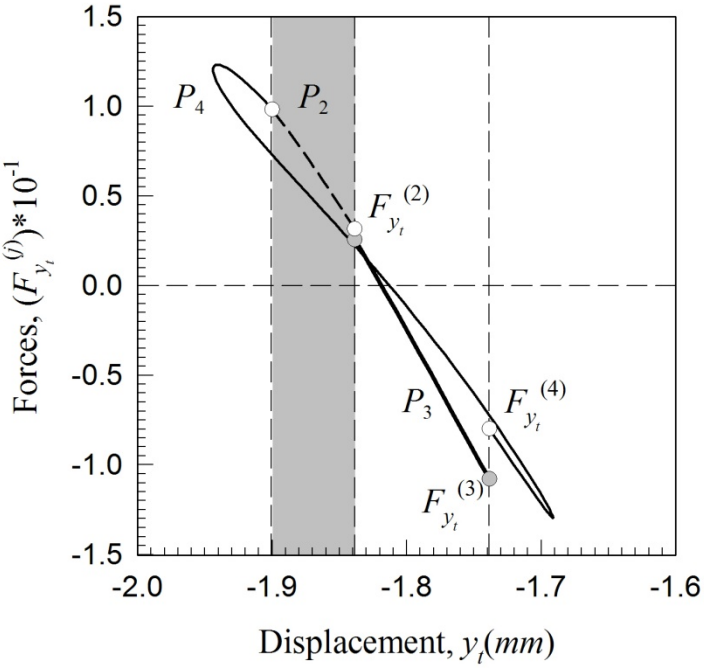

(b)

Fig. 98 Verification of non-stick periodic motion (P_{234}): (a) phase trajectory in phase plane $(y_t, \dot{y}_t)$, b) forces $(F_{y_t}^{(2)}, F_{y_t}^{(3)}, F_{y_t}^{(4)})$ versus $(y_t = \tilde{y})$, $L_c = 0.1(mm)$, $e = 0.1(mm)$ and $\Omega = 250(\frac{rad}{s})$.

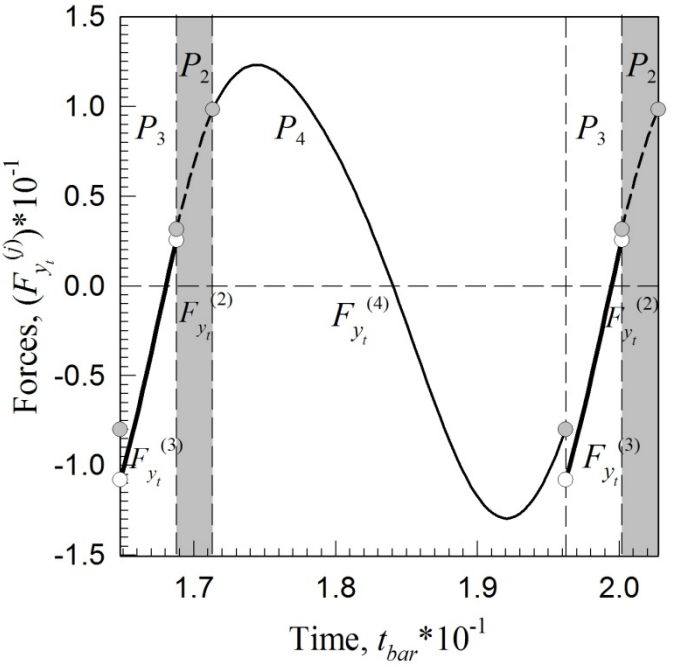

(a)

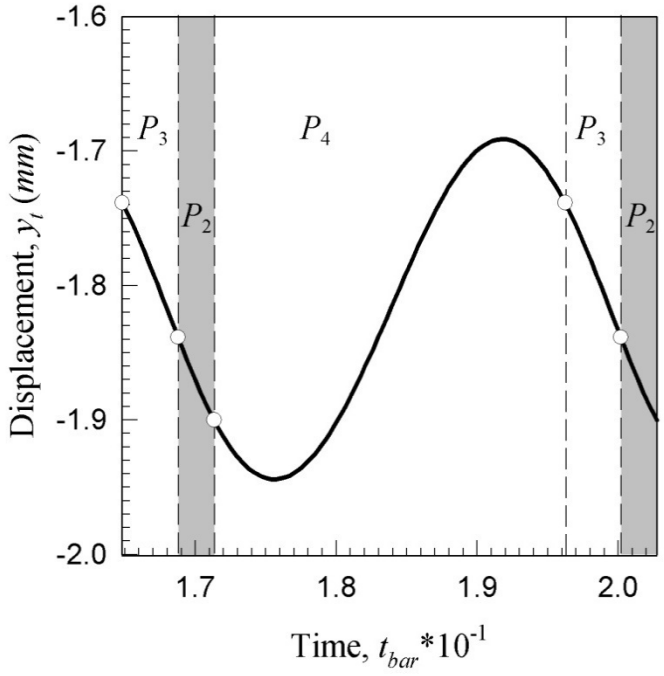

(b)

Fig. 99 Verification of non-stick periodic motion (P_{234}): (a) forces $(F_{y_t}^{(2)}, F_{y_t}^{(3)}, F_{y_t}^{(4)})$ time history and (b) displacement $(y_t = \tilde{y})$ time history $L_c = 0.1(mm)$, $e = 0.1(mm)$ and $\Omega = 250(\frac{rad}{s})$.

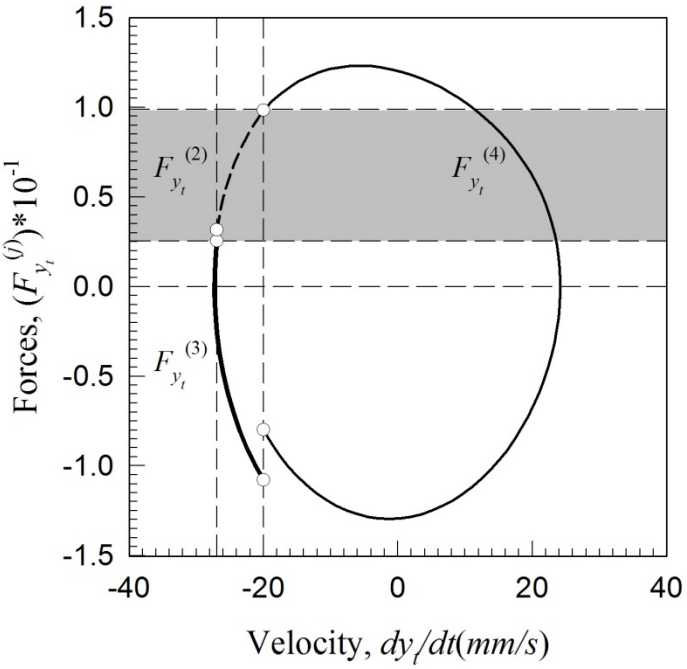

(a)

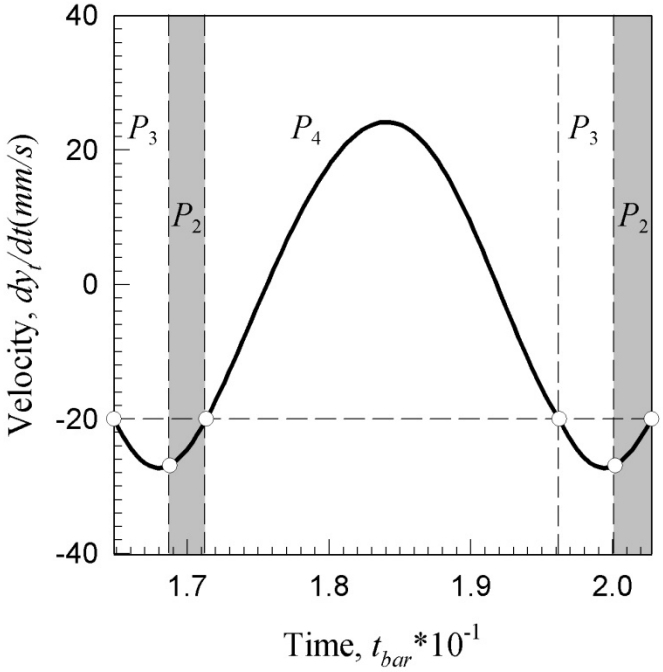

(b)

Fig. 100 Verification of non-stick periodic motion (P_{234}): (a) forces $(F_{y_t}^{(2)}, F_{y_t}^{(3)}, F_{y_t}^{(4)})$ versus $(\dot{y}_t = \dot{\tilde{y}})$ and (b) velocity $(\dot{y}_t = \dot{\tilde{y}})$ time history $L_c = 0.1(mm)$, $e = 0.1(mm)$ and $\Omega = 250(\frac{rad}{s})$.

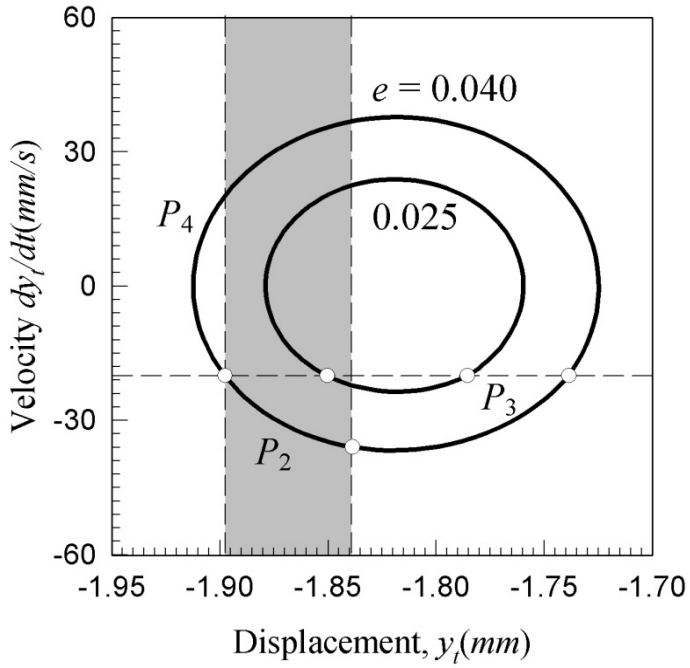

(a)

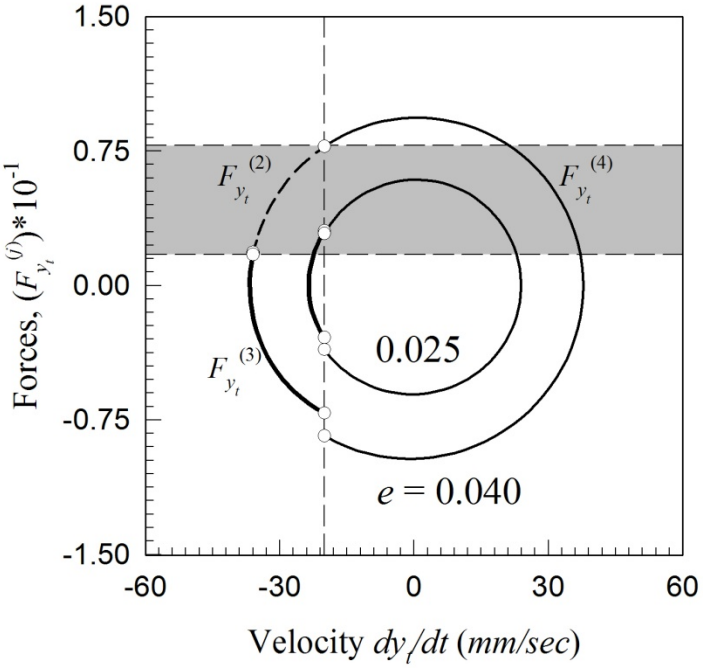

(b)

Fig. 101 Verification of non-stick periodic motions (P_{34}, P_{234}): (a) phase trajectories in phase plane $(y_t, \dot{y}_t)$, b) forces $(F_{y_t}^{(2)}, F_{y_t}^{(3)}, F_{y_t}^{(4)})$ versus $(\dot{y}_t = \dot{\tilde{y}})$, $L_c = 0.1(mm)$, $e = 0.025, 0.040(mm)$ and $\Omega = 400(\frac{rad}{s})$.

Fig. 101(a). This is verified by the forces $(F_{\tilde{y}}^{(i)})$ versus displacement $(y_t = \tilde{y})$ for each of the mappings in Fig. 101(b); where the forces versus velocity $(\dot{y}_t = \dot{\tilde{y}})$.

Notably the eccentricity amplitudes (e) are much lower for such a high eccentricity frequency (Ω). Implications of a trend to relate these parameters in two-dimensional space are apparent. Additionally, a limit could be found where the interruptions due to the friction and zero chip length boundaries have no adverse effects on the machine-tool system as similarly completed for the stability boundary in Gurney and Tobias [59]. A similar study was completed noting limit cycles and the jump phenomenon implying loss of contact or possibly friction chatter Vela-Martinez et. al. [17]. The stability boundary relating the operating frequency and depth of cut for a machine-tool system with regenerative cutting was also presented [17]. The simulations will be completed for

$$\Omega = 340 \text{ and } 400 \ (\tfrac{rad}{s}) \text{ for } e = 0.1 \ (mm)$$

in the next section.

Eccentricity Frequency (Ω)

Consider the periodic interrupted cutting motion defined by the mapping P_{234} with initial conditions, frequency (Ω) and eccentricity amplitude (e), $\Omega = 340.0,\ 400.0 \ (\tfrac{rad}{s})$ and $e = 0.100 \ (mm)$; respectively (see Fig. 102). Observe the motion through the phase plane where the P_3 mapping is followed by the mapping P_2 (tool and work-piece contact but no cutting), see Fig. 102(a). This is verified by the forces $(F_{\tilde{y}}^{(i)})$ versus displacement

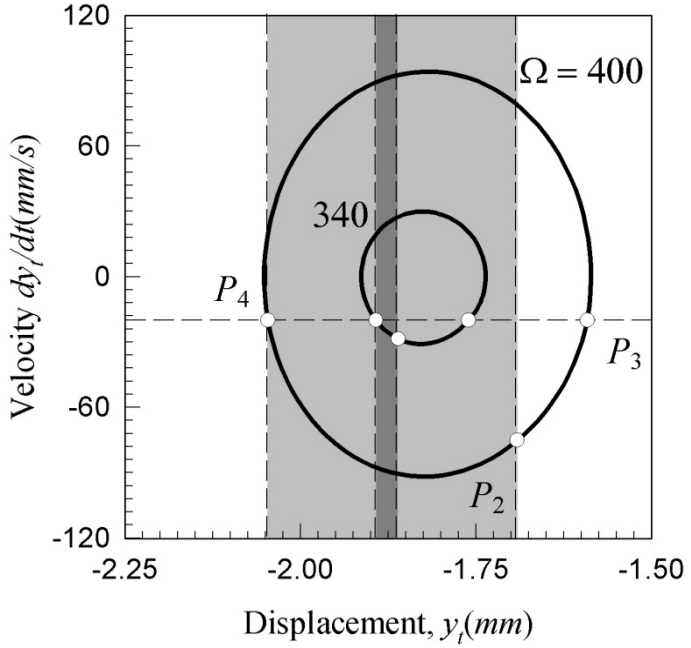

(a)

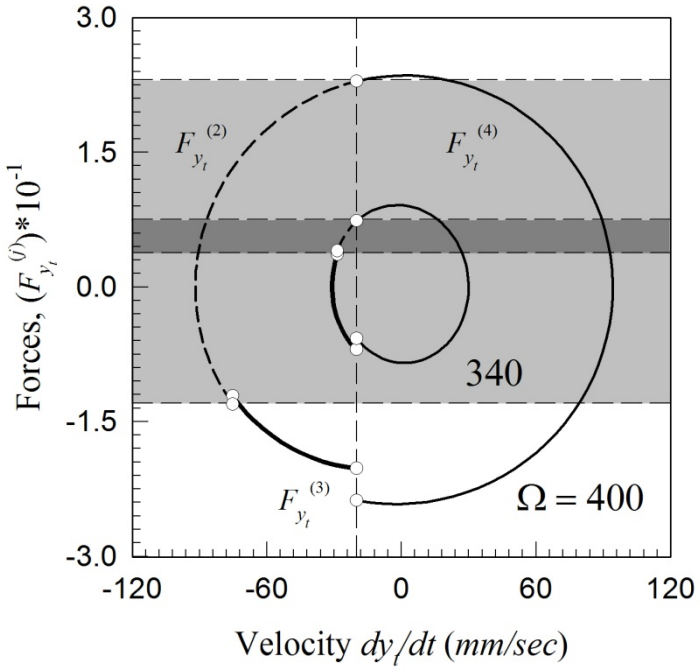

(b)

Fig. 102 Verification of non-stick periodic motions (P_{234}): (a) phase trajectory in phase plane $(y_t, \dot{y}_t)$, b) forces $(F_{y_t}^{(2)}, F_{y_t}^{(3)}, F_{y_t}^{(4)})$ versus $(\dot{y}_t = \dot{\bar{y}})$, $L_c = 0.1(mm)$, $e = 0.1(mm)$ and $\Omega = 340, 400(\frac{rad}{s})$.

$(y_t = \tilde{y})$ for each of the mappings in Fig. 102(b); where the forces $(F_{\tilde{y}}^{(i)})$ versus velocity $(\dot{y}_t = \dot{\tilde{y}})$. The orbit of the low eccentricity frequency $\Omega = 340.0$ $(\frac{rad}{s})$ is small compared to the orbit of the motion with eccentricity frequency $\Omega = 400.0$ $(\frac{rad}{s})$. This occurrence is explained by observing the natural frequencies for this machine-tool reside in two frequency ranges $\omega_n^i \in$ $([210.0, 230.0]$ and $[390.0, 420.0])$ $(\frac{rad}{s})$ for $i = 2, 3, 4$.

The grazing bifurcation of the chip/tool friction boundary could be expected to appear since the amplitude of the orbits reduce with eccentricity frequency (Ω). The simulations will be completed for

$$\Omega V = -20 \text{ and } -40 \ (\tfrac{mm}{s}) \text{ for } \Omega = 250 \ (\tfrac{rad}{s})$$

and

$$\Omega V = -20 \text{ and } -25 \ (\tfrac{mm}{s}) \text{ for } \Omega = 340 \ (\tfrac{rad}{s})$$

in the next section.

Chip Velocity (ΩV)

Consider the periodic interrupted cutting motion defined by the mapping P_{234} with initial conditions, eccentricity frequency (Ω) and chip velocity (ΩV); noted in Table 7, $\Omega = 250$ $(\frac{rad}{s})$ and $\Omega V = -20, -40$ $(\frac{mm}{s})$; respectively (see Fig. 103). Observe the motion through the phase plane where the P_4 mapping is followed by the mapping P_3 and P_2, see Fig. 103(a). This is verified by the forces $(F_{\tilde{y}}^{(i)})$ versus velocity $(\dot{y}_t = \dot{\tilde{y}})$, see Fig. 103(b), but show no potential for concern with this parameter set. The duration of the non-cutting phase (P_2) of the motion is shorter in length since the chip/tool

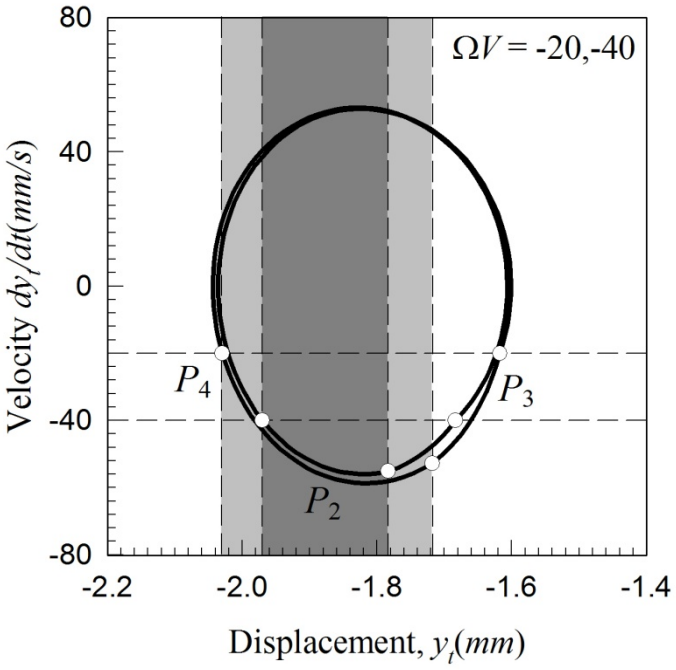

(a)

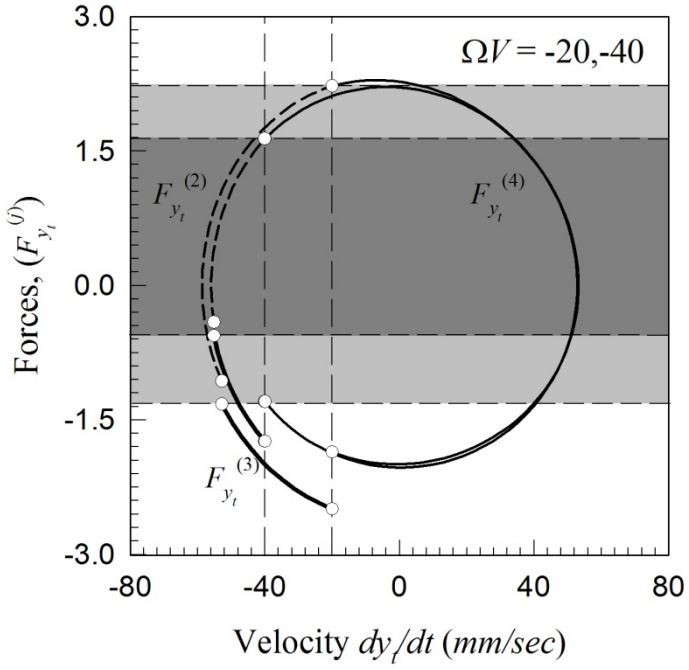

(b)

Fig. 103 Verification of non-stick periodic motions (P_{234}): (a) phase trajectory in phase plane $(y_t, \dot{y}_t)$, b) forces $(F_{y_t}^{(2)}, F_{y_t}^{(3)}, F_{y_t}^{(4)})$ versus $(\dot{y}_t = \dot{\tilde{y}})$, $L_c = 0.1(mm)$, $\Omega V = -20, -40$ $(\frac{mm}{s})$ and $\Omega = 250(\frac{rad}{s})$.

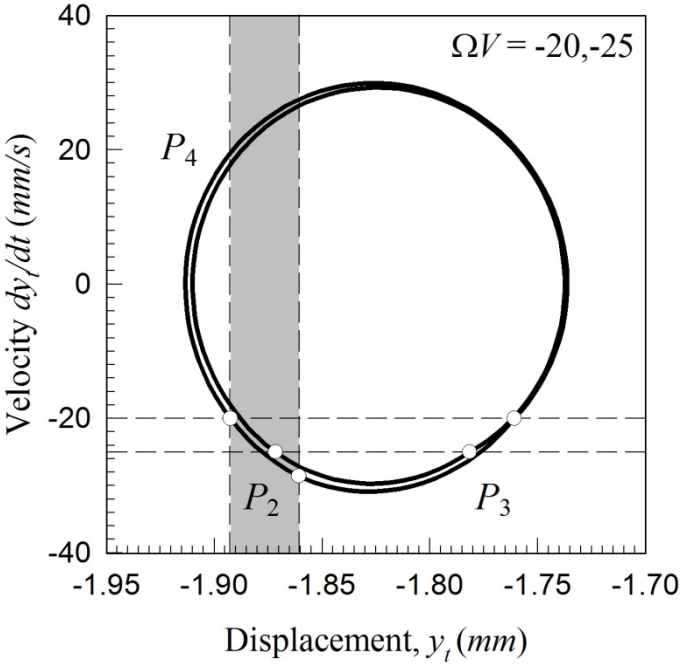

(a)

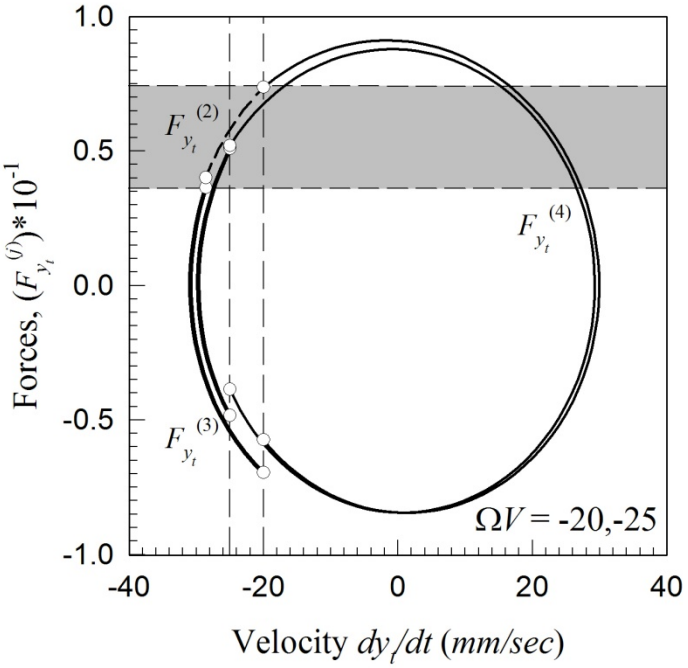

(b)

Fig. 104 Verification of non-stick periodic motions (P_{234}): (a) phase trajectory in phase plane $(y_t, \dot{y}_t)$, b) forces $(F_{y_t}^{(2)}, F_{y_t}^{(3)}, F_{y_t}^{(4)})$ versus $(\dot{y}_t = \dot{\tilde{y}})$, $L_c = 0.1(mm)$, $\Omega V = -20, -25$ $(\frac{mm}{s})$ and $\Omega = 340(\frac{rad}{s})$.

friction boundary interaction with the orbit much lower in the phase plane. Hence; the duration of the non-cutting phase (P_2) of interrupted cutting periodic motion can be reduced by decreasing the chip velocity (ΩV).

Consider the periodic interrupted cutting motion defined by the mapping P_{234} and P_{34} with initial conditions, eccentricity frequency (Ω) and chip velocity (ΩV); noted in Table 7, $\Omega = 340$ $(\frac{rad}{s})$ and $\Omega V = -20,\ -25$ $(\frac{mm}{s})$; respectively (see Fig. 104). Observe the motion through the phase plane where the P_4 mapping is followed by the mapping P_3 and P_2, see Fig. 104(a). This is verified by the forces $(F_{\tilde{y}}^{(i)})$ versus velocity $(\dot{y}_t = \dot{\tilde{y}})$, see Fig. 104(b). Drawing from the above conclusion the P_{34} motion appears as a result of decreasing the chip velocity (ΩV). The simulations will be completed for

$$\mu = 0.1 \text{ and } 2.0 \text{ for } \Omega = 250\ (\tfrac{rad}{s})$$

and

$$\mu = 0.1 \text{ and } 2.0 \text{ for } \Omega = 400\ (\tfrac{rad}{s})$$

in the next section.

Chip/Tool Friction Coefficient (μ)

Consider the periodic interrupted cutting motion defined by the mapping P_{234} with initial conditions, eccentricity frequency (Ω) and chip/tool friction coefficient (μ); noted in Table 7, $\Omega = 250$ $(\frac{rad}{s})$ and $\mu = 0.1,\ 2.0$; respectively (see Fig. 105). Observe the motion through the phase plane where the P_4 mapping is followed by the mapping P_3 and P_2, see Fig. 105(a). This is verified by the forces $(F_{\tilde{y}}^{(i)})$ versus velocity $(\dot{y}_t = \dot{\tilde{y}})$,

see Fig. 105(b). The increase chip/tool friction coefficient (μ) profoundly affects the orbit and slope of the orbit at the switching point on the chip/tool friction boundary (such a claim is supported by the forces plane). Consider the periodic interrupted cutting motion defined by the mapping P_{234} and P_{34} with initial conditions, eccentricity frequency (Ω) and chip/tool friction coefficient (μ); noted in Table 7, $\Omega = 400\ (\frac{rad}{s})$ and $\mu = 0.1,\ 2.0$; respectively (see Fig. 106). Observe the motion through the phase plane where the P_4 mapping is followed by the mapping P_3 and P_2, see Fig. 106(a).

This is verified by the forces $(F_{\tilde{y}}^{(i)})$ versus velocity $(\dot{y}_t = \dot{\tilde{y}})$, see Fig. 106(b). The effects of eccentricity frequency on the orbit of the interrupted cutting motions is varied with respect to the chip/tool friction coefficient (μ). The orbit in the phase plane $(\tilde{y}, \dot{\tilde{y}})$ is smaller in amplitude for

$$\mu = 0.1 \text{ and } \Omega = 250\ (\tfrac{rad}{s})$$

than the orbit for

$$\mu = 2.0 \text{ and } \Omega = 250\ (\tfrac{rad}{s}).$$

However, for the orbit in the phase plane $(\tilde{y}, \dot{\tilde{y}})$ is larger in amplitude for

$$\mu = 2.0 \text{ and } \Omega = 400\ (\tfrac{rad}{s})$$

than the orbit for

$$\mu = 0.1 \text{ and } \Omega = 400\ (\tfrac{rad}{s}).$$

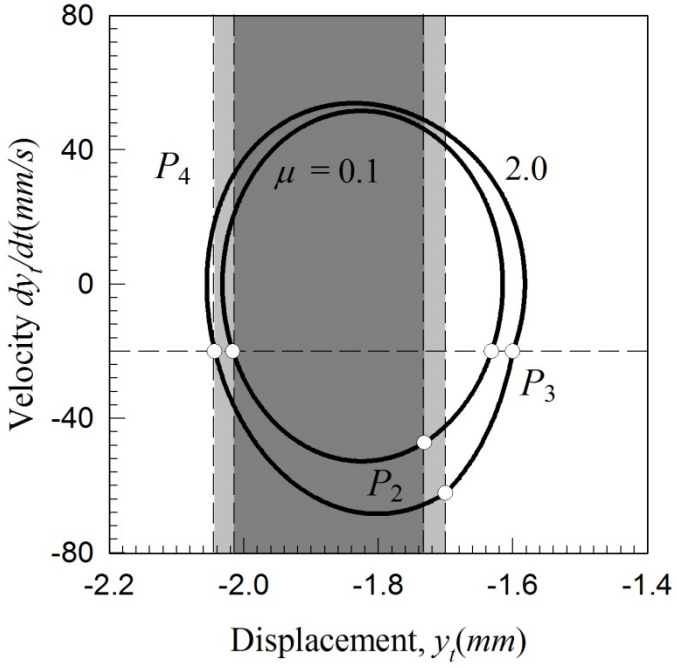

(a)

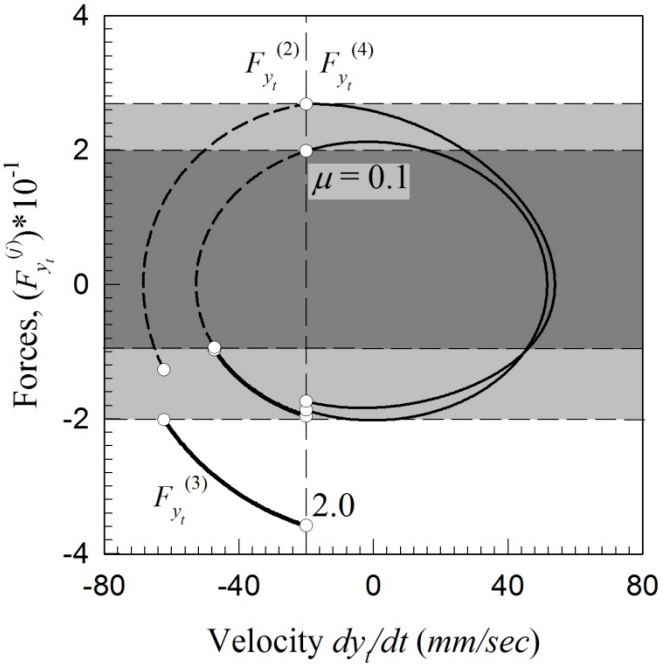

(b)

Fig. 105 Verification of non-stick periodic motions (P_{234}): (a) phase trajectory in phase plane $(y_t, \dot{y}_t)$, b) forces $(F_{y_t}^{(2)}, F_{y_t}^{(3)}, F_{y_t}^{(4)})$ versus $(\dot{y}_t = \dot{\tilde{y}})$, $L_c = 0.1(mm)$, $\mu = 0.1, 2.0$ and $\Omega = 250(\frac{rad}{s})$.

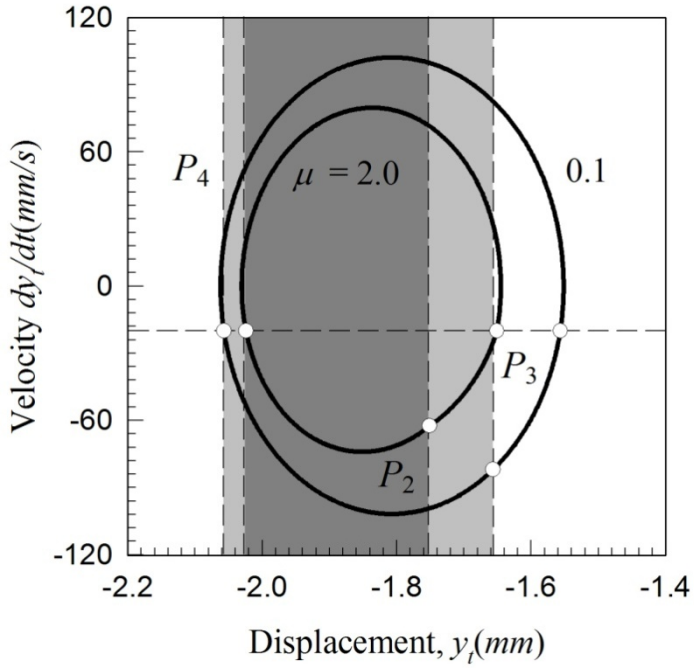

(a)

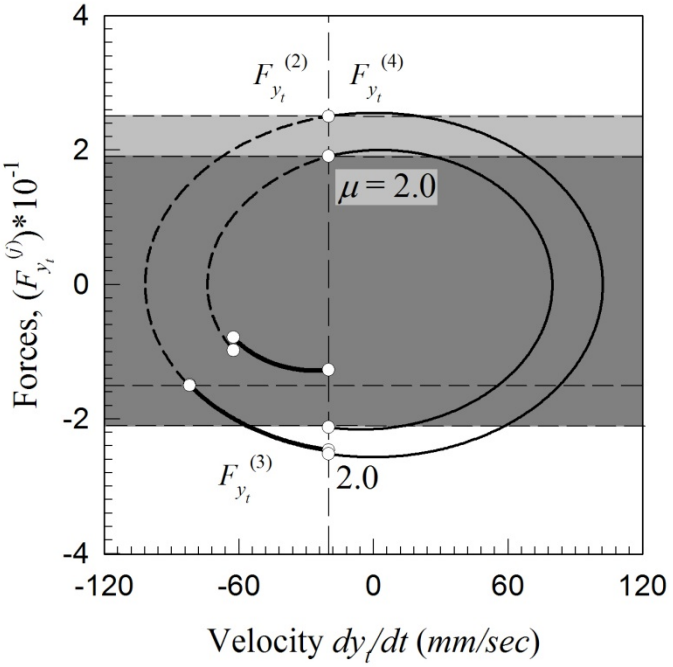

(b)

Fig. 106 Verification of non-stick periodic motions (P_{234}): (a) phase trajectory in phase plane $(y_t, \dot{y}_t)$, b) forces $(F_{y_t}^{(2)}, F_{y_t}^{(3)}, F_{y_t}^{(4)})$ versus $(\dot{y}_t = \dot{\tilde{y}})$, $L_c = 0.1(mm)$, $\mu = 0.1, 2.0$ and $\Omega = 400(\frac{rad}{s})$.

This observation can be summarized by the phase plane $(\tilde{y}, \dot{\tilde{y}})$ orbit amplitude is damped more for higher eccentricity frequencies rather than lower.

Such a qualitative description corresponds to excitation frequencies lower than the highest natural frequency. The simulations will be completed for

$$\Omega V = -20 \text{ and } -40 \ (\tfrac{mm}{s}) \text{ for } \Omega = 250 \ (\tfrac{rad}{s})$$

and

$$\Omega V = -20 \text{ and } -25 \ (\tfrac{mm}{s}) \text{ for } \Omega = 340 \ (\tfrac{rad}{s})$$

in the next section.

Chip Stiffness Coefficient (k_2)

Consider the periodic interrupted cutting motion defined by the mapping P_{234} with initial conditions, eccentricity frequency (Ω) and chip stiffness (k_2); noted in Table 7, $\Omega = 250 \ (\tfrac{rad}{s})$ and $k_2 = 150\text{k}, 400\text{k} \ (\tfrac{N}{mm})$; respectively (see Fig. 107). Observe the motion through the phase plane where the P_4 mapping is followed by the mapping P_3 and P_2, see Fig. 107(a). This is verified by the forces $(F_{\tilde{y}}^{(i)})$ versus velocity $(F_{\dot{\tilde{y}}}^{(i)})$, see Fig. 107(b). Observe how the forces in the force $(F_{\dot{\tilde{y}}}^{(i)})$ verse velocity $(\dot{y}_t = \dot{\tilde{y}})$ plane for $k_2 = 150k \ (\tfrac{N}{mm})$ is nearly zero. Such a point could possibly occur when the motion intersects the chip/tool friction boundary and cause a grazing bifurcation.

The increase of chip stiffness (k_2) corresponds to an increasing amplitude of the orbit in the $(\tilde{y}, \dot{\tilde{y}})$ phase plane. Consider the periodic interrupted cutting motion defined

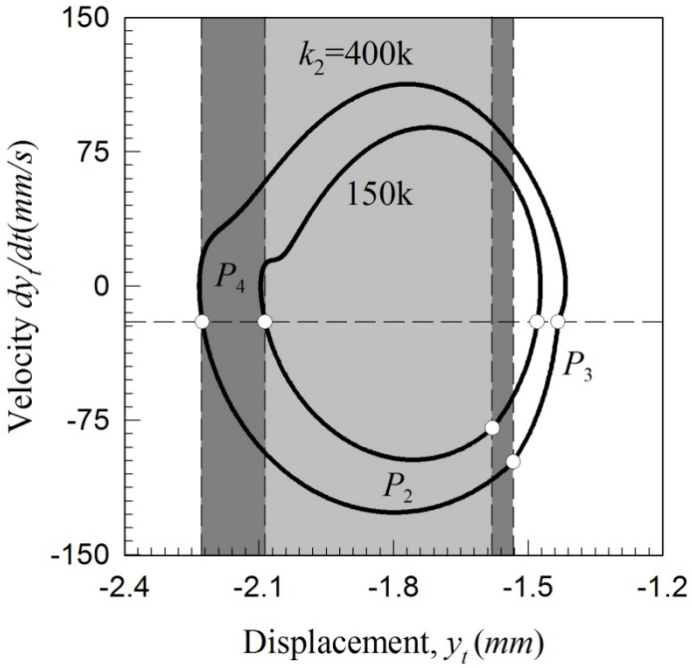

(a)

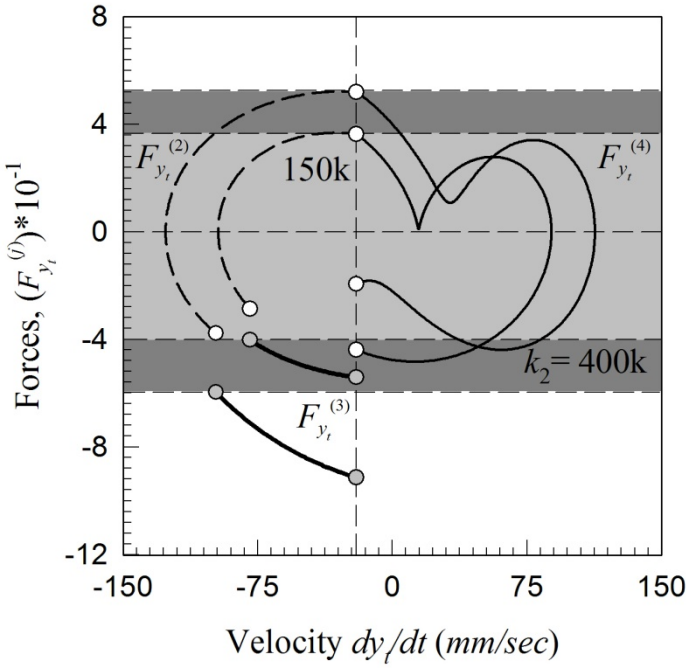

(b)

Fig. 107 Verification of non-stick periodic motions (P_{234}): (a) phase trajectory in phase plane $(y_t, \dot{y}_t)$, b) forces $(F_{y_t}^{(2)}, F_{y_t}^{(3)}, F_{y_t}^{(4)})$ versus $(\dot{y}_t = \dot{\tilde{y}})$, $L_c = 0.1(mm)$, $k_2 = 150k, 400k$ $(\frac{N}{mm})$ and $\Omega = 250(\frac{rad}{s})$.

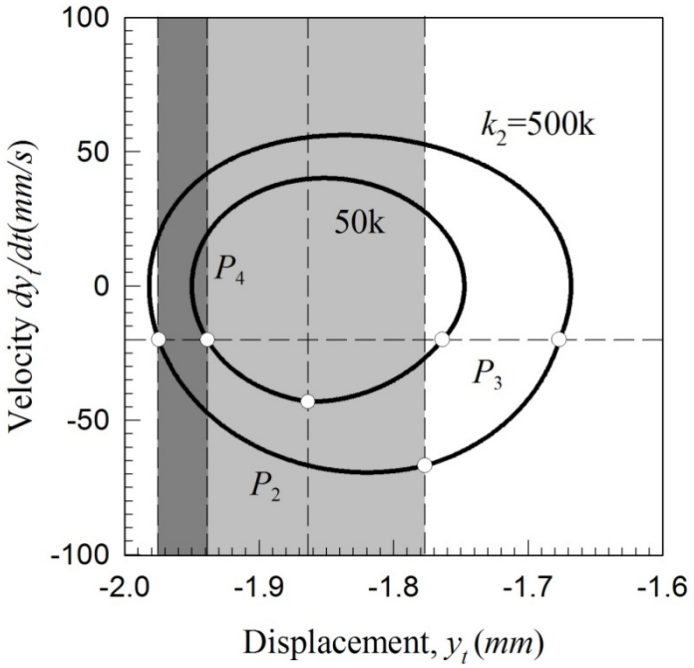

(a)

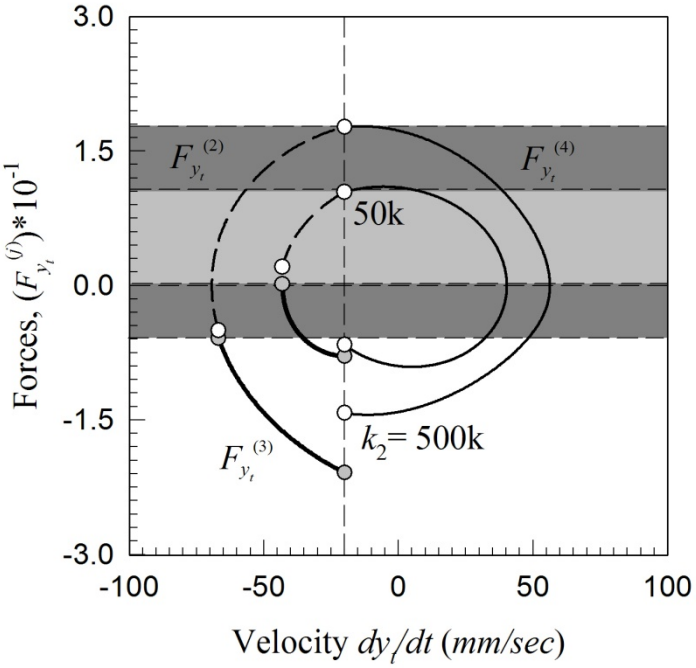

(b)

Fig. 108 Verification of non-stick periodic motions (P_{234}): (a) phase trajectory in phase plane $(y_t, \dot{y}_t)$, b) forces $(F_{y_t}^{(2)}, F_{y_t}^{(3)}, F_{y_t}^{(4)})$ versus $(\dot{y}_t = \dot{\tilde{y}})$, $L_c = 0.1(mm)$, $k_2 = 50k, 500k$ $(\frac{N}{mm})$ and $\Omega = 400(\frac{rad}{s})$.

by the mapping P_{234} with initial conditions, eccentricity frequency (Ω) and chip stiffness (k_2); noted in Table 7, $\Omega = 400\ (\frac{rad}{s})$ and $k_2 = 50\text{k},\ 500\text{k}\ (\frac{N}{mm})$; respectively (see Fig. 108). Observe the motion through the phase plane where the P_4 mapping is followed by the mapping P_3 and P_2, see Fig. 108(a). This is verified by the forces $(F_{\tilde{y}}^{(i)})$ versus velocity $(\dot{y}_t = \dot{\tilde{y}})$, see Fig. 108(b). The orbit in the phase plane $(\tilde{y}, \dot{\tilde{y}})$ is smaller for the chip stiffness,

$$k_2 = 50k\ \ (\tfrac{N}{mm})\ \text{for}\ \Omega = 400\ (\tfrac{rad}{s})$$

than

$$k_2 = 500k\ \ (\tfrac{N}{mm})\ \text{for}\ \Omega = 400\ (\tfrac{rad}{s})$$

and the eccentricity frequency has no effects to contradict this observation.

The flank wear of a tool-piece, when comparing conventional versus interrupted machining mode (IMM) cutting, is typically higher for IMM and especially SS 2541Ca Chandrasekaran and Thoors (1994). The simulations will be completed for

$$L_c = 0.1,\ 0.4\ \ (mm)\ \text{for}\ \Omega = 250\ (\tfrac{rad}{s})$$

in the next section.

Chip Contact Length (L_c)

Consider the periodic interrupted cutting motion defined by the mapping P_{234} with initial conditions, eccentricity frequency (Ω) and chip contact length (L_c); noted in Table 7,

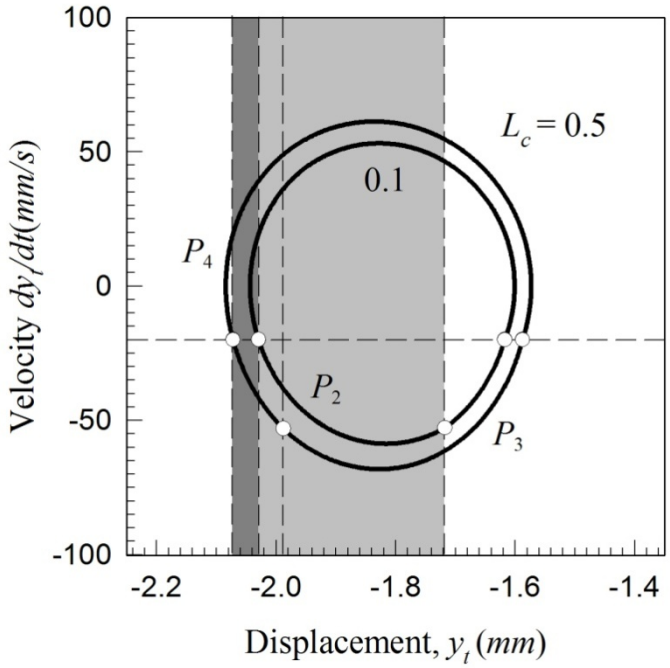

(a)

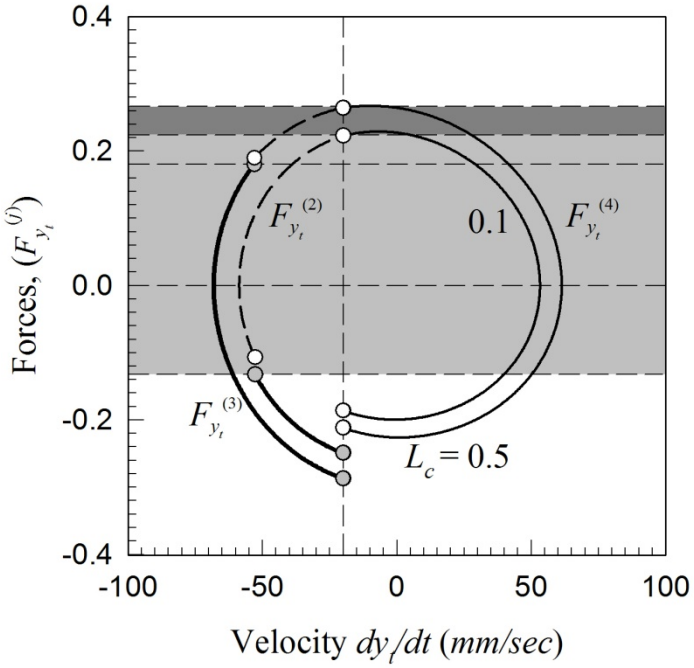

(b)

Fig. 109 Verification of non-stick periodic motions (P_{234}): (a) phase trajectory in phase plane $(y_t, \dot{y}_t)$, b) forces $(F_{y_t}^{(2)}, F_{y_t}^{(3)}, F_{y_t}^{(4)})$ versus $(\dot{y}_t = \dot{\tilde{y}})$, $L_c = 0.1, 0.4(mm)$ and $\Omega = 250(\frac{rad}{s})$.

$\Omega = 250\ (\frac{rad}{s})$ and $L_c = 0.1,\ 0.4\ (mm)$; respectively (see Fig. 107). Observe the motion through the phase plane where the P_4 mapping is followed by the mapping P_3 and P_2, see Fig. 107(a). This is verified by the forces $(F_{\tilde{y}}^{(i)})$ versus velocity $(\dot{y}_t = \dot{\tilde{y}})$, see Fig. 107(b). The increase chip contact length corresponds to an increased orbit in the phase plane. The effects of increased contact length are not significant since the typically observed characteristics of chip formation and dynamics are results of the continuous systems; hence, the contact length has no profound effect on the interaction of the boundaries considered herein due to the linear nature. Such effects are outside the scope of this study. The chip contact length and cutting depth models are validated through high speed micro-photography for interrupted cutting Sutter (2005). The summary / conclusion of this study is presented forthcoming.

CHAPTER XI

SUMMARY / CONCLUSIONS

Summation

Throughout this study the application of discontinuous systems theory by Luo [1] has been applied to a machine-tool analogy model. Such an application is the first among literature to completely define the pass-ability of motion for each of the boundaries considered to be fundamental to the machining process. These boundaries are: the tool/work-piece contact/impact boundary, the onset / disappearance of cutting boundary, the chip/tool friction boundary and the chip vanishing boundary. The discontinuous systems theory has well defined the necessary and sufficient conditions for the pass-ability of the motion. The definitions of the appropriate phase planes for this machine-tool system were developed to analyze the vector fields at the boundaries of the continuous dynamical systems.

The continuous dynamical systems (domains) are: the tool free running; the contact of the tool and work-pieces without cutting; the contact of the tool and work-pieces with cutting, $\dot{\tilde{y}} > V$; contact of the tool and work-pieces with cutting, $\dot{\tilde{y}} < V$; and contact of the tool and work-pieces with chip seizure motion, $\dot{\tilde{y}} \equiv V$. The mappings were developed to complete a structure which defines the periodic motions in this machine-tool system. Through this mapping structure the periodic motions and a range of internal and external dynamics were predicted numerically and analytically. The

extremes of this range illustrate the complex interactions of the continuous systems at the boundaries of these domains. This phenomenon is the stage for future research of this machine-tool system.

The analytical predictions of the cutting action for six system parameters: eccentricity/excitation amplitude (*e/A*), eccentricity frequency (Ω), chip velocity (ΩV), chip stiffness (k_2), chip/tool friction coefficient (μ) and chip contact length (L_c). The causes of interruptions of the periodic orbit by the chip seizure (stick motion) and grazing bifurcations of the frictional boundary (velocity boundary) being dominant routes to unstable motions in this machining system are well defined. The numerical predictions of Chapter VII define parameter boundaries for the chip seizure appearance/disappearance. Interruptions due to the chip/tool frictional force are dependent on critical values of the parameters; where, the eccentricity amplitude (e) has a lower boundary. The eccentricity frequency (Ω) has an upper and lower boundary; the chip velocity (ΩV) has and upper boundary; the friction coefficient (μ) has apparent boundary noting semi-stable motion; and the chip stiffness (k_2) has a value dependent upon the eccentricity frequency (Ω).

These critical values define the boundaries in the six parameter space $(A, \Omega, \Omega V, \mu, k_2, L_c)$ for the interrupted cutting periodic motion. Observing how the dynamics of the periodic cutting motions vary with respect to parameters shows a trend about the sensitivity of the motions to the parameters investigated herein. The dynamics of the machine tool in the cutting process is described through a two degree of freedom

oscillator with a discontinuity, subject to a periodical force input. The analytical solutions for the switching-ability of motion on the discontinuity are presented. The phase trajectory, velocity, and force responses are presented.

The switch ability of motion on the discontinuous boundary is illustrated through force distribution and force product on the boundary. The following conclusions are quantifiably verified in the predictions and simulations of the six parameter space studied.

Claims

The first parameter studied herein was the numerical prediction of the excitation amplitude (A). The periodic motion for this parameter was simplified as the eccentricity amplitude was increased. As observed in a different study the stick-slip combination was forced to purely slip (non-stick, cutting) motion by an appropriate amplitude Gegg et. al. [53]. For $e < 0.0803\ (mm)$ no motion intersected the discontinuity (or pure cutting occurs, no interruptions). The lower extreme of the eccentricity amplitude (e) range exhibited complex motions, such as pseudo-periodic/chaotic motion.

Such complexity trends are attributed to the susceptibility of reduced operating contact forces, thus allowing the chip/tool friction boundary to have increased effects. This is obvious by studding the definition of chip seizure motion defined herein as a negative force product at the switching point. The switching phase was observed to have a dense area of switching points which originated from the onset of *chip seizure.* Such

chip adhesion (seizure) is validated to occur at $e \approx 0.1822\ (mm)$ for $\Omega = 200\ (\frac{rad}{s})$ where added complexity in motion structure appeared as the eccentricity amplitude (e) decreased, see Fig. 22(a,b). Such an observation is concluded to be a route to chaos / unstable motions; which then leads to increased tool wear.

The numerical prediction of the eccentricity frequency (Ω) illustrated a different type of complexity due to the chip seizure motion. The moment the chip seizure motion appeared the chaotic / unstable motion immediately appeared, not the route to chaotic / unstable motion. Although the evolution of the motion is different from the study of eccentricity amplitude (e), the onset of the complex motion is caused again by the appearance of chip seizure. Such chip seizure (domain zero, $\dot{\tilde{y}} \equiv V$) is validated to occur at $\Omega \approx 225.6\ (\frac{rad}{s})$ and $e = 0.1\ (mm)$, see Fig. 26(a,b). The numerical predictions of chip velocity (ΩV) illustrate the route to chaos / semi-stable motion also.

As a result of the reducing chip velocity (ΩV), the contact switching forces oppose each other more readily, thus explaining the increased complexity at lower values. An obvious conclusion from these results is if the relative velocity of the chip and tool rake motion is high the appearance of chip seizure can be avoided. In addition the frictional coefficient must remain low; which is verified by the study of the chip/tool friction coefficient (μ). For this range there are two chip seizure bifurcations for $\Omega = 200\ (\frac{rad}{s})$ well defined at $\mu = 0.210,\ 0.884$ is concluded as the route to chaos / unstable motion for this machine-tool system, see Fig. 32. The grazing bifurcation at $\mu = 0.314$ immediately induces chaos / unstable motion.

The major difference between the opposing vector fields at the chip/tool friction boundary is the force due to friction, and not necessarily the stiffness and damping parameters. Hence, the larger the chip/tool friction coefficient the chip seizure motion will be more apparent. The numerical prediction of chip stiffness (k_2) leads to a similar conclusion that the motions were complicated due to the interaction with *chip seizure,* see Fig. 36. The grazing bifurcations occur at $k_2 = 46.80,\ 74.00,\ 133.20\ (\frac{kN}{mm})$ for $\Omega = 200\ (\frac{rad}{s})$ which further attributes to the complexity of the motions. As a result of varying the chip stiffness the natural frequencies of the machine-tool system vary and move towards one or more of the exciting frequencies; hence, the system experienced more near interruption (grazing bifurcations) possibilities due to the added energy.

The numerical predictions were extended to include the additional verification of analytical prediction. The prediction with regard to boundary three (chip/tool friction boundary) began with the excitation amplitude (A). This study noted parameter boundaries for both excitation amplitude (A) and excitation frequency (Ω), see Fig. 46. The chip seizure appearance parameter boundary is observed to vary with frequency and amplitude of excitation; which infers the energy input from the natural characteristics of the system affect the contact forces and tool velocities. Hence, the chip seizure can be avoided if these boundaries are noted and effective manipulation or control is completed.

The chip velocity (ΩV) directly governs the amount of interruption such a boundary as the chip/tool friction boundary will have on the motion. The chip velocity (ΩV) also exhibits a pure cutting parameter boundary with the chip/tool friction

interaction is noted to be dependent on the natural frequency characteristics of the machine-tool system, see Fig. 50. Similarly, an increasing stiffness coefficient (k_2) leads to a trend of potential stick-slip interruptions noted to be sensitive to chip resistance (k_2) and excitation frequency (Ω), see Fig. 56 and Fig. 58. A claim can be directly made that for high excitation frequencies (at or above the highest natural frequency) the chip seizure phenomenon is more likely to occur due to the grazing bifurcations of the chip/tool friction boundary. This can be attributed to the increase of chip resistance which prevents motion in the direction of the chip shearing. Hence, a reduction in the friction force during interaction with the chip/tool friction boundary (boundary three).

The chip vanishing and chip/tool friction boundaries in combination were also studied for the effects on the multiply connected (interaction with the chip vanishing boundary) continuous domains of this machine-tool system. The motion including the dynamics of reducing chip length (P_2), were studied for the several parameters. The change of eccentricity frequency (Ω) and amplitude (e) affect the magnitude of the switching characteristics; the grazing bifurcation of chip/tool friction boundary and the lower amplitude for the higher eccentricity frequency $e \approx 0.0203$ for $\Omega = 400$ $(\frac{rad}{s})$ and $e \approx 0.0805$ for $\Omega = 250$ $(\frac{rad}{s})$, see Fig. 61 and Fig. 62.

The eccentricity frequency (Ω) showed the grazing bifurcation of the chip/tool friction boundary appeared at $\Omega \approx 0.1915k$ $(\frac{rad}{s})$. By observation the reduction of amplitude between the natural frequency peaks could have led to pure cutting motions if the excitation of the system were reduced. Such an occurrence was discovered by

reducing the eccentricity amplitude where the grazing and chip seizure bifurcations occurred in the neighborhood of $\Omega \approx 0.2210k$, $0.2860k$ and $0.3660k$ $(\frac{rad}{s})$. Depending on the excitation amplitude (e) and frequency (Ω) of the external or self excitation, the *parameter boundary* of chip seizure-cutting motion (stick-slip) became bifurcated at $\Omega \approx 0.2210k$ $(\frac{rad}{s})$ and $0.2860k$ $(\frac{rad}{s})$ for $e = 0.050$ (mm) and $\Omega \approx 0.1910k$ $(\frac{rad}{s})$ for $e = 0.100$ (mm).

In this case, the *parameter boundary* describes the transition from pure cutting motion to stick-slip motion with respect to eccentricity frequency and amplitude (Ω, A), respectively. This can be observed in the results presented in Fig. 63 through Fig. 66. The chip vanishing *parameter boundary* was also shown in the results at $\Omega \approx 0.3780k$ $(\frac{rad}{s})$ for $e = 0.050$ (mm) and $\Omega \approx 0.1945k$ $(\frac{rad}{s})$ for $e = 0.100$ (mm). The *parameter boundary* of chip seizure/grazing bifurcation and chip vanishing varied with respect to chip velocity (ΩV) was defined at $\Omega V \approx 51.41$ $(\frac{mm}{s})$ for $\Omega = 250$ $(\frac{rad}{s})$ and $\Omega V \approx 28.62$ $(\frac{mm}{s})$ for $\Omega = 340$ $(\frac{rad}{s})$. The chip stiffness coefficient (k_2) were presented to show the apparent phase shifting or crossing of a single or group of natural frequencies for the mappings $P_{234} : [0, 500k]$ $(\frac{N}{mm})$, see Fig. 77.

This was also described as the movement of the natural frequencies of the system, due to the ranging of the chip stiffness coefficient (k_2), toward and eventually over, and past the eccentricity frequency (Ω). The chip contact length (L_c) illustrate the switching force products appear to be affected only in the range of $L_c < 0.488$ (mm) for

$\Omega = 250 \ (\frac{rad}{s})$. Hence, the chip contact length only affects the motion until the contact length becomes larger than the total width of the overall displacement orbit of the machine-tool.

The grazing bifurcation *parameter boundary* for these two studies was defined at $L_c \approx 0.488 \ (mm)$ for $\Omega = 250 \ (\frac{rad}{s})$ and $L_c \approx 0.455 \ (\frac{mm}{s})$ for $\Omega = 400 \ (\frac{rad}{s})$. Analytical prediction of these solution sets is successful in comparison to the numerical predictions and additional solutions are also computed and verified. As a result of this research, the loss of effective chip contact is observed to exist near specific points of excitation in this machine-tool system. These areas are in the neighborhood of the natural frequencies of this system. Further verification of the numerical and analytical predictions were completed for both of the analytically predicted mappings P_{34} and P_{234}.

The numerical simulations of analytical predictions for mapping P_{34} began with the excitation amplitude (*A*). The intuitive understanding of the response of linear systems with respect to an exciting amplitude, i.e. the amplitude of the displacement $(\tilde{y})$ and velocity $(\dot{\tilde{y}})$ response increased with an increase of the excitation amplitude (*A*) was observed. The excitation frequency (Ω) affected the amplitude of the orbit in the phase plane; which was noted to not only vary from $\Omega = 385$ to $\Omega = 480$, but the time the motion was affected by domain three (chip reduction, $\dot{\tilde{y}} < V$) parameters was extended. The simulation of two chip velocities (ΩV) show a possible grazing phenomenon occur if the velocity continued to decrease; such cases were observed for both $\Omega = 200, \ 400$

($\frac{rad}{s}$). Finally, the numerical simulations of analytical predictions for mapping P_{234} were verified first with eccentricity amplitude (e). Implications of a trend to relate these parameters in two-dimensional space were apparent.

Additionally, a limit was suggested where the interruptions due to the chip/tool friction and chip vanishing boundaries had no adverse effects on the machine-tool system as similarly completed for the stability boundary in Gurney and Tobias [59]. The orbit of the low eccentricity frequency $\Omega = 340.0$ ($\frac{rad}{s}$) was small compared to the orbit of the motion with eccentricity frequency $\Omega = 400.0$ ($\frac{rad}{s}$). This occurrence was explained by observing the natural frequencies for this machine-tool reside in two frequency ranges $\omega_n^i \in$ ($[210.0, 230.0]$ and $[390.0, 420.0]$) ($\frac{rad}{s}$) for i = 2, 3, 4. The grazing bifurcation of the chip/tool friction boundary could be expected to appear since the amplitude of the orbits reduced with eccentricity frequency (Ω). The chip velocity (ΩV) noted the duration of the non-cutting phase (P_2) of the motion was shorter in length since the chip/tool friction boundary interaction with the orbit is much lower in the phase plane.

Hence; the duration of the non-cutting phase (P_2) of interrupted cutting periodic motion could be reduced by decreasing the chip velocity (ΩV) or increasing the relative velocity between the chip and tool-piece. Drawing from the above conclusion the P_{34} motion appeared as a result of decreased chip velocity (ΩV) in Fig. 104. The chip/tool friction coefficient (μ) increase profoundly affected the orbit and slope of the orbit at the switching point on the chip/tool friction boundary (such a claim is supported by the

forces plane). The orbit in the phase plane $(\tilde{y}, \dot{\tilde{y}})$ is smaller in amplitude for $\mu = 0.1$ and $\Omega = 250$ $(\frac{rad}{s})$ than the orbit for $\mu = 2.0$ and $\Omega = 250$ $(\frac{rad}{s})$.

However, for the orbit in the phase plane $(\tilde{y}, \dot{\tilde{y}})$ was larger in amplitude for $\mu = 2.0$ and $\Omega = 400$ $(\frac{rad}{s})$ than the orbit for $\mu = 0.1$ and $\Omega = 400$ $(\frac{rad}{s})$. This observation can be summarized by the phase plane $(\tilde{y}, \dot{\tilde{y}})$ orbit amplitude was damped more for higher rather than lower eccentricity frequencies (Ω). Such a qualitative description corresponds to excitation frequencies lower than the highest natural frequency. The chip stiffness coefficient (k_2) increase corresponds to increased amplitude of the orbit in the $(\tilde{y}, \dot{\tilde{y}})$ phase plane. The orbit in the phase plane $(\tilde{y}, \dot{\tilde{y}})$ was smaller for the chip stiffness, $k_2 = 50k$ $(\frac{N}{mm})$ for $\Omega = 400$ $(\frac{rad}{s})$ than $k_2 = 500k$ $(\frac{N}{mm})$ for $\Omega = 400$ $(\frac{rad}{s})$ and the eccentricity frequency (Ω) had no effects to contradict this observation.

The chip contact length (L_c) increase corresponds to an increased orbit in the phase plane $(\tilde{y}, \dot{\tilde{y}})$. The effects of increased contact length (L_c) were not significant since the typically observed characteristics of chip formation and dynamics are results of the continuous systems; hence, the contact length has no profound effect on the interaction of the boundaries considered herein due to the defined linear nature. Such effects are outside the scope of this study. Additionally, when the contact length becomes longer than the width of the displacement orbit; the variation of the chip contact length will not have a profound effect on the motion.

Objective Completion

Ideal operation of a machine-tool system over a broad range of parameters exhibiting semi-stable / stable characteristics is the end goal of this research. In effort to achieve this end, the following items were completed:

1. This research established definitions of the underlying dynamics of interrupted cutting motions in a machining-system;
2. The modeling procedure for a machine-tool system with discontinuities was developed;
3. This research defined qualitative and quantitative definitions of how the semi-stable interrupted cutting periodic motions lead to unstable motions and vice versa.

The definitions of the underlying dynamics for interrupted cutting motion were developed through the application of discontinuous systems theory by Luo [1]. The pass-ability of the motion through and along the boundaries of this machine-tool model defined both qualitative and quantitative characteristics of the underlying dynamics. The derivation of the phase planes, domains, state, force vector fields, boundary dynamics and switching planes lends a path for modeling of any discontinuous system of a similar nature.

The mappings, mappings structures, and force conditions are the end result of this modeling procedure. Although the semi-stable motions do not contain purely desirable traits, the boundary interactions illustrate the possibility of stable motions due simply to the interaction. As noted in this dissertation, existing studies dominantly refer to the wear and maintenance issues are controllable if the underlying dynamics are completely

understood. Hence; this research completes the main objective by contributing an accurate method for interactions of a machine-tool model with various boundaries.

Research Pathway Completion and Extension

Although this research analyzes a machine-tool system inspired by the work of Wu and Liu [19,20] and Grabec [23,27], the model studied herein is more comprehensive in the number of boundaries considered. Hence, this machine-tool model herein is established as unique in nature and focus of study. Specifically, the research path of this dissertation begins with the application of discontinuous systems by Luo [1] to investigate a machine-tool system. This step was completed in Chapters I-IV, with many examples of equation breakdown and motion specific phenomena. The criteria for the interrupted cutting periodic motions was developed through the state and mapping forms for the four boundaries defined herein (Chapter IV).

The mappings for the specific motions considered herein are defined with simulated cases (Chapter V). The numerical and analytical prediction of solutions structure routine is developed for three specific types of interrupted cutting periodic motion (Chapter VI). The application of the prediction routines begin with numerical predictions of Chapter VII for various parameters. The analytical validation of numerically predicted interrupted cutting periodic motions is completed for two types of motions in Chapter IX. Additional verification of this analytically and numerically predicted motion is completed by numerical simulation in Chapters VIII and X. Specific to the phenomenon defined, predicted and observed herein are the near

interruption (grazing bifurcation) of cutting in the machine-tool system.

The chip and tool-piece seizure in the machine-tool system is also defined, predicted and observed specifically to induce route to unstable, pseudo-chaotic or chaotic motions in the machine-tool. The tasks noted at the beginning of this dissertation have been fulfilled beyond initial expectations and have led to qualitative and quantitative definitions of the underlying dynamics for this machine-tool system. These definitions are observed, noted, but not developed fully in literature; herein lays the significance.

REFERENCES

1. Luo, A. C., 2005, "A Theory for Non-Smooth Dynamical Systems on Connectable Domains," Communication in Nonlinear Science and Numerical Simulation, **10**, pp.1-55.

2. Merchant, M. E., 1945, "Mechanics of the Metal Cutting Process. I. Orthogonal Cutting and a Type 2 Chip," Journal of Applied Physics, **16**, pp.267-275.

3. Merchant, M. 1945, "Mechanics of Metal Cutting Process. II Plasticity Conditions in Orthogonal Cutting," Journal of Applied Physics, **16**(5), pp.318-324.

4. Oxley, P. L., 1961, "Mechanics of Metal Cutting," International Journal of Machine Tool Design Research, **1**, pp.89-97.

5. Childs, T.H.C., 2007, "Numerical Experiments on the Influence of Material and other Variables on Plane Strain Continuous Chip Formation in Metal Machining," International Journal of Mechanical Sciences, **48**, pp. 307-322.

6. Rubenstien, C. and Storie, R.M., 1969, "The Cutting of Polymers," International Journal of Machine Tool Design and Research, **9**, pp.117-130.

7. Shouchry, A., 1979, "Metal Cutting and Plasticity Theory," Wear, **55**, pp.313-329.

8. Basuray, P. M., 1977, "Transition from Plughing to Cutting During Machining with Blunt Tools," Wear, **43**, pp.341-349.

9. Wright, P.K., Horne, J.G., and Tabor, D., 1979, "Boundary Conditions at the Chip-Tool Interface in Machining: Comparison Between Seizure and Sliding Friction," Wear, **54**, pp.371-390.

10. Astakhov, V.P., Shvets, S.V. and Osman, M.O.M., 1997, "Chip Structure Classification Based on Mechanics of its Formation," Journal of Materials Processing Technology, **71**, pp.247-257.

11. Son, S., Lim, H., and Ahn, J., 2005, "Effects of the Friction Coefficient on the Minimum Cutting Thickness in Micro Cutting," International Journal of Machine Tools & Manufacture, **45**, pp.529-535.

12. Liu, K. and Melkote, S.N., 2006, "Effect of Plastic Side Flow on Surface Roughness in Micro-Turning Process," International Journal of Machine Tools & Manufacture, **46**, pp.1778-1785.

13. Son, S., Lim, H., and Ahn, J., 2006, "The Effect of Vibration Cutting on Minimum Cutting Thickness," International Journal of Machine Tools & Manufacture, **46**, pp.2066-2072.

14. Simoneau, A., Ng, E., and Elbestawi, M.A., 2006, "Chip Formation During Microscale Cutting of a Medium Carbon Steel," International Journal of Machine Tools & Manufacture, **46**, pp.467-481.

15. Woon, K. S., Rahman, M., Neo, K. S., and Liu, K., 2008, "The Effect of Tool Edge Radius on the Contact Phenomenon of Tool-Based Micromachining," International Journal of Machine Tools & Manufacture, **48**(12-13), pp.1395-1407.

16. Wahi, P. and Chatterjee, A., 2008, "Self-Interrupted Regenerative Metal Cutting in Turning," International Journal of Non-linear Mechanics, **43**, pp.111-123.

17. Vela-Martinez, L., Jauregui-Correa, J.C., Rubio-Cerda, E., Herrera-Ruiz, G. and Lozano-Guzman, A., 2008, "Analysis of Compliance Between the Cutting Tool and the Work Piece on the Stability of a Turning Process," International Journal of Machine Tools & Manufacture, **48**, pp.1054-1062.

18. Moon, F.C. and Kalmar-Nagy, T., 2001, "Nonlinear Models for Complex Dynamics in Cutting Materials," Philosophical Transactions of the Royal Society of London A, **359**, pp.695-711.

19. Wu, D.W. and Liu, C.R., 1984, "An Analytical Model of Cutting Dynamics. Part 1: Model Building," The American Society of Mechanical Engineers, 84-WA/Prod-**20**, pp.107-111.

20. Wu, D.W. and Liu, C.R., 1984, "An Analytical Model of Cutting Dynamics. Part 2: Verification," The American Society of Mechanical Engineers, 84-WA/Prod-**21**, pp.112-118.

21. Kim, J.S. and Lee, B.H., 1991, "An Analytical Model of Dynamic Cutting Forces in Chatter Vibration," International Journal of Machine Tools Manufacturing, **31**, pp.371-381.

22. Tarng, Y.S., Young, H.T., and Lee, B.Y., 1994, "An Analytical Model of Chatter Vibration in Metal Cutting," International Journal of Machine Tools Manufacturing, **34**, pp.183-197.

23. Grabec, I., 1988, "Chaotic Dynamics of the Cutting Process," International Journal of Machine Tools and Manufacturing, **28**, pp.19-32.

24. Wiercigroch, M. and Cheng, A.H-D.,1997, "Chaotic and Stochastic Dynamics of Orthogonal Metal Cutting," Chaos, Solitons & Fractals, **8**, pp.715-726.

25. Wiercigroch, M., 1997, "Chaotic Vibration of A Simple Model of the Machine Tool-Cutting Process System," Transactions of the ASME: Journal of Vibration and Acoustics, **119**, pp.468-475.

26. Berger, B.S., Rokni, M., and Minis, I., 1992, "The Nonlinear Dynamics of Metal Cutting," International Journal of Engineering Science, **30**, pp. 1433-1440.

27. Grabec, I., 1986, "Chaos Generated by the Cutting Process," Physics Letters A, **117**(8), pp.384-386.

28. Chandiramani, N.K. and Pothala, T., 2006, "Dynamics of 2-dof Regenerative Chatter During Turning," Journal of Sound and Vibration, **290**, pp.488-464.

29. Wiercigroch, M. and Budak, E., 2001, "Sources of Nonlinearities, Chatter Generation and Suppression in Metal Cutting," Philosophical Transactions of the Royal Society of London A , **359**, pp.663-693.

30. Fang, N. and Jawahir, I.S., 2002, "Analytical Predictions and Experimental Validation of Cutting Force Ratio, Chip Thickness, and Chip Back-Flow Angle in Restricted Contact Machining Using the Universal Slip-Line Model," International Journal of Machine Tools & Manufacture, **42**, pp.681-694.

31. Luo, A. C. and Gegg, B.C., 2004, "Grazing Phenomena in a Periodically Forced, Linear Oscillator with Dry Friction," Communications in Nonlinear Science and Numerical Simulation, **11**(7), pp.777-802.

32. Wiercigroch, M., 1994, "A Note on the Switch Function for the Stick-Slip Phenomenon," Journal of Sound and Vibration, **175**(5), pp.700-704.

33. Gegg, B. C., Suh, C. S. and Luo, A. C. J., 2008, "Chip Stick and Slip Periodic Motions of a Machine Tool in the Cutting Process," ASME Manufacturing Science and Engineering Conference Proceedings, *Proceedings of the ASME International Manufacturing Science and Engineering Conference,* MSEC ICMP2008/DYN-72052, October 7th-10th.

34. Wiercigroch, M. and de Kraker, B., 2000, "Applied Nonlinear Dynamics and Chaos of Mechanical Systems with Discontinuities," World Scientific Series A, **28**.

35. Warminski, J. Litak, G, Cartmell, M.P., Khanin, R., Wiercigroch, M., 2003, "Approximate Analytical Solution for Primary Chatter in the Non-Linear Metal Cutting Model," Journal of Sound and Vibration, **259**(4), pp.917-933.

36. Hartog, J. D., 1931, "Forced Vibrations with Coulomb and Viscous Damping," Transactions of the American Society of mechanical Engineers, **53**, pp.107-115.

37. Filippov, A.F., 1964, "Differential Equations with Discontinuous Right-hand Side," American Mathematical Society Translations, Series 2, **42**, pp. 199-231.

38. Filippov, A.F., 1988, *Differential Equations with Discontinuous Right-hand Sides*, Kluwer Academic Publishers, Boston.

39. Aubin, J.P. and Cellina, A., 1984, *Differential Inclusions*, Springer-Verlag: Berlin.

40. Aubin, J.P and Frankowska, H., 1989, *Set-Valued Analysis*, Birkhauser, Boston.

41. Luo, A., 2005, "Imaginary, Sink and Source Flows in the Vicinity of the Separatrix of Non-Smooth Dynamic System," Journal of Sound and Vibration, **285**, pp.443-456.

42. Luo, A.C.J. and Gegg, B.C., 2006, "Dynamics of a Harmonically Excited Oscillator with Dry-Friction on a Sinusoidally Time-Varying, Traveling Surface," International Journal of Bifurcation and Chaos, **16**(12), pp.3539-3566.

43. Luo, A.C.J. and Gegg. B.C., 2006, "Stick and Non-Stick Periodic Motions in a Periodically Forced, Linear Oscillator with Dry-Friction," Journal of Sound and Vibration, **291**, pp.132-168.

44. Luo, A.C.J. and Gegg, B.C. 2006, "Periodic Motions in a Periodically Forced Oscillator Moving on an Oscillating Belt with Dry Friction," Journal of Computational and Nonlinear Dynamics, **1**(3), pp.212-220.

45. Shaw, M., 2005, *Metal Cutting Principles*, Oxford University Press, Oxford.

46. Dassanayake, A. V., 2006, "Machining Dyanmics and Stability Analysis in Longitudinal Turning Involving Workpiece Whirling," Ph.D. Dissertaton, Texas A&M University, August.

47. Gegg, B.C., 2005 "Stick and Non-Stick Periodic Motions in a Periodically Forced, Linear Oscillator with Dry Friction," Master Thesis: Southern Illinois University at Edwardsville, August.

48. Heath, M.T., 2002, *Scientific Computing: An Introductory Survey*, 2nd Ed., McGraw-Hill Higher Education: Boston.

49. Chapra, S.C. and Canale, R.P. 2002, *Numerical Methods for Engineers*, 4th Ed., McGraw-Hill Higher Educaton: Boston.

50. Press, W.H., Flannery, B.P., Teukolsky, S.A., and Vetterling, W.T. 1986, *Numerical Recipes: The Art of Scientific Computing*, Cambridge University Press, Cambridge.

51. Devaney, R.L. 2003, *An Introduction to Chaotic Dynamical Systems*, 2nd Ed., Westview Press: Advanced Book Program, Boulder.

52. Devaney, R.L. 1992, *A First Course in Chaotic Dynamical Systems: Theory and Experiment*, Westview Press: Advanced Book Program, Studies in Nonlinearity, Westview.

53. Gegg, B.C., Suh, C.S. and Luo, A.C.J. 2007, "Periodic Motions of the Machine Tools in Cutting Process," *Proceedings of the ASME International Design Engineering and Technical Conference,* DETC2007/VIB-**35166**, Las Vegas, Nevada, September 4th-7th.

54. Chandrasekaran, H. and Thoors, H., 1994, "Tribology in Interrupted Machining: Role of Interruption Cycle and Work Material," Wear, **179**, pp.83-88.

55. Chou, Y.K. and Evans, C.J., 1999, "Cubic Boron Nitride Tool Wear in Interrupted Hard Cutting," Wear, **225-229**, pp.234-245.

56. Maity, K.P. and Das, N.S., 2001, "A Class of slipline Field Solutions for Metal Machining with slipping and Sticking Contact at the Chip-Tool Interface," International Journal of Mechanical Science, **43**, pp.2435-2452.

57. Gegg, B.C., Steve Suh, Albert C.J. Luo, "Analytical Prediction of Interrupted Cutting Periodic Motions in a Machine Tool," *Proceedings of the 2nd International Nonlinear Science and Complexity Conference,* NSC2008-**97**, NSC 2008 Porto, Portugal, July 28th-31st.

58. Gekonade, H.O. and Subramanian, S.V. 2002, "Tribology of Tool-Chip Interface and Tool Wear Mechanisms," Surface and Coatings Technology, **149**, pp.151-160.

59. Gurney, J.P. and Tobias, S.A., 1961, "A Graphical Method for the Determination of the Dynamic Stability of Machine Tools," International Journal of Machine Tool Design Research, **1**, pp.148-156.

APPENDIX

Discontinuous Systems Theory

For a general discontinuous system, consider a planar, dynamic system consisting of *n*-dynamic sub-systems in a universal domain $\Sigma \subset \Re^2$, divided into *n* accessible sub-domains Σ_i; and the union of all the accessible sub-domains $\bigcup_{i=1}^{n} \Sigma_i$, see Fig.A 1. On the *i*th sub-domain, there is a continuous system in the form of

$$\dot{\mathbf{x}} \equiv \mathbf{F}^{(i)}\left(\mathbf{x}, t, \boldsymbol{\mu}_i, \boldsymbol{\pi}\right) = \mathbf{f}^{(i)}\left(\mathbf{x}, \boldsymbol{\mu}_i\right) + \mathbf{g}(\mathbf{x}, t, \boldsymbol{\pi}), \quad \mathbf{x} = \left(x, y\right)^T \in \Sigma_i \tag{A1}$$

where $\mathbf{g} = \left(g_1, g_2\right)^T$ is a bounded, periodic vector function with period *T* and a parameter vector $\boldsymbol{\pi} = \left(\pi_1, \pi_2 \cdots, \pi_m\right)^T \in \Re^m$. Notice that the superscript "T" represents the transpose. The vector field $\mathbf{f}^{(i)} = \left(f_1^{(i)}, f_2^{(i)}\right)^T \in \Re^2$ with parameter vectors $\boldsymbol{\mu}_i = \left(\mu_{i1}, \mu_{i2}, \cdots, \mu_{in}\right)^T \in \Re^n$ is C^r-continuous ($r \geq 2$). The boundary dynamics will be presented in the next section. In all the accessible sub-domains Σ_i, the dynamical system in Eq.(A1) is continuous and the corresponding continuous flow is $\mathbf{x}^{(i)}\left(t\right) = \boldsymbol{\Phi}^{(i)}\left(\mathbf{x}^{(i)}\left(t_0\right), t, \boldsymbol{\mu}_i, \boldsymbol{\pi}\right)$ with $\mathbf{x}^{(i)}\left(t_0\right) = \boldsymbol{\Phi}^{(i)}\left(\mathbf{x}^{(i)}\left(t_0\right), t_0, \boldsymbol{\mu}_i, \boldsymbol{\pi}\right)$ accordingly. Figure A1 illustrates the connectable domains and the existence of an interface between the dynamic systems Σ_i and Σ_j, where $S_{ij} \subset \Re^1$ and $S \subset \Re^1$ are the bounds of sub-domains and bounds of the universal domain, respectively.

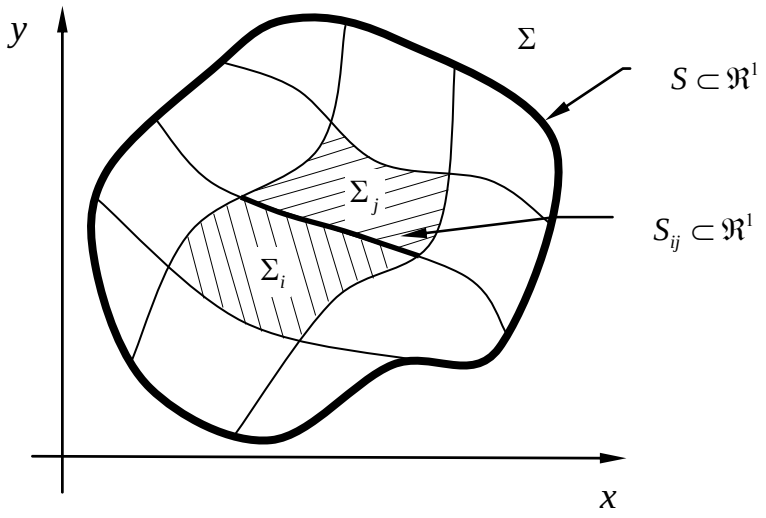

Fig.A 1 Phase space: connectable domain.

It is assumed, that the following conditions hold for the non-smooth dynamic system theory

A1: The switching between two adjacent sub-systems possesses time-continuity.

A2: For an unbounded, accessible sub-domain Σ_i, the corresponding vector field and flows are bounded in any bounded domain $\Sigma_i \subset \Sigma$, i.e., there exist constant K_1 and K_2 such that

$$\left\|\mathbf{f}^{(i)}\right\| + \left\|\mathbf{g}\right\| \le K_1 \text{ on } \Sigma_i, \text{ and } \left\|\mathbf{\Phi}^{(i)}\right\| \le K_2 \left(\text{const}\right) \text{ for } t \in \left[0,\infty\right). \tag{A2}$$

A3: For a bounded, accessible domain Σ_i, the corresponding vector field is bounded, but the flow may be unbounded in the bounded domain $\Sigma_i \subset \Sigma$, i.e.,

$$\left\|\mathbf{f}^{(i)}\right\|+\|\mathbf{g}\|\le K_1(\text{const}) \text{ on } \Sigma_i, \text{ and } \left\|\mathbf{\Phi}^{(i)}\right\|<\infty \text{ for } t\in[0,\infty). \tag{A3}$$

The boundary set in the 2-D phase space is defined as

$$\partial\Sigma_{ij}=\left\{(x,y)\middle|(x,y)\in\Sigma_i\bigcap\Sigma_j\subset\Re^1 \text{ satisfying } \varphi_{ij}(x,y)=0\right\}, \tag{A4}$$

see Fig.A 2. Generally, $\partial\Sigma_{ij}$ is a curve, which satisfies $\varphi_{ij}(x,y)=0$ for some φ_{ij}. The boundary set is a definition of the discontinuity and therefore the focal point.

The intersection and exiting of motion to and from the boundary set, respectively, exists in many forms and fashions. As in Luo [1], the real and imaginary flows concepts or intersecting and exiting the boundary set, are re-stated herein. The termed *real* flow, or actual motion, $\mathbf{x}_i^{(i)}(t)$ in Σ_i is governed by a dynamical system on its own domain;

$$\dot{\mathbf{x}}_i^{(i)}\equiv\mathbf{F}^{(i)}\left(\mathbf{x}_i^{(i)},t,\boldsymbol{\mu}_i,\boldsymbol{\pi}\right)\in\Re^2,\ \mathbf{x}_i^{(i)}=\left(x_i^{(i)},y_i^{(i)}\right)^T\in\Sigma_i, \tag{A5}$$

with the initial conditions

$$\mathbf{x}_i^{(i)}(t_0)=\mathbf{\Phi}^{(i)}\left(\mathbf{x}_i^{(i)}(t_0),t_0,\boldsymbol{\mu}_i,\boldsymbol{\pi}\right). \tag{A6}$$

The subscript and superscript on the $\mathbf{x}_i^{(i)}(t)$ denotes the flow in the i^{th} sub-domain Σ_i, governed by a dynamical system defined on the i^{th} sub-domain Σ_i. Consider the j^{th} imaginary flow in the i^{th}-domain Σ_i is a flow in Σ_i governed by the dynamical system defined on the j^{th}-sub-domain Σ_j.

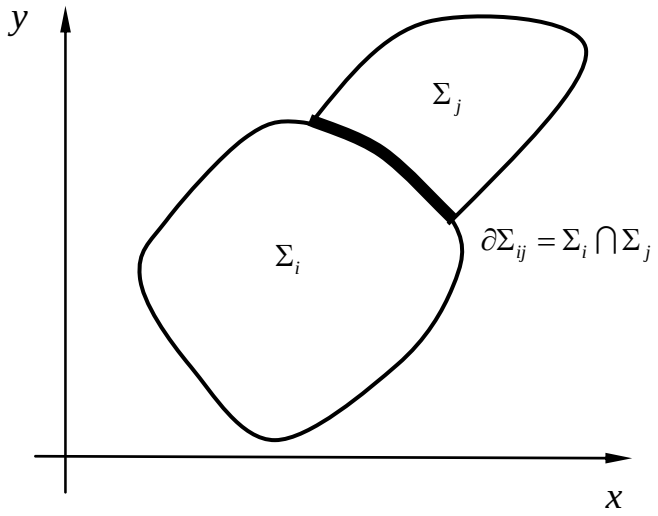

Fig.A 2 Sub-domains Σ_i and Σ_j, and the corresponding boundary $\partial\Sigma_{ij}$.

The flow is not a real one governed by the non-smooth dynamical system, thus this flow is also termed the *imaginary* flow, or imaginary motion, in this sense; i.e.,

$$\dot{\mathbf{x}}_i^{(j)} \equiv \mathbf{F}^{(j)}\left(\mathbf{x}_i^{(j)}, t, \boldsymbol{\mu}_j, \boldsymbol{\pi}\right) \in \Re^2, \ \ \mathbf{x}_i^{(j)} = \left(x_i^{(j)}, y_i^{(j)}\right)^T \in \Sigma_i, \tag{A7}$$

with the initial conditions

$$\mathbf{x}_i^{(j)}\left(t_0\right) = \boldsymbol{\Phi}^{(j)}\left(\mathbf{x}_i^{(j)}\left(t_0\right), t_0, \boldsymbol{\mu}_j, \boldsymbol{\pi}\right). \tag{A8}$$

The difference in the subscript and superscript on *x* denote such *imaginary* flow or application of the adjacent domain dynamic system parameters for computation of flow. The flow intersecting the boundary set utilizes the definitions of *real* and *imaginary* flow to define the existence of passage through the boundary set. The motion approaching and exiting the discontinuous boundary in the sub-domains for a semi-passable boundary

set $\overrightarrow{\partial\Sigma_{ij}}$ from the domain Σ_i to Σ_j convex to Σ_j is illustrated in Fig.A 3. The motion in a semi-passable boundary set $\overrightarrow{\partial\Sigma_{ij}}$ from the domain Σ_i to Σ_j convex to Σ_i is illustrated in Fig.A 4.

The curvature is denoted for the most general case and not particular to the results or specific model presented herein. The non-empty boundary set $\partial\Sigma_{ij}$ is semi-passable from the domain Σ_i to Σ_j if and only if

$$\left.\begin{array}{l}\text{either } \mathbf{n}_{\partial\Sigma_{ij}}^T \bullet \mathbf{F}_i^{(\alpha)}\left(t_{m-}\right) > 0 \text{ and } \mathbf{n}_{\partial\Omega_{ij}}^T \bullet \mathbf{F}_j^{(\beta)}\left(t_{m+}\right) > 0 \text{ for } \partial\Sigma_{ij} \text{ convex to } \Sigma_j, \\ \text{or} \quad \mathbf{n}_{\partial\Sigma_{ij}}^T \bullet \mathbf{F}_i^{(\alpha)}\left(t_{m-}\right) < 0 \text{ and } \mathbf{n}_{\partial\Omega_{ij}}^T \bullet \mathbf{F}_j^{(\beta)}\left(t_{m+}\right) < 0 \text{ for } \partial\Sigma_{ij} \text{ convex to } \Sigma_i \end{array}\right\} \tag{A9}$$

which simplifies to

$$\left[\mathbf{n}_{\partial\Sigma_{ij}}^T \bullet \mathbf{F}_i^{(\alpha)}\left(t_{m-}\right)\right] \times \left[\mathbf{n}_{\partial\Sigma_{ij}}^T \bullet \mathbf{F}_j^{(\beta)}\left(t_{m+}\right)\right] > 0, \tag{A10}$$

with $\mathbf{F}_i^{(\alpha)}\left(t_{m-}\right) = \mathbf{F}^{(\alpha)}\left(\mathbf{x}, t_{m-}, \boldsymbol{\mu}_i, \boldsymbol{\pi}\right)$ and $\mathbf{F}_j^{(\beta)}\left(t_{m+}\right) = \mathbf{F}^{(\beta)}\left(\mathbf{x}, t_{m+}, \boldsymbol{\mu}_j, \boldsymbol{\pi}\right)$ and the normal vector of the boundary $\partial\Sigma_{ij}$ is

$$\mathbf{n}_{\partial\Sigma_{ij}} = \nabla\varphi_{ij} = \left(\frac{\partial\varphi_{ij}}{\partial x}, \frac{\partial\varphi_{ij}}{\partial y}\right)_{(x_m, y_m)}^T. \tag{A11}$$

Since the semi passable boundary sets have been discussed the non-passable boundary sets will be developed. One type of non-passable boundary set is a sink boundary. In the traditional sense a sink is a point rather than a boundary. The length of the sink boundary depends on the initial conditions and parameters of the non-smooth system. The non-empty boundary set $\partial\Sigma_{ij}$ is a non-passable boundary of the first kind if only if

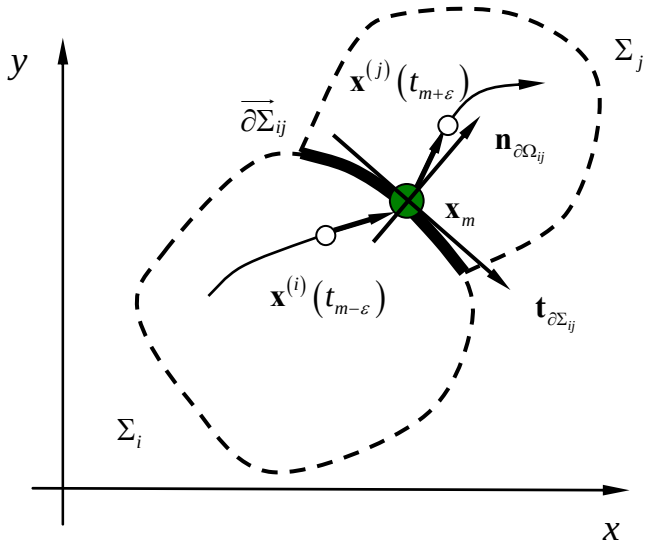

Fig.A 3Semi-passable boundary set $\overrightarrow{\partial\Sigma_{ij}}$ from the domain Σ_i to Σ_j convex to Σ_j.

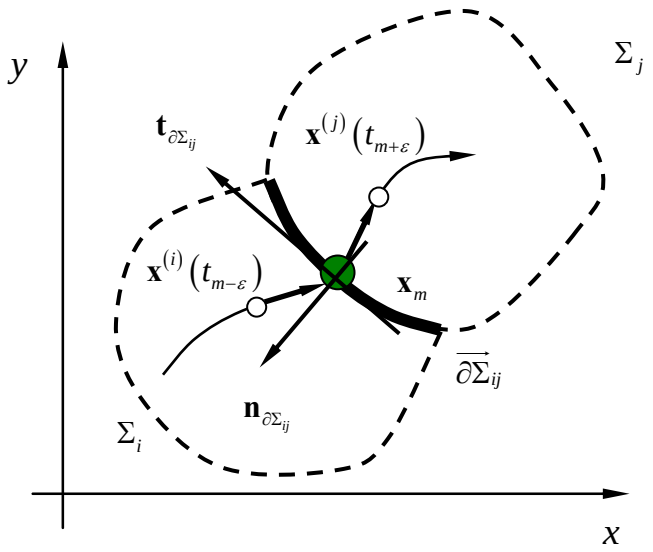

Fig.A 4 Semi-passable boundary set $\overrightarrow{\partial\Sigma_{ij}}$ from the domain Σ_i to Σ_j convex to Σ_i.

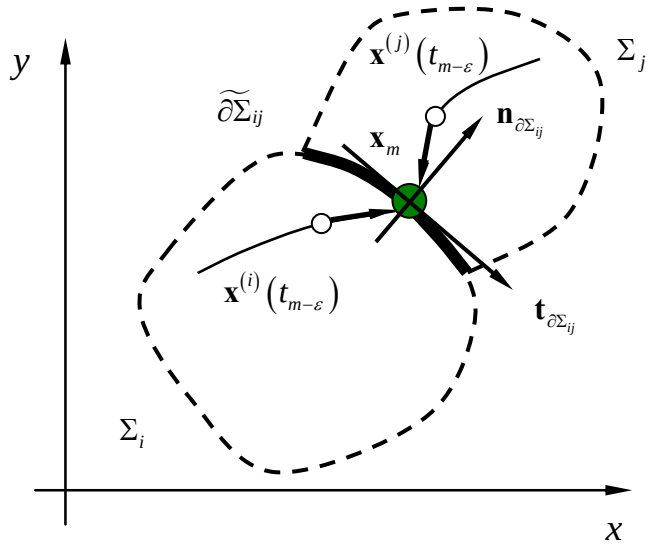

Fig.A 5 Non-passable boundary set $\overline{\partial\Sigma}_{ij} = \widetilde{\partial\Sigma}_{ij} \bigcup \widehat{\partial\Sigma}_{ij}$ the sink boundary.

$$\left[\mathbf{n}^T_{\partial\Sigma_{ij}} \bullet \mathbf{F}^{(i)}_i(t_{m-})\right] \times \left[\mathbf{n}^T_{\partial\Sigma_{ij}} \bullet \mathbf{F}^{(j)}_j(t_{m-})\right] < 0 \tag{A12}$$

where $\mathbf{F}^{(\alpha)}_{\alpha}(t_{m-}) \triangleq \mathbf{F}^{(\alpha)}(\mathbf{x}, t_{m-}, \boldsymbol{\mu}_{\alpha}, \boldsymbol{\pi})$ and $\mathbf{F}^{(\beta)}_{\alpha}(t_{m+}) \triangleq \mathbf{F}^{(\beta)}(\mathbf{x}, t_{m+}, \boldsymbol{\mu}_{\alpha}, \boldsymbol{\pi})$, see Fig.A 5. The proof of the theorems presented herein can be referred to in Luo [1,41].

Machine-Tool System Parameters

The dynamical system parameters for the machine-tool system in, the case the tool does not contact the work-piece, domain Ω_1 are

$$D^{(1)}_{11} = \tfrac{1}{m_{eq}\Omega} d_x,\ D^{(1)}_{12} = D^{(1)}_{21} = 0,\ D^{(1)}_{22} = \tfrac{1}{m_{eq}\Omega} d_y; \tag{A13}$$

$$K_{11}^{(1)} = \frac{1}{m_{eq}\Omega^2} k_x,\ K_{12}^{(1)} = K_{21}^{(1)} = 0,\ K_{22}^{(1)} = \frac{1}{m_{eq}\Omega^2} k_y; \tag{A14}$$

and

$$C_x^{(1)} = C_y^{(1)} = A_x^{(1)} = A_y^{(1)} = 0. \tag{A15}$$

The dynamical system parameters for this machine-tool system in, the case the tool contacts the work-piece where no cutting occurs, domain Ω_2 are

$$\left.\begin{aligned} D_{11}^{(2)} &= \frac{1}{m_{eq}\Omega}[d_x + d_1 \sin^2\beta],\ D_{12}^{(2)} = -\frac{1}{m_{eq}\Omega} d_1 \cos\beta \sin\beta, \\ D_{21}^{(2)} &= -\frac{1}{m_{eq}\Omega} d_1 \cos\beta \sin\beta,\ D_{22}^{(2)} = \frac{1}{m_{eq}\Omega}[d_y + d_1 \cos^2\beta]; \end{aligned}\right\} \tag{A16}$$

$$\left.\begin{aligned} K_{11}^{(2)} &= \frac{1}{m_{eq}\Omega^2}[k_x + k_1 \sin^2\beta],\ K_{12}^{(2)} = -\frac{1}{m_{eq}\Omega^2} k_1 \cos\beta \sin\beta, \\ K_{21}^{(2)} &= -\frac{1}{m_{eq}\Omega^2} k_1 \cos\beta \sin\beta,\ K_{22}^{(2)} = \frac{1}{m_{eq}\Omega^2}[k_y + k_1 \cos^2\beta]; \end{aligned}\right\} \tag{A17}$$

and

$$\left.\begin{aligned} C_x^{(2)} &= \frac{1}{m_{eq}\Omega^2}\{k_1[x_1^* \sin\beta - y_1^* \cos\beta]\sin\beta, \\ C_y^{(2)} &= \frac{1}{m_{eq}\Omega^2}\{-k_1[x_1^* \sin\beta - y_1^* \cos\beta]\cos\beta, \\ A_x^{(2)} &= \frac{A}{m_{eq}\Omega^2}\sin\eta,\ A_y^{(2)} = \frac{A}{m_{eq}\Omega^2}\cos\eta. \end{aligned}\right\} \tag{A18}$$

The amplitude A is the force amplitude, such as an eccentricity force. The dynamical system parameters for this machine-tool system in, the case the tool contacts the work-piece and cutting occurs where $\dot{z} < 0$ and $D_4 > 0$, domain Ω_3 and $\dot{z} > 0$, domain Ω_4;

$$\left.\begin{aligned} D_{11}^{(j)} &= \tfrac{1}{m_{eq}\Omega}[d_x + d_1 \sin^2\beta + d_2 \cos\alpha(\cos\alpha + (-1)^{j-1}\mu\sin\alpha)], \\ D_{12}^{(j)} &= \tfrac{1}{m_{eq}\Omega}[-d_1 \cos\beta\sin\beta - d_2 \sin\alpha(\cos\alpha + (-1)^{j-1}\mu\sin\alpha)], \end{aligned}\right\} \tag{A19}$$

$$\left.\begin{aligned} D_{21}^{(j)} &= \tfrac{1}{m_{eq}\Omega}[-d_1 \sin\beta\cos\beta - d_2 \cos\alpha(\sin\alpha + (-1)^{j}\mu\cos\alpha)], \\ D_{22}^{(j)} &= \tfrac{1}{m_{eq}\Omega}[d_y + d_1 \cos^2\beta + d_2 \sin\alpha(\sin\alpha + (-1)^{j}\mu\cos\alpha)]; \end{aligned}\right\} \tag{A20}$$

$$\left.\begin{aligned} K_{11}^{(j)} &= \tfrac{1}{m_{eq}\Omega^2}[k_x + k_1 \sin^2\beta + k_2 \cos\alpha(\cos\alpha + (-1)^{j-1}\mu\sin\alpha)], \\ K_{12}^{(j)} &= \tfrac{1}{m_{eq}\Omega^2}[-k_1 \cos\beta\sin\beta + k_2 \sin\alpha(\cos\alpha + (-1)^{j-1}\mu\sin\alpha)], \\ K_{21}^{(j)} &= \tfrac{1}{m_{eq}\Omega^2}[-k_1 \cos\beta\sin\beta - k_2 \cos\alpha(\sin\alpha + (-1)^{j}\mu\cos\alpha)], \\ K_{22}^{(j)} &= \tfrac{1}{m_{eq}\Omega^2}[k_y + k_1 \cos^2\beta + k_2 \sin\alpha(\sin\alpha + (-1)^{j}\mu\cos\alpha)]; \end{aligned}\right\} \tag{A21}$$

and

$$\begin{aligned} C_x^{(j)} = \tfrac{1}{m_{eq}\Omega^2}\{&k_1[x_1^* \sin\beta - y_1^* \cos\beta]\sin\beta \\ &+k_2[x_2^* \cos\alpha - y_2^* \sin\alpha][\cos\alpha + (-1)^{j-1}\mu\sin\alpha]\}, \end{aligned} \tag{A22}$$

$$\begin{aligned} C_y^{(j)} = \tfrac{1}{m_{eq}\Omega^2}\{&-k_1[x_1^* \sin\beta - y_1^* \cos\beta]\cos\beta \\ &+k_2[-x_2^* \cos\alpha + y_2^* \sin\alpha][\sin\alpha + (-1)^{j}\mu\cos\alpha]\}, \end{aligned} \tag{A23}$$

$$A_x^{(j)} = \frac{A}{m_{eq}\Omega^2}\sin\eta,\ A_y^{(j)} = \frac{A}{m_{eq}\Omega^2}\cos\eta. \tag{A24}$$

Equations A19-A24 are for j = 3,4; respectively.

The parameters for the machine-tool where the chip seizes to the tool-piece rake face ($\dot{z} \equiv 0$) are,

$$d = \frac{1}{2m_{eq}\Omega}\left[d_2 + d_1 \sin^2(\alpha+\beta) + d_x \cos^2\alpha + d_y \sin^2\alpha \right], \tag{A25}$$

$$\omega^2 = \frac{1}{m_{eq}\Omega^2}\left[k_1 \sin^2(\alpha+\beta) + k_2 + k_x \cos^2\alpha + k_y \sin^2\alpha \right], \tag{A26}$$

$$A_0 = \frac{A}{m_{eq}\Omega^2}\sin(\eta-\alpha), \tag{A27}$$

$$B_0 = \frac{V}{m_{eq}\Omega^2}\left[k_1 \cos(\alpha+\beta)\sin(\alpha+\beta) + (k_x - k_y)\cos\alpha\sin\alpha \right], \tag{A28}$$

$$\begin{aligned} C_0 = \frac{1}{m_{eq}\Omega^2}\big(& \{[d_1 V - k_1(Vt_0 + \tilde{y}_0)]\cos(\alpha+\beta) \\ & + k_1[x_1^* \sin\beta - y_1^* \cos\beta]\}\sin(\alpha+\beta) \\ & + [V(d_x - d_y) + (Vt_0 + \tilde{y}_0)(k_y - k_x)]\cos\alpha\sin\alpha \\ & + k_2 \tilde{x}_2^* \big). \end{aligned} \tag{A29}$$

Closed Form Solution to Linear Two Degree of Freedom System

The exact solution for this machine-tool system is presented as follows

(i) For λ_σ ($\sigma = 1, 2, \cdots, 4$) is real,

$$\begin{aligned} \begin{Bmatrix} x(t) \\ y(t) \end{Bmatrix} = & C_1 \begin{Bmatrix} 1 \\ r_{11} \end{Bmatrix} e^{\lambda_1 (t-t_0)} + C_2 \begin{Bmatrix} 1 \\ r_{12} \end{Bmatrix} e^{\lambda_2 (t-t_0)} + C_3 \begin{Bmatrix} 1 \\ r_{21} \end{Bmatrix} e^{\lambda_3 (t-t_0)} + C_4 \begin{Bmatrix} 1 \\ r_{22} \end{Bmatrix} e^{\lambda_4 (t-t_0)} \\ & + \begin{Bmatrix} A_{Px} \\ A_{Py} \end{Bmatrix} \cos(t) + \begin{Bmatrix} B_{Px} \\ B_{Py} \end{Bmatrix} \sin(t) + \begin{Bmatrix} C_{Px} \\ C_{Py} \end{Bmatrix} \end{aligned} \tag{A30}$$

(ii) For $\lambda_{1,2,3,4} = \alpha_1 \pm \beta_1 i,\ \alpha_2 \pm \beta_2 i$,

$$\begin{aligned}\begin{Bmatrix} x \\ y \end{Bmatrix} &= e^{\alpha_1 (t-t_0)} (C_1 \begin{Bmatrix} 1 \\ r_{11} \end{Bmatrix} \cos\left[\beta_1 (t-t_0)\right] + C_2 \begin{Bmatrix} 1 \\ r_{12} \end{Bmatrix} \sin\left[\beta_1 (t-t_0)\right]) \\ &+ e^{\alpha_2 (t-t_0)} (C_3 \begin{Bmatrix} 1 \\ r_{21} \end{Bmatrix} \cos\left[\beta_2 (t-t_0)\right] + C_4 \begin{Bmatrix} 1 \\ r_{22} \end{Bmatrix} \sin\left[\beta_2 (t-t_0)\right]) \\ &+ \begin{Bmatrix} A_{Px} \\ A_{Py} \end{Bmatrix} \cos(t) + \begin{Bmatrix} B_{Px} \\ B_{Py} \end{Bmatrix} \sin(t) + \begin{Bmatrix} C_{Px} \\ C_{Py} \end{Bmatrix},\end{aligned} \tag{A31}$$

(iii) For $\lambda_{1,2,3,4} = \alpha_1 \pm \beta_1 i,\quad \lambda_3$ and λ_4 are real

$$\begin{aligned}\begin{Bmatrix} x \\ y \end{Bmatrix} &= e^{\alpha_1 (t-t_0)} (C_1 \begin{Bmatrix} 1 \\ r_{11} \end{Bmatrix} \cos\left[\beta_1 (t-t_0)\right] + C_2 \begin{Bmatrix} 1 \\ r_{12} \end{Bmatrix} \sin\left[\beta_1 (t-t_0)\right]) \\ &+ C_3 \begin{Bmatrix} 1 \\ r_{21} \end{Bmatrix} e^{\lambda_3 (t-t_0)} + C_4 \begin{Bmatrix} 1 \\ r_{22} \end{Bmatrix} e^{\lambda_4 (t-t_0)} + \begin{Bmatrix} A_{Px} \\ A_{Py} \end{Bmatrix} \cos(t) \\ &+ \begin{Bmatrix} B_{Px} \\ B_{Py} \end{Bmatrix} \sin(t) + \begin{Bmatrix} C_{Px} \\ C_{Py} \end{Bmatrix}.\end{aligned} \tag{A32}$$

The constants $C_1^{(1)}$, $C_1^{(2)}$, $C_1^{(3)}$, $C_1^{(4)}$ for the system undergoing forced vibration can be found for cases (i)-(iii)

$$\begin{bmatrix} 1 & 1 & 1 & 1 \\ r_{11} & r_{12} & r_{21} & r_{22} \\ \lambda_1 & \lambda_2 & \lambda_3 & \lambda_4 \\ r_{11}\lambda_1 & r_{12}\lambda_2 & r_{21}\lambda_3 & r_{22}\lambda_4 \end{bmatrix} \begin{Bmatrix} C_1 \\ C_2 \\ C_3 \\ C_4 \end{Bmatrix} = \begin{Bmatrix} A \\ B \\ C \\ D \end{Bmatrix}, \tag{A33}$$

$$\begin{bmatrix} 1 & 0 & 1 & 0 \\ A_1 & B_1 & A_2 & B_2 \\ \alpha_1 & \beta_1 & \alpha_2 & \beta_2 \\ (A_1\alpha_1 - B_1\beta_1) & (B_1\alpha_1 + A_1\beta_1) & (A_2\alpha_2 - B_2\beta_2) & (B_2\alpha_2 + A_2\beta_2) \end{bmatrix} \begin{Bmatrix} C_1 \\ C_2 \\ C_3 \\ C_4 \end{Bmatrix} = \begin{Bmatrix} A \\ B \\ C \\ D \end{Bmatrix} \tag{A34}$$

$$\begin{bmatrix} 1 & 0 & 1 & 1 \\ r_{11} & 0 & r_{21} & r_{22} \\ \alpha_1 & \beta_1 & \alpha_2 & \beta_2 \\ \left(A_1\alpha_1 - B_1\beta_1\right) & \left(B_1\alpha_1 + A_1\beta_1\right) & r_{21}\lambda_3 & r_{22}\lambda_4 \end{bmatrix} \begin{Bmatrix} C_1 \\ C_2 \\ C_3 \\ C_4 \end{Bmatrix} = \begin{Bmatrix} A \\ B \\ C \\ D \end{Bmatrix} \tag{A35}$$

respectively. A_i and $B_i, (i = 1, 2)$ are the real and imaginary parts of the modal ratios from the eigenvalues of the machine tool system, such that

$$r_{ij} = A_i \pm B_j \text{ for } i, j = 1, 2; \tag{A36}$$

and if $B_j = 0$ then

$$r_{ij} = A_i \text{ for } i, j = 1, 2. \tag{A37}$$

The constant vector on the right-hand side of Eqs.(A33-A35), is

$$\begin{Bmatrix} A \\ B \\ C \\ D \end{Bmatrix} = \begin{Bmatrix} x_0 - A_{Px}\cos\left(\Omega t_0\right) - B_{Px}\sin\left(\Omega t_0\right) - C_{Px} \\ y_0 - A_{Py}\cos\left(\Omega t_0\right) - B_{Py}\sin\left(\Omega t_0\right) - C_{Py} \\ \dot{x}_0 + \Omega\left[A_{Px}\sin\left(\Omega t_0\right) - B_{Px}\cos\left(\Omega t_0\right)\right] \\ \dot{y}_0 + \Omega\left[A_{Py}\sin\left(\Omega t_0\right) - B_{Py}\cos\left(\Omega t_0\right)\right] \end{Bmatrix}. \tag{A38}$$

The particular solution coefficients are

$$\begin{bmatrix} \left(K_{11} - m\Omega^2\right) & K_{12} & \Omega D_{11} & \Omega D_{12} \\ K_{21} & \left(K_{22} - m\Omega^2\right) & \Omega D_{21} & \Omega D_{22} \\ -\Omega D_{11} & -\Omega D_{12} & \left(K_{11} - m\Omega^2\right) & K_{12} \\ -\Omega D_{21} & -\Omega D_{22} & K_{21} & \left(K_{22} - m\Omega^2\right) \end{bmatrix} \begin{Bmatrix} A_{Px} \\ A_{Py} \\ B_{Px} \\ B_{Py} \end{Bmatrix} = \begin{Bmatrix} A_x \\ A_y \\ 0 \\ 0 \end{Bmatrix} \tag{A39}$$

also,

$$\begin{bmatrix} C_{Px} \\ C_{Py} \end{bmatrix} = \frac{1}{K_{11}K_{22} - K_{12}K_{21}} \begin{bmatrix} K_{22} & -K_{12} \\ -K_{21} & K_{11} \end{bmatrix} \begin{bmatrix} C_x \\ C_y \end{bmatrix}. \tag{A40}$$

The analytical solution for the chip seizure motion for the special case $d^2 > \omega^2$ is

$$\begin{aligned} \tilde{x}(t) &= \tilde{C}_1 e^{-(d-\omega_d)(t-t_0)} + \tilde{C}_2 e^{-(d+\omega_d)(t-t_0)} \\ &\quad + A_5 \cos(\Omega t) + B_5 \sin(\Omega t) + C_5 t + D_5, \end{aligned} \tag{A41}$$

where

$$\begin{aligned} \tilde{C}_1 &= \frac{1}{2\omega_d}\Big\{(\tilde{x}_0 - C_5 t_0 - D_5)(d + \omega_d) - \left[A_5(d + \omega_d) + B_5\Omega\right]\cos(\Omega t_0) \\ &\quad + \left[A_5\Omega - B_5(d + \omega_d)\right]\sin(\Omega t_0) - C_5 + \dot{\tilde{x}}_0, \\ \tilde{C}_2 &= \frac{1}{2\omega_d}\Big\{(C_5 t_0 + D_5 - \tilde{x}_0)(d - \omega_d) - \dot{\tilde{x}}_0 + \left[B_5\Omega + A_5(d - \omega_d)\right]\cos(\Omega t_0) \\ &\quad + \left[B_5(d - \omega_d) - A_5\Omega\right]\sin(\Omega t_0) + C_5. \end{aligned} \tag{A42}$$

For the special case $d^2 < \omega^2$,

$$\begin{aligned} \tilde{x}(t) &= e^{-d(t-t_0)}\left\{\tilde{A}\cos\left[\omega_n(t - t_0)\right] + \tilde{B}\sin\left[\omega_n(t - t_0)\right]\right\} \\ &\quad + A_5 \cos(\Omega t) + B_5 \sin(\Omega t) + C_5 t + D_5; \end{aligned} \tag{A43}$$

where,

$$\begin{aligned} \tilde{A} &= \tilde{x}_0 - \left[A_5 \cos(\Omega t_0) + B_5 \sin(\Omega t_0) + C_5 t_0 + D_5\right], \\ \tilde{B} &= \frac{1}{\omega_d}\Big[(\Omega A_5 - dB_5)\sin(\Omega t_0) - (\Omega B_5 + dA_5)\cos(\Omega t_0) \\ &\quad + \dot{\tilde{x}}_0 + d\tilde{x}_0 - dC_5 t_0 - dD_5 - C_5\Big]. \end{aligned} \tag{A44}$$

For the special case $d^2 = \omega^2$,

$$\tilde{x}(t) = e^{-d(t-t_0)}\left[\tilde{C}_1 + \tilde{C}_2(t-t_0)\right] + A_5\cos(\Omega t) + B_5\sin(\Omega t) + C_5 t + D_5, \tag{A45}$$

where

$$\begin{aligned}
\tilde{C}_1 &= \tilde{x}_0 - \left[A_5\cos(\Omega t_0) + B_5\sin(\Omega t_0) + C_5 t_0 + D_5\right], \\
\tilde{C}_2 &= \begin{bmatrix} \dot{\tilde{x}}_0 + d\tilde{x}_0 - (dA_5 + \Omega B_5)\cos(\Omega t_0) \\ +(\Omega A_5 - dB_5)\sin(\Omega t_0) - dC_5 t_0 - dD_5 + C_5. \end{bmatrix}
\end{aligned} \tag{A46}$$

The particular solution coefficients are,

$$\begin{aligned}
A_5 &= \frac{A_F\sin(\eta-\alpha)(\omega^2-\Omega^2)}{m\left[(\omega^2-\Omega^2)^2 + (2d\Omega)^2\right]}, \\
B_5 &= \frac{2A_F d\Omega\sin(\eta-\alpha)}{m\left[(\omega^2-\Omega^2)^2 + (2d\Omega)^2\right]}, \\
C_5 &= B_0/\omega^2,\ D_5 = \frac{1}{\omega^4}(C_0\omega^2 - 2dB_0).
\end{aligned} \tag{A47}$$

VITA

Name:	Brandon Christopher Gegg
Address:	Texas A&M University, Mailstop: 3123 Department of Mechanical Engineering, College Station, Texas 77843
Email Address:	brandon_gegg@tamu.edu
Education:	Bachelor of Science in Mechanical Engineering, Southern Illinois University at Edwardsville, 2002. Master of Science in Mechanical Engineering, Southern Illinois University at Edwardsville, 2005. Doctor of Philosophy in Mechanical Engineering, Texas A&M University, 2009.